

Investigation of Ligand Field Modifications on Lanthanide<sup>III</sup>  
Complexes: Structure, Magnetism and Optical Properties

Zur Erlangung des akademischen Grades eines

DOKTORS DER NATURWISSENSCHAFTEN

(Dr. rer. nat.)

von der KIT-Fakultät für Chemie und Biowissenschaften

des Karlsruher Instituts für Technologie (KIT)

genehmigte

DISSERTATION

von

Luis Basche, M. Sc.

1. Referentin: Prof. Dr. Annie K. Powell

2. Referent: Prof. Dr. Horst Geckeis

Tag der mündlichen Prüfung: 19.07.2023



This document is licensed under a Creative Commons Attribution-NonCommercial-ShareAlike 4.0 International License (CC BY-NC-SA 4.0):  
<https://creativecommons.org/licenses/by-nc-sa/4.0/deed.en>

# EIDESSTÄTLICHE ERKLÄRUNG

Eidesstattliche Versicherung gemäß § 13 Absatz 2 Ziffer 3 der Promotionsordnung des Karlsruher Instituts für Technologie für die KIT-Fakultät für Chemie und Biowissenschaften:

1. Bei der eingereichten Dissertation zu dem Thema **Investigation of Ligand Field Modifications on Lanthanide<sup>III</sup> Complexes: Structure, Magnetism and Optical Properties** handelt es sich um meine eigenständig erbrachte Leistung.
2. Ich habe nur die angegebenen Quellen und Hilfsmittel benutzt und mich keiner unzulässigen Hilfe Dritter bedient. Insbesondere habe ich wörtlich und sinngemäß aus anderen Werken übernommene Inhalte als solche kenntlich gemacht.
3. Die Arbeit oder Teile davon habe ich bislang nicht an einer Hochschule des In- und Auslands als Bestandteil einer Prüfungs- oder Qualifikationsleistung vorgelegt.
4. Die Richtigkeit der vorstehenden Erklärungen bestätige ich.
5. Die Bedeutung der eidesstattlichen Versicherung und die strafrechtlichen Folgen einer unrichtigen oder unvollständigen eidesstattlichen Versicherung sind mir bekannt.

Ich versichere an Eides statt, dass ich nach bestem Wissen die reine Wahrheit erkläre und nichts verschwiegen habe.

.....

Ort und Datum

.....

Unterschrift

## ACKNOWLEDGEMENT

The work in this PhD thesis was completed between April 2020 and May 2023 at KIT under the supervision of Prof. Dr. Annie K. Powell. I want to thank her for accepting me as her student and giving me the opportunity to write this thesis.

I also like to thank the other members of campus south for their help. Dr. Christopher Anson concluded crystallographic analyses for me. Dr. Rouven F. Pflieger supervised me during my “Vertiefer” and master thesis. Dr. Umaira Shuaib helped me proofreading and training my English. Gertraud Amschlinger assisted me dealing with bureaucratic tasks.

I also received a lot of support from members of campus north. Dr. Olaf Fuhr, Dr. Andreas Eichhöfer and Prof. Dr. Dieter Fenske helped me with single crystal and powder X-ray measurements. Dr. Krisana Peewasan showed me strategies in organic syntheses. Sören Schlittenhardt and Dr. Senthil Kumar Kuppusamy performed magnetic analyses on my samples and assisted me handling the data. Christian Pacht calculated models for several compounds and helped explaining their magnetic behaviour. Nikolai Bartnick proceeded the elemental analyses of my samples and ordered needed commodities and chemicals for me.

But of course I also received a lot of support from my family and friends. On the one hand there are my parents, Pia and Gerd, without whose upbringing I would not have become the person I am today. On the other hand, there is my grandfather Heinz-Josef who always believed in me. My friends, Ulf, Andi and Felix, have accepted me for who I am and have included me in their hobbies. The most essential support on my path was given from my partner Laura by always being on my side.

## ABSTRACT

This work deals with lanthanide complexes, their structure, magnetism and optical properties. Scandium, yttrium and the lanthanides reaching from lanthanum to lutetium are the rare-earth elements. They generally show similar chemical and physical properties. Starting with cerium and ending with lutetium, the 4f orbitals are progressively filled. These elements generally adopt a stable oxidation state of +3.

The first focus of this work is on the molecular structures of lanthanide complexes. A ligand system was designed which can be easily modified, in order to understand how changes in the structure of the ligand affect the geometry of the resulting complexes. The changes to the ligand were intentionally kept small to understand better the effects of these changes. In total, seven related ligands were used. In addition, different lanthanide ions were tested for some of these systems. Due to the lanthanide contraction, their ionic radius decreases sharply across the series. This can change the coordination number, the metal-ligand bond length and the molecular structure. In the context of this work, the molecular structure of sixteen complexes, ten of which are dinuclear compounds and six are mononuclear compounds were determined by X-ray crystallography. The investigations are supported by SHAPE analyses of the coordination polyhedra. The dinuclear compounds are composed of seven phenolate and three acetate bridged structures.

The second focus is on the magnetic properties of these complexes. Since Dy<sup>III</sup> ions are most commonly used for lanthanide-based single-molecule magnets (SMMs) due to their combination of a strong uniaxial magnetic moment and a high  $m_J$  value of  $\pm 15/2$ , the focus of this work is on the synthesis of Dy<sup>III</sup> complexes. Magnetic investigations of five dinuclear Dy<sup>III</sup> compounds were carried out on a SQUID magnetometer and AC measurements were carried out to better understand the SMM behaviour. Three of the presented compounds show fast relaxation processes and one shows no SMM behaviour. On the other hand, compound  $[\text{Dy}_2(\text{L}2)_2(\text{CH}_3\text{COO})_4(\text{CH}_3\text{OH})_2]$  (**6**) turns out to be an excellent SMM. It has an energy barrier  $U_{\text{eff}}$  of 50(10) K and a relaxation time  $\tau_0$  of  $7(5) \cdot 10^{-6}$  s and shows SMM behaviour up to a temperature of 15 K.

Furthermore, *ab-initio* calculations were performed for these five compounds to estimate the energy levels of the excited Kramer doublets and the preferred orientation of the anisotropic axes in the ground doublets. The anisotropy axes were also calculated using MAGELLAN and compared with the *ab-initio* results. The calculated Kramer doublets agree well with the measured magnetic behaviour. The alignment of the anisotropy axes illustrates why the acetate-bridged dimers are better suited for preventing spin reversal than the phenolate-bridged dimers.

The third focus is on the optical properties of such lanthanide complexes. Extensive series of measurements were carried out on the optical absorption behaviour of the ligand 2,6-(1-(2-(1H-benzimidazol-2-yl)hydrazineylidene)ethyl)pyridine (HL7) and its complexes with all lanthanide ions. An equilibrium in solution was discovered by adding acid and base, between the isolated protonated ligand, the protonated complex and the deprotonated complex. Concentration-dependent measurements show that this equilibrium also changes at different concentrations, indicating an intermolecular interaction between the molecules in solution.

## ZUSAMMENFASSUNG

Diese Arbeit befasst sich mit Lanthanoidkomplexen, ihrer Struktur, ihrem Magnetismus und ihren optischen Eigenschaften. Scandium, Yttrium und die Lanthanoide von Lanthan bis Lutetium sind die Elemente der Seltenen Erden. Sie weisen im Allgemeinen ähnliche chemische und physikalische Eigenschaften auf. Beginnend mit Cer und endend mit Lutetium werden die 4f-Orbitale nach und nach gefüllt. Diese Elemente nehmen im Allgemeinen eine stabile Oxidationsstufe von +3 an.

Der erste Schwerpunkt dieser Arbeit liegt auf den molekularen Strukturen von Lanthanoidkomplexen. Es wurde ein Ligandensystem entworfen, das leicht modifiziert werden kann, um zu verstehen, wie sich Änderungen in der Struktur des Liganden auf die Geometrie der resultierenden Komplexe auswirken. Die Änderungen am Liganden wurden bewusst klein gehalten, um die Auswirkungen dieser Änderungen besser zu verstehen. Insgesamt wurden sieben verwandte Liganden verwendet. Darüber hinaus wurden für einige dieser Systeme unterschiedliche Lanthanoidionen getestet. Aufgrund der Lanthanoidkontraktion nimmt ihr Ionenradius im Laufe der Reihe stark ab. Dadurch können sich die Koordinationszahl, die Metall-Ligand-Bindungslänge und die Molekülstruktur verändern. Im Rahmen dieser Arbeit wurde die Molekülstruktur von sechzehn Komplexen, davon zehn zweikernige Verbindungen und sechs einkernige Verbindungen, durch Röntgenkristallographie bestimmt. Unterstützt werden die Untersuchungen durch SHAPE-Analysen der Koordinationspolyeder. Die zweikernigen Verbindungen bestehen aus sieben Phenolat- und drei Acetat-verbunden Strukturen.

Der zweite Schwerpunkt liegt auf den magnetischen Eigenschaften dieser Komplexe. Da Dy<sup>III</sup>-Ionen aufgrund ihrer Kombination aus einem starken uniaxialen magnetischen Moment und einem hohen  $m_J$ -Wert von  $\pm 15/2$  am häufigsten für Lanthanoid-basierte Einzelmolekülmagnete (SMMs) verwendet werden, liegt der Schwerpunkt dieser Arbeit auf der Synthese von Dy<sup>III</sup>-Komplexe. Magnetische Untersuchungen von fünf zweikernigen Dy<sup>III</sup>-Verbindungen wurden an einem SQUID-Magnetometer durchgeführt und AC-Messungen wurden durchgeführt, um das SMM-Verhalten besser zu verstehen. Drei der vorgestellten Verbindungen zeigen schnelle Relaxationsprozesse und eine zeigt kein SMM-Verhalten. Andererseits erweist sich die Verbindung  $[\text{Dy}_2(\text{L}2)_2(\text{CH}_3\text{COO})_4(\text{CH}_3\text{OH})_2]$  (**6**) als ausgezeichnetes SMM.

Es hat eine Energiebarriere  $U_{\text{eff}}$  von 50(10) K und eine Relaxationszeit  $\tau_0$  von  $7(5) \cdot 10^{-6}$  s und zeigt SMM-Verhalten bis zu einer Temperatur von 15 K. Darüber hinaus wurden für diese fünf Verbindungen *ab-initio*-Rechnungen durchgeführt, um die Energieniveaus der angeregten Kramer-Dubletts und die bevorzugte Ausrichtung der anisotropen Achsen in den Grunddubletts abzuschätzen. Die Anisotropieachsen wurden ebenfalls mit MAGELLAN berechnet und mit den *ab-initio*-Ergebnissen verglichen. Die berechneten Kramer-Dubletts stimmen gut mit dem gemessenen magnetischen Verhalten überein. Die Ausrichtung der Anisotropieachsen verdeutlicht, warum die Acetat-verbrückten Dimere besser geeignet sind, eine Spinumkehr zu verhindern als die Phenolat-verbrückten Dimere.

Der dritte Schwerpunkt liegt auf den optischen Eigenschaften solcher Lanthanoidkomplexe. Umfangreiche Messreihen wurden zum optischen Absorptionsverhalten des Liganden 2,6-(1-(2-(1H-Benzimidazol-2-yl)hydrazineyliden)ethyl)pyridin (HL7) und seiner Komplexe mit allen Lanthanoidionen durchgeführt. Durch Zugabe von Säure und Base wurde in Lösung ein Gleichgewicht zwischen dem isolierten protonierten Liganden, dem protonierten Komplex und dem deprotonierten Komplex gefunden. Konzentrationsabhängige Messungen zeigen, dass sich dieses Gleichgewicht auch bei unterschiedlichen Konzentrationen ändert, was auf eine intermolekulare Wechselwirkung zwischen den Molekülen in Lösung hinweist.

# INDEX

|   |            |
|---|------------|
| <b><u>ACKNOWLEDGEMENT</u></b> .....                 | <b>I</b>   |
| <b><u>ABSTRACT</u></b> .....                        | <b>II</b>  |
| <b><u>ZUSAMMENFASSUNG</u></b> .....                 | <b>IV</b>  |
| <b><u>INDEX</u></b> .....                           | <b>VI</b>  |
| <b><u>LIST OF FIGURES</u></b> .....                 | <b>IX</b>  |
| <b><u>LIST OF TABLES</u></b> .....                  | <b>XIV</b> |
| <b><u>LIST OF FORMULAS</u></b> .....                | <b>XIV</b> |
| <b><u>LIST OF ABBREVIATES</u></b> .....             | <b>XV</b>  |
| <b><u>1 INTRODUCTION</u></b> .....                  | <b>1</b>   |
| <b><u>2 THEORETICAL BACKGROUND</u></b> .....        | <b>3</b>   |
| <u>2.1 Magnetism</u> .....                          | 3          |
| 2.1.1 Matter in magnetic fields.....                | 3          |
| 2.1.2 Magnetic moment.....                          | 5          |
| 2.1.3 Diamagnetism.....                             | 7          |
| 2.1.4 Paramagnetism.....                            | 8          |
| 2.1.5 Spin order and magnetization.....             | 12         |
| <u>2.2 Single-molecule magnetism</u> .....          | 15         |
| 2.2.1 Overview of single-molecule magnets.....      | 15         |
| 2.2.2 Lanthanide-based single-molecule magnets..... | 17         |
| <u>2.3 Photoluminescence</u> .....                  | 22         |
| 2.3.1 Luminescence in coordination compounds.....   | 23         |
| <u>2.4 Coordination compounds</u> .....             | 24         |
| 2.4.1 Bonding theories.....                         | 25         |
| 2.4.1.1 Crystal field theory.....                   | 26         |
| 2.4.1.2 Ligand field theory.....                    | 28         |
| <u>2.5 Designing lanthanide complexes</u> .....     | 29         |

|   |            |
|---|------------|
| 2.6 Schiff bases.....   | 31         |
| <b>3 MOTIVATION.....</b>  | <b>33</b>  |
| <b>4 RESULTS AND DISCUSSION.....</b>  | <b>34</b>  |
| 4.1 Dinuclear lanthanide systems.....   | 35         |
| 4.1.1 Dinuclear lanthanide complexes (1) to (4) obtained from HL1.....                          | 37         |
| 4.1.1.1 Magnetic properties of complexes (1), (3) and (4).....                                  | 49         |
| 4.1.2 Dinuclear dysprosium complexes (5) and (6) obtained from HL2.....                         | 59         |
| 4.1.2.1 Magnetic properties of complexes (5) and (6).....                                       | 67         |
| 4.1.3 Dinuclear dysprosium complex (7) obtained from HL3.....                                   | 75         |
| 4.1.4 Dinuclear dysprosium complex (8) obtained from HL4.....                                   | 80         |
| 4.1.5 Dinuclear dysprosium complexes (9) and (10) obtained from HL5.....                        | 85         |
| 4.2 Mononuclear lanthanide systems with pentaaza ligands.....                                   | 95         |
| 4.2.1 Mononuclear dysprosium complexes (11) and (12) obtained from L6.....                      | 96         |
| 4.2.2 Mononuclear dysprosium complexes (13) to (16) obtained from HL7.....                      | 105        |
| 4.2.2.1 Optical properties of complexes obtained from HL7.....                                  | 119        |
| <b>5 CONCLUSIONS.....</b>   | <b>129</b> |
| 5.1 Dinuclear coordination compounds.....   | 129        |
| 5.2 Mononuclear coordination compounds.....   | 131        |
| <b>6 EXPERIMENTAL.....</b>  | <b>133</b> |
| <b>7 SYNTHESIS.....</b>   | <b>135</b> |
| 7.1 Synthesis of ligands.....   | 135        |
| 7.1.1 2-(2-(1H-benzoimidazol-2-yl)hydrazineylidene)methyl-6-methoxyphenol<br>(HL1).....         | 135        |
| 7.1.2 2-methoxy-6-(pyridin-2-yl-hydrazonomethyl)phenol (HL2).....                               | 135        |
| 7.1.3 2-((2-(1H-benzoimidazol-2-yl)hydrazineylidene)methyl)-6-ethoxyphenol<br>(HL3).....        | 136        |
| 7.1.4 2-(2-(1H-benzoimidazol-2-yl)hydrazineylidene)methyl-4-bromo-6-methoxyphenol<br>(HL4)..... | 136        |

|  |            |
|--|------------|
| 7.1.5 4-chloro-2-methoxy-6-((2-(pyridin-2-yl)hydrazineylidene)methyl)phenol (HL5).....   | 137        |
| 7.1.6 1,1-(pyridine-2,6-diyl)bis(N-(pyridin-2-ylmethyl)methanimine) (L6).....  | 137        |
| 7.1.7 2,6-(1-(2-(1H-benzoimidazol-2-yl)hydrazineylidene)ethyl)pyridine (HL7).....  | 138        |
| <b>7.2 Synthesis of complexes</b> .....  | <b>139</b> |
| 7.2.1 [Dy <sub>2</sub> (L1) <sub>2</sub> (NO <sub>3</sub> ) <sub>4</sub> ].2CH <sub>3</sub> CN (1).....  | 139        |
| 7.2.2 [Nd <sub>2</sub> (L1) <sub>2</sub> (NO <sub>3</sub> ) <sub>4</sub> CH <sub>3</sub> OH].CH <sub>3</sub> CN (2).....   | 139        |
| 7.2.3 [Dy <sub>2</sub> (L1) <sub>2</sub> (H <sub>2</sub> O) <sub>6</sub> ]Cl <sub>4</sub> .2.5CH <sub>3</sub> OH.2.5CH <sub>3</sub> CN (3).....  | 140        |
| 7.2.4 [Dy <sub>2</sub> (L1) <sub>2</sub> (H <sub>2</sub> O) <sub>6</sub> ]Br <sub>4</sub> .2CH <sub>3</sub> OH.2CH <sub>3</sub> CN (4).....  | 140        |
| 7.2.5 [Dy <sub>2</sub> (L2) <sub>2</sub> (NO <sub>3</sub> ) <sub>4</sub> ].2CH <sub>3</sub> CN (5).....  | 140        |
| 7.2.6 [Dy <sub>2</sub> (L2) <sub>2</sub> (CH <sub>3</sub> COO) <sub>4</sub> (CH <sub>3</sub> OH) <sub>2</sub> ].4CH <sub>3</sub> OH (6).....   | 141        |
| 7.2.7 [Dy <sub>2</sub> (L3) <sub>2</sub> (CH <sub>3</sub> COO) <sub>4</sub> (H <sub>2</sub> O) <sub>2</sub> ].2H <sub>2</sub> O.4CH <sub>3</sub> OH (7).....                                       | 141        |
| 7.2.8 [Dy <sub>2</sub> (L4) <sub>2</sub> (H <sub>2</sub> O) <sub>6</sub> ]Cl <sub>4</sub> .2CH <sub>3</sub> CN (8).....  | 141        |
| 7.2.9 [Dy <sub>2</sub> (L5) <sub>2</sub> (CH <sub>3</sub> COO) <sub>4</sub> (CH <sub>3</sub> OH) <sub>2</sub> ] (9).....   | 142        |
| 7.2.10 [Dy <sub>2</sub> (L5) <sub>4</sub> (μ-H <sub>2</sub> O)]Cl <sub>2</sub> .H <sub>2</sub> O.CH <sub>3</sub> OH.CH <sub>3</sub> CN.(CH <sub>3</sub> CH <sub>2</sub> ) <sub>2</sub> O (10)..... | 142        |
| 7.2.11 [DyL6(H <sub>2</sub> O) <sub>4</sub> ]Cl <sub>3</sub> .6H <sub>2</sub> O (11).....  | 143        |
| 7.2.12 [DyL6(H <sub>2</sub> O) <sub>4</sub> ]Br <sub>3</sub> .4.5H <sub>2</sub> O (12).....  | 143        |
| 7.2.13 [Pr(HL7)(NO <sub>3</sub> ) <sub>2</sub> CH <sub>3</sub> OH]NO <sub>3</sub> .2CH <sub>3</sub> OH.H <sub>2</sub> O (13).....  | 143        |
| 7.2.14 [Sm(HL7)(NO <sub>3</sub> ) <sub>2</sub> CH <sub>3</sub> OH]NO <sub>3</sub> .CH <sub>3</sub> OH (14).....  | 144        |
| 7.2.15 [DyL7(NO <sub>3</sub> ) <sub>2</sub> ].CH <sub>3</sub> OH (15).....   | 144        |
| 7.2.16 [Dy(HL7)(CH <sub>3</sub> COO) <sub>2</sub> ]CF <sub>3</sub> SO <sub>3</sub> .CH <sub>3</sub> OH (16).....   | 145        |
| <b>8 REFERENCES</b> .....  | <b>146</b> |
| <b>9 APPENDIX</b> .....  | <b>151</b> |
| 9.1 Crystallographic data.....   | 151        |

## LIST OF FIGURES

|   |    |
|---|----|
| <b>Figure 1:</b> Magnetic field lines of an external homogeneous field penetrate matter. The diamagnetic substance is pushed out of the inhomogeneous field, the paramagnetic substance is drawn into the field.....  | 4  |
| <b>Figure 2:</b> Dependence of susceptibility on temperature (black curve: paramagnetism; blue curve: ferromagnetism; green curve: ferrimagnetism; dark red line: antiferromagnetism).....  | 9  |
| <b>Figure 3:</b> Magnetic moments of the trivalent lanthanides $\text{Ln}^{\text{III}}$ . The black dots show the experimentally measured values, the blue line represents the calculated values. <sup>[1]</sup> .....  | 11 |
| <b>Figure 4:</b> Schematic representation of a hysteresis loop of a ferromagnetic material. The magnetic moments of Weiss' areas are arranged according to the magnetic field lines of the external magnetic field.....   | 13 |
| <b>Figure 5:</b> Schematic representation of the different spin orientation below the Curie temperature $T_C$ (ferro and ferri) and below the Néel temperature $T_N$ (antiferro) for different types of material.....   | 14 |
| <b>Figure 6:</b> Energy barrier to spin relaxation using the example of the first SMM, the $\text{Mn}_{12}$ -cluster. <sup>[10]</sup> ...   | 16 |
| <b>Figure 7:</b> Schematic view of the core of the $\text{Mn}_{12}$ cluster. Rose atoms represent $\text{Mn}^{\text{III}}$ ( $S = 2$ ), pink atoms present $\text{Mn}^{\text{IV}}$ ( $S = 3/2$ ) and the small red atoms represent bridging oxygen atoms.....                 | 16 |
| <b>Figure 8:</b> Schematic visualization of the magnetization and magnetic relaxation processes in a single molecule magnet.....  | 16 |
| <b>Figure 9:</b> Visualization of the most common relaxation paths. Starting from a state with maximal magnetization in the ground-state doublet to the time-reversed state in lanthanide single-molecule magnets. <sup>[10]</sup> .....                                      | 18 |
| <b>Figure 10:</b> Quadrupole approximation of the electron density distribution of the 4f shell of the $\text{Ln}^{\text{III}}$ ions. <sup>[3, 23]</sup> .....  | 19 |
| <b>Figure 11:</b> Approximations of the angular dependence of the total 4f charge density for $m_J$ states. <sup>[3, 24]</sup>  | 19 |
| <b>Figure 12:</b> Plots of low- and high-energy configuration f-orbital electron density versus crystal field environment for a stretched 4f ion. The green arrow represents the orientation of the spin angular momentum coupled to the orbital period. <sup>[3]</sup> ..... | 20 |
| <b>Figure 13:</b> Jablonski diagram showing the possible transitions of valence electrons in various excited states after absorbing light. There is the singlet ground $S_0$ , the singlet excited state $S_1$ and the triplet excited state $T_1$ .....                      | 22 |
| <b>Figure 14:</b> Ferrocene $[\text{Fe}(\eta^5\text{-C}_5\text{H}_5)_2]$ is an electron donor–acceptor complex with a metal ion acceptor and two aromatic $\pi$ -donors. <sup>[30]</sup> .....  | 23 |
| <b>Figure 15:</b> The $[\text{Fe}(\text{C}_5\text{Me}_5)_2]^+$ cation can act as a donor and the corresponding anion can act as an electron acceptor. <sup>[31]</sup> .....   | 23 |
| <b>Figure 16:</b> The complex cation $[\text{Co}(\text{NH}_3)_6]^{3+}$ presenting the charge distribution as a result from a 100% covalent model (a) or 100% ionic model (b). Applying the electroneutrality principle results in model (c).....                              | 25 |
| <b>Figure 17:</b> Changes in the energies of the 3d-orbitals of an ion. The metal centre is surrounded by no ligands (left), by point charge ligands spherically (middle) and by point charge ligands octahedral (right).....   | 26 |
| <b>Figure 18:</b> Relative magnitudes of the perturbations in the 4f ions shown for $\text{Dy}^{\text{III}}$ . <sup>[3]</sup> .....   | 27 |
| <b>Figure 19:</b> High- and low-spin arrangement of electrons for the $d^4$ to $d^7$ configurations between the $t_{2g}$ and $e_g$ levels.....  | 28 |
| <b>Figure 20:</b> The ionic radii throughout the lanthanide series, visualising lanthanide contraction. Values are taken from R. D. Shannon. <sup>[36]</sup> .....  | 29 |

|  |    |
|--|----|
| <b>Figure 21:</b> Complex formation of $C_{38}H_{47}Br_2N_{14}O_{14}Yb$ . <sup>[37]</sup> .....  | 30 |
| <b>Figure 22:</b> The four dinuclear lanthanide complexes using HL1 as ligand $[Dy_2(L1)_2(NO_3)_4]$ (1), $[Nd_2(L1)_2(NO_3)_4CH_3OH]$ (2), $[Dy_2(L1)_2(H_2O)_6]Cl_4$ (3) and $[Dy_2(L1)_2(H_2O)_6]Br_4$ (4)..... | 38 |
| <b>Figure 23:</b> Powder patterns of $[Ln_2(L1)_2(NO_3)_4] \cdot 2CH_3CN$ (Ln = Gd to Lu).....   | 39 |
| <b>Figure 24:</b> Powder patterns of $[Ln_2(L1)_2(NO_3)_4MeOH] \cdot CH_3CN$ (Ln = Pr to Sm) versus the simulated pattern of (2).....  | 40 |
| <b>Figure 25:</b> The measured powder pattern of the Eu-L1 complex versus the simulated patterns of (1) and (2).....   | 40 |
| <b>Figure 26:</b> Powder pattern of (3) simulated versus measured.....   | 41 |
| <b>Figure 27:</b> Powder pattern of (4) simulated versus measured.....   | 41 |
| <b>Figure 28:</b> Structure of (1) and (2) with selected atoms labelled.....   | 42 |
| <b>Figure 29:</b> Structure of (3) and (4) with selected atoms labelled.....   | 43 |
| <b>Figure 30:</b> Nine-vertex polyhedron around the dysprosium centre of (1) with SHAPE values.....  | 44 |
| <b>Figure 31:</b> Nine-vertex polyhedra around the neodymium centres of (2) with SHAPE values.....   | 45 |
| <b>Figure 32:</b> Eight-vertex polyhedron around the dysprosium centre of (3) with SHAPE values.....   | 45 |
| <b>Figure 33:</b> Eight-vertex polyhedron around the dysprosium centre of (4) with SHAPE values.....   | 46 |
| <b>Figure 34:</b> Compound (1) showing the hydrogen-bonds as green dashed lines (left, hydrogen on carbon atoms not displayed) and unit cell (right).....  | 46 |
| <b>Figure 35:</b> Compound (2) showing the hydrogen-bonds as green dashed lines (left) and the unit cell packing (right).....  | 47 |
| <b>Figure 36:</b> Unit cell packing of (3) (top) and (4) (bottom) showing the hydrogen bonds as green dashed lines.....  | 48 |
| <b>Figure 37:</b> Plot of $\chi T$ versus temperature for compound (1) (top), (3) (middle) and (4) (bottom).....   | 49 |
| <b>Figure 38:</b> The anisotropy of the 4f shell electron distribution from quadrupole approximations for $Dy^{III}$ along the Ising axis. <sup>[10]</sup> .....   | 50 |
| <b>Figure 39:</b> Plot of $\chi''$ versus frequency for (1) at different temperatures and 4400 Oe.....   | 50 |
| <b>Figure 40:</b> Plot of $\chi''$ versus frequency for (3) at different temperatures.....   | 52 |
| <b>Figure 41:</b> Plot of $\ln(\tau_0)$ versus $1/T$ for (3).....  | 52 |
| <b>Figure 42:</b> Plot of $\chi''$ versus frequency for (4) at 2 Kelvin and different strengths of an external magnetic field.....   | 53 |
| <b>Figure 43:</b> Plot of $\chi''$ versus frequency for (4) at different temperatures and 3000 Oe.....   | 53 |
| <b>Figure 44:</b> Plot of $\ln(\tau_0)$ versus $1/T$ for (4).....  | 54 |
| <b>Figure 45:</b> Zero Field splitting calculated for the dinuclear Dy-compounds (1), (3) and (4).....   | 55 |
| <b>Figure 46:</b> Anisotropy axis calculated via <i>ab-initio</i> (green) and with MAGELLAN (light blue) for compound (1).....   | 57 |
| <b>Figure 47:</b> Anisotropy axis calculated via <i>ab-initio</i> (green) and with MAGELLAN (light blue) for compound (3).....   | 57 |
| <b>Figure 48:</b> Anisotropy axis calculated via <i>ab-initio</i> (green) and with MAGELLAN (light blue) for compound (4).....   | 57 |
| <b>Figure 49:</b> The two dinuclear lanthanide complexes using HL2 as ligand $[Dy_2(L2)_2(NO_3)_4]$ (5) and $[Dy_2(L1)_2(CH_3COO)_4(MeOH)_2]$ (6).....   | 59 |

|  |    |
|--|----|
| <b>Figure 50:</b> Powder patterns of $[\text{Ln}_2(\text{L}2)_2(\text{NO}_3)_4]\cdot 2\text{CH}_3\text{CN}$ for Ln= Eu to Lu.....  | 61 |
| <b>Figure 51:</b> Powder pattern of (6) versus simulated powder pattern.....   | 61 |
| <b>Figure 52:</b> Structure of (5) (left) and (6) (right) with selected atoms labelled. A potential ninth coordination mode in compound (6) is shown as a dashed green line.....                                     | 62 |
| <b>Figure 53:</b> Nine-vertex polyhedron around the dysprosium centre of (5) with SHAPE values.....  | 63 |
| <b>Figure 54:</b> Nine-vertex polyhedron (top) and eight-vertex polyhedron (bottom) around the dysprosium centre of (6) with SHAPE values.....   | 64 |
| <b>Figure 55:</b> Ladder-like inter-nitrate interactions in the structure of (5). The hydrogen bonds shown as green dashed lines, supramolecular interactions shown as light green dashed lines.....                 | 65 |
| <b>Figure 56:</b> Unit cell packing of compound (5).....   | 66 |
| <b>Figure 57:</b> Unit cell packing of (6) showing the hydrogen bonds as green dashed lines. For clarity hydrogen atoms on carbon are not displayed.....   | 66 |
| <b>Figure 58:</b> Plot of $\chi T$ versus temperature for compound (5) (top) and (6) (bottom).....   | 67 |
| <b>Figure 59:</b> Plot of $\chi''$ versus frequency for (5) at different temperatures at an external field of 5250 Oe..  | 68 |
| <b>Figure 60:</b> Plot of $\chi''$ versus frequency for (6) at different temperatures. Due to a restart during the measurement, there is a gap from 9 to 11 Kelvin in the data.....                                  | 69 |
| <b>Figure 61:</b> Plot of $1/(\tau_0)$ versus T for (6). The vertical red lines are error bars, the blue curve is the fit...70   | 70 |
| <b>Figure 62:</b> Plot of $\ln(\tau_0)$ versus $1/T$ for (6).....  | 70 |
| <b>Figure 63:</b> Zero Field splitting calculated for the dinuclear Dy-compounds (5) and (6).....  | 71 |
| <b>Figure 64:</b> Zero Field splitting calculated for the dinuclear Dy-compounds (1), (3), (4), (5) and (6).....   | 72 |
| <b>Figure 65:</b> Anisotropy axis calculated via <i>ab-initio</i> (green) and with MAGELLAN (light blue) for compound (5).....   | 74 |
| <b>Figure 66:</b> Anisotropy axis calculated via <i>ab-initio</i> (green) and with MAGELLAN (light blue) for compound (6).....   | 74 |
| <b>Figure 67:</b> The dinuclear lanthanide complexes using HL3 as ligand $[\text{Dy}_2(\text{L}3)_2(\text{CH}_3\text{COO})_4(\text{H}_2\text{O})_2]$ (7).....  | 75 |
| <b>Figure 68:</b> Measured powder pattern of (7) versus simulated pattern from single crystal data.....  | 76 |
| <b>Figure 69:</b> Structure of (7) with selected atoms labelled. A potential ninth coordination mode is shown as a dashed green line.....  | 77 |
| <b>Figure 70:</b> Nine-vertex polyhedron (top) and eight-vertex polyhedron (bottom) around the dysprosium centre of (7) with SHAPE values.....   | 78 |
| <b>Figure 71:</b> Unit cell packing of (7) showing the hydrogen bonds as green dashed lines. Disordered lattice solvent molecules are omitted for clarity.....   | 79 |
| <b>Figure 72:</b> The dinuclear lanthanide complex $[\text{Dy}_2(\text{L}4)_2(\text{H}_2\text{O})_6]\text{Cl}_4\cdot 2\text{CH}_3\text{CN}$ (8) using HL4 as a ligand.....   | 80 |
| <b>Figure 73:</b> Measured powder pattern of (8) versus simulated pattern from single crystal data.....  | 81 |
| <b>Figure 74:</b> Structure of (8) with selected atoms labelled. The hydrogen bonds shown as green dashed lines. The halogen-halogen bonds shown as red dashed lines.....  | 82 |
| <b>Figure 75:</b> Eight-vertex polyhedron of (8) with SHAPE values.....  | 83 |
| <b>Figure 76:</b> Intermolecular interactions of (8). Hydrogen bonds are shown as green dashed lines, chloride-bromine bonds as red dashed lines. The complex was reduced to a monomer for better visualisation..... | 84 |

|   |     |
|---|-----|
| <b>Figure 77:</b> Unit cell packing of compound (8).....  | 84  |
| <b>Figure 78:</b> The dinuclear lanthanide complexes (9) and (10) using HL5 as a ligand.....  | 86  |
| <b>Figure 79:</b> Measured powder pattern of (9) versus simulated pattern from single crystal data.....   | 88  |
| <b>Figure 80:</b> Measured powder pattern of (10) versus simulated pattern from single crystal data.....  | 88  |
| <b>Figure 81:</b> Structure of (9) with selected atoms labelled.....  | 89  |
| <b>Figure 82:</b> Structure of (10) with selected atoms labelled.....   | 90  |
| <b>Figure 83:</b> Nine-vertex polyhedron of (9) with SHAPE values.....  | 91  |
| <b>Figure 84:</b> Nine-vertex polyhedron of (10) with SHAPE values.....   | 91  |
| <b>Figure 85:</b> Intermolecular interactions of (9). Hydrogen bonds are shown as green dashed lines, chlorine- $\pi$ -system interactions shown as light green dashed lines. Only the asymmetric unit is shown for clarity. Hydrogen atoms on carbon are not displayed for better visualisation.....                         | 92  |
| <b>Figure 86:</b> Intermolecular interactions of (10). The two different orientations for the lattice acetonitrile molecule are presented. Hydrogen bonds are shown as green dashed lines. The complex's asymmetric unit is shown for better visualisation.....   | 93  |
| <b>Figure 87:</b> Unit cell packing of (9). Hydrogen atoms are not displayed for clarity.....   | 94  |
| <b>Figure 88:</b> Unit cell packing of (10). For clarity hydrogen atoms are not displayed.....  | 94  |
| <b>Figure 89:</b> The mononuclear dysprosium complexes [DyL6(H <sub>2</sub> O) <sub>4</sub> ]Cl <sub>3</sub> ·6H <sub>2</sub> O (11) and [DyL6(H <sub>2</sub> O) <sub>4</sub> ]Br <sub>3</sub> ·4.5 H <sub>2</sub> O (12) using L6 as a ligand.....   | 97  |
| <b>Figure 90:</b> Compound (11) with a green plane crossing through the pyridine's nitrogen atoms.....  | 97  |
| <b>Figure 91:</b> Compound (11) (left) and compound (12) (right) viewed from the side of the (N1)-(N4)-(N7)-plane. Hydrogen atoms have been removed for clarity.....  | 98  |
| <b>Figure 92:</b> Measured powder pattern of (11) versus simulated pattern from single crystal data.....  | 99  |
| <b>Figure 93:</b> Measured powder pattern of (12) versus simulated pattern from single crystal data.....  | 99  |
| <b>Figure 94:</b> Structure of (11) (right) and (12) (left) with selected atoms labelled.....   | 100 |
| <b>Figure 95:</b> Nine-vertex polyhedron of (11) with SHAPE values.....   | 101 |
| <b>Figure 96:</b> Nine-vertex polyhedron of (12) with SHAPE values.....   | 101 |
| <b>Figure 97:</b> Intermolecular interactions of (11). Selected atoms are labelled. Hydrogen bonds are shown as green dashed lines.....   | 102 |
| <b>Figure 98:</b> Intermolecular interactions of (12). Selected atoms are labelled. Hydrogen bonds are shown as green dashed lines. The hydrogen atoms of the lattice water are disordered and cannot be displayed.....   | 103 |
| <b>Figure 99:</b> Unit cell packing of compound (11).....   | 104 |
| <b>Figure 100:</b> Unit cell packing of compound (12). Hydrogen atoms on lattice water are disordered and cannot be displayed.....  | 104 |
| <b>Figure 101:</b> The four mononuclear lanthanide complexes using HL7 as ligand [Pr(HL7)(NO <sub>3</sub> ) <sub>2</sub> CH <sub>3</sub> OH] (13), [Sm(HL7)(NO <sub>3</sub> ) <sub>2</sub> CH <sub>3</sub> OH] (14), [Dy(L7)(NO <sub>3</sub> ) <sub>2</sub> ] (15) and [Dy(HL7)(CH <sub>3</sub> COO) <sub>2</sub> ] (16)..... | 106 |
| <b>Figure 102:</b> Compound (14) viewed from the top and side of the plane spanned through N(1), N(5) and N(9). Hydrogen atoms have been removed for clarity.....   | 107 |
| <b>Figure 103:</b> Powder patterns of [Ln(HL7)(NO <sub>3</sub> ) <sub>2</sub> CH <sub>3</sub> OH]NO <sub>3</sub> ·2CH <sub>3</sub> OH·H <sub>2</sub> O (Ln = Pr and Nd) versus the simulated pattern of (13).....   | 108 |
| <b>Figure 104:</b> Powder patterns of [Ln(HL7)(NO <sub>3</sub> ) <sub>2</sub> CH <sub>3</sub> OH]NO <sub>3</sub> ·CH <sub>3</sub> OH (Ln = Sm and Eu) versus the simulated pattern of (14).....   | 108 |

|  |     |
|--|-----|
| <b>Figure 105:</b> Measured powder pattern of (15) versus simulated pattern from single crystal data.....  | 109 |
| <b>Figure 106:</b> Measured powder pattern of (16) versus simulated pattern from single crystal data.....  | 109 |
| <b>Figure 107:</b> Structure of (13) (right) and (14) (left) with selected atoms labelled.....   | 110 |
| <b>Figure 108:</b> Structure of (15) (right) and (16) (left) with selected atoms labelled.....   | 111 |
| <b>Figure 109:</b> Ten-vertex polyhedron of (13) with SHAPE values.....  | 112 |
| <b>Figure 110:</b> Ten-vertex polyhedron of (14) with SHAPE values.....  | 112 |
| <b>Figure 111:</b> Nine-vertex polyhedron of (15) with SHAPE values.....   | 112 |
| <b>Figure 112:</b> Nine-vertex polyhedron of (16) with SHAPE values.....   | 112 |
| <b>Figure 113:</b> Intermolecular interactions of (13). Hydrogen bonds are shown as green dashed lines. The hydrogen atoms of the lattice water O(13A) are disordered and cannot be displayed.....   | 113 |
| <b>Figure 114:</b> Intermolecular interactions of (14). Hydrogen bonds are shown as green dashed lines. The nitrate-nitrate interactions are displayed as a pink dashed lines.....   | 114 |
| <b>Figure 115:</b> Intermolecular interactions of (15). Hydrogen bonds are shown as green dashed lines...  | 115 |
| <b>Figure 116:</b> Intermolecular interactions of (16). Hydrogen bonds are shown as green dashed lines...  | 116 |
| <b>Figure 117:</b> Unit cell packing of compound (13). For clarity hydrogen atoms are not displayed.....   | 117 |
| <b>Figure 118:</b> Unit cell packing of compound (14).....   | 117 |
| <b>Figure 119:</b> Unit cell packing of compound (15).....   | 118 |
| <b>Figure 120:</b> Unit cell packing of compound (16). For clarity hydrogen atoms are not displayed.....   | 118 |
| <b>Figure 121:</b> Combining $\text{Eu}(\text{NO}_3)_3 \cdot 5\text{H}_2\text{O}$ and HL7 in methanol yields an isostructural complex of (14). Additionally, in the left vial one drop of acetic acid was added, in the right vial one drop of triethylamine was added.....    | 119 |
| <b>Figure 122:</b> Absorption spectra of HL7 isolated and as complex with $\text{Ln}(\text{NO}_3)_3$ (La-Er and Yb) in methanol with a concentration $c = 66.7 \mu\text{mol/L}$ .....  | 120 |
| <b>Figure 123:</b> Absorption spectra of HL7 isolated and as complex with $\text{Eu}(\text{NO}_3)_3 \cdot 5\text{H}_2\text{O}$ in methanol at a concentration of $c = 33 \mu\text{mol/L}$ . Acetic acid was added in the beginning, then triethylamine subsequently.....       | 121 |
| <b>Figure 124:</b> Gaussian fit of the absorption pattern with four functions. As example the spectrum of $\text{Eu}(\text{NO}_3)_3$ in methanol at a concentration of $c = 33 \mu\text{mol/L}$ and acetic acid and triethylamine at $c = 20 \text{ mmol/L}$ is displayed..... | 122 |
| <b>Figure 125:</b> Plot of the areas of the bands versus the concentration of triethylamine in solution.....   | 123 |
| <b>Figure 126:</b> Absorption spectra of $\text{Nd}(\text{NO}_3)_3$ -HL7 complex in methanol at different concentrations....   | 124 |
| <b>Figure 127:</b> Absorption spectra of $\text{Eu}(\text{NO}_3)_3$ -HL7 complex in methanol at different concentrations....   | 124 |
| <b>Figure 128:</b> Areas of absorption bands of the $\text{Eu}(\text{NO}_3)_3$ -HL7 (left) and $\text{Dy}(\text{NO}_3)_3$ -HL7 complex (right) in methanol plotted logarithmic versus concentration.....   | 125 |
| <b>Figure 129:</b> Absorption maxima at different concentrations for selected $\text{Ln}(\text{NO}_3)_3$ -HL7 complexes in methanol.....   | 126 |
| <b>Figure 130:</b> Absorption spectra of $\text{Fe}(\text{NO}_3)_3$ -HL7 complex in methanol at different concentrations....   | 127 |
| <b>Figure 131:</b> Absorption and emission spectra of the Nd-HL7-complex (top) and the ligand HL7 (bottom) in methanol. The samples were excited at 209 nm (left), 244 nm (middle) and 286 nm (right).....   | 128 |

## LIST OF TABLES

|   |     |
|---|-----|
| <b>Table 1:</b> Ground State, <i>g</i> -values, and room temperature $\chi$ -values for lanthanide <sup>III</sup> ions. <sup>[25]</sup> .....   | 21  |
| <b>Table 2:</b> Selected bond lengths and angles of compound (1) (right) and (2) (left).....  | 42  |
| <b>Table 3:</b> Selected bond lengths and angles of compound (3) and (4).....   | 43  |
| <b>Table 4:</b> The <i>g</i> -factors for the ground Kramer doublets in (1), (3) and (4) and the angles $\alpha$ between the calculated anisotropy axes and the Dy-Dy vector. Anisotropy axis calculated via <i>ab-initio</i> are shown in green and calculated via MAGELLAN are shown in light blue..... | 56  |
| <b>Table 5:</b> Angles between anisotropy axis as calculated by MAGELLAN versus calculated using <i>ab-initio</i> -calculations.....  | 58  |
| <b>Table 6:</b> Selected bond lengths and angles of compound (5) (left) and (6) (right).....  | 62  |
| <b>Table 7:</b> The <i>g</i> -factors for the ground Kramer doublets in (1), (3) and (4) and the angles $\alpha$ between the calculated anisotropy axes and the Dy-Dy vector. Anisotropy axis calculated via <i>ab-initio</i> are shown in green and calculated via MAGELLAN are shown in light blue..... | 73  |
| <b>Table 8:</b> Angles between anisotropy axis as calculated by MAGELLAN versus calculated using <i>ab-initio</i> -calculations.....  | 74  |
| <b>Table 9:</b> Selected bond lengths and angles of compound (7).....   | 77  |
| <b>Table 10:</b> Selected bond lengths and angles of compound (8).....  | 82  |
| <b>Table 11:</b> Selected bond lengths and angles of compound (9).....  | 89  |
| <b>Table 12:</b> Selected bond lengths and angles of compound (10).....   | 90  |
| <b>Table 13:</b> Selected bond lengths and angles of compound (11) (right) and (12) (left).....   | 100 |
| <b>Table 14:</b> Selected bond lengths and angles of compound (13) (right) and (14) (left).....   | 110 |
| <b>Table 15:</b> Selected bond lengths and angles of compound (15) (right) and (16) (left).....   | 111 |
| <b>Table 16:</b> Crystallographic data and structure refinement for (1) and (2).....  | 151 |
| <b>Table 17:</b> Crystallographic data and structure refinement for (3) and (4).....  | 152 |
| <b>Table 18:</b> Crystallographic data and structure refinement for (5) and (6).....  | 153 |
| <b>Table 19:</b> Crystallographic data and structure refinement for (7) and (8).....  | 154 |
| <b>Table 20:</b> Crystallographic data and structure refinement for (9) and (10).....   | 155 |
| <b>Table 21:</b> Crystallographic data and structure refinement for (11) and (12).....  | 156 |
| <b>Table 22:</b> Crystallographic data and structure refinement for (13) and (14).....  | 157 |
| <b>Table 23:</b> Crystallographic data and structure refinement for (15) and (16).....  | 158 |

## LIST OF FORMULAS

|   |    |
|---|----|
| <b>Formula 1:</b> Most common fit with one exponential factor.....                  | 51 |
| <b>Formula 2:</b> Equation suggested by Gu und Wu with two exponential factors..... | 51 |

## LIST OF ABBREVIATIONS

|                        |                                      |
|------------------------|--------------------------------------|
| Å                      | Angstrom                             |
| AC                     | alternating current                  |
| ACN                    | acetonitrile                         |
| <i>C</i>               | Curie-constant                       |
| °C                     | degree Celsius                       |
| cm                     | centimetre(s)                        |
| 3D                     | three dimensional                    |
| DC                     | direct current                       |
| <i>H</i>               | magnetic field                       |
| Hz                     | hertz                                |
| K                      | kelvin                               |
| Ln                     | lanthanide                           |
| M                      | molar                                |
| <i>M</i>               | magnetisation                        |
| <i>m<sub>J</sub></i>   | magnetic state with quantum number J |
| nm                     | nanometre(s)                         |
| Oe                     | oersted                              |
| RT                     | room temperature                     |
| s                      | second(s)                            |
| SIM                    | single ion magnet                    |
| SMM                    | single molecule magnet               |
| SQUID                  | super conducting interference device |
| T                      | temperature                          |
| <i>U<sub>eff</sub></i> | energy barrier                       |
| QTM                    | quantum tunnelling of magnetisation  |
| <i>X</i>               | susceptibility                       |
| $\tau_0$               | relaxation time                      |

# 1 INTRODUCTION

Lanthanides have become indispensable in everyday life. They are installed in a large number of technical devices in daily use or are required for their production. For example, lanthanide oxides are used as catalysts in the heterogeneous catalysis of many industrial processes.<sup>[1]</sup> Lanthanide ions are used in materials with luminescence properties, particularly in the Nd:YAG laser.<sup>[2]</sup> They are also used in the batteries and magnets of electric vehicles. This means that lanthanides are now indispensable in optics and semiconductor technology.<sup>[3]</sup> Since their role in industry has grown vastly in recent years lanthanides have now acquired political importance. For example, the United States wants to reduce its dependency on importing rare-earth elements and instead mine more themselves. Today, around 70% of the global demand on lanthanides is satisfied by mining in China.<sup>[4]</sup> The rare-earth elements include scandium, yttrium and the lanthanum to lutetium. The term "rare-earth elements" is somewhat misleading, since they are more common than all precious metals.<sup>[1, 5]</sup> Nevertheless, lanthanides are comparatively expensive. This is a result of the fact that on the one hand, lanthanides are not found in deposits in a particularly high concentration. On the other hand, their separation is very complex and resource-intensive as a result of their similar chemical properties.<sup>[5]</sup> This means that the mining process poses an environmental problem.<sup>[5]</sup>

The addition of lanthanides can significantly change the optical properties of a material. They form so-called luminescent complexes, which can switch to a state of separated charge through the absorption of light.<sup>[6]</sup> Such a complex can then return to the ground state by emitting at longer wavelengths. This shift is called the Stokes shift.<sup>[7, 8]</sup> Partial charge transfer occurs in lanthanide chelates by transferring an electron from the metal atom to the ligand.<sup>[7, 8]</sup> The transition is from an occupied f-orbital of the donor metal into an empty  $\pi^*$ -orbital of the acceptor ligand.<sup>[7, 8]</sup> These luminescent properties of the lanthanides play a particularly important role in LEDs or pharmacy.<sup>[9]</sup> Time-resolved fluorometry is an essential investigation method in drug research.<sup>[6]</sup>

Lanthanides are very important in magnetic materials such as magnets the size of individual atoms or molecules are a promising approach that could increase the storage density many times over compared to today's devices.<sup>[3, 10]</sup> The prime example of lanthanides in modern medicine is the gadolinium complex gadopentetic acid.<sup>[11, 12]</sup> It is used as a contrast agent for examinations in magnetic resonance imaging.<sup>[11, 12]</sup>

The seven unpaired 4f electrons of the gadolinium ion make the compound highly paramagnetic.<sup>[1, 8, 12]</sup>

It has been circa 30 years since the first molecule, Mn<sub>12</sub>-acetate, showing molecular based magnetic properties characteristic for bulk material was reported.<sup>[13]</sup> It possesses an energy barrier for realignment of the molecular magnetic moment.<sup>[10, 13]</sup> In such a molecule, a slow relaxation of its magnetic moment to an applied alternating magnetic field can be observed.<sup>[10]</sup> Such molecules are therefore called single-molecule magnets, or SMMs for short. Research on single-molecule magnets brings together different fields of science such as chemistry, physics and materials science.<sup>[3]</sup> SMMs are a candidate for replacing classic hard drives. Since information can be stored about the orientation of their spin and this can be read and overwritten, they would be ideal for increasing storage density.<sup>[3]</sup> One can think of such a single molecule as the basic unit of information called bit. Furthermore, single-molecule magnets are also researched in the fields of quantum computing and spintronics, due to their coherent quantum properties and their magnetic behavior.<sup>[3, 10]</sup> However, their application is hampered by major hurdles. First, SMMs only retain their magnetic properties at very low temperatures. And second, the magnetic relaxation, i.e. the transition to the ground state, often takes place in very short periods of time.<sup>[10]</sup>

## 2 THEORETICAL BACKGROUND

### 2.1 Magnetism

#### 2.1.1 Matter in magnetic fields

The reason for the magnetism of a material are the magnetic moments of its individual atoms. The alignment of these moments induces an external magnetic field. The two physical quantities that define magnetic fields are the magnetic induction  $B$  and the magnetic field strength  $H$ . The following applies to the vacuum:<sup>[14]</sup>

$$B = \mu_0 \cdot H$$

The magnetic field constant  $\mu_0$  is  $4\pi \cdot 10^{-7}$  Vs/Am and corresponds to the permeability of the vacuum. Visually, magnetic induction can be imagined as the distance between the field lines.<sup>[14]</sup>

If an external homogeneous magnetic field penetrates matter, then this does not have the induction of the external field  $B_{\text{external}}$ . A new induction  $B_{\text{internal}}$  appears.

$$B_{\text{internal}} = \mu_r \cdot B_{\text{external}}$$

The relationship between the two inductions is described by the dimensionless constant of proportionality  $\mu_r$ . One can think of this as the penetrability for external magnetic fields.<sup>[14]</sup>

The difference between internal and external induction in a material is called magnetic polarization  $J$ .<sup>[14]</sup>

$$B_{\text{internal}} = B_{\text{external}} + J$$

$$J = \chi_v \cdot B_{\text{external}}$$

The volume magnetic susceptibility  $\chi_v$  (often simplified as susceptibility  $\chi$ ) of a substance is obtained from the ratio of the external induction to the magnetic polarization. It is a dimensionless constant of proportionality that can be illustrated as the receptivity for external magnetic fields (see Figure 1).<sup>[1, 14]</sup>

There is one other commonly used measure for magnetic susceptibility. The magnetic mass susceptibility  $\chi_m$  is defined as:

$$\chi_m = \frac{\chi_v}{\rho} = \chi_v \cdot \frac{V}{m}$$

Another important physical quantity is the magnetization  $M$ . It is proportional to the external field strength and polarization.<sup>[14]</sup>

$$M = \chi_v \cdot H_{\text{external}}$$

$$J = \mu_0 \cdot M$$

Thus, one can describe the magnetic behaviour of matter with two quantities, the permeability  $\mu$  and the susceptibility  $\chi_v$ .<sup>[14]</sup>

There are three types of materials: (Figure 1 and 2).

Diamagnetic materials:  $\mu_r < 1$   $\chi_v < 0$

Paramagnetic materials:  $\mu_r > 1$   $\chi_v > 0$

Ferromagnetic materials:  $\mu_r \gg 1$   $\chi_v \gg 0$

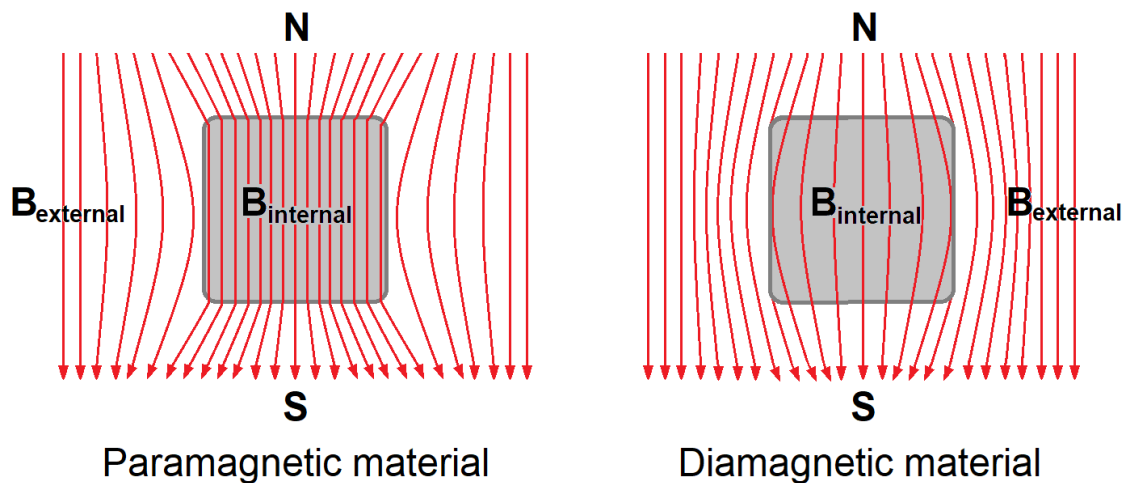


**Figure 1:** Magnetic field lines of an external homogeneous field penetrate matter. The diamagnetic substance is pushed out of the inhomogeneous field, the paramagnetic substance is drawn into the field.

## 2.1.2 Magnetic moment

A magnetic field is created whenever a charge moves. This is best illustrated using the example of a coil through which an electric current flows. The magnetic field is always aligned parallel to the coil axis. The coil behaves like a magnetic dipole. This dipole has a magnetic moment  $\mu_{\text{mag}}$ . This is proportional to the product of the strength of the current  $I$  and the enclosed circular area with radius  $r$ .<sup>[1, 14]</sup>

$$\mu_{\text{mag}} = I \cdot r^2 \cdot \pi$$

Electrons that “circulate” around an atomic nucleus behave in a similar way. Electrons spin around their own axis, resulting in an intrinsic angular momentum, also called spin. In addition, they also induce a magnetic field, since they have an electric charge. When there is a contribution from orbital angular momentum, they will also be an orbital magnetic moment. This spin and its charge also cause a magnetic spin moment. The total resulting magnetic moment  $\mu_J$  of an electron results from the sum of these two values:<sup>[1, 14]</sup>

$$\mu_J = \mu_l + \mu_s$$

The magnitude of the magnetic moment of particles is determined in Bohr magnetons. The Bohr magneton  $\mu_B$  is the magnitude of the magnetic moment that a charged entity generates through its orbital angular momentum. A Bohr magneton is the minimum magnitude of a magnetic moment.<sup>[1, 14]</sup>

$$\mu_B = \frac{e\hbar}{2m_e}$$

For example, protons and neutrons also have a spin and thus contribute to the magnetic moment of an atom, ion or molecule. However, their mass is much larger in relation to that of the electron. Since the particle mass is in the denominator of Bohr's magneton, the contribution of the protons is often ignored.<sup>[14]</sup>

$$\text{Atom cores: } \mu_N = \frac{e\hbar}{2m_p c} \quad \text{Electrons: } \mu_B = \frac{e\hbar}{2m_e c} \gg \mu_N$$

( $\mu_N$  = nuclear magneton;  $m_p$  = proton mass;  $\mu_B$  = Bohr magneton;  $m_e$  = electron mass;  $e$  = elementary charge;  $\hbar$  = reduced Planck constant)

The electronic magnetic orbital moment  $\mu_l$  and the spin moment  $\mu_s$  result from the following two formulas:

$$\mu_l = \sqrt{l(l+1)}\mu_B \quad \mu_s = g\sqrt{s(s+1)}\mu_B$$

The so-called g-factor is required as a quotient for the spin moment, it takes the gyromagnetic anomaly into account. When you have a lot of spin orbit coupling g is not exact equals 2 anymore. The secondary quantum number  $l$  stands for the orbital angular momentum quantum number and  $s$  for the spin quantum number.<sup>[1]</sup>

### 2.1.3 Diamagnetism

Diamagnetism is a property of matter that occurs when all of the electrons in the substance are paired. No outward magnetic moment emanates from the atoms, ions or molecules. If all shells and subshells are occupied in a material, then it is diamagnetic. Each orbital of a shell is doubly occupied by two electrons. The antiparallel alignment of their spins causes the spin and orbital moments to cancel each other out. Diamagnetic materials are very common because the unpaired electrons of the atom are used to form chemical bonds. Every material has diamagnetism except hydrogen atom. A perfect diamagnet is a superconductor.<sup>[1, 15]</sup>

An external magnetic field causes a magnetic polarization in such a diamagnetic substance. This counteracts the external field and reduces the susceptibility in the material.<sup>[1, 14]</sup>

The field strength and the temperature have no influence on the susceptibility. It results from the sum of the individual amounts of the atoms and bonds of the molecules.<sup>[1, 14, 15]</sup>

$$\chi_{\text{dia}} < 0 \quad \chi_{\text{dia}} = \sum \chi_{\text{atom}} + \sum \chi_{\text{bond}}$$

### 2.1.4 Paramagnetism

Paramagnetism is a property of matter that occurs when unpaired electrons are present. However, the magnetic moments of such atoms, ions or molecules are statistically distributed in all spatial directions. Therefore, paramagnetic substances do not initially have a magnetic moment. However, if such a substance is in an external magnetic field, the magnetic moments of the particles with unpaired electrons are oriented along the magnetic field lines. This creates its own magnetic field, which points in the same direction as the external field.<sup>[1]</sup>

The field strength has no influence on the susceptibility, but it is influenced by the temperature. High temperatures make it difficult for permanent magnets to orient themselves in an external field.<sup>[1]</sup>

Virtually all materials exhibit some diamagnetic effect. However, diamagnetism is usually several orders of magnitude smaller than paramagnetism.<sup>[14]</sup>

The measurable susceptibility  $\chi$  of paramagnetic substances results from the sum of both parts. It is smaller than the actual paramagnetic susceptibility  $\chi_{para}$  since  $\chi_{dia}$  is negative.<sup>[1]</sup>

$$\chi = \chi_{dia} + \chi_{para}$$

The susceptibility of paramagnetic substances depends on the temperature and is defined according to the Curie-Weiss law above the Curie temperature.

$$\chi_{para} = \frac{C}{T - \theta}$$

( $T$  = temperature;  $\theta$  = Curie temperature;  $C$  = Curie constant)

It is worth mentioning that his law only works at high temperatures and low fields.

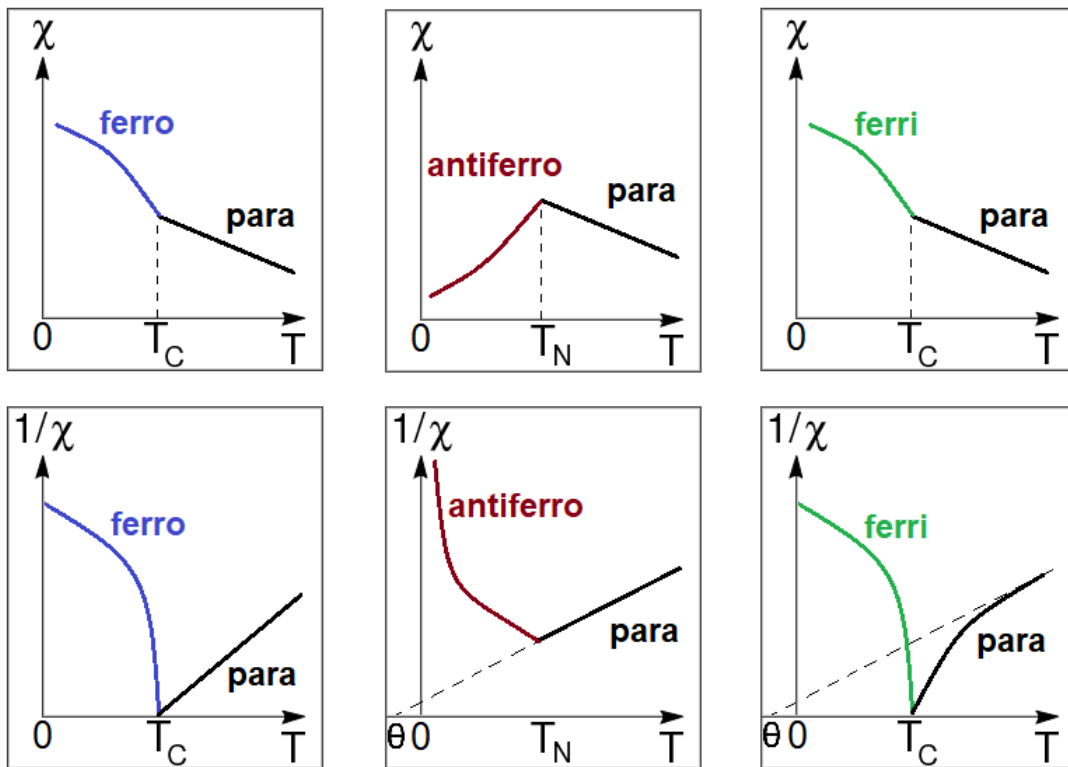


**Figure 2:** Dependence of susceptibility on temperature (black curve: paramagnetism; blue curve: ferromagnetism; green curve: ferrimagnetism; dark red line: antiferromagnetism).

The paramagnetic Curie temperature  $\Theta$ , sometimes referred as  $T_C$  or Weiss constant, can have a positive or negative value. This means that the magnetic dipoles of the atoms or molecules in the material influence each other. Their orientation depends on the orientation of the adjacent dipoles. The Curie constant  $C$  is obtained from the following formula:<sup>[1, 15]</sup>

$$C = \mu_0 \cdot \frac{N}{V} \cdot \frac{\mu^2}{3k_B}$$

( $C$  = Curie constant;  $\mu_0$  = vacuum permeability;  $N/V$  = particle density;  $\mu$  = permeability of the substance;  $k_B$  = Boltzmann constant)<sup>[1]</sup>

If one wants to solve structural problems using a magnetochemical approach, the effective magnetic moment  $\mu_{eff}$  is determined in an experiment and compared with the theoretical magnetic moment.<sup>[1]</sup>

$$\mu_{eff} = \sqrt{\frac{3k_B}{\mu_0 N_A} \chi_{para} (T - \theta)}$$

To do this, the volume-related susceptibility is measured and the molar susceptibility is calculated from this. The diamagnetic component is subtracted from this. This is how one arrives at the paramagnetic susceptibility. In the end you get the magnetic moment.<sup>[1]</sup>

When determining this magnetic moment, there are two special cases that can be used. In the first case the coupling between total orbital angular momentum and spin is like this large that the multiplet splitting is much stronger than  $\chi T$ . It follows that all particles are in their lowest energetic state. This state is given by the quantum number  $J$ .<sup>[1, 15]</sup>

This occurs, for example, with the lanthanides. Their paramagnetic moment is caused by the 4f electrons. The 4f shell is further inside the lanthanides, which means that these electrons do not participate in bonds and from outside Ligand fields are largely shielded.<sup>[1, 15]</sup>

The anisotropy of lanthanides can be described as the single-ion model of magnetic anisotropy. It is mainly derived from the internal composition of 4f ions, while the crystal-field interaction is only a small disturbance to spin-orbital coupling.<sup>[10]</sup>

The magnetic moment is calculated according to the relationship:

$$\mu = g_J \sqrt{J(J + 1)} \mu_B$$

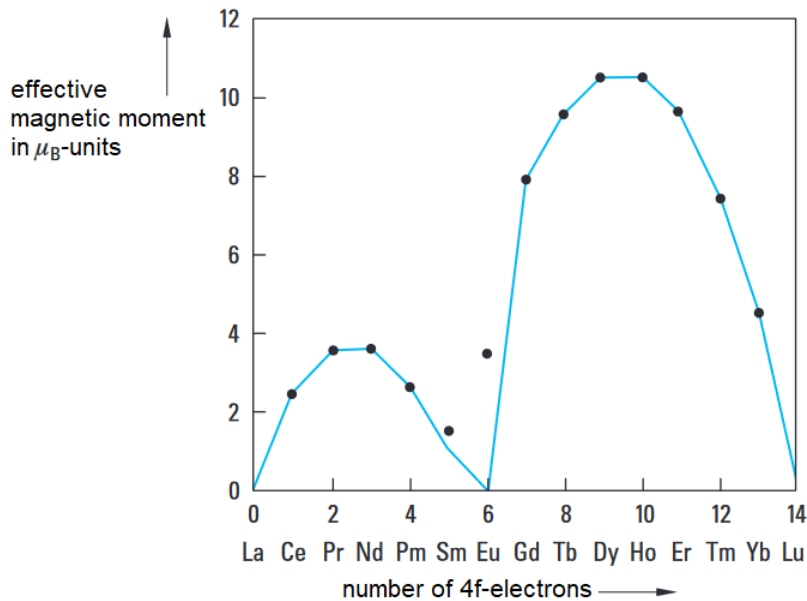


**Figure 3:** Magnetic moments of the trivalent lanthanides  $\text{Ln}^{\text{III}}$ . The black dots show the experimentally measured values, the blue line represents the calculated values. For  $\text{Sm}^{\text{III}}$  and  $\text{Eu}^{\text{III}}$  the experimental values are higher. Reason is that at both ions the first excited state is close to the ground state. This is therefore partially occupied at room temperature. The  $J$  values of the excited state are larger than those of the ground state, which explains the deviation.<sup>[1]</sup>

In the second case, the multiplet splitting is significantly lower than  $\chi T$ . This occurs when the spin-orbit coupling is small. The total angular momentum of atoms and molecules is not determined by the quantum number  $J$ . Orbital angular momentum and spin do not affect each other and are free to point in any direction. If the orbital moment has no influence,  $L$  is equal to zero and speaks of so-called "spin-only" values.<sup>[1, 15]</sup>

$$\mu_{eff} = 2\mu_B\sqrt{S(S+1)}$$

### 2.1.5 Spin order and magnetization

The magnetic character in the case of diamagnetism and paramagnetism results from the sum of the properties of the individual atoms, ions or molecules. There is no exchange between the particles in the solid.<sup>[1, 15]</sup>

Cooperative magnetism can arise when an exchange between the spins takes place in a paramagnetic material. This type of interaction can take place directly between adjacent particles or indirectly, through the exchange interaction of the electrons of diamagnetic ions.<sup>[1, 15]</sup>

There is a material-specific temperature below which, due to the spin-spin interaction, a spin order is established, which leads to magnetization. No external magnetic field is required for this. The following different spin orders exist here.<sup>[1, 15]</sup>

Below the Curie temperature  $T_C$  all the domain walls are abolished. When this happens in a ferromagnetic material all spins align in parallel (see Figure 4 and 5). These small domains are also called Weiss areas, in which the spins of neighboring atoms exhibit parallel coupling. The susceptibility is several orders of magnitude higher than that of paramagnets. Its theoretical maximum is at a temperature of 0 Kelvin. The susceptibility decreases with increasing temperature, and the spin coupling stops when the Curie temperature is exceeded.<sup>[1, 14]</sup>

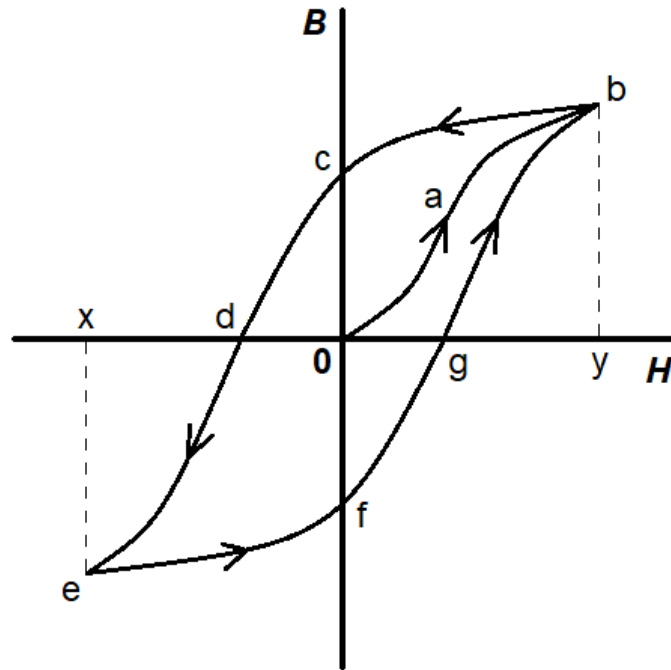


**Figure 4:** Schematic representation of a hysteresis loop of a ferromagnetic material. The magnetic moments of Weiss' areas are arranged according to the magnetic field lines of the external magnetic field ( $B$  = magnetization,  $H$  = field strength,  $a$  = new curve,  $b$  = point of saturation magnetization,  $c$  = remanence magnetization,  $d$  = coercive field strength,  $e = -b$ ,  $f = -c$ ,  $g = -d$ ,  $x = -y$ ,  $y$  = field strength full spin alignment).

In ferrimagnetism, the equivalent spins align antiparallel (see Figure 5). This also happens below the Curie temperature  $T_c$  within the Weiss domains. However, the magnitude of the coupling of the spins is not the same here. As a result, a magnetic moment arises, which leads to spontaneous magnetization. However, there is no externally measurable magnetization, since the orientation of the moments of the individual domains are distributed statistically and thus cancel each other out. However, one can magnetize a ferrimagnetic material by an external magnetic field. The relationship between susceptibility and temperature hardly differs from that of ferromagnetic materials.<sup>[1, 14]</sup>

In antiferromagnetism, the spins align antiparallel (see Figure 5). This occurs below the Néel temperature  $T_N$  within Weiss' domains. The magnitude of the spin couplings is the same. At  $T = 0$  K, the spin couplings cancel each other out resulting in the cancellation of the magnetic moment. The substance behaves like a diamagnetic. As the temperature increases, the thermal motion of the particles increases. This increases the disorder of the particles and the susceptibility increases.<sup>[15]</sup>

At  $T_N$  the susceptibility is at a maximum. If the temperature increases further, the spin order ceases and the substance behaves paramagnetically.<sup>[1, 14]</sup>



**Figure 5:** Schematic representation of the different spin orientation below the Curie temperature  $T_C$  (ferro and ferri) and below the Néel temperature  $T_N$  (antiferro) for different types of material.

## 2.2 Single-molecule magnetism

### 2.2.1 Overview of single-molecule magnets

The magnetism discussed above is a property of macroscopic bodies that is known from everyday life. However, if one goes for the top-down approach and divide such a body again and again, it becomes smaller and smaller and new properties appear. The surface effects are gaining in importance and magnetization from the outside is not retained. If there is no permanent magnetization even below the Curie temperature, it is about superparamagnetism. However, there is still a blocking temperature below which permanent magnetization is retained. This new threshold is at a lower temperature than the Curie temperature. If one continues breaking down antiferromagnetic bulk material, you first reach Nano scale particles. Going smaller one will receive single domain particles. Those will have uncompensated spins on the surface. If one continues to divide these particles, in the end there are only individual atoms or molecules, so the orientation of the spins would be statistically distributed in space. There would be no preferred orientation as none would be vigorously favored.<sup>[16-18]</sup>

However, to arrive at molecules that retain their magnetic orientation one can go for the bottom-up approach and design a molecule out of smaller components. In order to be considered a single-molecule magnet, such molecules must have certain properties. The spin of single-molecule magnets has such a preferred orientation, also called anisotropy. This spin is related to the spatial orientation of the orbit via spin-orbit coupling. Magnetic anisotropy is the reason that the magnetization vector shows spatially along the energetically favorable position. The magnetization is a vector quantity, which is illustrated with an arrow. Therefore, without an external field, there are always two energetically lowest orientations in the Space. The anisotropy is the reason why the transition between both orientations is slowed down by an energy barrier.<sup>[16-18]</sup>

The very first molecule identified as such a single molecule magnet was a molecule containing twelve manganese ions at different charges. Its energy barrier inhibiting spin relaxation is displayed in Figure 6. [10, 13]

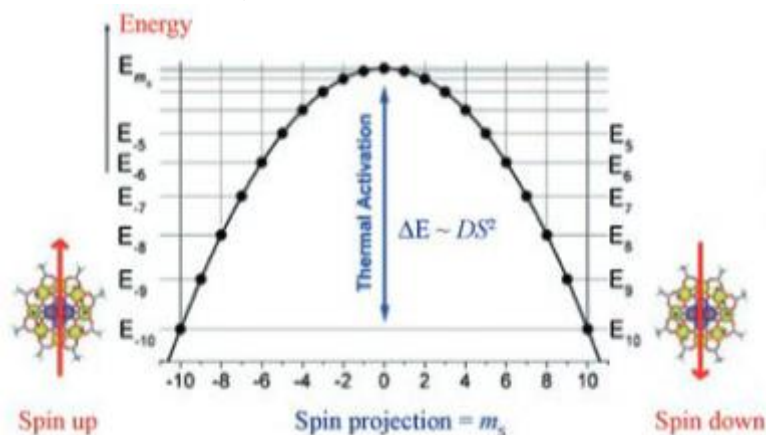


**Figure 6:** Energy barrier to spin relaxation using the example of the first SMM, the Mn<sub>12</sub>-cluster. [10]

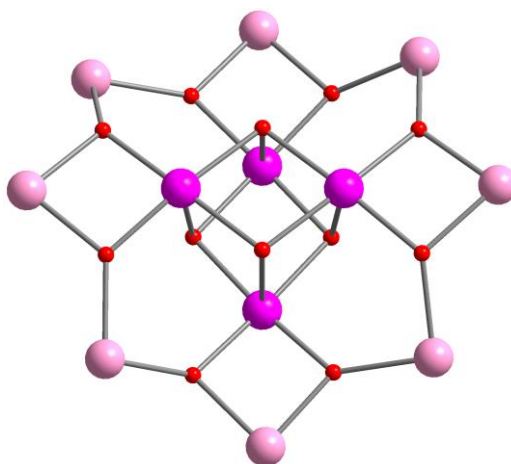


**Figure 7:** Schematic view of the core of the Mn<sub>12</sub> cluster. Rose atoms represent Mn<sup>III</sup> ( $S = 2$ ), pink atoms present Mn<sup>IV</sup> ( $S = 3/2$ ) and the small red atoms represent bridging oxygen atoms.

The preservation of the anisotropy and thus the expansion of the energy barrier are a step in the direction of getting the best possible SMM. A further step is the suppression of tunneling effects to obtain a stable magnetic alignment. [10]

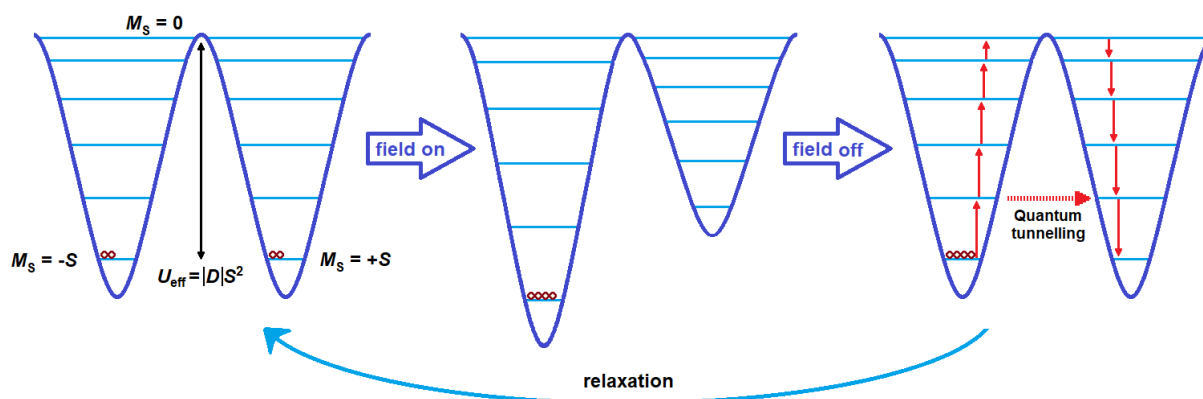


**Figure 8:** Schematic visualization of the magnetization and magnetic relaxation processes in a single molecule magnet.

### 2.2.2 Lanthanide-based single-molecule magnets

In the search for single-molecule magnets, research was initially carried out into synthesizing molecules with the highest possible total spin. At that time, it was believed that this was the sole basis for magnetic properties. In this way it was possible to produce the famous  $Mn_{19}$ -cluster with a spin of  $83/2$ , which nevertheless did not show any SMM behavior.<sup>[19]</sup> Magnetic anisotropy is essential for SMM behavior. It is responsible for the coupling of matter to the crystal lattice.<sup>[16, 20]</sup>

In research, the f-elements increasingly came to the fore. Due to their electronic structure, their ground state is doubly degenerate and they have a high value for the magnetic quantum number of the total angular momentum  $\pm m_J$ . This results in a high magnetic moment in the temperature range in which predominantly only the ground state is occupied.<sup>[3, 21]</sup>

Furthermore, the anisotropy is increased when the distance between the bistable ground state and the first Kramer and non-Kramer state is large. The greater this distance the more energy is required for spin relaxation. At higher temperatures, this mechanism is facilitated.<sup>[3, 21]</sup>

In addition, quantum tunneling should be suppressed as much as possible. The symmetry within the molecule and the distribution of the charge density play a decisive role here. Tunnel effects are not yet fully understood and are subject of current research. If these conditions are met, a magnetic ground state can be established and the magnetic relaxation via excited states becomes strong slowed down. To do this, the temperature must be low enough so that the first excited state is not populated.<sup>[3, 22]</sup>

Not only hysteresis, but also temperature dependent spin lattice paths appear as relaxation paths, which seem to be dominant in high-temperature SMMs. Direct processes always involve single acoustic phonons. However, these are rare because the density of states is low in this energy range. Orbach and Raman processes involve higher energy states and two phonons. In Orbach processes, the energy for the state transition of lattice phonon states is released or absorbed. In Raman processes, the energy needed for the transition is given or taken by the superposition of two phonons that form a virtual state.<sup>[10]</sup>

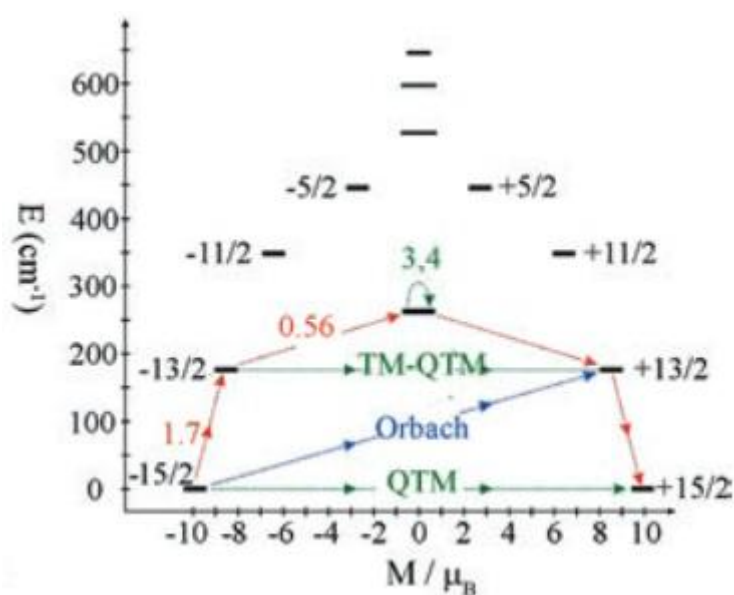


**Figure 9:** Visualization of the most common relaxation paths. Starting from a state with maximal magnetization in the ground-state doublet to the time-reversed state in lanthanide single-molecule magnets.<sup>[10]</sup>

The lanthanide<sup>III</sup> ion can fulfill these conditions. The shapes of its 4f electron densities in their ground states is shown in Figure 10. The shape of their 4f shells can be either prolate, oblate, or spherical.<sup>[3]</sup>

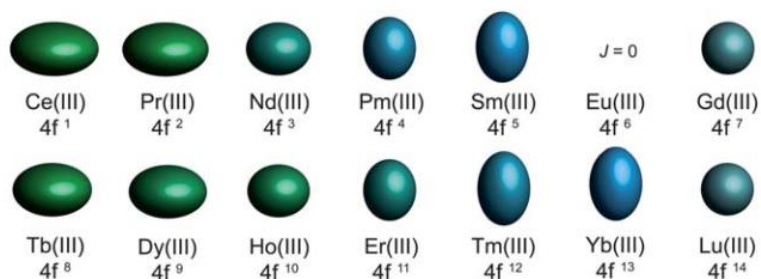


**Figure 10:** Quadrupole approximation of the electron density distribution of the 4f shell of the Ln<sup>III</sup> ions.<sup>[3, 23]</sup>

If one looks at the anisotropy of each individual  $m_J$  state, Figure 11 is a graphical representation of the angular dependence of the 4f charge density of the various  $m_J$  states. In the absence of a crystal field, all  $m_J$  states for each lanthanide<sup>III</sup> ion are degenerate.<sup>[3]</sup>

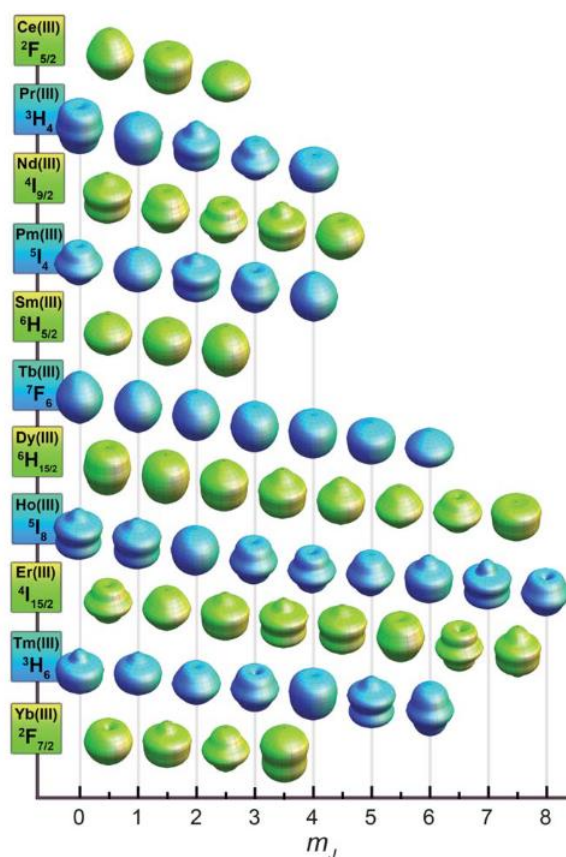


**Figure 11:** Approximations of the angular dependence of the total 4f charge density for  $m_J$  states.<sup>[3, 24]</sup>

Knowing the free electron density of the f-orbitals of the lanthanides in the ground state, it is possible to design a model of the crystal field that leads to a maximum of the anisotropy. The magnetic anisotropy of a complex with a central atom, which has a prolate magnetic ground state is maximized when a crystal field is established by the ligands in which the electron density of the ligands is equatorially concentrated in the xy-plane around the central atom. Such an environment leads to a bistable orientation of the ground state, which is parallel or antiparallel to the molecular axis. The shape leads to less strong repulsion of the ligand and the charge of the stretched 4f electron cloud in the crystal field (see Figure 12).<sup>[3, 10]</sup>

If a prolate ion cannot achieve an equatorially-coordinating geometry it will force its f-electron charge cloud into direct contact with the ligands, resulting in a high-energy state. (see Figure 12).<sup>[3, 10]</sup>

The opposite is true for oblate 4f shells. To increase the anisotropy of such an ion, it must be placed in a crystal field where the electron density is located above and below the xy-plane. Ligands with nitrogen carrying pi-systems can offer such a geometry. In that type of environment, the crystal field the ground state will have bistable orientations of  $m_J$  parallel and antiparallel to the molecular axis. This arrangement reduces repulsive forces between the ligand and f-electron shell (see Figure 12).<sup>[3, 10]</sup>

If the orientation has a low magnitude  $m_J$  the f-electron charge cloud will be pushed into the charge cloud of the ligands, leading to a higher-energy state (see Figure 12).<sup>[3, 10]</sup>

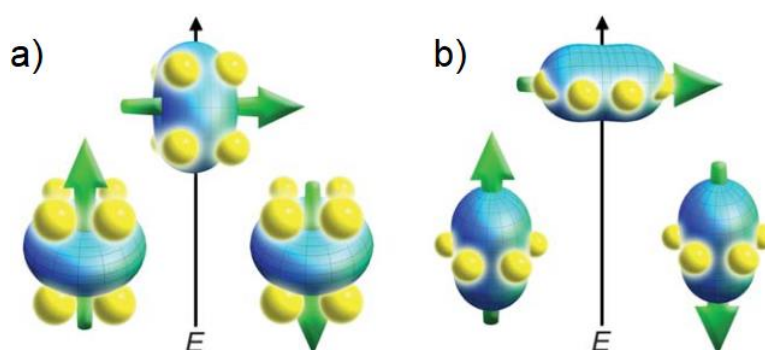


**Figure 12:** Plots of low- and high-energy configuration f-orbital electron density versus crystal field environment for a stretched 4f ion. The green arrow represents the orientation of the spin angular momentum coupled to the orbital period.<sup>[3]</sup>

Most used lanthanides for constructing a single-molecule magnet are Terbium, Dysprosium, Holmium and Erbium. They show the highest  $m_J$  values and have an oblate (Tb, Dy, Ho) or a prolate (Er) 4f shape. This often leads to very axial  $g$  values (see Table 1).

| trivalent ion | configuration   | ground state                   | $g_J$ | $\chi T$ (emu mol <sup>-1</sup> K) |
|---------------|-----------------|--------------------------------|-------|------------------------------------|
| Ce            | f <sup>1</sup>  | <sup>2</sup> F <sub>5/2</sub>  |       | 0.80                               |
| Pr            | f <sup>2</sup>  | <sup>3</sup> H <sub>4</sub>    | 4/5   | 1.60                               |
| Nd            | f <sup>3</sup>  | <sup>4</sup> I <sub>9/2</sub>  | 8/11  | 1.64                               |
| Pm            | f <sup>4</sup>  | <sup>5</sup> I <sub>4</sub>    | 3/5   | 0.90                               |
| Sm            | f <sup>5</sup>  | <sup>6</sup> H <sub>5/2</sub>  | 2/7   | 0.09                               |
| Eu            | f <sup>6</sup>  | <sup>7</sup> F <sub>0</sub>    |       |                                    |
| Gd            | f <sup>7</sup>  | <sup>8</sup> S <sub>7/2</sub>  | 2     | 7.88                               |
| Tb            | f <sup>8</sup>  | <sup>7</sup> F <sub>6</sub>    | 3/2   | 11.82                              |
| Dy            | f <sup>9</sup>  | <sup>6</sup> H <sub>15/2</sub> | 4/3   | 14.17                              |
| Ho            | f <sup>10</sup> | <sup>5</sup> I <sub>8</sub>    | 5/4   | 14.07                              |
| Er            | f <sup>11</sup> | <sup>4</sup> I <sub>15/2</sub> | 6/5   | 11.48                              |
| Tm            | f <sup>12</sup> | <sup>3</sup> H <sub>6</sub>    | 7/6   | 7.15                               |
| Yb            | f <sup>13</sup> | <sup>2</sup> F <sub>7/2</sub>  | 8/7   | 2.57                               |

**Table 1:** Ground State,  $g$ -values, and room temperature  $\chi$ -values for lanthanide<sup>III</sup> ions.<sup>[25]</sup>

## 2.3 Photoluminescence

When an electron absorbs an electromagnetic wave, the energy of that photon is transmitted to the electron. That will excite the electron from the ground state to a state of higher energy. The path back from such a state in the ground state is called relaxation and is visualised in the Jablonski diagram (see Figure 13).<sup>[26]</sup>

In most molecules the energy is emitted via vibronic relaxation without emitting light. The energy is transferred to neighbouring molecules, like neighbouring solvent molecules, by exciting their translation, rotation and oscillation states. On a macroscopic scale that translates to an increased temperature. An electronically excited state can change via internal conversion in a lower electronically excited state of the same multiplicity. Again, on a macroscopic scale that would cause a temperature increase. An excited singlet state can transfer into an excited triplet state via intersystem crossing. An excited singlet state can transfer into an excited triplet state via intersystem crossing.<sup>[26]</sup>

There are also two possible paths to a lower state by emitting light, what is described luminescence. First, the transition from one singlet state to another is called fluorescence. Second, following an internal conversion the transition from excited triplet state to the ground state is known as phosphorescence. The path of phosphorescence typically takes much longer than the fluorescence.<sup>[26]</sup>

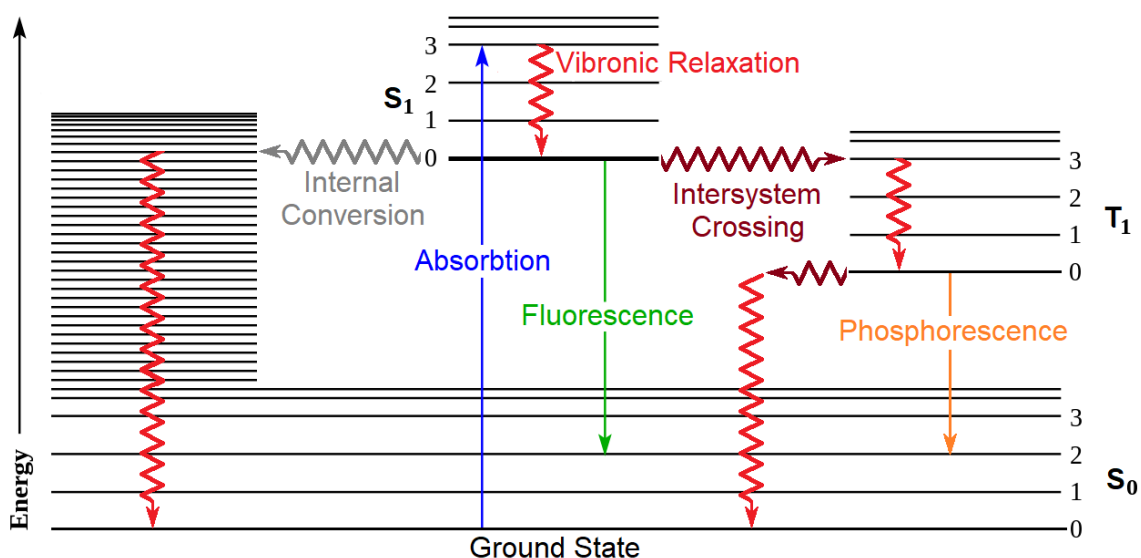


**Figure 13:** Jablonski diagram showing the possible transitions of valence electrons in various excited states after absorbing light. There is the singlet ground  $S_0$ , the singlet excited state  $S_1$  and the triplet excited state  $T_1$ .

### 2.3.1 Luminescence in coordination compounds

In chemistry, an electron-donor-acceptor complex is a molecule composed of two or more subunits that are attracted to each other. They are often equated with the charge-transfer complexes, but strictly speaking charge-transfer complexes form a subclass of electron-donor-acceptor complexes. The subunits are attracted to each other by electrostatic forces because one is positively charged and the other negatively charged. The electron-receiving part is also called the electron acceptor, the electron-donating part the electron donor. Those complexes can absorb light, what causes a separation of charge. Often they show an intensive colour.<sup>[27-29]</sup>

Charge-transfer complexes are often molecules with organic ligands and a metal centre. Partial charge transfer is possible in both directions, i.e. from the ligand to the metal or vice versa. Highly charged cations such as the  $\text{Mn}^{\text{VII}}$  and  $\text{Cr}^{\text{VI}}$  ions are suitable for the transition from ligand to metal.<sup>[27-29]</sup>

On the other hand, ligands with an empty  $\pi^*$ -orbital, such as carbon monoxide, pyridine, or other aromatic compounds, are suitable for the transition from metal to ligands.<sup>[27-29]</sup>

There can also be transitions between the ligands and metals among themselves. In solution, the solvents also often form complexes.<sup>[27-29]</sup>

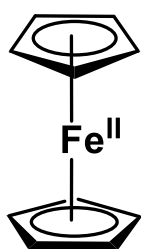


**Figure 14:** Ferrocene  $[\text{Fe}(\eta^5\text{-C}_5\text{H}_5)_2]$  is an electron donor–acceptor complex with a metal ion acceptor and two aromatic  $\pi$ -donors.<sup>[30]</sup>

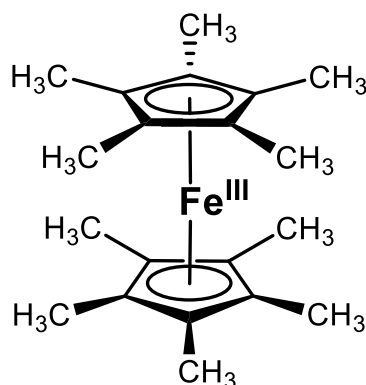


**Figure 15:** The  $[\text{Fe}(\text{C}_5\text{Me}_5)_2]^+$  cation can act as a donor and the corresponding anion can act as an electron acceptor.<sup>[31]</sup>

## 2.4 Coordination compounds

The chemistry of complexes encompasses an area in inorganic chemistry. It is also called coordination chemistry. Complexes are made up of several parts. They have a ligand shell and a coordination center. The ligand shell can be either ionic or electrically neutral. The coordination center, also known as the central particle, consists of the metal atom or ion. The coordination number is the number of bonds from the central atom to its nearest neighbors. In the case of complex compounds, this corresponds to the number of times the coordination center binds to a ligand. There are both mononuclear complexes and polynuclear complexes.<sup>[1, 32]</sup>

The chemical properties of transition metals complexes are caused by the interaction of the s- and p-orbitals of the donor ligand-atom and the d-orbitals of the metal ions. The number of s-, p- and d-orbital electrons sums up to 18, which is described in the 18-electron rule. The structure of most complexes is built up to a regular polyhedron. The metal ion in the center is coordinated to the atom of the ligand which represent the corners of that polyhedron. This regular geometry can be disrupted by different bond lengths, the size of the ligand and other effects, such as Jahn-Teller distortion.<sup>[7, 8]</sup>

Complex compounds have a large number of characteristic features. This includes, for example, their typical colours. Transition metals complexes often feature a wide variety of colours due to electronic transitions by the absorption of light. The majority of this interactions are d-d transitions or charge transfer processes. As a result of these properties pigments often contain transition metal complexes.<sup>[7, 8]</sup>

The electrical conductivity of complexes in solution depends on which ions are free to move and which act as ligands. The reaction behavior of complex compounds can differ greatly from that of the individual ions because, for example, the central atom is shielded by the ligand. An example of this would be the contrast agent gadoteric acid from medicine. Free gadolinium ions are toxic, but the complexed form is well tolerated.<sup>[1, 11, 12]</sup>

### 2.4.1 Bonding theories

The  $[\text{Co}(\text{NH}_3)_6]^{3+}$  complex as an easy model to understand the charge distribution in coordination compounds. In Figure 16 model (a) of the given complex causes an issue in the terms of electron-withdrawing power. The cobalt<sup>III</sup> centre in this model is negatively charged and the nitrogen is positively charged. This is unrealistic, because nitrogen has a higher electronegativity than cobalt and you should expect the nitrogen-cobalt bond to be polarized in a manner of  $\text{N}^{\delta-}-\text{Co}^{\delta+}$ . This indicates that the charge distribution in model (a) makes little sense.<sup>[7, 8, 33]</sup>

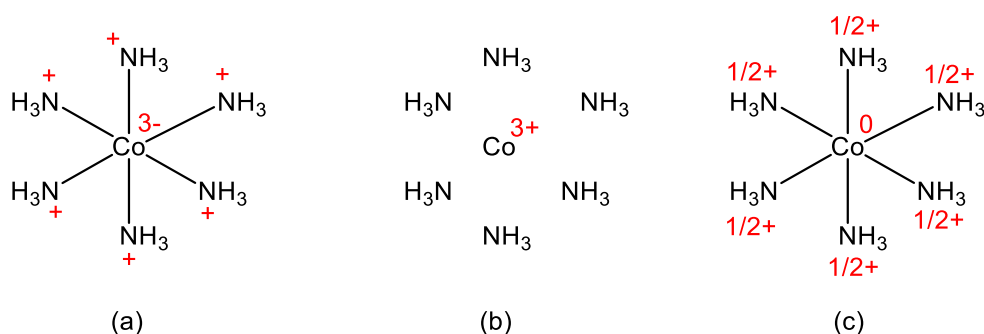


**Figure 16:** The complex cation  $[\text{Co}(\text{NH}_3)_6]^{3+}$  presenting the charge distribution as a result from a 100% covalent model (a) or 100% ionic model (b). Applying the electroneutrality principle results in model (c).

Model (b) of a wholly ionic complex does not help to characterize the interactions between the metal ion and the ligand either. Positive particles do not attract neutral particles. In this model the  $\text{NH}_3$  would just leave the cobalt ion.<sup>[7, 8, 33]</sup>

To address this problem Pauling proposed the electroneutrality principle. It defines the distribution of charges in a molecule or ion. There each atom should have a charge within the range of +1 to -1, ideally close to zero. By applying this principle on the example of  $[\text{Co}(\text{NH}_3)_6]^{3+}$ , the cobalt centre has a net charge of zero. Each of the six  $\text{NH}_3$  donates half an electron (-1/2 charge) adding up to a total of three electrons for the Co. As a result, each  $\text{NH}_3$  remains with a charge of +1/2 (model (c)). Of course the electroneutrality principle is only an approximation to help estimate the charge distribution in coordination compounds. It's a good principle to estimate the stability of complexes.<sup>[7, 8, 33]</sup>

Pauling's theory of hybridization is largely not appropriate for describing metal complexes, since electronic interactions are not possible in a hybridized system.

### 2.4.1.1 Crystal field theory

The Crystal Field Theory was first proposed by Bethe and added to from van Vleck to describe the physical properties of transition metals complexes. Coordination compounds can show magnetic and optical properties which could not be well explained by that time. It is a purely electrostatic model. Neither a wholly ionic nor a wholly covalent bonding are in line with the Pauling's electroneutrality principle. The idea is that ligands can be seen as negative point charges and there is no covalent bonding between the metal and the ligand.<sup>[7, 8, 34]</sup>

The electrostatic field of these ligands affects the d-electrons in the d-orbitals of the metal centre. By the term "crystal field" you view the complex with a classical understanding of a crystal. The ligands only have an effect on their nearest neighbours.<sup>[7, 8, 34]</sup>

This model helps to explain the electronic spectroscopic and magnetic characteristics of d-block metal complexes.<sup>[7, 8, 34]</sup>

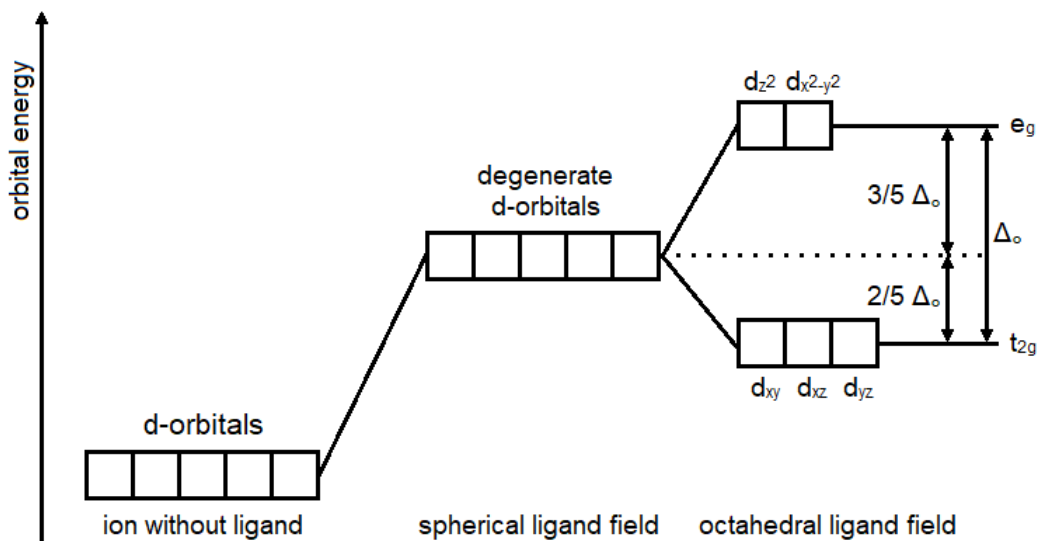


**Figure 17:** Changes in the energies of the 3d-orbitals of an ion. The metal centre is surrounded by no ligands (left), by point charge ligands spherically (middle) and by point charge ligands octahedral (right).

In an octahedral arrangement, the energy of the 3d-orbitals which point directly at the ligands is increased, while the energy of the orbitals that point between the ligands is decreased.<sup>[7, 8, 34]</sup>

The spin-orbit coupling is an interaction occurring in the scale of quantum mechanics. The strength of this coupling depends on the position of the particle's spin relative to its orbital angular momentum. This spin-orbit interaction leads to a splitting of energy levels. This splitting results in the fine structure of the energy levels. The effect of the electrons in the atomic shell is important in this chapter, because it has implications for the atomic structure.<sup>[10]</sup>

If one compares the orbital energies of the 3d metals with those of the 4f metals, one immediately notices that the orbital energies of the 4f elements are much larger (see Figure 17 and 18). For them, spin-orbit coupling dominates over the crystal field. With the 3d-elements it is exactly the other way round.<sup>[3]</sup>

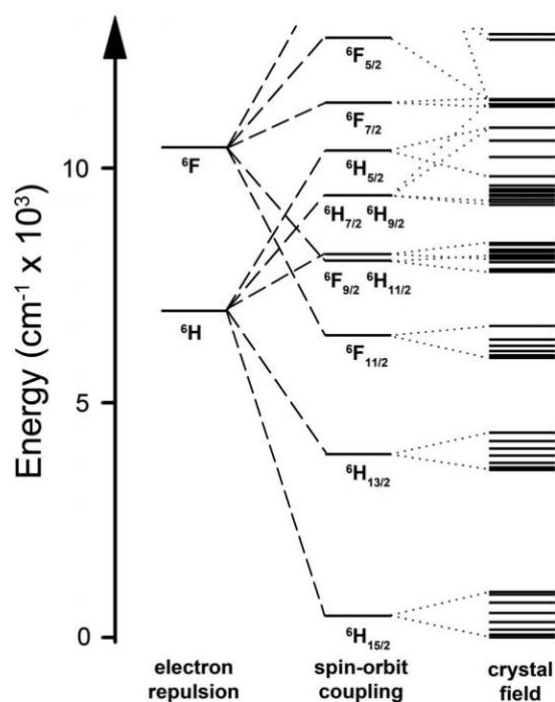


**Figure 18:** Relative magnitudes of the perturbations in the 4f ions shown for Dy<sup>III</sup>.<sup>[3]</sup>

### 2.4.1.2 Ligand field theory

The ligand field theory results from the work of John Stanley Griffith and Leslie Orgel. It deals with the bonds and orbital arrangements of coordination compounds. This theory emerges from molecular orbital theory and the crystal field theory. It is an alternative model to crystal field theory to explain other physical properties. With the help of the ligand field theory, for example, the visible spectra of transition metal complexes in solution can be described.<sup>[1, 7, 35]</sup>

Here, the valence orbitals of the transition metals are considered. The nine valence atom orbitals of the d-block metal ions provide sufficient energy for possible binding to the ligand. These include one s orbital, the three p orbitals  $p_z$ ,  $p_x$ , and  $p_y$ , and the five d orbitals  $d_{z^2}$ ,  $d_{xz}$ ,  $d_{yz}$ ,  $d_{xy}$ , and  $d_{x^2-y^2}$ . This explains why the main reason for the different colours in transition metal complexes in solution is the incompletely occupied subshells of the d-block orbitals. The geometry of such a coordination compound must also be taken into account for energetic considerations.<sup>[1, 7, 35]</sup>

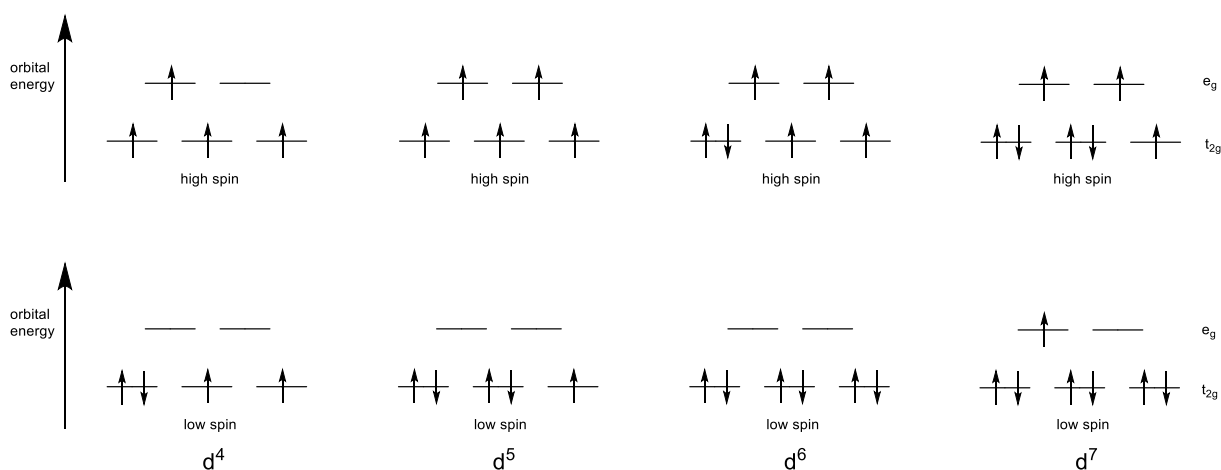


**Figure 19:** High- and low-spin arrangement of electrons for the d<sup>4</sup> to d<sup>7</sup> configurations between the  $t_{2g}$  and  $e_g$  levels.

## 2.5 Designing lanthanide complexes

A crucial aspect for the formation of complexes is the size of the central atom and the distance between the coordination sites in the chelating ligand. The 4f atomic orbitals are diffuse and only poorly shield the nuclear charge. The ionic radius of trivalent six-coordinate lanthanide ions decreases from lanthanum at 103 pm to lutetium at 86 pm as result of the lanthanide contraction.<sup>[5]</sup>

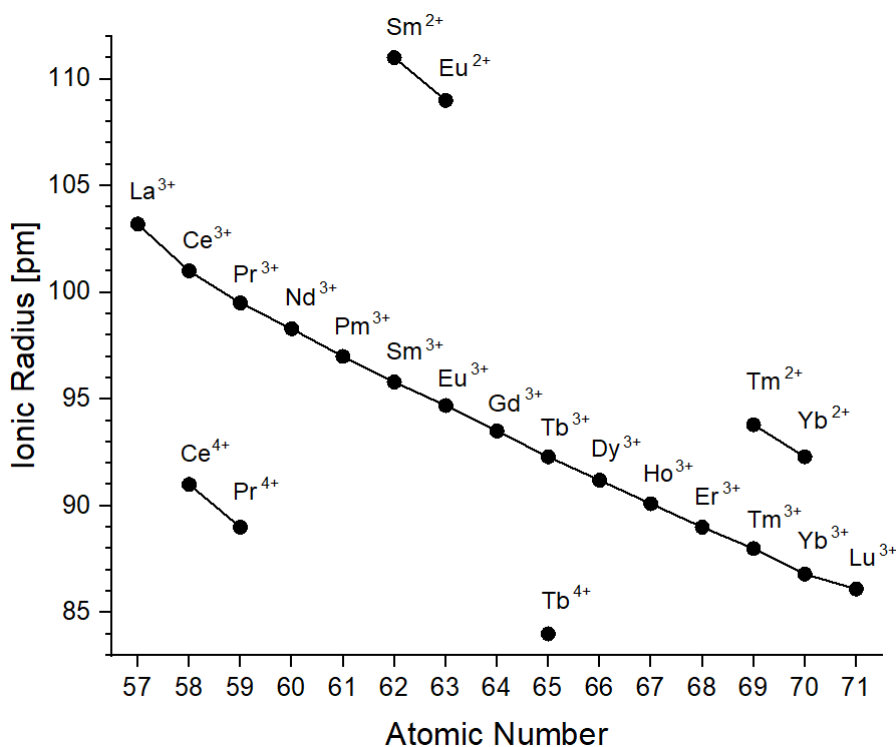


**Figure 20:** The ionic radii throughout the lanthanide series, visualising lanthanide contraction. Values are taken from R. D. Shannon.<sup>[36]</sup>

Lanthanides in lanthanide complexes tend to have a higher coordination number due to being larger than 3d-metal ions. If a ligand can grab a metal particle with multiple coordination sites, it is called polydentate. If a multidentate ligand forms several coordination sites for the same central particle, this ligand is also referred to as a chelating ligand. Complexes formed from this often exhibit higher thermodynamic and kinetic stability. This is because, compared to complexes with monodentate ligands, they have a higher entropy increase during complex formation. If one takes into account the molecules released from the solvation shell of the metal ion, multidentate ligands leads to a higher number of free molecules.<sup>[1, 8, 32]</sup>

When designing a multidentate ligand, the number and distance between coordinating functional groups in the ligand plays an important role. This will determine the ligands size. Another important aspect is whether the ligand only has double bonds or also single bonds. If it has no single bonds, the molecular framework is rigid and not very flexible.<sup>[1, 8, 32]</sup>

Peewasan designed large Schiff base ligands featuring multiple pockets (see Figure 21). Those lanthanide complexes feature optical properties in the visible range.<sup>[37]</sup>

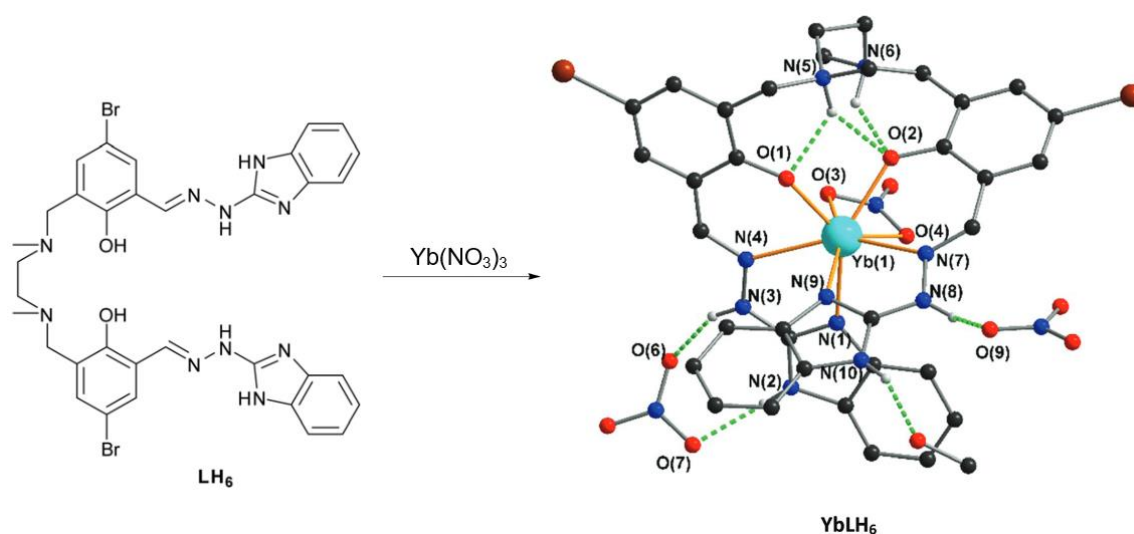
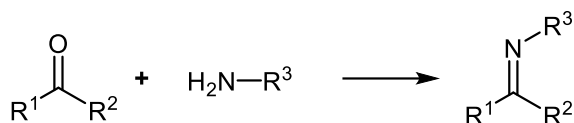


**Figure 21:** Complex formation of C<sub>38</sub>H<sub>47</sub>Br<sub>2</sub>N<sub>14</sub>O<sub>14</sub>Yb.<sup>[37]</sup>

## 2.6 Schiff bases

The organic ligands in a complex compound often coordinate via nitrogen or oxygen atoms. Imine compounds are usually obtained by nucleophilic addition of a primary amine with an aldehyde or a ketone.<sup>[32, 38]</sup>

Hydrazone compounds are synthesized analogously via a reaction of an aldehyde or ketone with a hydrazine derivative.<sup>[32, 38]</sup>



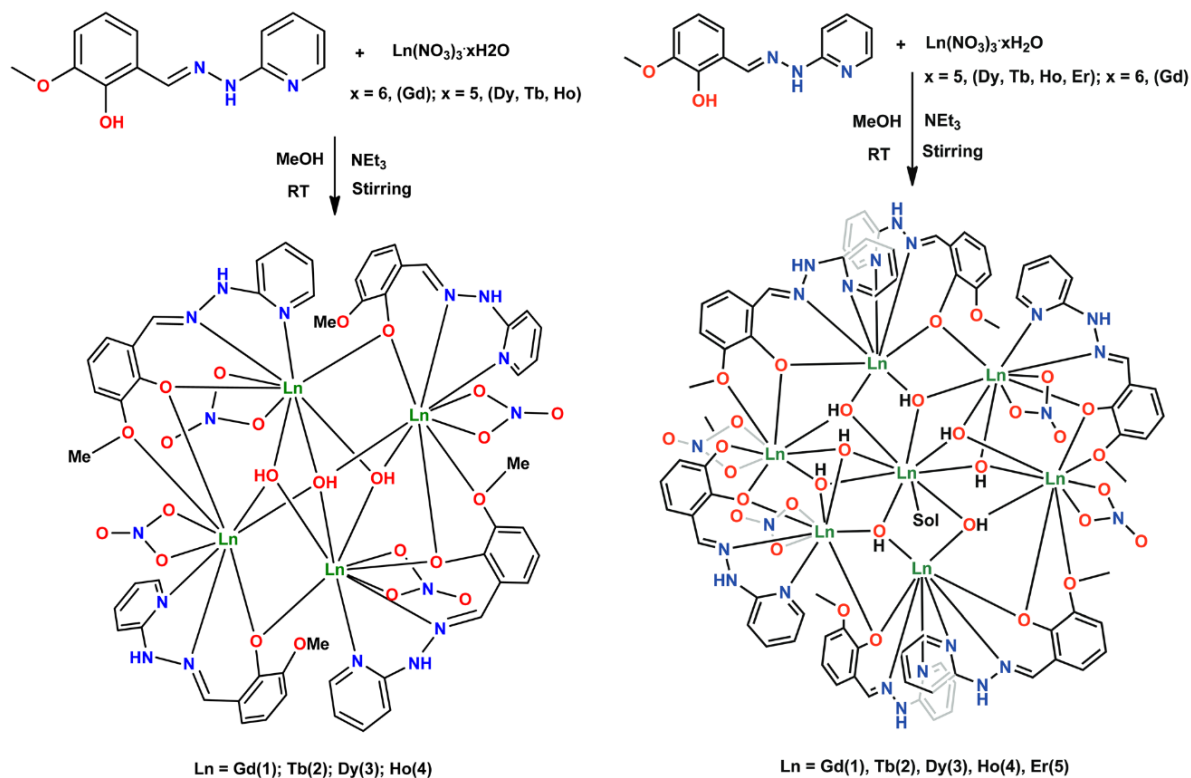
$\text{R}^1$  and  $\text{R}^2$  alkyl, aryl or hydrogen;  $\text{R}^3$  = alkyl or aryl group.

**Scheme 1:** Schematic representation of the synthesis of imines.

Schiff bases have the general structural formula shown in Scheme 1. They can be viewed as a subcategory of imines and are therefore secondary ketimines or aldimines. Schiff bases are particularly suitable as ligands for coordination compounds with metal ions, since the nitrogen atom can be functionalized via its lone pair of electrons. Schiff bases are one of the most used ligands in coordination chemistry. The imine nitrogen can act as a base or be used as a  $\pi$ -acceptor.<sup>[32, 38]</sup>

Ligands with alcohol or phenol groups are used for oxygen-coordinating complexes. Alcohols can be obtained by many reactions. For example, via the reduction of the corresponding carboxylic acid or via the Ziegler-Alfol synthesis. Phenol can be synthesized via the Cumene process using benzene, propylene and oxygen in several steps. The oxygen atom on the alcohol or phenol group coordinates either as an OH group or in its deprotonated form as an  $\text{O}^-$  group.<sup>[32, 38]</sup>

Chandrasekhar and colleagues were able to produce a series of 4- and 7-nuclear lanthanide clusters (see Scheme 2). Some of these coordination compounds made by using such a Schiff base-ligand system are showing a magnetocaloric effect.<sup>[39, 40]</sup>



**Scheme 2:** Schematic representation of the synthesis of the homo-metallic  $\text{Ln}_4$ - (left) and  $\text{Ln}_7$ -complexes (right).<sup>[39, 40]</sup>

### 3 MOTIVATION

The aim of this work is to contribute to the understanding of lanthanide-based compounds. For this purpose, a series of lanthanide complexes was synthesised and their properties examined. The focus of these investigations was on their molecular structure, their magnetic and optical properties. When designing compounds with lanthanides, it must be kept in mind that their cations are larger than most those of other metals, and therefore form a higher number of bonds. Therefore, in this work, ligands whose pockets provide sufficient space as well as sufficient oxygen and nitrogen atoms were used for complex formation for coordination with large metal ions.

It is the magnetic properties in particular that make lanthanide compounds exciting. In the field of single-molecule magnets, the goal is to design compounds that exhibit the slowest possible magnetic relaxation at the highest possible temperatures. In this way, their preferred magnetic orientation can be retained for as long as possible, which brings them closer to practical applications. However, the understanding of exactly how such an SMM must be constructed is still quite limited. The approach in this work is to design a series of similar molecules in order to then create a better comparability. The differences in structure between the designed compounds are intentionally slight, so that it can be observed how the changes made to the ligand field affect the magnetic properties. Conclusions can be drawn as to what alteration in the structure influences the magnetic anisotropy and the relaxation pathways. The magnetic measurements on the target compounds are also supported by computer-based simulations.

The optical properties of lanthanide complexes can also be of interest. In particular, compounds that absorb light in the visible range have been sought. The UV/Vis spectra of these compounds were measured. Again, only minor changes were made to the ligand system by replacing the lanthanide ion. Although the size of the lanthanides decreases from left to right in the periodic table, neighbouring lanthanide ions can provide isostructural compounds for comparison. The aim of these measurements was to get a better understanding of optical processes and how the ionic radius affects luminescence.

## 4 RESULTS AND DISCUSSION

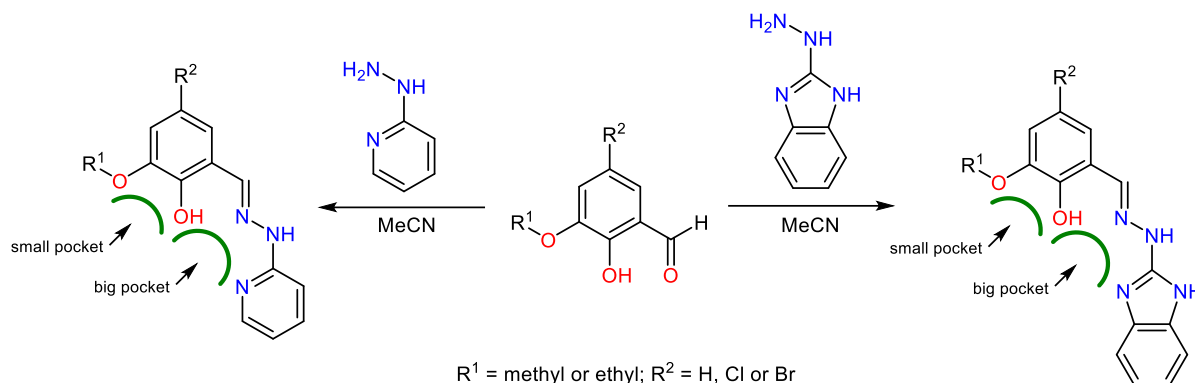
In order to implement the objectives of this work, a concept for the construction of the ligand field is required, which in turn requires suitable ligands. Schiff bases are particularly good for this because they can be easily synthesised with primary amines and carbonyl compounds. Schiff bases can be obtained in high yield and purity by nucleophilic addition and subsequent dehydrogenation.<sup>[32]</sup> A nitrogen atom of the newly created imine group can serve as a coordination partner for the metal ion.<sup>[39, 40]</sup>

For the first group of target compounds, it is desired that slow magnetic relaxation is favoured. The lanthanide ion Dy<sup>III</sup> is the first choice for this. Its anisotropy ellipsoid exhibits an oblate shape in its <sup>6</sup>H<sub>15/2</sub> ground state, favouring an axial ligand field. In order to preserve the ellipsoid shape of Dy<sup>III</sup>, the ligands should coordinate with uncharged N atoms in the equatorial plane and with negatively charged atoms in the axial position. This should preserve the magnetic anisotropy and suppress relaxation processes.<sup>[3]</sup>

For the second group of target compounds, those that support photoluminescence are sought. Complexes with a conjugated  $\pi$ -system are chosen for the luminescence studies. These should absorb light strongly in the visible range of 380-750 nm. Ligands with pyridine and benzimidazole groups are suitable for this. Emission measurements can be used to find out in which wavelength range the complex compounds emit light. This should contribute to the understanding of the relaxation processes of charge-transfer complexes.<sup>[27-29]</sup>

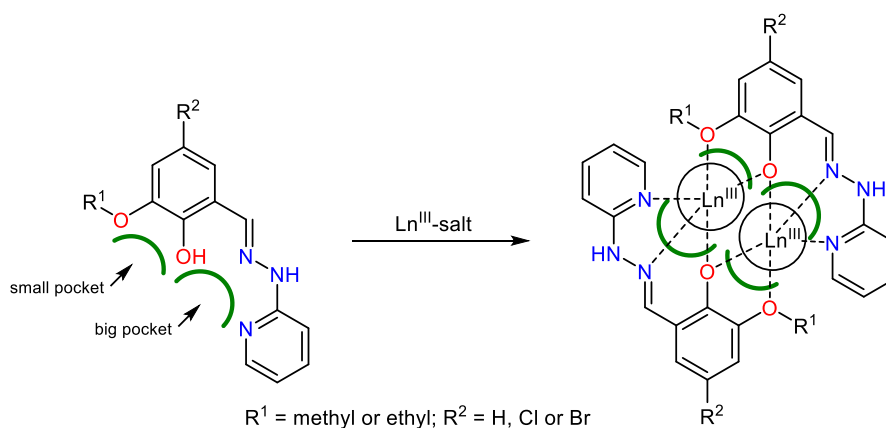
## 4.1 Dinuclear lanthanide systems

A two-pocket ligand system was chosen for the synthesis of the dinuclear lanthanide complexes. The large pocket can coordinate with a metal ion up to three times and a small one up to two times (see Scheme 3).



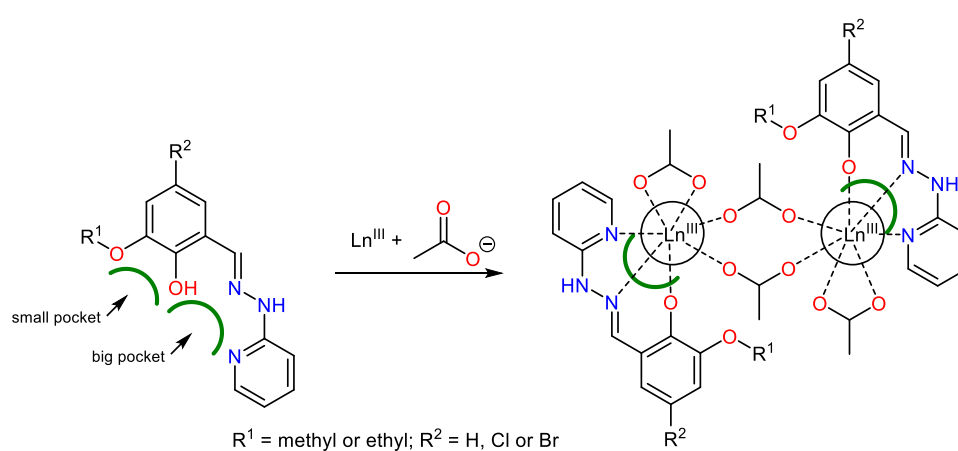
**Scheme 3:** Reaction scheme for the synthesis of all double pocket Schiff-base ligands.

Although a lanthanide<sup>III</sup> ion can occupy in both pockets, these are not yet completely enclosed. It takes another molecule of the ligand in the equatorial plane to enclose the lanthanide ions. Solvent molecules or anions can coordinate axially to them. With this system, a dinuclear structure consisting of two lanthanides and two ligand molecules can be formed with a high probability (see Scheme 4).



**Scheme 4:** Reaction scheme for the formation of the dinuclear lanthanide complexes.

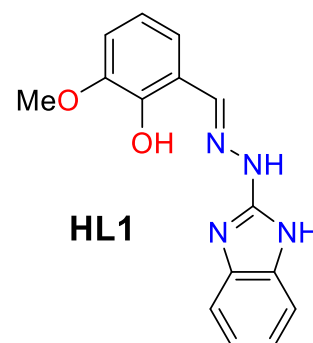
Alternatively, one can add an anion to the ligand system, which acts as an additional co-ligand. The acetate anion is the co-ligand of choice. Similar to nitrate, acetate can coordinate twice with its oxygen atoms to a lanthanide. However, it also has a strong tendency to bridge between two lanthanide ions. As a result, the lanthanides only occupy in the large pocket of the ligand and form bonds with three acetates, two bonds with one acetate and a single bond with two bridging acetates. Again this leads to a dinuclear coordination compound and there is an inversion centre in the middle between the lanthanide ions. In addition, another solvent molecule, such as water or methanol, can coordinate to each metal.



**Scheme 5:** Reaction scheme for the formation of the acetate bridged lanthanide complexes.

#### 4.1.1 Dinuclear lanthanide complexes (1) to (4) obtained from HL1

The four compounds presented here can be obtained in two steps. Firstly, the ligand HL1 was synthesised using a Schiff-base reaction with *o*-vanillin and 2-hydrazino-1H-benzimidazole as reactants. Then the ligand was mixed with a given lanthanide salt in a 1:1 mixture of methanol and acetonitrile. Slow evaporation of the solvents at room temperature was chosen as crystallisation technique. The lanthanide complexes (1), (2), (3) and (4) (Figure 22) were synthesised this way.



$[\text{Dy}_2(\text{L1})_2(\text{NO}_3)_4] \cdot 2\text{CH}_3\text{CN}$  (1) was obtained using  $\text{Dy}(\text{NO}_3)_3 \cdot 5\text{H}_2\text{O}$  as lanthanide salt and  $[\text{Nd}_2(\text{L1})_2(\text{NO}_3)_4\text{CH}_3\text{OH}] \cdot \text{CH}_3\text{CN}$  (2) in the same way using  $\text{Nd}(\text{NO}_3)_3 \cdot 6\text{H}_2\text{O}$ . After five days, yellow block-shaped crystals suitable for X-ray diffraction analysis had formed.

Combining  $\text{Ln}(\text{NO}_3)_3$  and HL1 resulted in two types of structures. The larger lanthanide ions ( $\text{Ln} = \text{Pr}$  to  $\text{Sm}$ ) form ten coordinate compounds isostructural to (2). The smaller lanthanides ions ( $\text{Ln} = \text{Gd}$  to  $\text{Lu}$ ) lead to nine coordinate complexes isostructural to (1). In the lanthanide series,  $\text{Eu}^{\text{III}}$  is the border between these two structural types. Its powder pattern shows it is a mixture of both types.

$[\text{Dy}_2(\text{L1})_2(\text{H}_2\text{O})_6]\text{Cl}_4 \cdot 2.5\text{CH}_3\text{OH} \cdot 2.5\text{CH}_3\text{CN}$  (3) and  $[\text{Dy}_2(\text{L1})_2(\text{H}_2\text{O})_6]\text{Br}_4 \cdot 2\text{CH}_3\text{OH} \cdot 2\text{CH}_3\text{CN}$  (4) were obtained using  $\text{DyCl}_3 \cdot 6\text{H}_2\text{O}$  and  $\text{DyBr}_3 \cdot x\text{H}_2\text{O}$  as lanthanide salt.

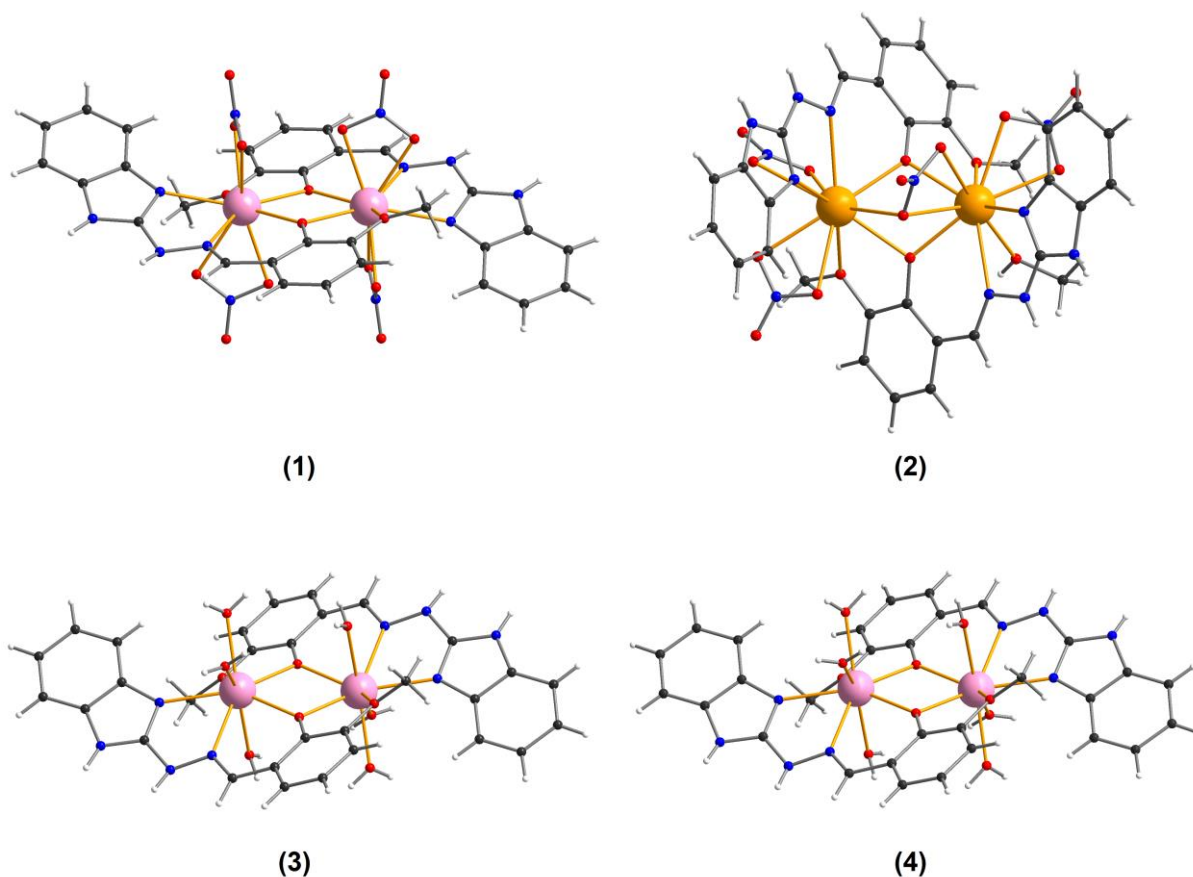


**Figure 22:** The four dinuclear lanthanide complexes using HL1 as ligand  $[Dy_2(L1)_2(NO_3)_4]$  (1),  $[Nd_2(L1)_2(NO_3)_4CH_3OH]$  (2),  $[Dy_2(L1)_2(H_2O)_6]Cl_4$  (3) and  $[Dy_2(L1)_2(H_2O)_6]Br_4$  (4). Colour code: white = H; black = C; blue = N; red = O; light orange = Nd; rose = Dy.

All four compounds have similar structures. They consist of two  $Ln^{III}$  ions and two deprotonated molecules of the ligand ( $L1$ )<sup>-</sup>. Each ligand coordinates to Ln(1) via the imidazole and imino nitrogen atoms. The deprotonated phenoxo oxygen atom form bridges between the lanthanides. This ligand also coordinates with these phenoxo oxygen as well as methoxy oxygen. That leads to a molecule centre of two  $Ln^{III}$  doubly bridged by two oxygen. In total each lanthanide is five coordinated from the ligands with two nitrogens and three oxygens laying in the equatorial plane (see Figure 22).

Different co-ligands occupy the axial positions. The nature of these leads to the differences between in the equatorial plain of compounds (1) - (4). For (1), (3) and (4) the inversion centre is the centre of the complex in the middle between the  $Ln^{III}$  ions making both sides of the molecule identical. In contrast compound (2) has its inversion centre outside the molecule.

Compound (1) has two nitrates chelating each Dy<sup>III</sup> ion with two oxygens in axial position. Compounds (3) and (4) have three water molecules bonding to each Dy<sup>III</sup> with their oxygen atom, one from one side and two from the other side. To balance out their charges (3) has four chloride and (4) has four bromide counter ions. Two of those halides are weakly bonded to hydrogen atoms of the water and two to the hydrogen atoms of the hydrazone groups (see dashed bonds Figure 29). That sums up to making the Dy<sup>III</sup> ions in compound (1) nine, in compound (3) and (4) eight coordinate. The larger ionic radius of Nd<sup>III</sup> compared to Dy<sup>III</sup> forces the structure to lead to a higher coordination number of ten.

One of the oxygens of a nitrate ligand chelating to Nd(1) also bridges to Nd(2). The coordination number of Nd(1) is increased by addition of a methanol ligand. More importantly, the presence of the chelating-bridging nitrate results in the two hydrazone ligands now being almost planar. Their respective planes are almost perpendicular to each other. There is a minor (8%) disorder of the central nitrate in (2), in which the nitrate now chelates Nd(2) and the oxygen bridges to Nd(1). This would lead to the coordination numbers for Nd(1) and Nd(2) in this minor conformer being 9 and 11.

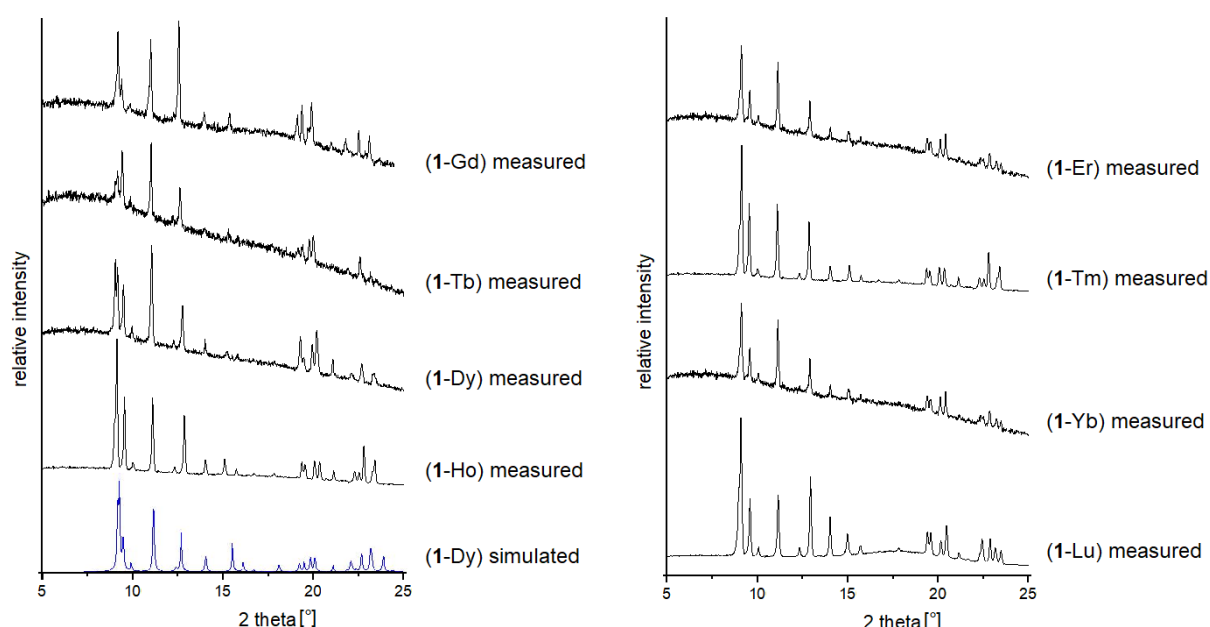


**Figure 23:** Powder patterns of  $[\text{Ln}_2(\text{L1})_2(\text{NO}_3)_4] \cdot 2\text{CH}_3\text{CN}$  ( $\text{Ln} = \text{Gd to Lu}$ ).

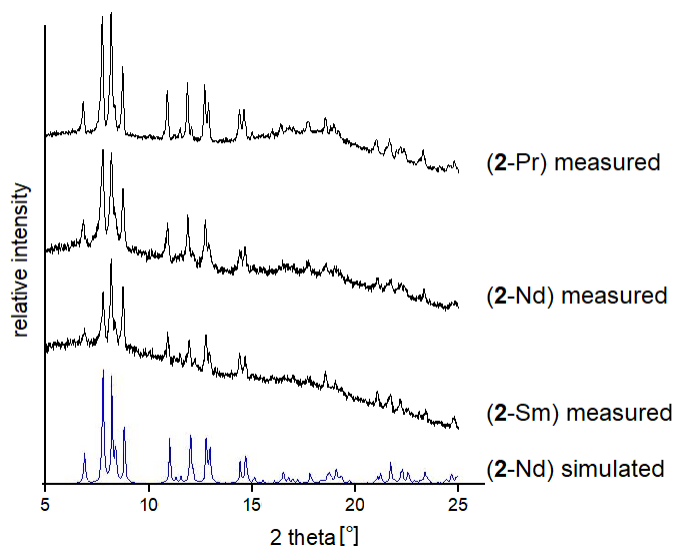


**Figure 24:** Powder patterns of  $[\text{Ln}_2(\text{L1})_2(\text{NO}_3)_4\text{MeOH}] \cdot \text{CH}_3\text{CN}$  ( $\text{Ln} = \text{Pr}$  to  $\text{Sm}$ ) versus the simulated pattern of (2).

The measured powder patterns for compound (1) and (2) match with the simulated patterns from the single crystal data.

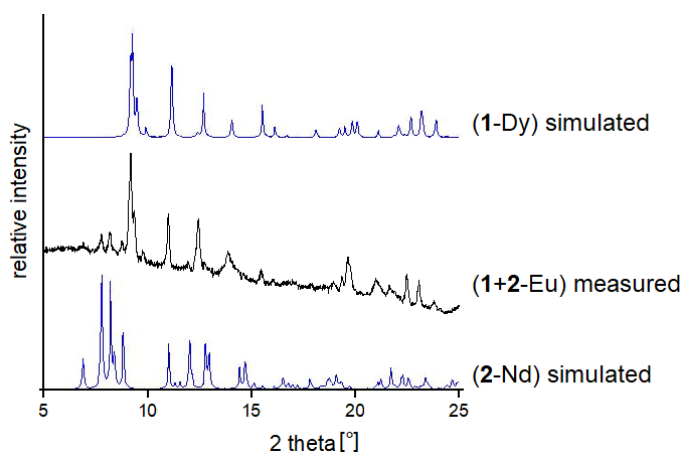


**Figure 25:** The measured powder pattern of the Eu-L1 complex versus the simulated patterns of (1) and (2).

In Figure 25 it can be seen that Eu represents the border between the two structural families. The powder pattern of the Eu compound is an overlap of the Pr-Sm type and the Gd-Lu type. This compound forms a mixture of crystals of both types of structural families.

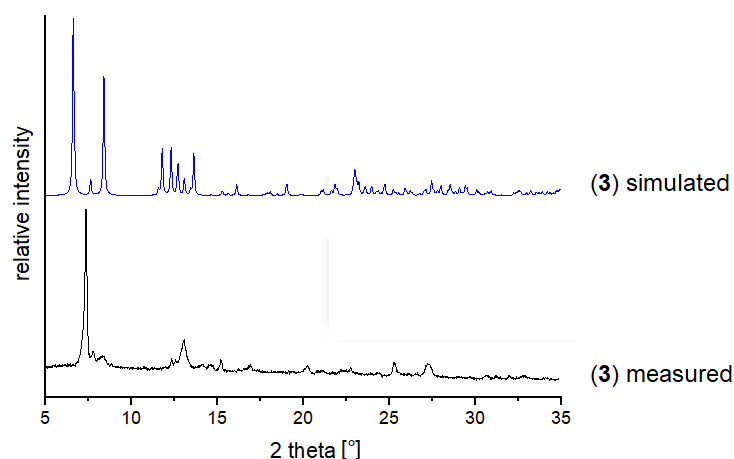


**Figure 26:** Powder pattern of **(3)** simulated versus measured.

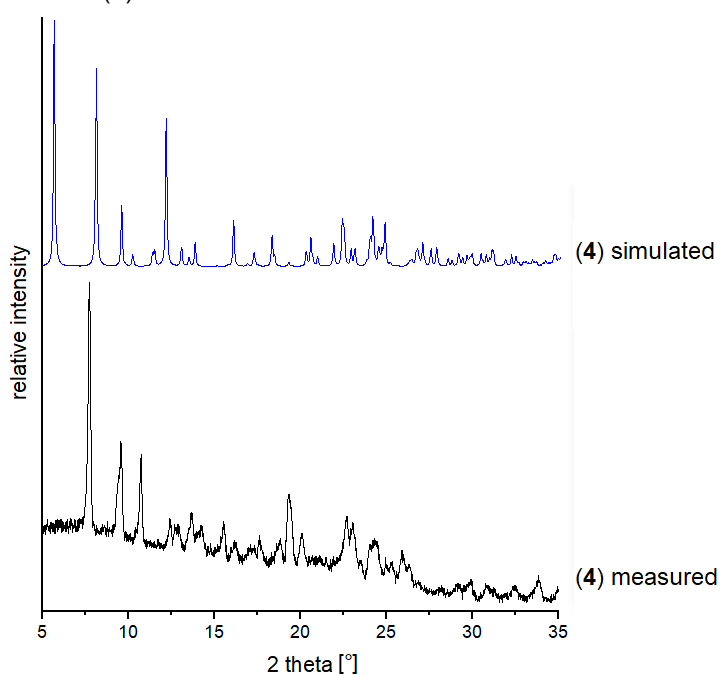


**Figure 27:** Powder pattern of **(4)** simulated versus measured.

Both measured powder patterns of compound **(3)** and **(4)** do not match with the simulated patterns from the single crystal data. This is likely due to a loss of the solvent molecules and a partial collapse of the crystal structure. The shiny crystals turn opaque immediately after being exposed to air. The CHNS analyses of **(3)** and **(4)** do not agree with the sum formulas received from the single-crystal X-ray diffraction. This is because the sum formulas include all the solvent molecules. However, if one removes four solvent molecules from **(3)** results a sum formula of  $[\text{Dy}_2(\text{L1})_2(\text{H}_2\text{O})_6]\text{Cl}_4 \cdot 0.5\text{CH}_3\text{OH} \cdot 0.5\text{CH}_3\text{CN}$ , which agrees with the CHNS analysis. If three solvent molecules from **(4)** are removed a sum formula of  $[\text{Dy}_2(\text{L1})_2(\text{H}_2\text{O})_6]\text{Br}_4 \cdot 0.5\text{CH}_3\text{OH} \cdot 0.5\text{CH}_3\text{CN}$  results, which would agree to the corresponding CHNS analysis (see Experimental section).

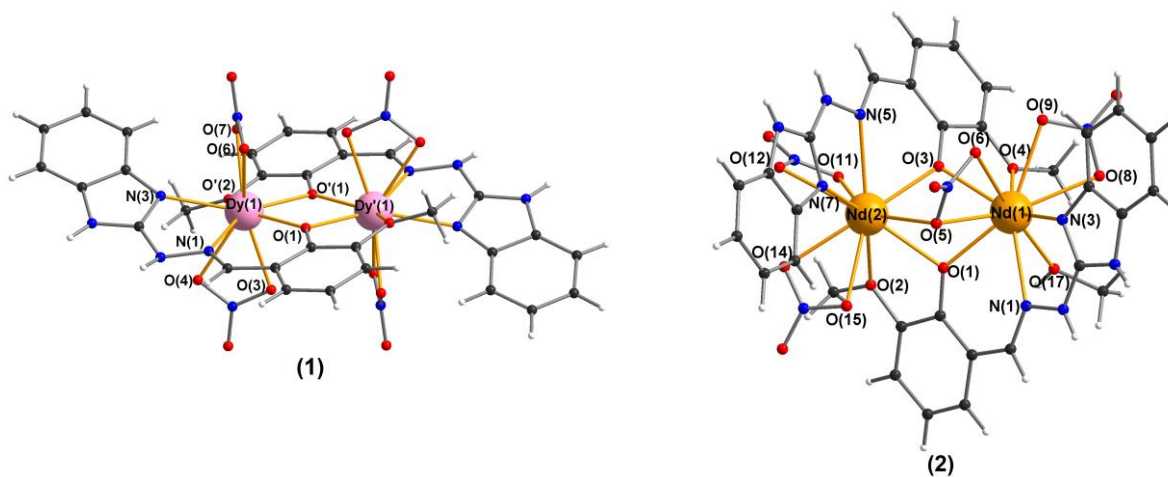


**Figure 28:** Structure of (1) and (2) with selected atoms labelled.

| Atom  | Atom   | Distance [Å] |
|-------|--------|--------------|
| Dy(1) | Dy'(1) | 3.7384(5)    |
| Dy(1) | O(1)   | 2.293(5)     |
| Dy(1) | O'(1)  | 2.388(4)     |
| Dy(1) | O'(2)  | 2.404(5)     |
| Dy(1) | O(3)   | 2.497(5)     |
| Dy(1) | O(4)   | 2.534(6)     |
| Dy(1) | O(6)   | 2.449(6)     |
| Dy(1) | O(7)   | 2.406(5)     |
| Dy(1) | N(1)   | 2.468(6)     |
| Dy(1) | N(3)   | 2.460(5)     |

| Atoms             | Angle [°]  |
|-------------------|------------|
| Dy(1)-O(1)-Dy'(1) | 105.97(17) |
| O(1)-Dy(1)-O'(1)  | 74.03(17)  |

| Atom  | Atom  | Distance [Å] |
|-------|-------|--------------|
| Nd(1) | Nd(2) | 3.7962(4)    |
| Nd(1) | O(1)  | 2.359(2)     |
| Nd(1) | O(3)  | 2.391(3)     |
| Nd(1) | O(4)  | 2.744(3)     |
| Nd(1) | O(8)  | 2.557(3)     |
| Nd(1) | O(9)  | 2.559(3)     |
| Nd(1) | O(17) | 2.459(3)     |
| Nd(1) | N(1)  | 2.667(3)     |
| Nd(1) | N(3)  | 2.551(3)     |
| Nd(1) | N(10) | 2.983(3)     |
| Nd(1) | O(5)  | 2.656(3)     |
| Nd(1) | O(6)  | 2.756(3)     |
| Nd(2) | O(1)  | 2.486(3)     |
| Nd(2) | O(2)  | 2.779(3)     |
| Nd(2) | O(3)  | 2.367(2)     |
| Nd(2) | O(11) | 2.494(3)     |
| Nd(2) | O(12) | 2.692(3)     |
| Nd(2) | O(14) | 2.570(3)     |
| Nd(2) | O(15) | 2.591(2)     |
| Nd(2) | N(5)  | 2.662(3)     |
| Nd(2) | N(7)  | 2.553(3)     |
| Nd(2) | O(5)  | 2.616(3)     |

| Atoms            | Angle [°] |
|------------------|-----------|
| Nd(1)-O(1)-Nd(2) | 103.14(9) |
| Nd(1)-O(3)-Nd(2) | 105.84(9) |
| O(1)-Nd(1)-O(3)  | 68.58(9)  |
| O(1)-Nd(2)-O(3)  | 66.88(8)  |

**Table 2:** Selected bond lengths and angles of compound (1) (right) and (2) (left).

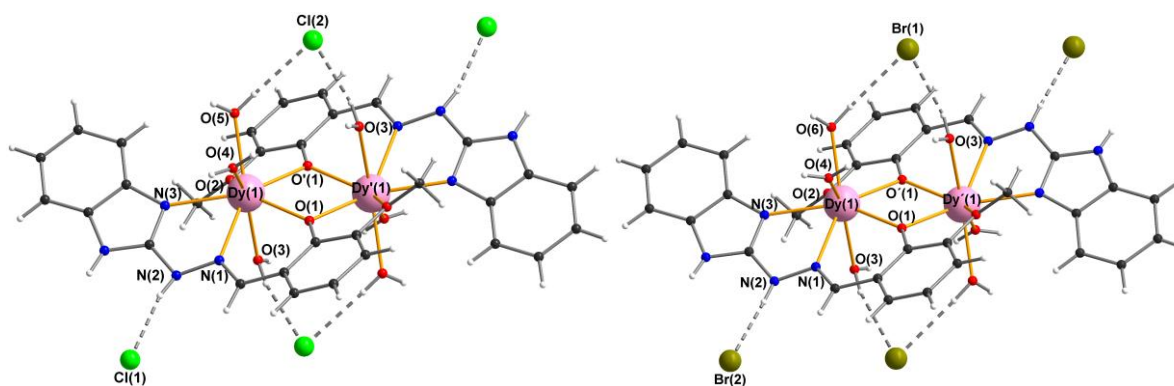


**Figure 29:** Structure of (3) and (4) with selected atoms labelled.

| Atom  | Atom   | Distance [Å] |
|-------|--------|--------------|
| Dy(1) | Dy'(1) | 3.7041(4)    |
| Dy(1) | O(1)   | 2.2879(19)   |
| Dy(1) | O'(1)  | 2.330(2)     |
| Dy(1) | O'(2)  | 2.482(2)     |
| Dy(1) | O(3)   | 2.352(2)     |
| Dy(1) | O(4)   | 2.355(2)     |
| Dy(1) | O(5)   | 2.373(2)     |
| Dy(1) | N(1)   | 2.504(2)     |
| Dy(1) | N(3)   | 2.413(2)     |
| Cl(1) | N(2)   | 3.075(3)     |
| Cl(2) | O(5)   | 3.151(2)     |
| Cl(2) | O(3)   | 3.108(3)     |

| Atoms             | Angle [°] |
|-------------------|-----------|
| Dy(1)-O(1)-Dy'(1) | 106.65(8) |
| O(1)-Dy(1)-O'(1)  | 73.35(8)  |

| Atom  | Atom   | Distance [Å] |
|-------|--------|--------------|
| Dy(1) | Dy'(1) | 3.6954(4)    |
| Dy(1) | O(1)   | 2.2724(19)   |
| Dy(1) | O'(1)  | 2.3298(19)   |
| Dy(1) | O'(2)  | 2.4708(19)   |
| Dy(1) | O(3)   | 2.365(2)     |
| Dy(1) | O(4)   | 2.365(2)     |
| Dy(1) | O(6)   | 2.368(2)     |
| Dy(1) | N(1)   | 2.503(2)     |
| Dy(1) | N(3)   | 2.405(2)     |
| Br(1) | O(3)   | 3.317(3)     |
| Br(1) | O(6)   | 3.351(2)     |
| Br(2) | N(2)   | 3.213(5)     |

| Atoms             | Angle [°] |
|-------------------|-----------|
| Dy(1)-O(1)-Dy'(1) | 106.82(7) |
| O(1)-Dy(1)-O'(1)  | 73.18(7)  |

**Table 3:** Selected bond lengths and angles of compound (3) and (4).

All the shown distances in compound (1) to (4) do agree with those in the literature.<sup>[41]</sup> By comparing (1) and (2), it can be seen, that (2) has longer Ln-X bond lengths, since Nd<sup>III</sup> has a larger ionic radius than Dy<sup>III</sup>. Also the coordination number has an effect on bond lengths. By comparing (3) and (4) both compounds are essentially isostructural.

The shapes of the coordination polyhedra were calculated using SHAPE.<sup>[42]</sup> The results show the three best fitting polyhedra and the arithmetic deviations in percent. For compound (1) to (4) five coordinating partners are the same. Two nitrogen atoms were provided from the imidazole and imine group, two oxygen atoms from the bridging phenoxy groups and one oxygen atom from the methoxy group. It should be noted that none of the compounds have very high conformity with the calculated shapes due to the stiffness of the ligand molecules. The results of the best fitting shapes may be close to each other, so the top 3 results are displayed.

The DyO<sub>7</sub>N<sub>2</sub> polyhedron of (1) is the result of two nitrates chelating with two oxygen atoms from the axial positions respectively. The best fitting polyhedron is a muffin.

| Polyhedron                        | Deviation [%] |
|-----------------------------------|---------------|
| Muffin                            | 7.459         |
| Capped square antiprism           | 7.763         |
| Spherical capped square antiprism | 8.036         |

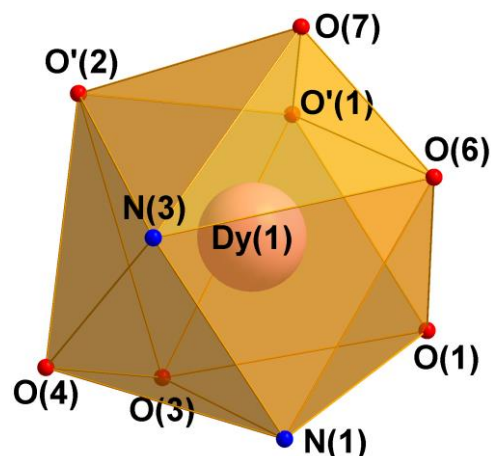
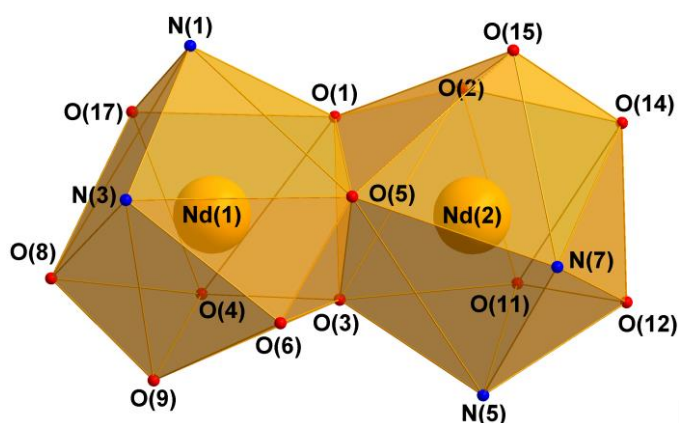


**Figure 30:** Nine-vertex polyhedron around the dysprosium centre of (1) with SHAPE values.

As a result of the lack of an inversion centre in the molecule compound (2) is asymmetrical. The larger size of the Nd<sup>III</sup> ion compared to Dy<sup>III</sup> leads to a coordination number of ten. The same nine functional groups as in (1) are chelating but Nd(1) is connected to an additional oxygen atom from a methanol molecule. Nd(2) is bridged to one nitrate oxygen which also coordinates to Nd(1) leading to two different polyhedra Nd(1)O<sub>8</sub>N<sub>2</sub> and Nd(2)O<sub>8</sub>N<sub>2</sub>.



| Polyhedron Nd(1)          | Deviation [%] |
|---------------------------|---------------|
| Sphenocorona              | 4.893         |
| Bicapped square antiprism | 8.121         |
| Tetradecahedron           | 9.701         |

| Polyhedron Nd(2)       | Deviation [%] |
|------------------------|---------------|
| Sphenocorona           | 9.086         |
| Staggered Dodecahedron | 10.574        |
| Bicapped cube          | 11.563        |

**Figure 31:** Nine-vertex polyhedra around the neodymium centres of (2) with SHAPE values.

The coordination environment of Nd(1) and Nd(2) in (2) can be described best with the shape of a sphenocorona.

The coordination environment of compound (3) and (4) are very similar and can be discussed together. Both complexes are ionic and need four halides anions to balance their charges. Each Dy<sup>III</sup> ion is coordinated by the oxygen atoms from three water molecules, two from one side and one from the other. That leads to an eight coordinated DyN<sub>2</sub>O<sub>6</sub> polyhedron for both compounds.

| Polyhedron                 | Deviation [%] |
|----------------------------|---------------|
| Triangular dodecahedron    | 10.587        |
| Biaugmented trigonal prism | 12.033        |
| Square antiprism           | 12.332        |

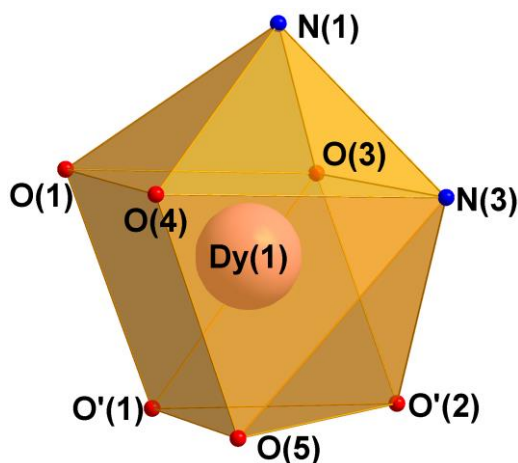
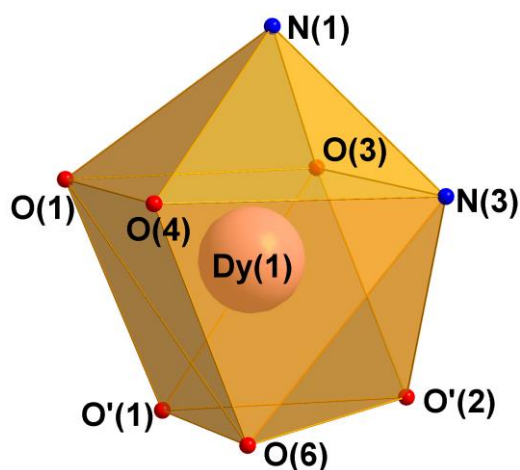


**Figure 32:** Eight-vertex polyhedron around the dysprosium centre of (3) with SHAPE values.



| Polyhedron                       | Deviation [%] |
|----------------------------------|---------------|
| Triangular dodecahedron          | 9.637         |
| Biaugmented trigonal prism       | 10.609        |
| Biaugmented trigonal prism (J50) | 10.898        |

**Figure 33:** Eight-vertex polyhedron around the dysprosium centre of **(4)** with SHAPE values.

None of the calculated shapes for the polyhedra of **(3)** and **(4)** fit well.

All four complexes presented here crystallise in the triclinic space group  $\bar{P}1$ . The packing of the molecule **(1)** is stabilised by two groups forming hydrogen bonds. Firstly, the lattice solvent acetonitrile has interactions to the hydrazone N-H group. Secondly, there is an intramolecular between the oxygen of the chelating nitrate and benzimidazole N-H group (see Figure 34). This together with  $\pi$ - $\pi$  stacking interactions form the main supramolecular interactions in the structure of **(1)**.

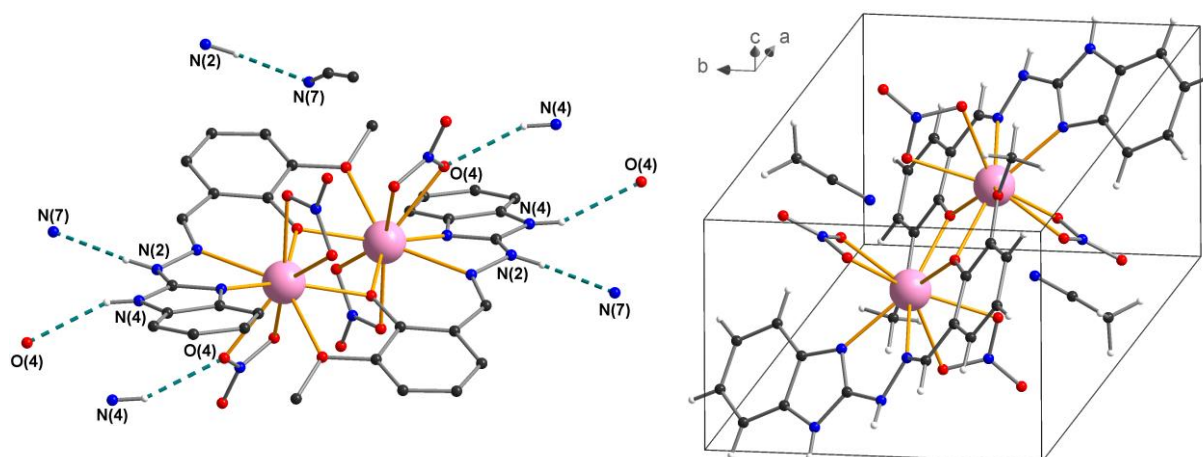


**Figure 34:** Compound **(1)** showing the hydrogen-bonds as green dashed lines (left, hydrogen on carbon atoms not displayed) and unit cell (right).

Compound (2) crystallises in the triclinic space group  $\bar{P}1$ . Unlike the other complexes in this chapter, here the inversion centre is between two molecules. That leads to two inverted molecules in the unit cell and two acetonitrile solvent molecules. The acetonitrile interacts via its nitrile group to the O-H group of the chelating methanol connected to Nd(1). All other hydrogen bonds are formed from the nitrate anions. The oxygen from the non-bridging nitrate O(9) on Nd(1) interacts with the N-H group from a neighbouring benzimidazole group. The first nitrate of Nd(2) bonds with O(13) to a N-H from a benzimidazole. The other nitrate anion of Nd(2) has O(15) and O(16) forming hydrogen bonds to N-H of a hydrazone group and O(16) to a N-H from a benzimidazole group.

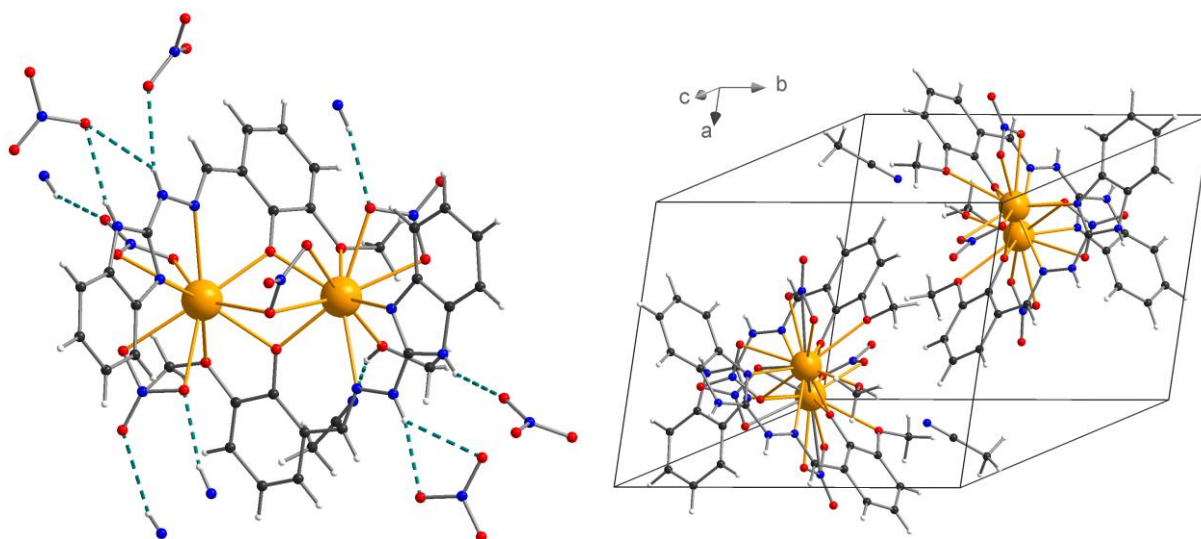


**Figure 35:** Compound (2) showing the hydrogen-bonds as green dashed lines (left) and the unit cell packing (right).

Compounds (3) and (4) have a very similar packing and can be discussed together. They crystallise in the triclinic space group  $P\bar{1}$ . Each unit cell contains one molecule of the complex, four halogen counter ions and acetonitrile and methanol molecules as lattice solvent. Hydrogen bonds are again present. There are two groups of halide anions. The first group bonds four-times with the hydrogen atoms from the coordinating water molecules. The second group bonds three-times to the N-H group of the benzimidazole, the hydrazone group and the O-H group of lattice methanol. The coordinating water molecules also interact with the oxygen of the lattice methanol and the nitrile group of the lattice acetonitrile.

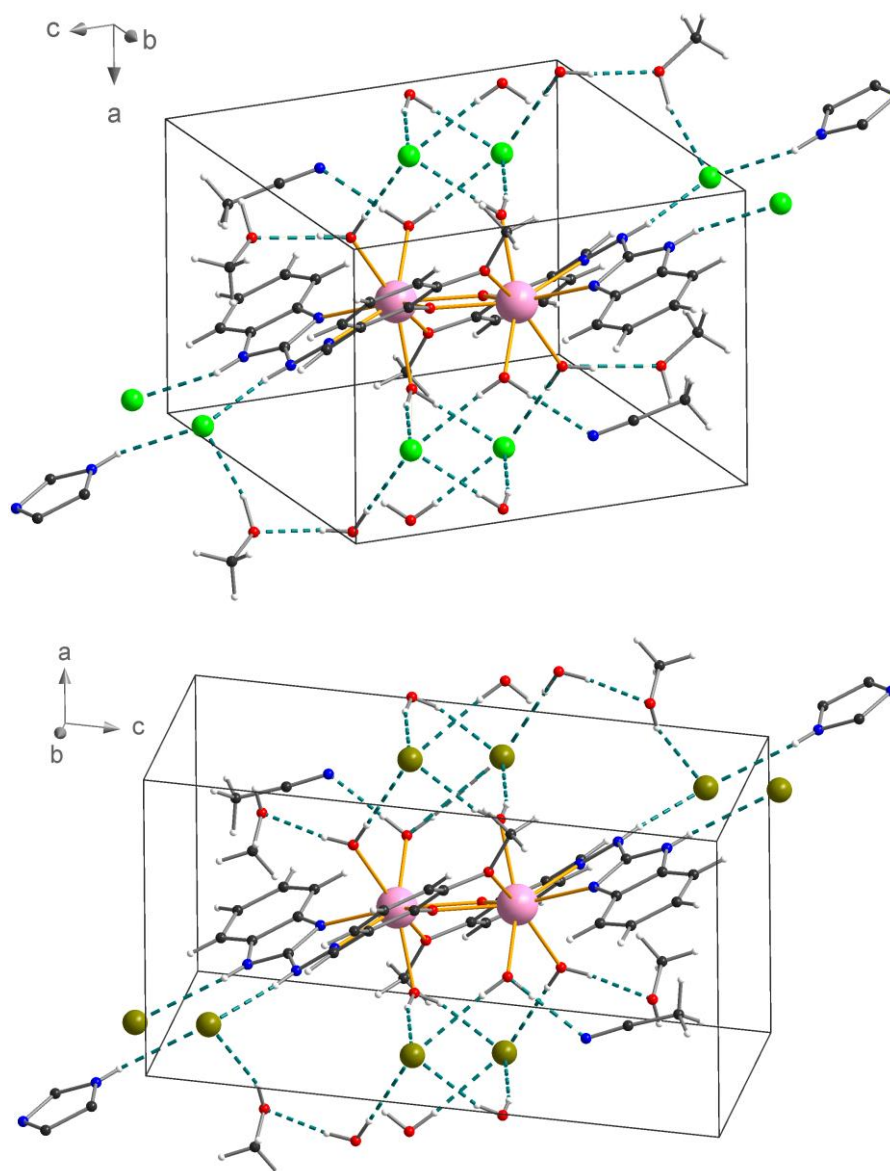


**Figure 36:** Unit cell packing of (3) (top) and (4) (bottom) showing the hydrogen bonds as green dashed lines.

#### 4.1.1.1 Magnetic properties of complexes (1), (3) and (4)

The Dy<sup>III</sup> compounds of this chapter were selected for magnetic studies since the properties of Dy<sup>III</sup> ions tend to be the most magnetically interesting. DC measurements on (1), (3) and (4) were performed on a Quantum Design MPMS-XL SQUID magnetometer. The room temperature  $\chi T$  values are 28.28 cm<sup>3</sup> K mol<sup>-1</sup> for (1), 28.09 cm<sup>3</sup> K mol<sup>-1</sup> for (3) and 28.24 cm<sup>3</sup> K mol<sup>-1</sup> for (4). This is in good agreement with the theoretical value of 28.34 cm<sup>3</sup> K mol<sup>-1</sup> for two non-interacting Dy<sup>III</sup> ions. The  $\chi T$  value decreases sharply below 25 K, indicating significant anisotropy in all three compounds and possibly antiferromagnetic interactions (Figure 37) in addition to the depopulation of Stark sublevels.<sup>[25]</sup>

Comparing the shapes of the three curves one can see that the curve of compound (1) falls much steeper towards lower temperatures. The curves of compound (3) and (4) are flatter and have a similar shape.

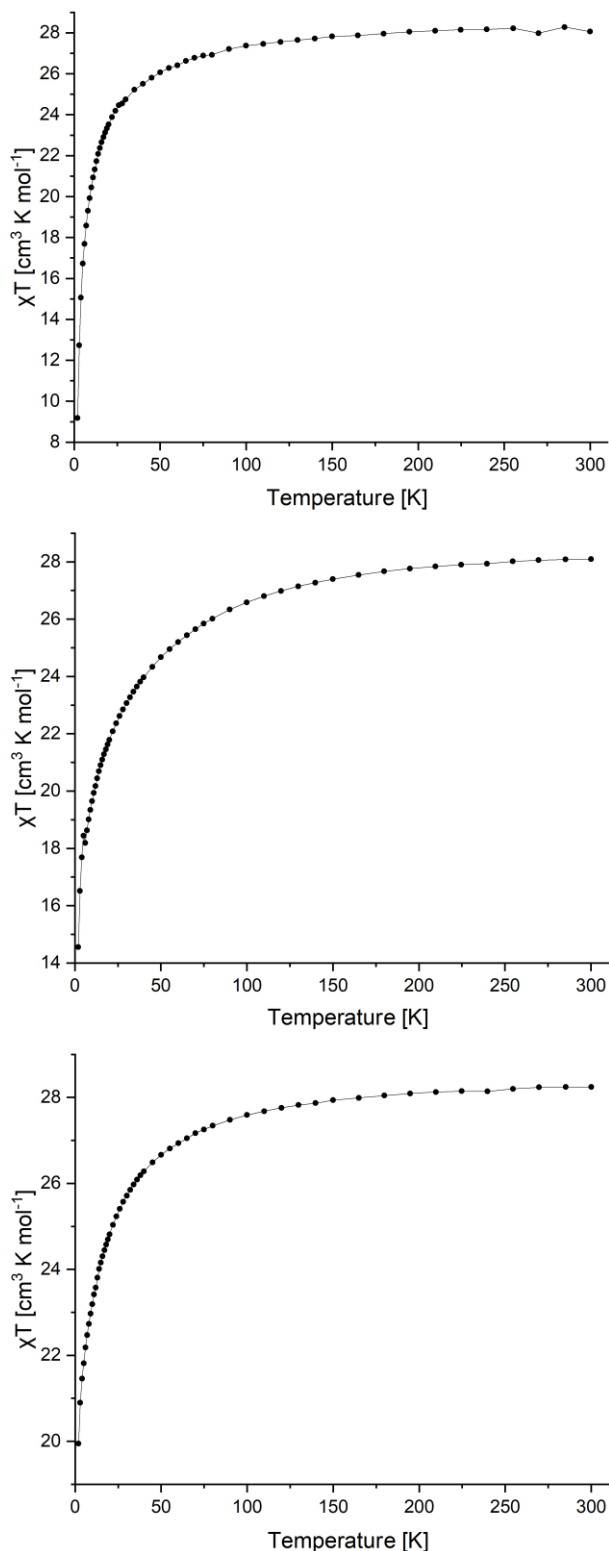


**Figure 37:** Plot of  $\chi T$  versus temperature for compound (1) (top), (3) (middle) and (4) (bottom).



For the anisotropy of an ellipsoid the direction of the principal "Ising axis" is defined by the z-direction. For (1), (3) and (4) it should be defined along the axis with the polar ligands.

**Figure 38:** The anisotropy of the 4f shell electron distribution from quadrupole approximations for Dy<sup>III</sup> along the Ising axis.<sup>[10]</sup>

Due to the anisotropy ellipsoid of Dy<sup>III</sup>, having largely charged ligands in axial positions is deemed beneficial to Dy-SMM behaviour. Using this model, the interaction between the presented dinuclear Dy-compounds can be explained. With their coordinating water molecules (3) and (4) have polar terminal ligands in axial positions, dominating the electrostatic field. A possible antiferromagnetic behaviour might be observed.

In order to investigate the dynamic magnetic behaviour, AC susceptibility measurements were performed on compound (1), (3) and (4).

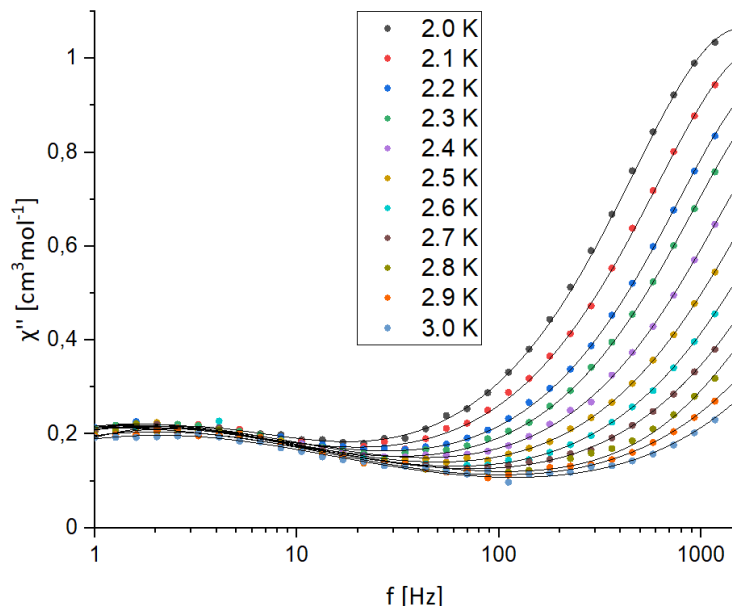


**Figure 39:** Plot of  $\chi''$  versus frequency for (1) at different temperatures and 4400 Oe.

An external field of 4400 Oe had to be applied to detected  $\chi''$  signals. The signals indicate a relaxation of magnetisation for compound (1). Unfortunately, this process seems to be relatively fast, so that the maximum values for each temperature fall outside the measurement window (see Figure 39).

First the data were fitted using the widely used equation where the last term corresponds an Orbach process following an Arrhenius law:

$$\tau(T)^{-1} = AT + B + CT^n + \tau_0^{-1} e^{\frac{U_b}{k_B T}}$$

(A, C = pre-factors; B = constant; T = temperature; n = Raman exponent;  $\tau_0$  = relaxation time;  $U_{\text{eff}}/U_b$  = energy barrier;  $k_B$  = Boltzmann constant)

**Formula 1:** Most common fit with one exponential factor.

This gave a  $U_{\text{eff}}$  of 39(3) K. Afterwards,  $\tau$  was fit with an equation of Gu and Wu according to exponential behaviour:<sup>[43]</sup>

$$\tau(T)^{-1} = AT + B + \tau_{0a}^{-1} e^{\frac{U_a}{k_B T}} + \tau_{0b}^{-1} e^{\frac{U_b}{k_B T}}$$

**Formula 2:** Equation suggested by Gu und Wu with two exponential factors.<sup>[43]</sup>

This gives better results than fits with the conventional description for the Raman term using a power law. The fitting gave a dependency that can be described by two exponential terms with the calculated energy barriers of  $U_a = 8(2)$  K and  $U_b = 47(6)$  K. The calculated relaxation times are  $\tau_{0a} = 2(2) \cdot 10^{-6}$  s and  $\tau_{0b} = 5(10) \cdot 10^{-13}$  s. Since the actual maxima fall outside of the measurement window the high uncertainties on these values are to be expected.

Those compound (1) shows SMM behaviour even through the relaxation of the magnetisation  $\tau_0$  happens in relative short time. The fact, that the maximum values of  $\chi''$  could not be measured led to additional uncertainty for the fitting and can be seen from the large uncertainties of the  $\tau$  values. Therefore, the calculated values have to be considered with caution, the relaxation is too fast to quantify them more precisely.

Compound **(3)** contains the same ligand as **(1)** but is a charged complex with a coordination number of 8 instead of 9. To investigate what effect this change in the ligand field has in the dynamic magnetic behaviour, AC susceptibility measurements were also performed on compound **(3)**. At first sight the  $\chi''$  signal seems to indicate a relaxation of magnetisation. However, the maxima for the  $\chi''$  signals have relatively low values (see Figure 40).

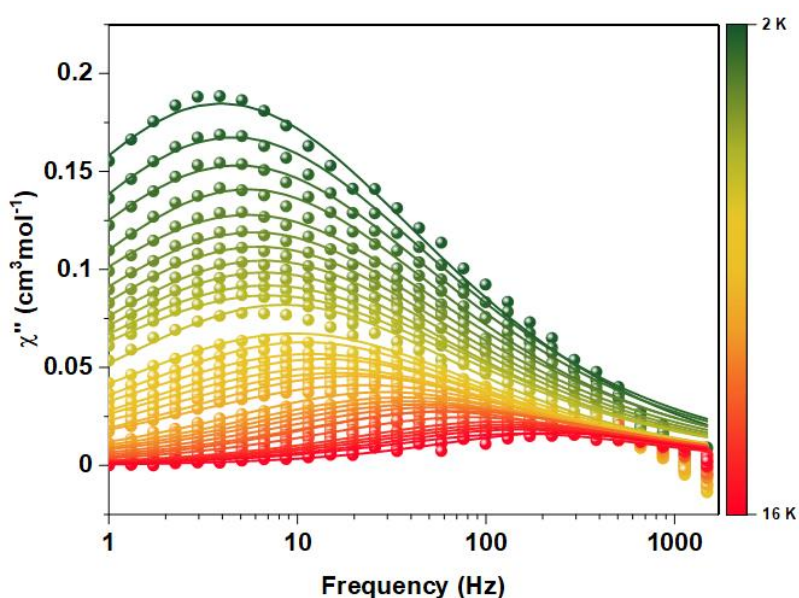


**Figure 40:** Plot of  $\chi''$  versus frequency for **(3)** at different temperatures.

By plotting the AC data as the natural logarithm versus the inverse temperature you can reveal the molecular interactions to get a better picture (see Figure 41).

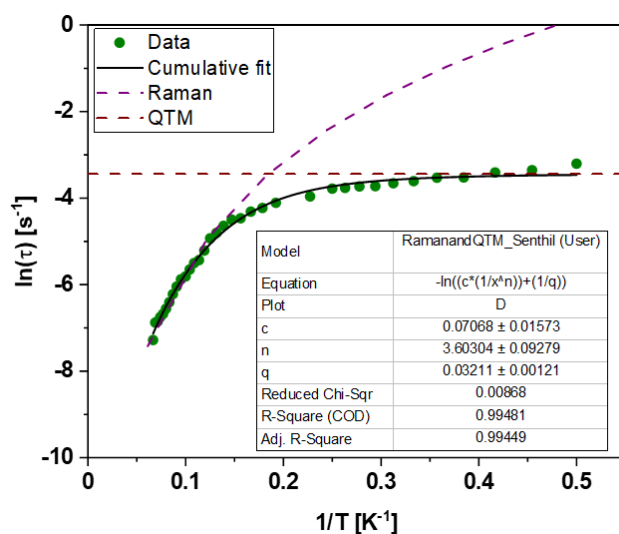


**Figure 41:** Plot of  $\ln(\tau_0)$  versus  $1/T$  for **(3)**.

The plot shows that the magnetisation relaxation in the dinuclear compound (3) is a combination of quantum tunnelling of the magnetisation and a Raman process.

Compound (4) has a very similar ligand field to (3), the only difference is a bromide counter ion instead of chloride. To investigate what effect this change in the structure has on the dynamic magnetic behaviour, AC susceptibility measurements were performed on compound (4). The relaxation process is faster than in (3). To find an optimal applied magnetic field in order to bring the maxima into the measurement window an external magnetic field at various strengths was applied. The optimal field was found at 3000 Oe (see Figure 42 and 43).

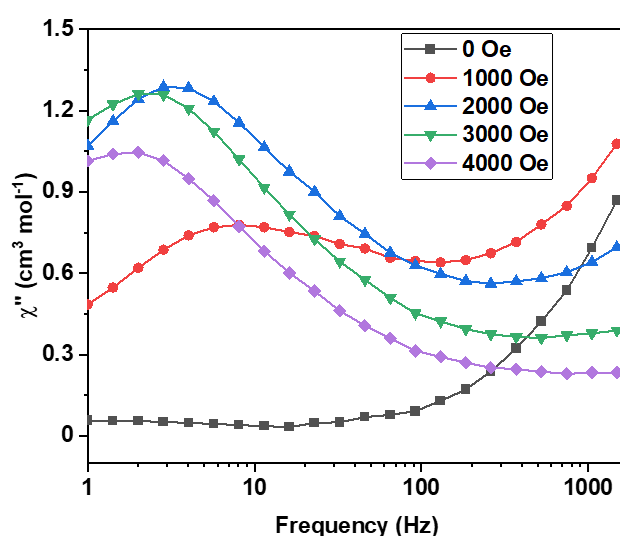


**Figure 42:** Plot of  $\chi''$  versus frequency for (4) at 2 Kelvin and different strengths of an external magnetic field.

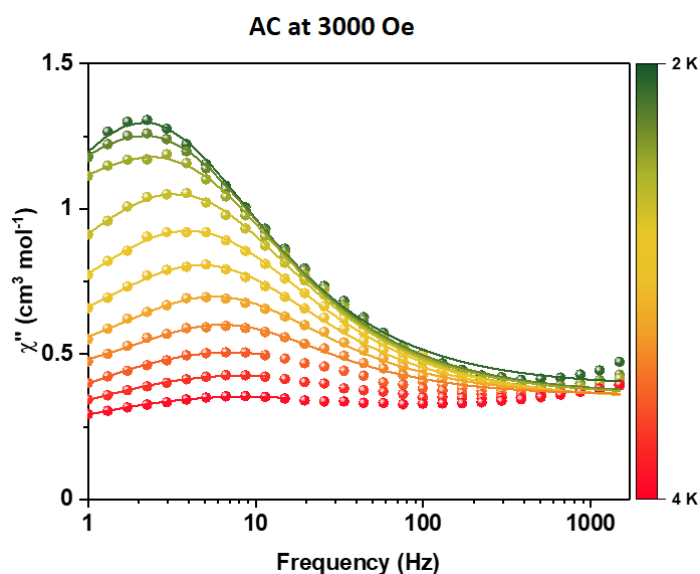


**Figure 43:** Plot of  $\chi''$  versus frequency for (4) at different temperatures and 3000 Oe.

The plot in Figure 44 shows that the magnetisation relaxation in the dinuclear compound (**4**) is a combination of quantum tunnelling of the magnetisation and a Raman process.

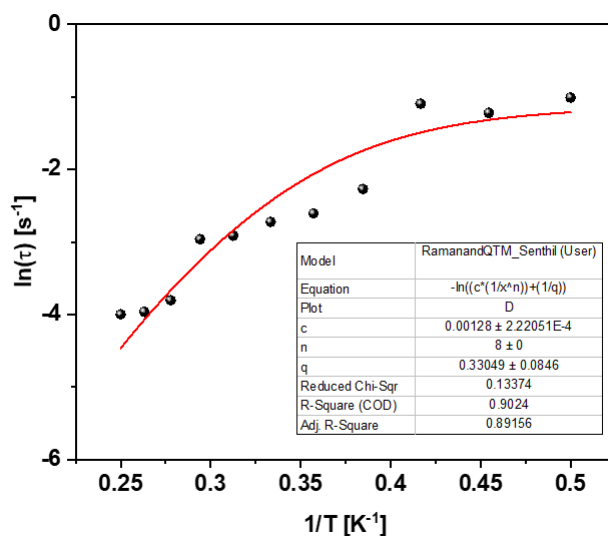


**Figure 44:** Plot of  $\ln(\tau_0)$  versus  $1/T$  for (**4**).

This set of data is pretty noisy and not reliable. It would have been of interest to compare the magnetic behaviour of (**3**) and (**4**) to determine the effect of exchanging bromide with chloride counter ions. However, the powder diffraction data shows that the bulk sample for compound (**4**) did not correspond to the calculated powder pattern from the single crystal data. This makes the magnetic data not very useful.

All in all, all three presented dinuclear dysprosium compounds showed magnetic properties at low temperatures. Unfortunately, none of those three compounds seem to suppress relaxation processes or quantum tunnelling well.

*Ab-initio* calculations have been performed by Christian Pachl for these three compounds to investigate their electronic structure, Zero-Field Splitting and anisotropy.<sup>[44]</sup> The lowest eight Kramer doublets energies of each compound are summarized in Figure 45. Notable, since all exhibit symmetry only the splitting of one dysprosium ion is displayed. The remaining compound however still shows very similar behaviour for both centres, so there is no exception made for it.

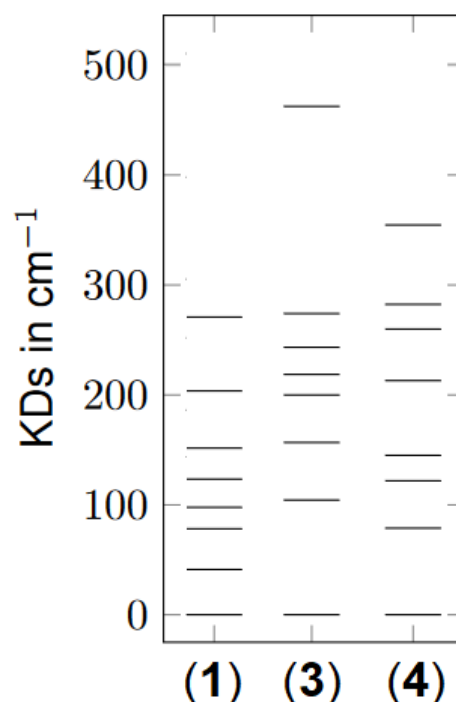


**Figure 45:** Zero Field splitting calculated for the dinuclear Dy-compounds (1), (3) and (4).

The calculation shows that the first excited Kramer doublet for (1) is at  $41.2 \text{ cm}^{-1}$  and for (4) at  $78.6 \text{ cm}^{-1}$  above the ground doublet, while the corresponding gap for (3) at  $104.3 \text{ cm}^{-1}$  is much larger. Comparison of the *ab-initio* calculations for (3) and (4) indicate that the bromide counter ion lowers the energy of the first excited Kramer doublet from  $104.3$  to  $78.6 \text{ cm}^{-1}$ .

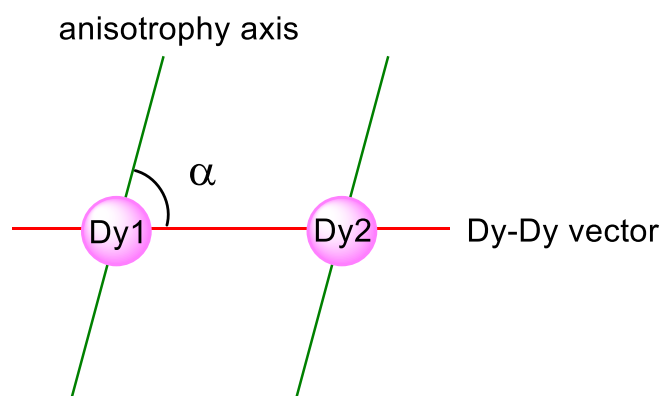
The differences in the calculations are consistent with their magnetic behaviour. Of the three compounds shown here, (1) shows the weakest and (3) the strongest SMM behaviour. Had it been possible to prepare a bulk sample for (4), its magnetic relaxation behaviour would probably been similar to (3).

Table 4 summarizes the energy splitting, anisotropy main axis contribution as well as angles of each Kramer doublets main axis with respect to the ground state Kramer doublet, Dy-Dy axis and the main axis of the other Dy (see Scheme 6).

MAGELLAN simulations were also performed to calculate the orientation of the anisotropies axis.<sup>[45]</sup> It is a purely electrostatic approach where you assign charges to atoms in the ligands. Afterwards, the program calculates the interaction of this electrostatic field with the  $m_J = 15/2$  ground state of Dy<sup>III</sup> ion.

| Compound | KD | Dy  | $g_x$ | $g_y$ | $g_z$  | $\alpha$ [°] | $\alpha$ [°] |
|----------|----|-----|-------|-------|--------|--------------|--------------|
| (1)      | 1  | Dy1 | 0.267 | 0.796 | 17.632 | 57.2         | 86.9         |
|          |    | Dy2 | 0.265 | 0.790 | 17.615 | 56.9         | 86.9         |
| (3)      | 1  | Dy1 | 0.051 | 0.082 | 19.405 | 76.1         | 77.9         |
|          |    | Dy2 | 0.051 | 0.082 | 19.337 | 76.0         | 80.7         |
| (4)      | 1  | Dy1 | 0.157 | 0.307 | 19.082 | 77.1         | 72.4         |
|          |    | Dy2 | 0.157 | 0.307 | 19.004 | 77.1         | 72.4         |

**Table 4:** The  $g$ -factors for the ground Kramer doublets in (1), (3) and (4) and the angles  $\alpha$  between the calculated anisotropy axes and the Dy-Dy vector. Anisotropy axis calculated via *ab-initio* are shown in green and calculated via MAGELLAN are shown in light blue.



**Scheme 6:** Visualisation of the angles from the calculated anisotropy axes.

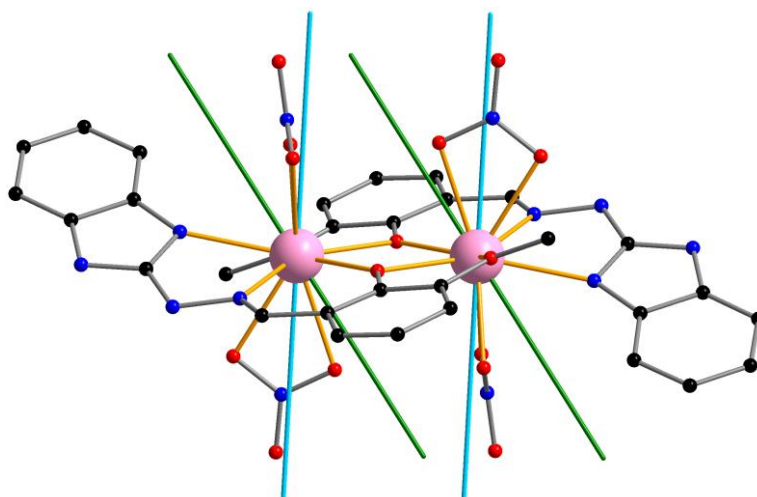


**Figure 46:** Anisotropy axis calculated via *ab-initio* (green) and with MAGELLAN (light blue) for compound (1).

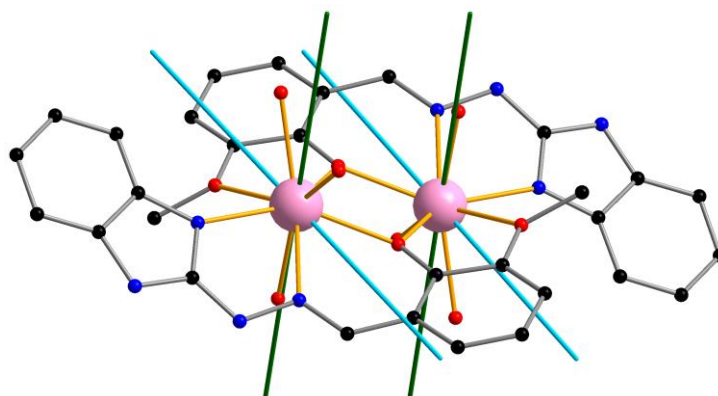


**Figure 47:** Anisotropy axis calculated via *ab-initio* (green) and with MAGELLAN (light blue) for compound (3).

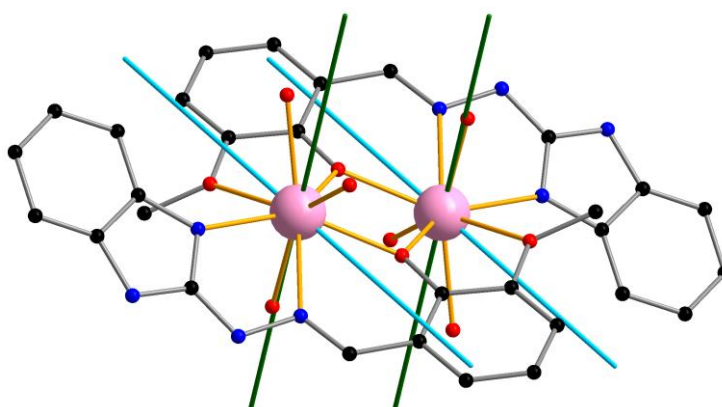
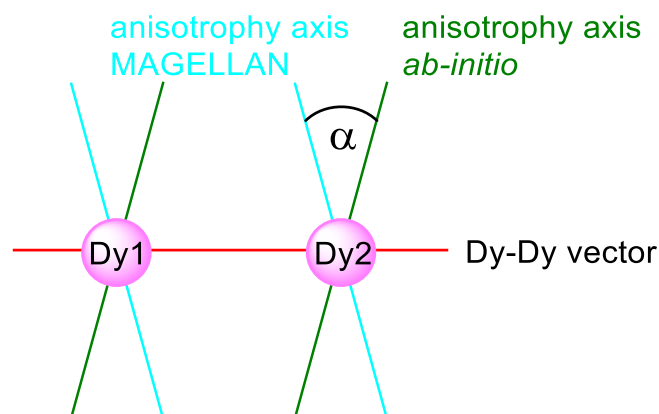


**Figure 48:** Anisotropy axis calculated via *ab-initio* (green) and with MAGELLAN (light blue) for compound (4).

Now we compare the anisotropy axes from the *ab-initio* calculation with the MAGELLAN calculation (see Scheme 7).



**Scheme 7:** Visualisation of the angle between the two differently calculated anisotropy axes.

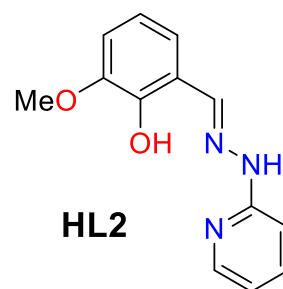
| Compound     | (1)  | (3)  | (4)  |
|--------------|------|------|------|
| $\alpha$ [°] | 37.8 | 82.1 | 82.8 |

**Table 5:** Angles between anisotropy axis as calculated by MAGELLAN versus calculated using *ab-initio*-calculations.

Both methods results do not agree on compound (3) and (4). The differences both compounds can be explained. Even though a coordinating water molecule is treated as uncharged in MAGELLAN they do have a large influence on the anisotropy axis.<sup>[46]</sup>

#### 4.1.2 Dinuclear dysprosium complexes (5) and (6) obtained from HL2

The two compounds presented here can be obtained in two steps. The utilized literature-known ligand HL2 is a modified version of HL1.<sup>[47]</sup> Firstly, the ligand HL2 was synthesised using a Schiff-base reaction with *o*-vanillin and 2-hydrazino-pyridine as reactants. Then the ligand was mixed with a given lanthanide salt and other reagents in a 1:1 mixture of methanol and acetonitrile. Slow evaporation of the solvents at room temperature was chosen as crystallisation technique. The lanthanide complexes (5) and (6) (Figure 49) were synthesised this way.



[Dy<sub>2</sub>(L2)<sub>2</sub>(NO<sub>3</sub>)<sub>4</sub>]-2CH<sub>3</sub>CN (5) was obtained using Dy(NO<sub>3</sub>)<sub>3</sub>·5H<sub>2</sub>O. After five days, yellow block-shaped crystals suitable for X-ray diffraction analysis had formed.

The combination of HL2 with lanthanide nitrates from Eu to Lu gave complexes isostructural to (5).

[Dy<sub>2</sub>(L2)<sub>2</sub>(CH<sub>3</sub>COO)<sub>4</sub>(CH<sub>3</sub>OH)<sub>2</sub>]-4CH<sub>3</sub>OH (6) was obtained using Dy(CF<sub>3</sub>SO<sub>3</sub>)<sub>3</sub>, anhydrous sodium acetate as co-ligand and triethylamine as base. After one day, yellow block-shaped crystals suitable for X-ray diffraction analysis had formed.

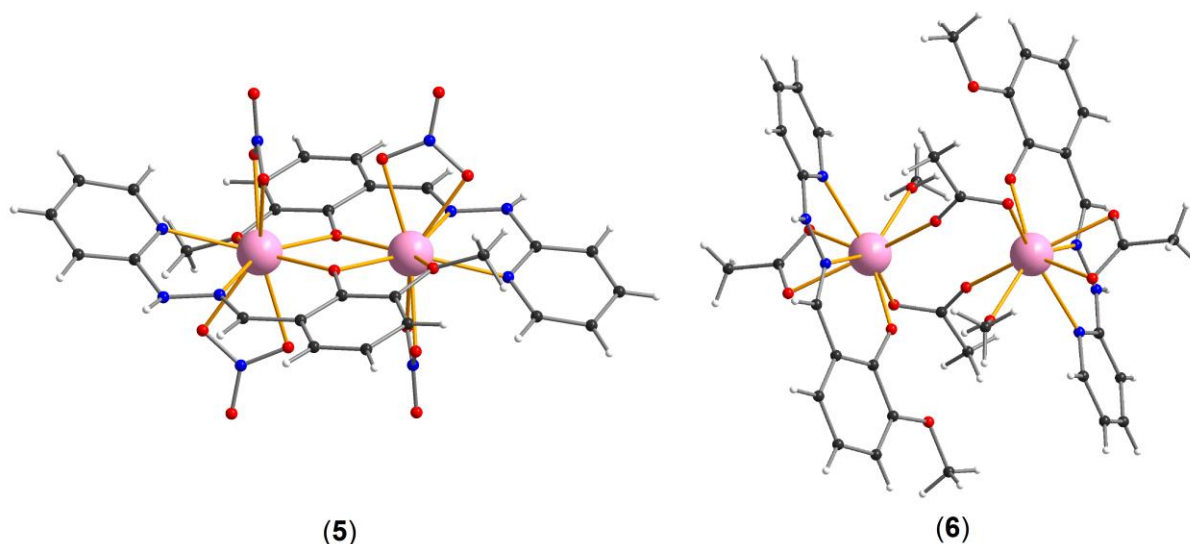


**Figure 49:** The two dinuclear lanthanide complexes using HL2 as ligand [Dy<sub>2</sub>(L2)<sub>2</sub>(NO<sub>3</sub>)<sub>4</sub>] (5) and [Dy<sub>2</sub>(L1)<sub>2</sub>(CH<sub>3</sub>COO)<sub>4</sub>(MeOH)<sub>2</sub>] (6). Colour code: white = H; black = C; blue = N; red = O; rose = Dy.

Compound **(5)** has a very similar structure to compound **(1)** presented in 4.1.1. It consists of two Dy<sup>III</sup> ions and two deprotonated molecules of the ligand (L2). Each ligand coordinates to Dy(1) via pyridyl and imino nitrogen atoms and with its deprotonated phenoxo oxygen atom which forms a bridge between the two Dy<sup>III</sup>. The same ligand also chelates Dy'(1) with that phenoxo oxygen and its methoxy oxygen. This leads to a molecule with two Dy<sup>III</sup> doubly bridged by two phenoxo oxygens. In total each dysprosium is five coordinate from the ligands with two nitrogens and three oxygens defining in the equatorial plane. Compound **(5)** has two nitrates chelating each Dy<sup>III</sup> ion in axial positions. An inversion centre sits in the middle of the complex (see Figure 49).

Compound **(6)** is also a dinuclear complex, built up from planar Dy(L2) units. The Dy<sup>III</sup> ion sit in the ligand's pocket consisting of the pyridyl and imino nitrogen and the phenoxy oxygen. However, in contrast to the previous dimers, in **(6)** the Dy(L2) units are not coplanar, but are linked by two *syn-anti* acetate bridges that are between the two Dy(L2) planes. An additional acetate and a methanol molecule are coordinating to each Dy<sup>III</sup> ion resulting in a coordination number of eight (see Figure 49).

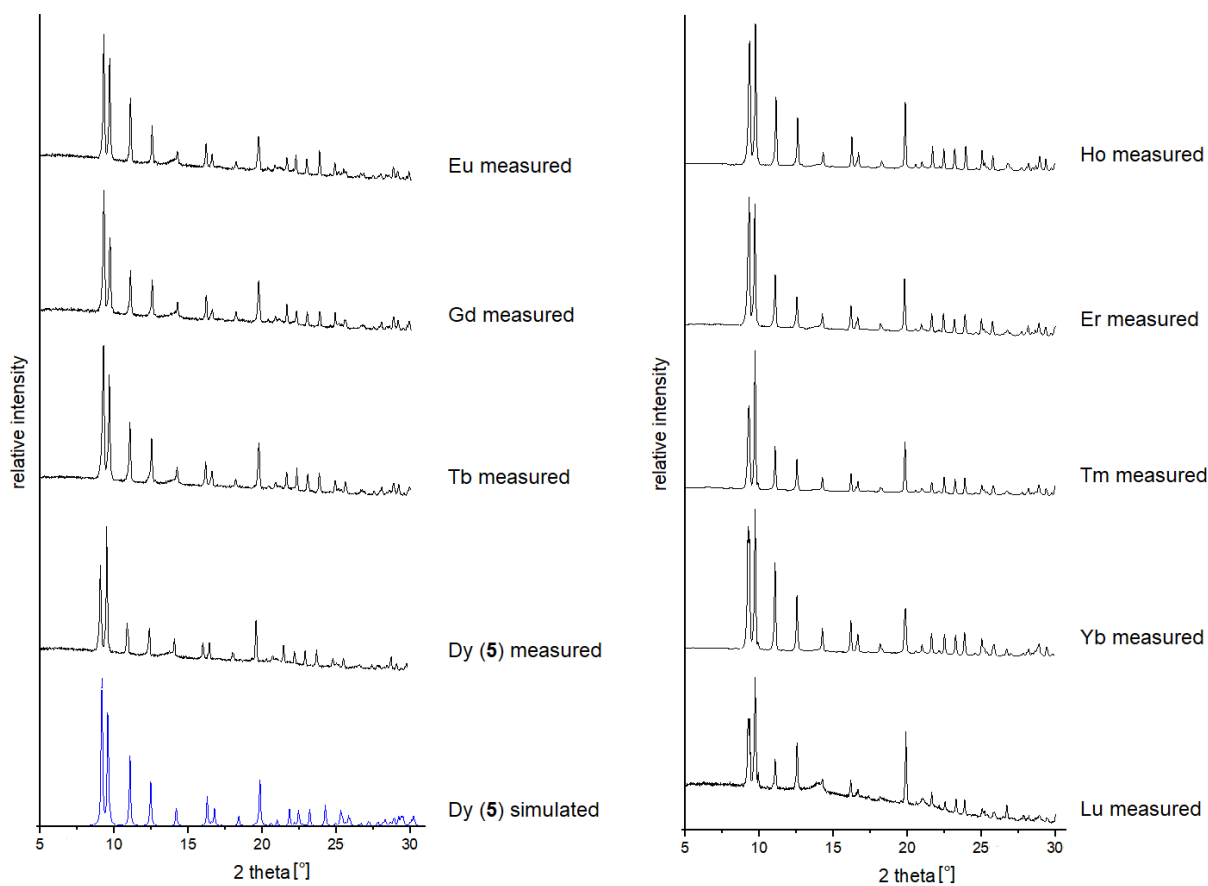


**Figure 50:** Powder patterns of  $[\text{Ln}_2(\text{L}2)_2(\text{NO}_3)_4] \cdot 2\text{CH}_3\text{CN}$  for Ln= Eu to Lu.

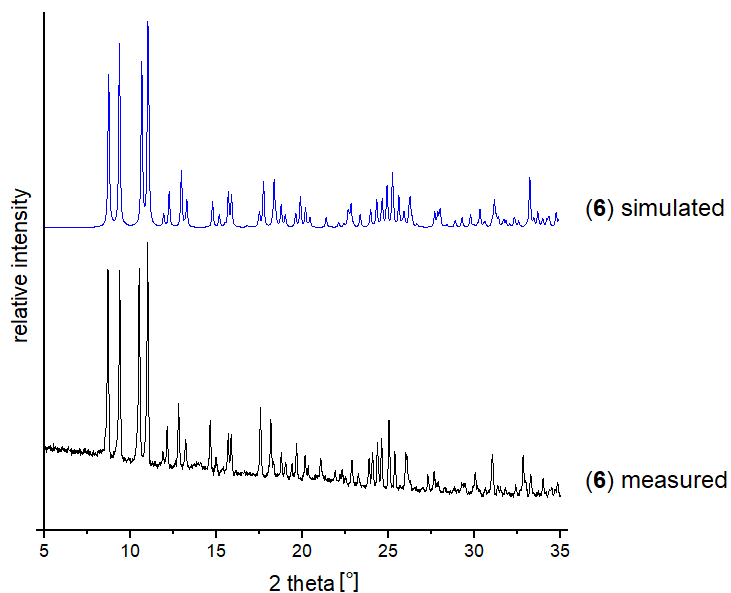


**Figure 51:** Powder pattern of (6) versus simulated powder pattern.

The measured powder patterns of the family of (5) and of compound (6) match with the simulated pattern from the single crystal data.

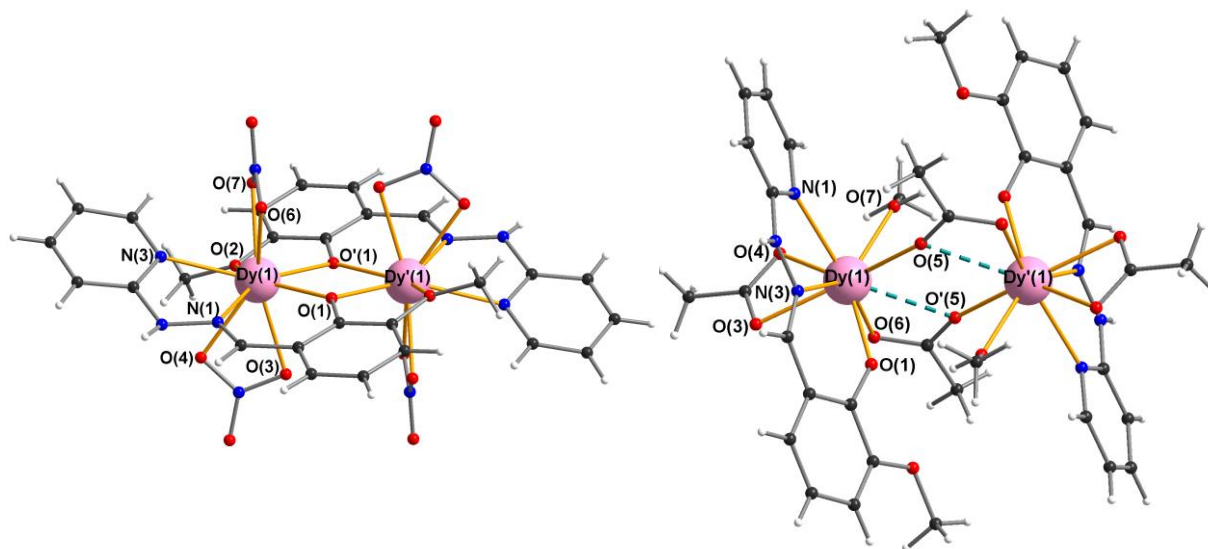


**Figure 52:** Structure of (5) (left) and (6) (right) with selected atoms labelled. A potential ninth coordination mode in compound (6) is shown as a dashed green line.

| Atom  | Atom   | Distance [Å] |
|-------|--------|--------------|
| Dy(1) | Dy'(1) | 3.7149(4)    |
| Dy(1) | O(1)   | 2.304(2)     |
| Dy(1) | O'(1)  | 2.351(2)     |
| Dy(1) | O'(2)  | 2.417(2)     |
| Dy(1) | O(3)   | 2.475(3)     |
| Dy(1) | O(4)   | 2.470(2)     |
| Dy(1) | O(6)   | 2.442(2)     |
| Dy(1) | O(7)   | 2.438(3)     |
| Dy(1) | N(1)   | 2.453(3)     |
| Dy(1) | N(3)   | 2.492(3)     |

| Atoms             | Angle [°] |
|-------------------|-----------|
| Dy(1)-O(1)-Dy'(1) | 105.91(9) |
| O(1)-Dy(1)-O'(1)  | 74.09(9)  |

| Atom  | Atom   | Distance [Å] |
|-------|--------|--------------|
| Dy(1) | Dy'(1) | 4.2320(4)    |
| Dy(1) | O(1)   | 2.230(4)     |
| Dy(1) | O(3)   | 2.407(4)     |
| Dy(1) | O(4)   | 2.462(4)     |
| Dy(1) | O(5)   | 2.325(4)     |
| Dy(1) | O'(5)  | 2.792(4)     |
| Dy(1) | O'(6)  | 2.427(4)     |
| Dy(1) | O(7)   | 2.378(4)     |
| Dy(1) | N(1)   | 2.517(5)     |
| Dy(1) | N(3)   | 2.566(5)     |

| Atoms             | Angle [°]  |
|-------------------|------------|
| Dy(1)-O(5)-Dy'(1) | 111.26(15) |
| O(5)-Dy(1)-O'(5)  | 68.74(15)  |

**Table 6:** Selected bond lengths and angles of compound (5) (left) and (6) (right).

The distances and angles shown for compound (5) are very close to those of (1) since they are essentially isostructural. For complex (6) it is unclear whether Dy(1) is coordinating to O'(5), the second oxygen atom of the bridging acetate (see dashed lines Figure 52). The distance is 2.792 Å which is slightly higher than the largest Dy-O distance of 2.652 Å which can be considered a bond according to literature.<sup>[41]</sup> Whether or not this counts as a bond, would either lead to an eight- or nine-vertex polyhedron.

The following results from the SHAPE calculation show the best fitting polyhedra and the mathematical deviations in percent. For compound (5) and (6) the coordinating partners are the same. Two nitrogen atoms were provided from the pyridine and imine groups and one oxygen atoms from the phenoxy groups. Again none of the presented compounds have very high conformity with the calculated shapes due to the stiffness of the ligand molecules. The results of the best fitting shapes may be close to each other, so the three best fitting results are displayed.

The DyO<sub>7</sub>N<sub>2</sub> polyhedron of (5) is the result of two nitrates chelating with two oxygen atoms from the axial positions respectively. The best fitting geometrical shape is a muffin. The suggested polyhedra and deviations are similar to those of compound (1).

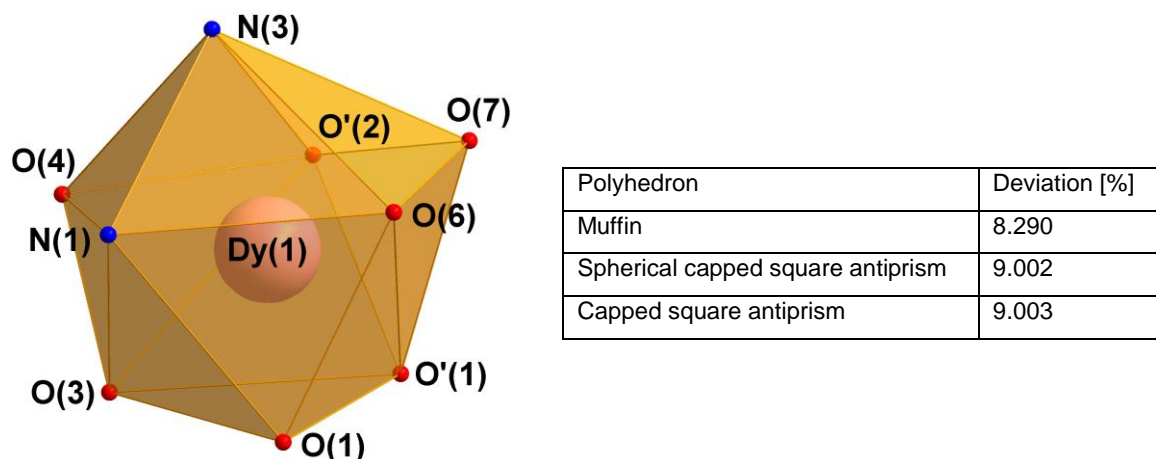
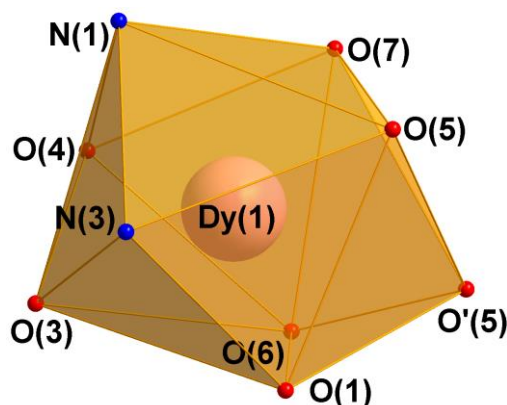


**Figure 53:** Nine-vertex polyhedron around the dysprosium centre of (5) with SHAPE values.

For compound (6) two calculations were performed. One for a coordination number of eight, the other included O'(5) and was done for a coordination sphere of 9 atoms around Dy(1). Together with the organic ligand, chelating acetate, methanol and the bridging acetate it adds up either a DyO<sub>6</sub>N<sub>2</sub> or a DyO<sub>7</sub>N<sub>2</sub> polyhedron.

| Polyhedron                         | Deviation [%] |
|------------------------------------|---------------|
| Spherical tricapped trigonal prism | 5.188         |
| Muffin                             | 6.093         |
| Spherical capped square antiprism  | 6.474         |



| Polyhedron                       | Deviation [%] |
|----------------------------------|---------------|
| Biaugmented trigonal prism (J50) | 6.554         |
| Square antiprism                 | 6.679         |
| Biaugmented trigonal prism       | 7.322         |

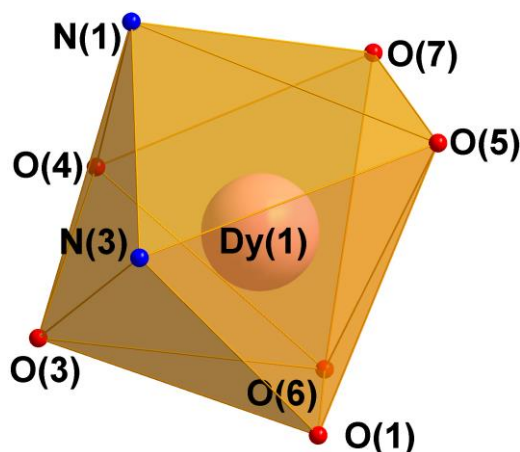


**Figure 54:** Nine-vertex polyhedron (top) and eight-vertex polyhedron (bottom) around the dysprosium centre of (6) with SHAPE values.

For the nine-vertex polyhedron a spherical tricapped trigonal prism would be the best fitting shape. For the eight-vertex polyhedron without O'(5) either a Johnson-biaugmented trigonal prism or a square antiprism would be the best result. There is no significant difference in the deviations of both polyhedra. If one of them would have a well-fitting shape and the other not, that would indicate whether the Dy<sup>III</sup> in compound (6) is eight- or nine-times coordinated. But since neither of the two results fits particularly well, it suggests that it could be an intermediate form. There is probably an increased electron density between Dy(1) and O'(5) but not as much to count as an adequate coordinate covalent bond. In the end the coordination number of the Dy<sup>III</sup> in compound (6) is likely between 8 and 9.

Compound (**5**) crystallises in the triclinic space group  $\bar{P}1$ . Each unit cell contains one molecule of the complex and two acetonitrile lattice molecules. In addition to their intramolecular interactions, the nitrate ligands in compound (**5**) are also responsible for the dominant supramolecular interactions. There are no  $\pi$ - $\pi$  intermolecular interactions between the pyridine groups. The O(5)···O(8ii) distance is 3.280(4) Å and the N(4)-O(5)···O(8ii) and O(5)···O(8ii)-N(5ii) angles 146.8(3)° and 154.4(3)°, respectively. These interactions result in ladder-like chains of molecules running parallel to b-c plane in the crystal (see Figure 55). The hydrazone N-H group forms a hydrogen bond to the nitrile group of the lattice acetonitrile. Thus, these unusual inter-nitrate contacts are the only direct supramolecular interactions in the crystal structure of (**5**). The O(5)-O(8) distance is 3.280(4) Å and O(3)-N'(5) distance is 3.126(4) Å.

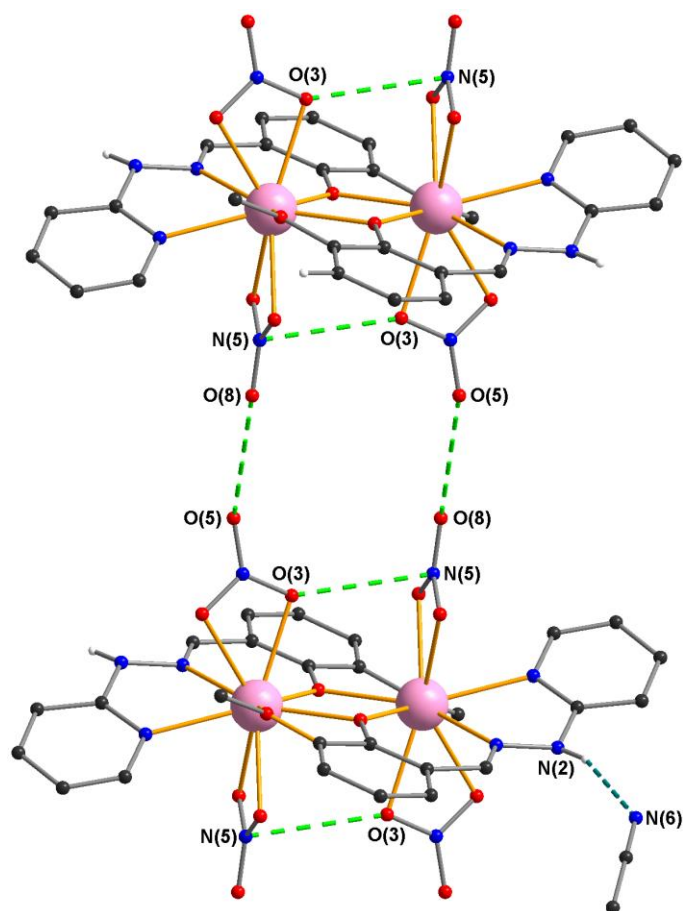


**Figure 55:** Ladder-like inter-nitrate interactions in the structure of (**5**). The hydrogen bonds shown as green dashed lines, supramolecular interactions shown as light green dashed lines.

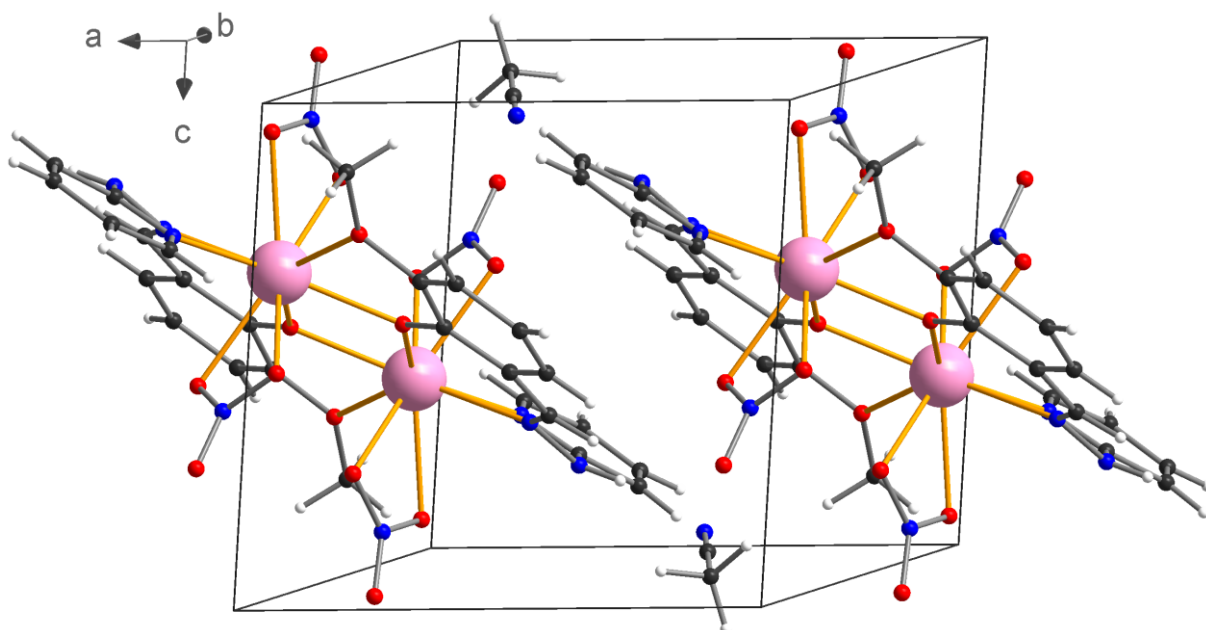


**Figure 56:** Unit cell packing of compound (5).

Compound (6) crystallises in the triclinic space group  $\bar{P}1$ . Each unit cell contains one molecule of the complex and four lattice methanol molecules. In compound (6) all intermolecular hydrogen bonds involve the lattice methanol molecules. There are four solvent molecules in the unit cell each of which accepts a hydrogen bond from the hydrazone NH and makes forms a hydrogen bond to a chelating acetate oxygen. Each of the methanol ligands forms a intramolecular hydrogen bond to the phenoxy oxygen.

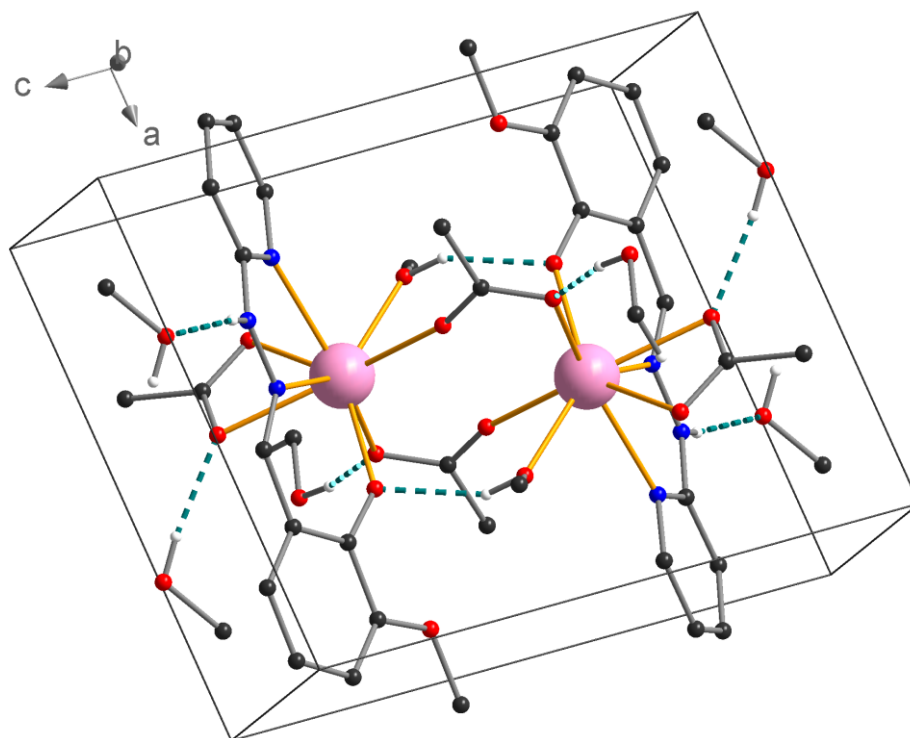


**Figure 57:** Unit cell packing of (6) showing the hydrogen bonds as green dashed lines. For clarity hydrogen atoms on carbon are not displayed.

#### 4.1.2.1 Magnetic properties of complexes (5) and (6)

The compounds presented here were selected for magnetic studies. DC measurements on (5) and (6) were performed on a Quantum Design MPMS-XL SQUID magnetometer. The room temperature  $\chi T$  values are  $28.19 \text{ cm}^3 \text{ K mol}^{-1}$  for (5) and  $28.31 \text{ cm}^3 \text{ K mol}^{-1}$  for (6). This is in good agreement with the theoretical value of  $28.34 \text{ cm}^3 \text{ K mol}^{-1}$  for two non-interacting  $\text{Dy}^{\text{III}}$  ions. One single  $\text{Dy}^{\text{III}}$  ion has the ground state  $^6\text{H}_{15/2}$ , a  $g_J$  value of  $4/3$  and a  $\chi T$  value of  $14.17 \text{ cm}^3 \text{ K mol}^{-1}$ .<sup>[10]</sup> The  $\chi T$  value decreases sharply below 25 K, indicating significant anisotropy in both compounds and possibly antiferromagnetic interactions in addition to the depopulation of Stark sublevels (see Figure 58).<sup>[25]</sup>

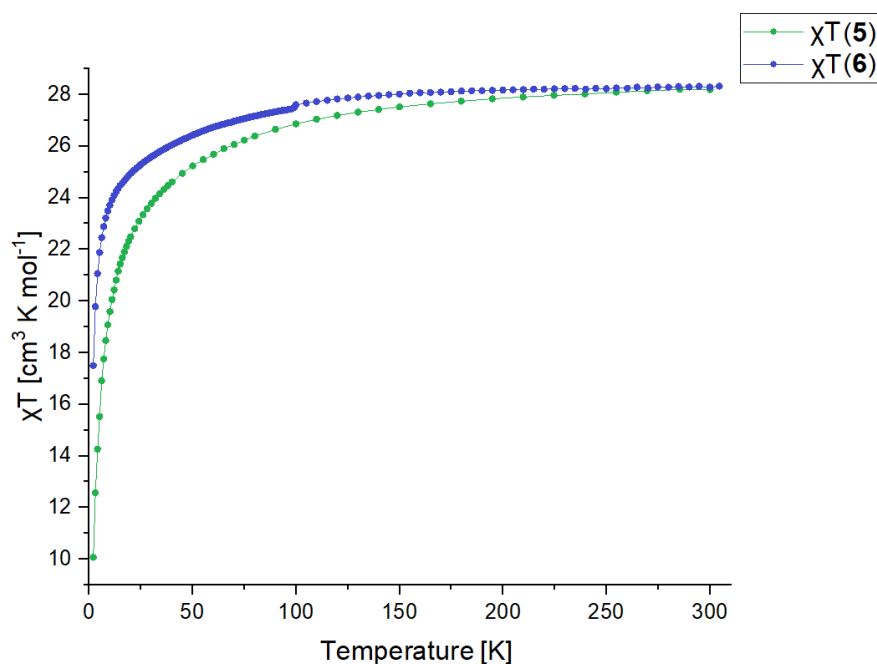


**Figure 58:** Plot of  $\chi T$  versus temperature for compound (5) (top) and (6) (bottom).

Comparing the shapes of these two curves with the previous shapes of compound (1), (3) and (4) one can see similarities. The curve of compound (5) has a similar shape as the from (1). This is not surprising due to their similar structure. The curve of (5) decreases sharply below 25 K while the curve of (6) decreases sharply below 15 K. The curve of (5) ends at a value of  $10 \text{ cm}^3 \text{ K mol}^{-1}$ , (6) ends at a value of  $17 \text{ cm}^3 \text{ K mol}^{-1}$ .

Compound **(5)** should show a similar magnetic behaviour than **(1)** due to having a similar ligand field around its Dy<sup>III</sup> ions. Surprisingly, **(5)** does not show any slow magnetic relaxation (see Figure 59).

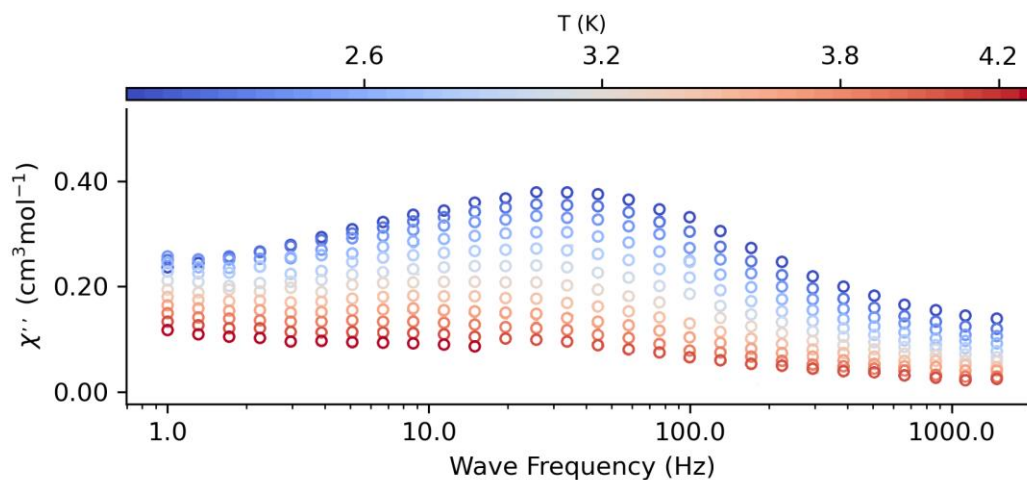


**Figure 59:** Plot of  $\chi''$  versus frequency for **(5)** at different temperatures at an external field of 5250 Oe.

Even at a high external magnetic field of 5250 Oersted and a temperature of 2 Kelvin compound **(5)** hardly shows any signal. A very weak and broad signal could be observed for AC susceptibility measurements. It therefore makes little sense to fit the data according to a Debye model. Compound **(5)** shows no SMM behaviour.

The lack of AC signals could be the result of the nitrate-nitrate interaction. This intermolecular interaction could enable pathways for relaxation processes.

In order to investigate the dynamic magnetic behaviour, AC susceptibility measurements were performed on compound (**6**). The  $\chi''$  signals indicate a slow relaxation of magnetisation (see Figure 60).

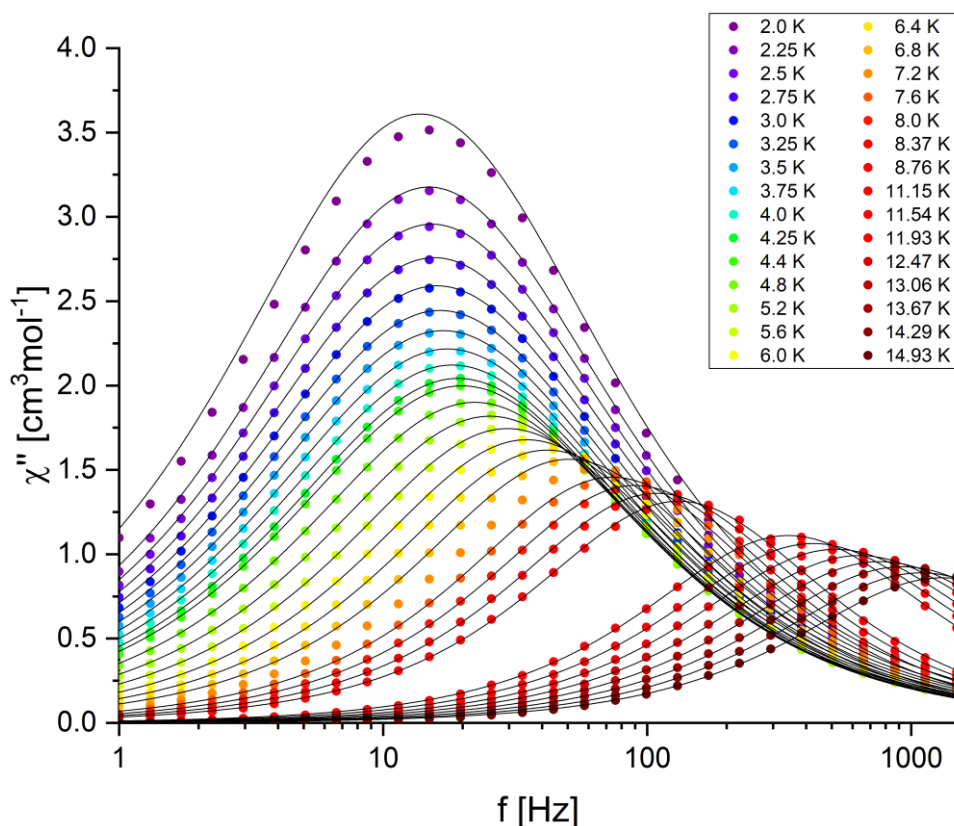


**Figure 60:** Plot of  $\chi''$  versus frequency for (**6**) at different temperatures. Due to a restart during the measurement, there is a gap from 9 to 11 Kelvin in the data.

Compound (**6**) shows SMM behaviour. A magnetic behaviour could be observed up to a temperature of 15 K. First the data were fitted using the widely used equation where the last term corresponds an Orbach process following an Arrhenius law. Raman processes and quantum tunnelling of magnetisation gave the best fit (see Figure 61 and Formula 1).

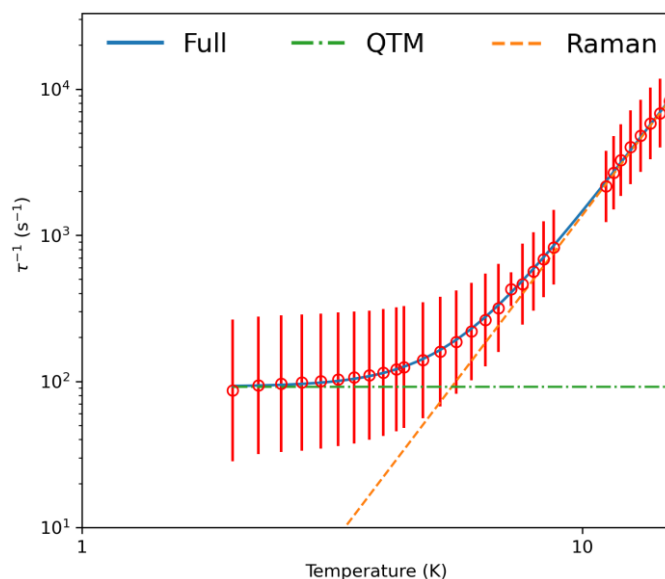


**Figure 61:** Plot of  $1/(\tau_0)$  versus  $T$  for **(6)**. The vertical red lines are error bars, the blue curve is the fit.

According to an Orbach fit compound **(6)** has an energy barrier  $U_{\text{eff}}$  of 50(10) K and a magnetic relaxation time  $\tau_0$  of  $7(5) \cdot 10^{-6}$  s.

Next, the measured data were fitted with two exponential factors using a model by Gu and Wu.<sup>[43]</sup> The agreement with the model is given (see Figure 62 and Formula 2).

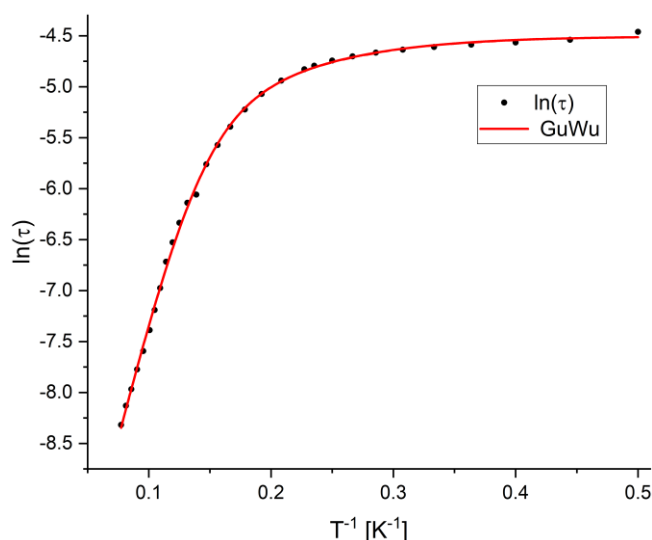
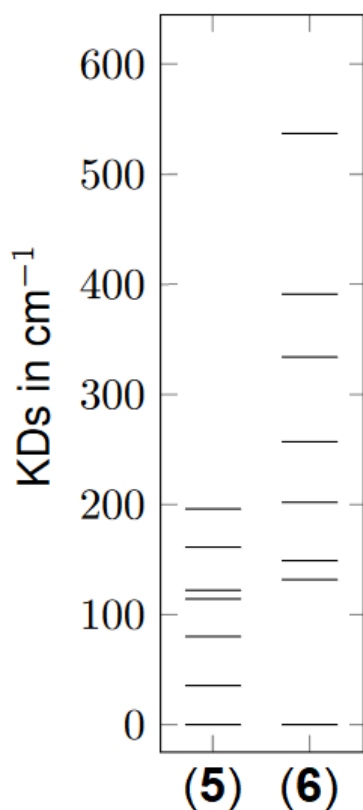


**Figure 62:** Plot of  $\ln(\tau_0)$  versus  $1/T$  for **(6)**.

According to an Gu and Wu-fit compound **(6)** has an energy barrier  $U_a$  of 13(3) K and  $U_b$  of 49(2) K a magnetic relaxation time  $\tau_{0a}$  of  $1.4(7) \cdot 10^{-7}$  s and  $\tau_{0b}$  of  $5.9(8) \cdot 10^{-6}$  s.

Both the simple fit with one exponential function and the more complex fit with two exponential functions give very similar results. However, the errors are smaller when calculating according to Gu and Wu.



The *ab-initio* calculation for **(5)** and **(6)** have been performed by Christian Pachl. The calculation shows that the first excited Kramer doublet for **(5)** is at 35.5 cm<sup>-1</sup> above the ground doublet. The corresponding gap for **(6)** at 131.8 cm<sup>-1</sup> is much larger.

**Figure 63:** Zero Field splitting calculated for the dinuclear Dy-compounds **(5)** and **(6)**.

The differences in the calculations are consistent with their magnetic behaviour. From both compounds shown in this chapter, **(5)** shows no and **(6)** SMM behaviour.

The *ab-initio* calculations for all compound in this chapter should be compared due to their similarities in structure. For compound (1) and (5) nitrate ligands are posing as terminal ligands and therefore do not impose a strictly anti-ferromagnetic behaviour. Due to the fact that nitrogen donor atoms are causing a smaller crystal field splitting than oxygen atoms it is not surprising that the first excited Kramer doublets is below 50  $\text{cm}^{-1}$ . This can lead to a mixing of  $m_J$ -states. Now, which of those are mixing to become the ground state is predominantly influenced by the electrostatic interaction of ligands and lanthanide ion which requires a good description of the ground state electron density of the ligand.

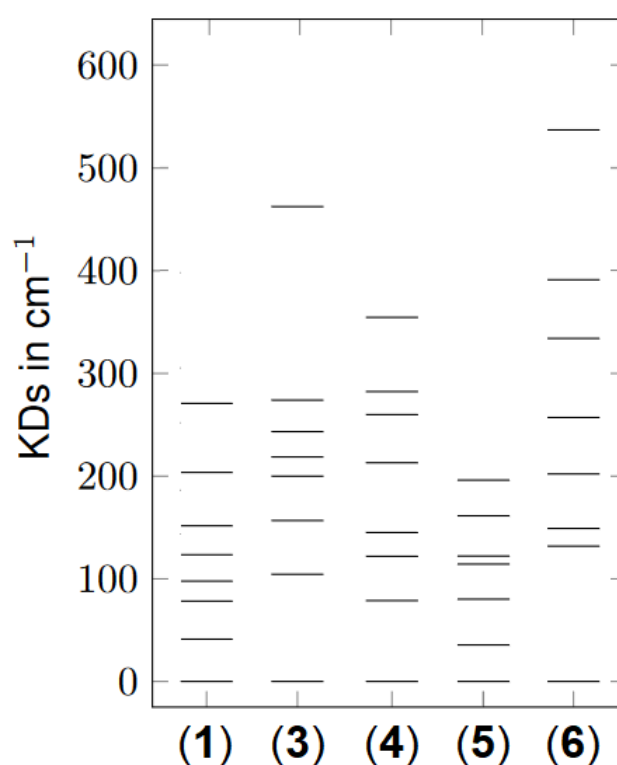


**Figure 64:** Zero Field splitting calculated for the dinuclear Dy-compounds (1), (3), (4), (5) and (6).

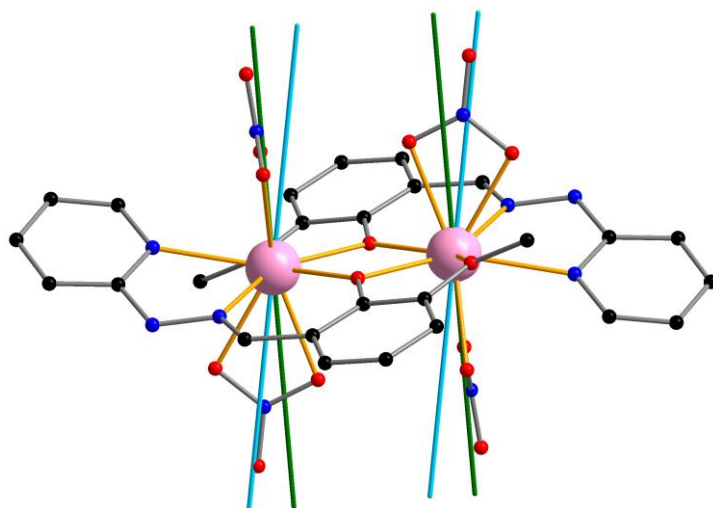
The *ab-initio* calculations are consistent with the magnetic behaviour of (1), (3), (4) and (6). The calculation predicts a slightly weak SMM behaviour for (5) than for (1) due to the decrease of the first excited Kramer doublet from 41.2 to 35.5  $\text{cm}^{-1}$ . Possibly the ladder-like inter-nitrate interactions of compound (5) supports magnetic relaxation processes (see Figure 55).

Table 7 summarizes the energy splitting, anisotropy main axis contribution as well as angles of each Kramer doublets main axis with respect to the ground state Kramer doublet, Dy-Dy axis and the main axis of the other Dy (see Scheme 6).

MAGELLAN simulations were also performed to calculate the orientations of the anisotropies axis.<sup>[45]</sup> It is a purely electrostatic approach where you assign charges to atoms in the ligands. Afterwards, the program calculates the interaction of this electrostatic field with the  $m_J = 15/2$  ground state of Dy<sup>III</sup> ion.

| Compound | KD | Dy  | $g_x$ | $g_y$ | $g_z$  | $\alpha$ [°] | $\alpha$ [°] |
|----------|----|-----|-------|-------|--------|--------------|--------------|
| (5)      | 1  | Dy1 | 0.396 | 0.918 | 18.047 | 89.8         | 79.6         |
|          |    | Dy2 | 0.398 | 0.914 | 17.986 | 89.8         | 79.5         |
| (6)      | 1  | Dy1 | 0.011 | 0.017 | 19.813 | 77.5         | 60.9         |
|          |    | Dy2 | 0.011 | 0.017 | 19.753 | 77.5         | 60.9         |

**Table 7:** The  $g$ -factors for the ground Kramer doublets in (1), (3) and (4) and the angles  $\alpha$  between the calculated anisotropy axes and the Dy-Dy vector. Anisotropy axis calculated via *ab-initio* are shown in green and calculated via MAGELLAN are shown in light blue.



**Figure 65:** Anisotropy axis calculated via *ab-initio* (green) and with MAGELLAN (light blue) for compound (5).

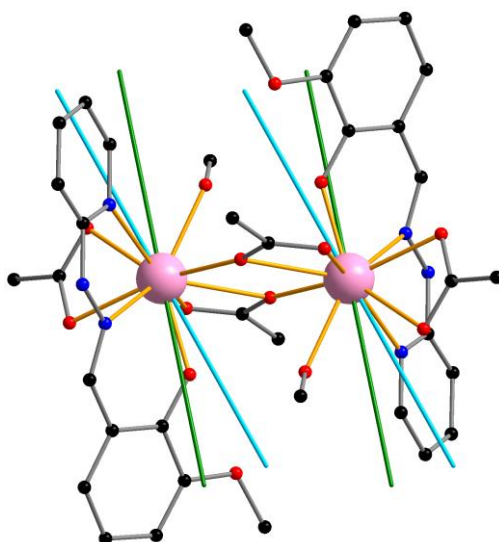


**Figure 66:** Anisotropy axis calculated via *ab-initio* (green) and with MAGELLAN (light blue) for compound (6).

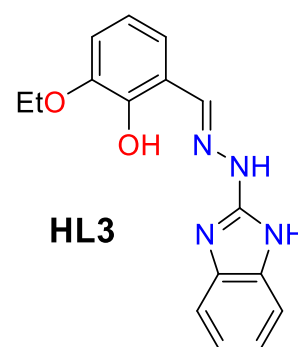
| Compound     | (5)  | (6)  |
|--------------|------|------|
| $\alpha$ [°] | 11.0 | 16.7 |

**Table 8:** Angles between anisotropy axis as calculated by MAGELLAN versus calculated using *ab-initio*-calculations.

Both methods results agree on compound (5) and (6). There are no coordinating water molecules in both compounds having a negative influence on the MAGELLAN calculation.

### 4.1.3 Dinuclear dysprosium complex (7) obtained from HL3

The compound presented here can be obtained in two steps. The utilized ligand HL3 is a modified version of HL1 with the methoxy group replaced by an ethoxy group. Firstly, the ligand HL3 was synthesised using a Schiff-base reaction with 3-ethoxy-2-hydroxybenzaldehyde and 2-hydrazino-1H-benzimidazole as reactants. Then the ligand was mixed with a given lanthanide salt and other reagents in a 1:1 mixture of methanol and acetonitrile.



Slow evaporation of the solvents at room temperature was chosen as crystallisation technique. The lanthanide complex (7) was synthesised this way (Figure 67).

$[\text{Dy}_2(\text{L3})_2(\text{CH}_3\text{COO})_4(\text{H}_2\text{O})_2] \cdot 2\text{H}_2\text{O} \cdot 4\text{CH}_3\text{OH}$  (7) was obtained using  $\text{Dy}(\text{CF}_3\text{SO}_3)_3$  and anhydrous sodium acetate as co-ligand. After ten days, yellow block-shaped crystals suitable for X-ray diffraction analysis had formed.

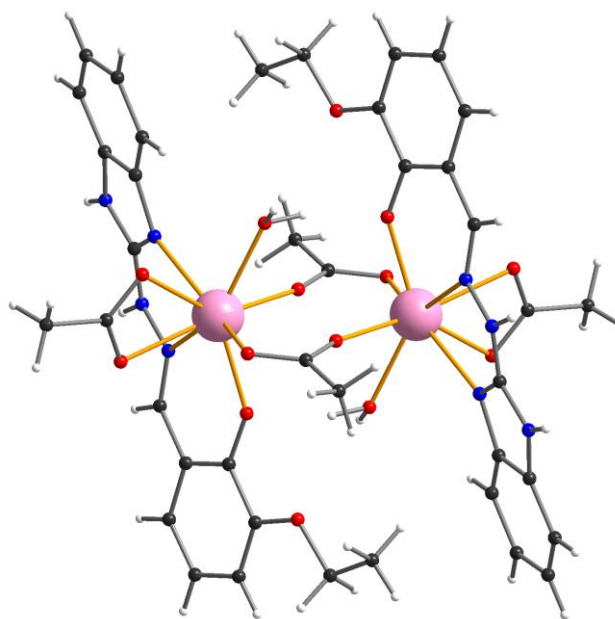


**Figure 67:** The dinuclear lanthanide complexes using HL3 as ligand  $[\text{Dy}_2(\text{L3})_2(\text{CH}_3\text{COO})_4(\text{H}_2\text{O})_2]$  (7). Colour code: white = H; black = C; blue = N; red = O; rose = Dy.

Compound **(7)** shares many similarities with compound **(6)**. It is a dinuclear complex built up from two units of the deprotonated ligand (L3)<sup>-</sup> and two Dy<sup>III</sup> ions. The metal ions sit in the ligand's pocket consisting of the benzimidazole and imino nitrogen and the phenoxy oxygen. The other pocket made of the phenoxy oxygen and the methoxy oxygen is empty. The two Dy<sup>III</sup> ions are linked by two *syn-anti* acetate bridges. An additional acetate molecule coordinate to each metal. In contrast to compound **(6)** water is bound to the Dy<sup>III</sup> ions rather than of methanol. This gives a coordination number of eight.

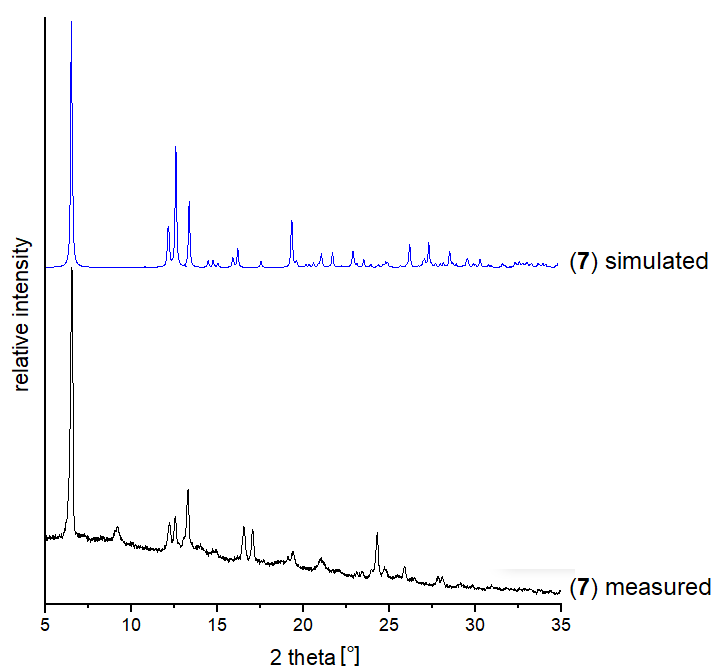


**Figure 68:** Measured powder pattern of **(7)** versus simulated pattern from single crystal data.

The measured powder pattern of **(7)** matches with the simulated one.

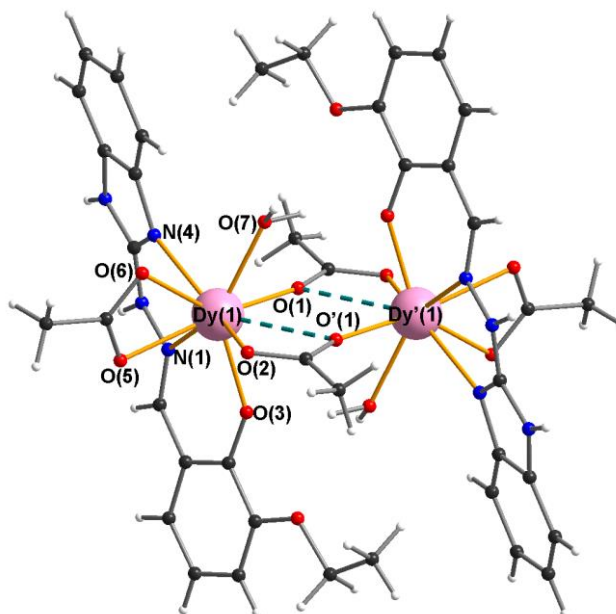


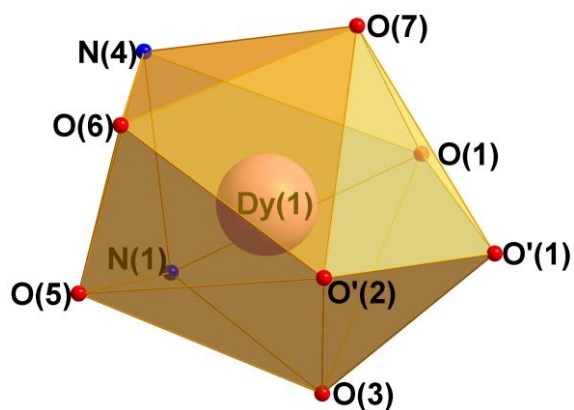
**Figure 69:** Structure of (7) with selected atoms labelled. A potential ninth coordination mode is shown as a dashed green line.

| Atom  | Atom   | Distance [Å] |
|-------|--------|--------------|
| Dy(1) | Dy'(1) | 4.2643(4)    |
| Dy(1) | O(1)   | 2.318(2)     |
| Dy(1) | O'(1)  | 2.826(3)     |
| Dy(1) | O'(2)  | 2.411(2)     |
| Dy(1) | O(3)   | 2.236(2)     |
| Dy(1) | O(5)   | 2.403(2)     |
| Dy(1) | O(6)   | 2.503(2)     |
| Dy(1) | O(7)   | 2.375(2)     |
| Dy(1) | N(1)   | 2.571(3)     |
| Dy(1) | N(4)   | 2.470(3)     |

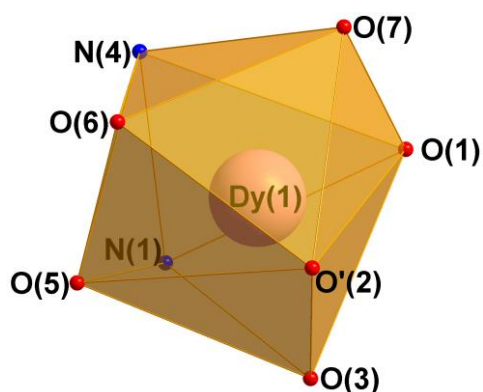
| Atoms             | Angle [°] |
|-------------------|-----------|
| Dy(1)-O(1)-Dy'(1) | 111.61(9) |
| O(1)-Dy(1)-O'(1)  | 68.39(10) |

**Table 9:** Selected bond lengths and angles of compound (7).

Due to the similarities in structure of compound (6) and (7) distances and angles for compound (7) are comparable to the ones of (6). The distance between Dy(1) and O'(1) at 2.826 Å is even higher than the Dy(1)-O'(5) at 2.792 Å from compound (6). All other bond lengths have typical values.



| Polyhedron                     | Deviation [%] |
|--------------------------------|---------------|
| Capped square antiprism (J10)  | 10.678        |
| Tricapped trigonal prism (J51) | 10.823        |
| Muffin                         | 12.825        |



| Polyhedron                       | Deviation [%] |
|----------------------------------|---------------|
| Triangular dodecahedron          | 9.018         |
| Biaugmented trigonal prism       | 10.502        |
| Biaugmented trigonal prism (J50) | 11.329        |

**Figure 70:** Nine-vertex polyhedron (top) and eight-vertex polyhedron (bottom) around the dysprosium centre of (7) with SHAPE values.

No reasonably fitting shape could be found neither for an eight- or nine-vertex polyhedron. That can be explained by taking a closer look at the ligand field around Dy(1). The ligand (L3)<sup>-</sup> is tridentate and stiff. Also the distance between two oxygen atoms from the bidentate chelating acetate has a fixed distance. In contrast to compound (6) there is a bulkier ethoxy group instead of a methoxy group which requires more space. This is likely to be the reason why water rather than methanol is coordinating. Similar to the situation with compound (6) there is no clear answer whether this complex has a coordination number of 8 or 9.

Compound (7) crystallises in the triclinic space group  $\bar{P}1$  and all intermolecular hydrogen bonds involve the lattice methanol or water molecules. The unit cell contains four methanol solvent molecules, two water solvent molecules and one molecule of the complex. The lattice water forms three hydrogen bonds. The hydrogen atoms point towards a chelating acetate oxygen and a neighbouring oxygen from a bridging acetate. The oxygen atom bonds to a hydrogen atom of a neighbouring hydrazone group. Two methanol molecules bridge via two hydrogen bonds between the imidazole group and acetate group of the molecule in the next crystal cell, respectively. Two lattice methanol molecules occupy the gap between the ethoxy group the coordinating water molecule and are heavily disordered. The coordinating water molecules form intramolecular hydrogen bonds to the neighbouring phenoxy groups.

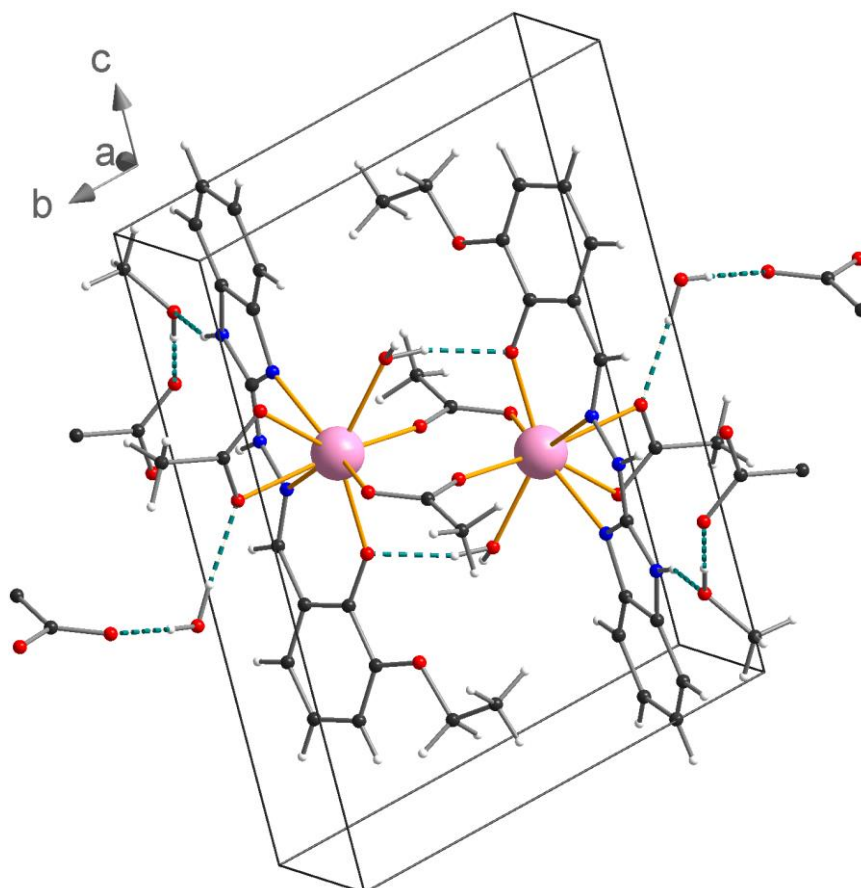
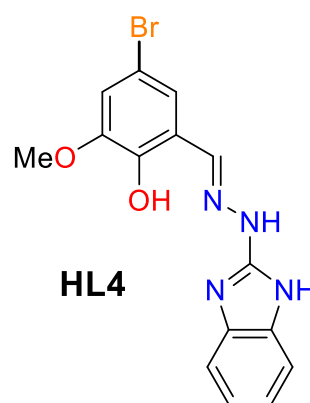


**Figure 71:** Unit cell packing of (7) showing the hydrogen bonds as green dashed lines. Disordered lattice solvent molecules are omitted for clarity.

#### 4.1.4 Dinuclear dysprosium complex (8) obtained from HL4

The compound presented here can also be obtained in two steps. The ligand HL4 is a slightly modified version of HL1. The hydrogen atom at the 5-position of *o*-vanillin was replaced with a bromine atom. This small change in the structure leads to a similar complex to the presented compound (3). In the first step, the ligand HL4 was synthesised using a Schiff-base reaction with 5-brom-2-hydroxy-3-methoxybenzaldehyde and 2-hydrazino-1H-benzimidazole as reactants. In the second step, the ligand was mixed with a given lanthanide salt in a 1:1 mixture of methanol and acetonitrile. Slow evaporation of the solvents at room temperature was chosen as crystallisation technique. The lanthanide complex (8) was synthesised this way (Figure 72).



$[\text{Dy}_2(\text{L4})_2(\text{H}_2\text{O})_6]\text{Cl}_4 \cdot 2\text{CH}_3\text{CN}$  (8) was obtained using  $\text{DyCl}_3 \cdot 6\text{H}_2\text{O}$ . After ten days, yellow block-shaped crystals suitable for X-ray diffraction analysis had formed.

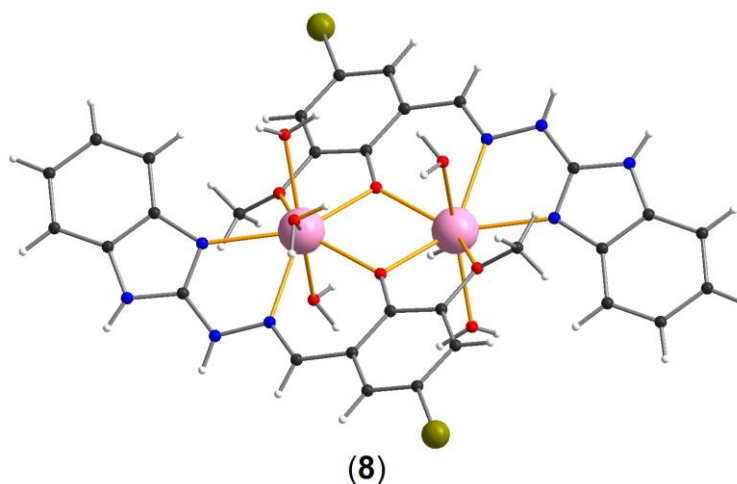


**Figure 72:** The dinuclear lanthanide complex  $[\text{Dy}_2(\text{L4})_2(\text{H}_2\text{O})_6]\text{Cl}_4 \cdot 2\text{CH}_3\text{CN}$  (8) using HL4 as a ligand. Colour code: white = H; black = C; blue = N; red = O; dark yellow = Br; rose = Dy.

The structure of compound **(8)** is very similar to compound **(3)**. Again, it is a dinuclear complex built up from two units of the deprotonated ligand (L4)<sup>-</sup> and two Dy<sup>III</sup> ions. The inversion centre is located in the middle of the complex. The metal ions occupy both ligand's pockets. One pocket is formed by the benzimidazole and imino nitrogen and the bridging phenoxy oxygen, the other pocket is formed by the same phenoxy oxygen and the methoxy oxygen. The two Dy<sup>III</sup> ions are bridged by two phenoxy groups of both ligands. Three additional water molecules coordinate to each metals. This gives a coordination number of eight. There are four chloride counter ions and two acetonitrile molecules in the lattice. The main difference to compound **(3)** is the replacement of a hydrogen with a bromine atom at the *para* position of the phenoxy subunit.

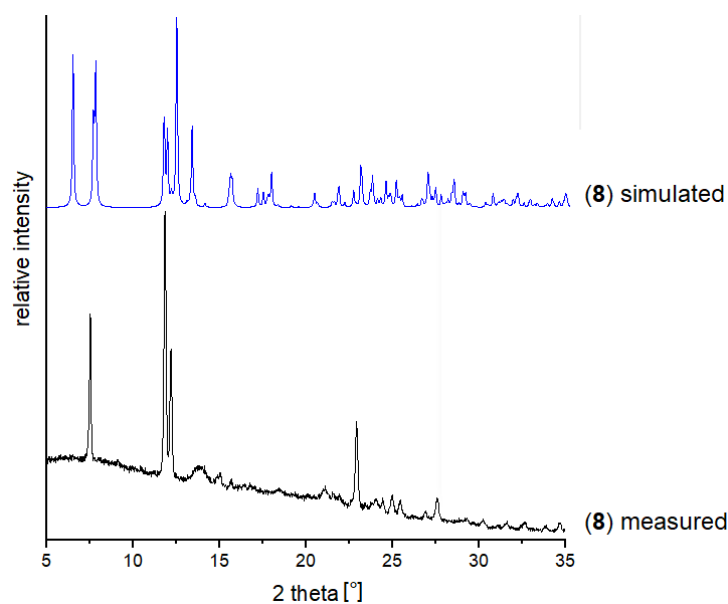


**Figure 73:** Measured powder pattern of **(8)** versus simulated pattern from single crystal data.

The measured powder pattern of **(8)** does not match with simulated one. This is not surprising since as for compound **(3)** the crystals turn opaque on isolation from solution.

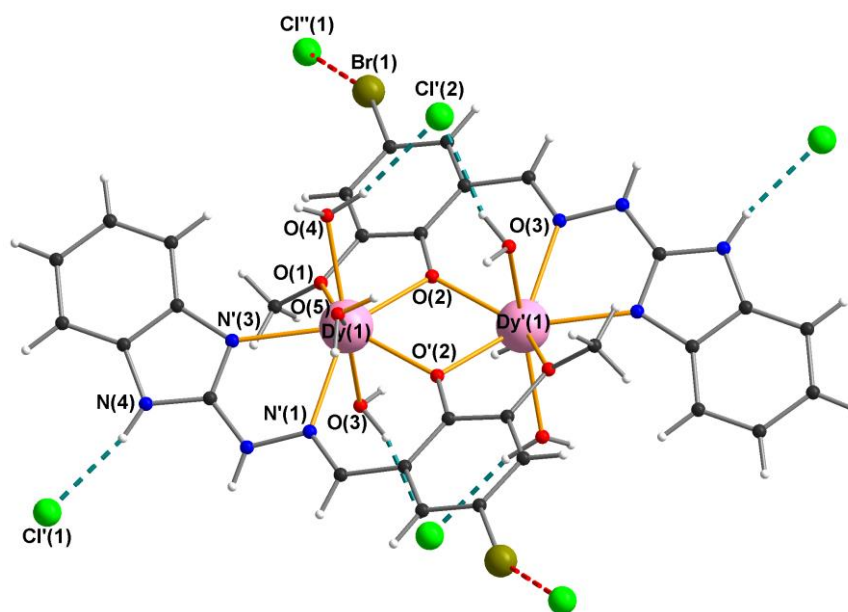


**Figure 74:** Structure of (**8**) with selected atoms labelled. The hydrogen bonds shown as green dashed lines. The halogen-halogen bonds shown as red dashed lines.

| Atom   | Atom    | Distance [Å] |
|--------|---------|--------------|
| Dy(1)  | Dy'(1)  | 3.7135(4)    |
| Dy(1)  | O(1)    | 2.482(3)     |
| Dy(1)  | O(2)    | 2.335(3)     |
| Dy(1)  | O'(2)   | 2.285(4)     |
| Dy(1)  | O(3)    | 2.357(4)     |
| Dy(1)  | O(4)    | 2.380(4)     |
| Dy(1)  | O(5)    | 2.375(4)     |
| Dy(1)  | N'(1)   | 2.501(4)     |
| Dy(1)  | N'(3)   | 2.409(4)     |
| Cl'(1) | N(4)    | 3.119(5)     |
| Cl'(2) | O(3)    | 3.120(4)     |
| Cl'(2) | O(4)    | 3.169(4)     |
| Br(1)  | Cl''(1) | 3.474(4)     |

| Atoms             |            |
|-------------------|------------|
| Dy(1)-O(2)-Dy'(1) | 106.98(13) |
| O(2)-Dy(1)-O'(2)  | 73.02(13)  |

**Table 10:** Selected bond lengths and angles of compound (**8**).

The shown distances and angles for compound (**8**) are in line with what can be found in the literature.<sup>[41]</sup> They are close to the ones of (**3**) due to their similar structures. The most notable feature of this compound is its halogen-halogen bond between the bromine atom and the chloride anion. The van der Waals radius of chlorine is 1.75 Å and of bromine 1.85 Å which adds up to 3.60 Å.<sup>[48]</sup> Here the found chloride-bromine distance is 3.473 Å which is significantly smaller. This shows that the outer shells of these atoms are overlapping which indicates there are intermolecular halogen-halogen interactions. The C-Br-Cl angle is 155°.

| Polyhedron                       | Deviation [%] |
|----------------------------------|---------------|
| Triangular dodecahedron          | 10.076        |
| Biaugmented trigonal prism (J50) | 10.458        |
| Biaugmented trigonal prism       | 10.954        |

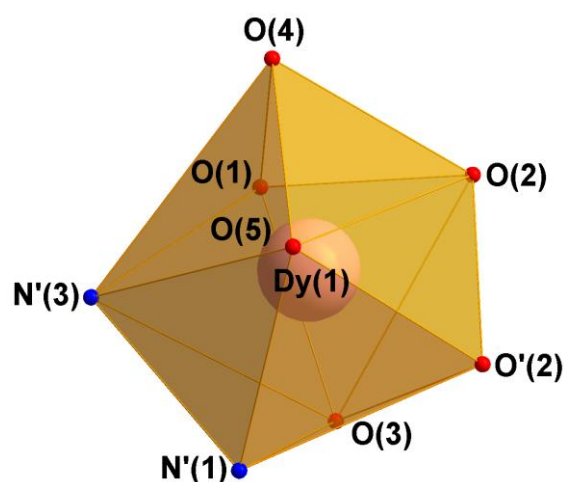


**Figure 75:** Eight-vertex polyhedron of (**8**) with SHAPE values.

Like in compound (**3**) none of the calculated shapes for the polyhedron of (**8**) fit particularly well.

Like the previous complexes, compound (**8**) crystallises in the triclinic space group  $\bar{P}1$  resulting in an inversion centre in the centre of the complex. The crystal cell contains one molecule of the complex, four chloride counter ions and two units of acetonitrile as lattice solvent. The intermolecular interactions of this compound are quite similar to compound (**3**) and (**4**). There are four chloride anions per unit cell splitting up as two groups of two. The first group is three-times coordinated to the hydrazone group, the imidazole group and the bromine. The second group of chlorides making four bonds each. All these hydrogen bonds are made with water molecules chelating to the dysprosium. Then there are two acetonitrile acting as lattice solvent per unit cell. They are coordinating with der nitrile groups to one water molecule, respectively.

The big difference in the molecule stacking to (3) and (4) is that there is no methanol in the crystal structure. The introduced bromine replaces it and does the third coordination with the first group of chlorides.

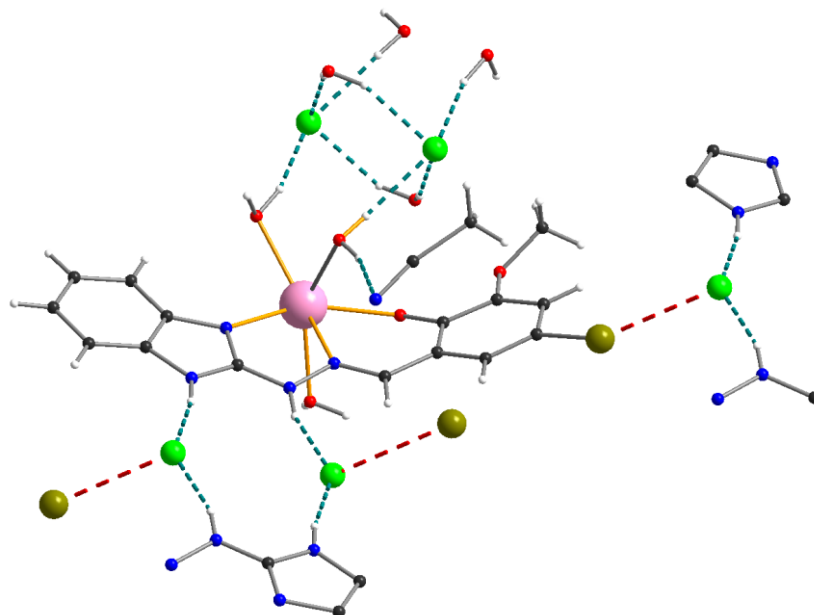


**Figure 76:** Intermolecular interactions of (8). Hydrogen bonds are shown as green dashed lines, chloride-bromine bonds as red dashed lines. The complex was reduced to a monomer for better visualisation.

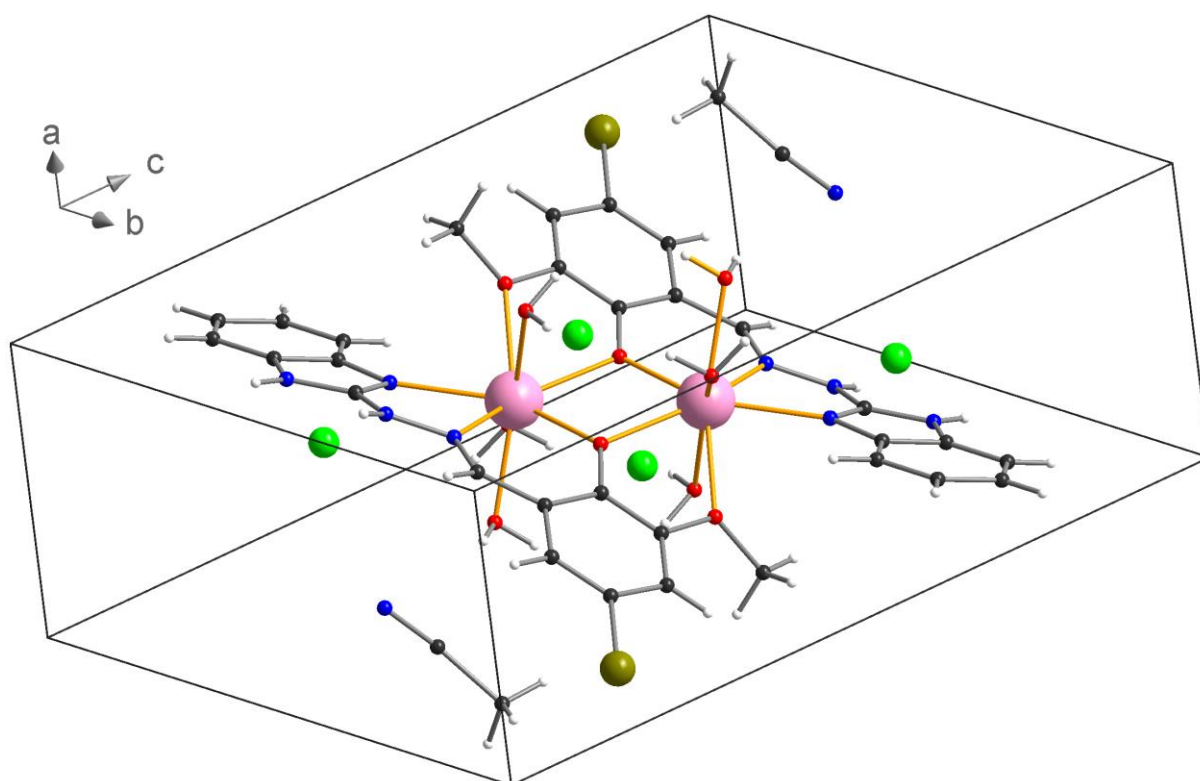
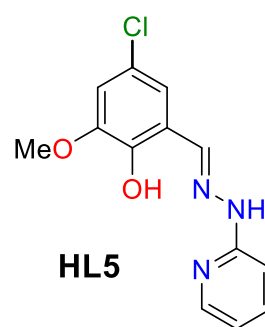


**Figure 77:** Unit cell packing of compound (8).

#### 4.1.5 Dinuclear dysprosium complexes (9) and (10) obtained from HL5

The two compounds presented here can be obtained in two steps. The ligand HL5 is a slightly modified version of HL2. The hydrogen atom at the 5-position of *o*-vanillin is occupied by a chlorine atom. This small change in the ligand structure leads to two new complexes that have certain similarities to previous compounds. In the first step, the ligand HL5 was synthesised using a Schiff-base reaction with 5-chloro-2-hydroxy-3-methoxybenzaldehyde and 2-hydrazineylpyridine as reactants. In the second step, the ligand was mixed with a given lanthanide salt in a mixture of solvents. Slow evaporation of the solvents at room temperature was chosen as crystallisation technique. The lanthanide complexes (9) and (10) were synthesised this way (Figure 78).



$[\text{Dy}_2(\text{L5})_2(\text{CH}_3\text{COO})_4(\text{CH}_3\text{OH})_2]$  (9) was obtained using  $\text{Dy}(\text{CF}_3\text{SO}_3)_3$  and anhydrous sodium acetate as co-ligand. The solvent mixture was methanol-acetonitrile 1:1. After ten days, yellow block-shaped crystals suitable for X-ray diffraction analysis had formed.

$[\text{Dy}_2(\text{L5})_4(\mu\text{-H}_2\text{O})]\text{Cl}_2\cdot\text{H}_2\text{O}\cdot\text{CH}_3\text{OH}\cdot\text{CH}_3\text{CN}\cdot(\text{CH}_3\text{CH}_2)_2\text{O}$  (10) was obtained using  $\text{DyCl}_3\cdot 6\text{H}_2\text{O}$ . The solvent mixture was methanol-acetonitrile-diethylether 1:1:1. After twenty days, yellow block-shaped crystals suitable for X-ray diffraction analysis had formed.

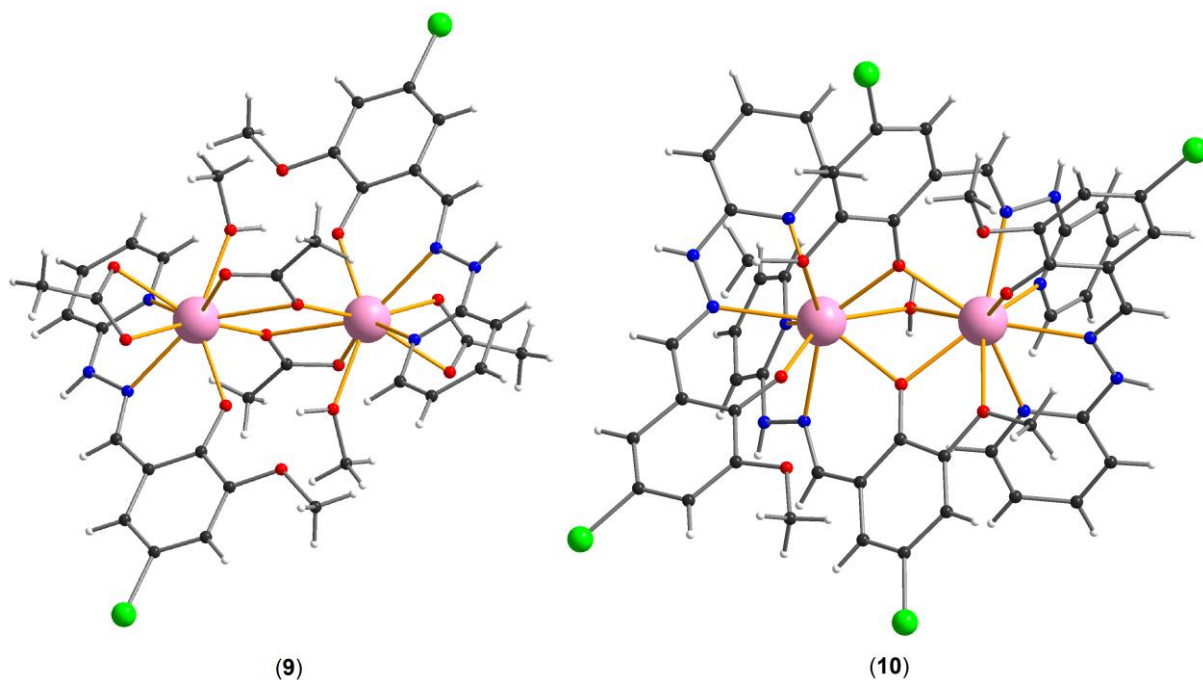
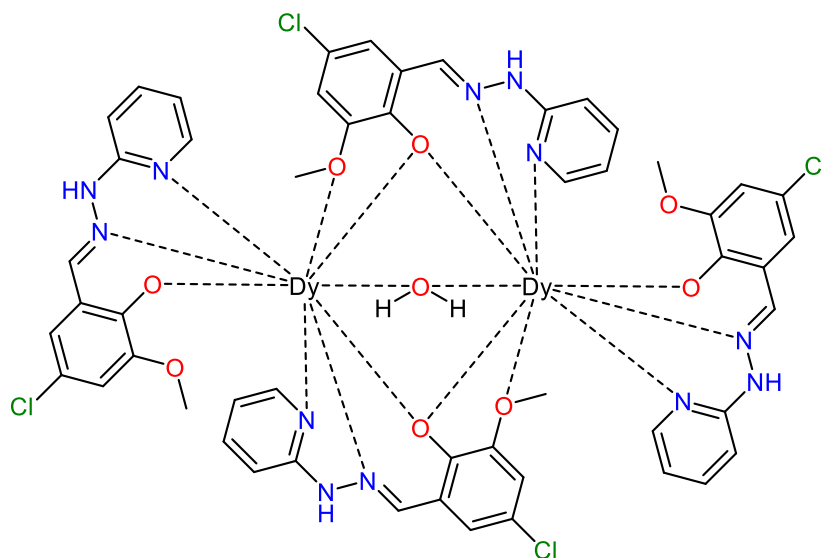


**Figure 78:** The dinuclear lanthanide complexes **(9)** and **(10)** using HL5 as a ligand. Colour code: white = H; black = C; blue = N; red = O; green = Cl; rose = Dy.

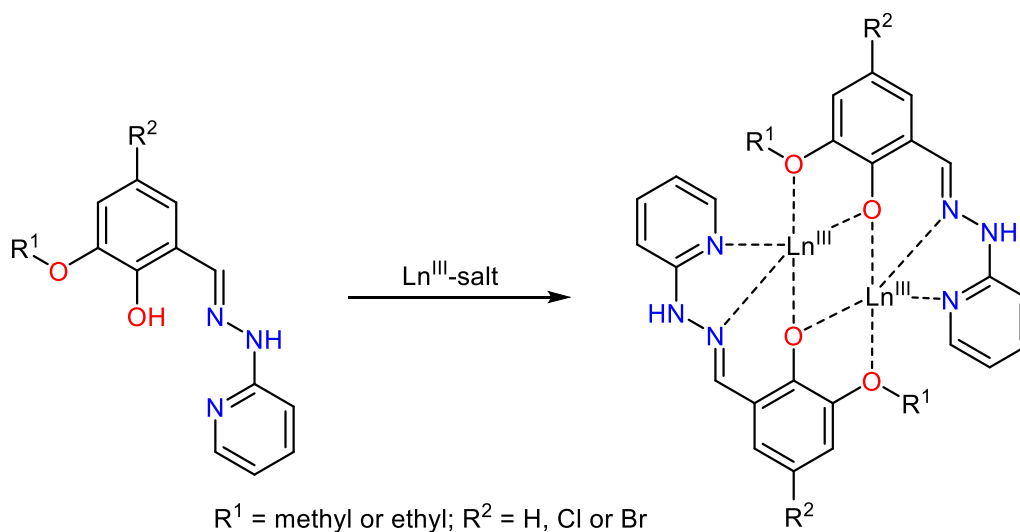
At first sight compound **(9)** looks very much like compound **(6)** but with a chlorine atom at the *para*-position of the phenoxy group. It is another dinuclear complex built up from two units of the deprotonated ligand (L5)<sup>-</sup> and two Dy<sup>III</sup> ions. The metal ions sit in the ligand's pocket consisting of the pyridyl and imino nitrogens and the phenoxy oxygen. The other pocket remains unoccupied. Each Dy<sup>III</sup> ion is coordinated by a bidentate acetate molecule, a bridging bidentate acetate and a methanol molecule. This gives a coordination number of nine.

The structural description of compound **(10)** is supported by a scheme (see Scheme 8). The complex consists of two Dy<sup>III</sup> ion, four deprotonated ligands (L5)<sup>-</sup> and one water molecule. The ligand splits up in two groups of two units. The first group coordinates with its big pocket consisting of the pyridine, hydrazone and phenoxy group to the Dy<sup>III</sup> ion and with its small pocket consisting of the phenoxy and methoxy group to the other Dy<sup>III</sup> ion. The second group only chelates with its big pocket to one metal, respectively. The small pocket stays empty. There is one water molecule  $\mu$ -bridging between the metal ions, adding up to a coordination number of 9 for the Dy<sup>III</sup> ions. A dinuclear Dy<sup>III</sup> complex containing a bridging water molecule has also been reported in the literature.<sup>[49]</sup>



**Scheme 8:** Schematic structure of the molecular structure of (10).

Ignoring the two ligands bound to the Dy<sup>III</sup> ions with only one pocket and the bridging water molecule, one returns to the [Ln<sub>2</sub>(ligand)<sub>2</sub>] core structure of the previous discussed compounds (1) to (5) and (8) (see Scheme 9).



**Scheme 9:** Reaction scheme leading to the [Ln<sub>2</sub>(ligand)<sub>2</sub>] core structure of (1) to (5) and (8).

All synthesis using the two-pocket ligands HL1 to HL5 but not using acetate lead to a structure with two Ln<sup>III</sup> ions and two ligands in the centre. Both ligand's pockets are occupied.

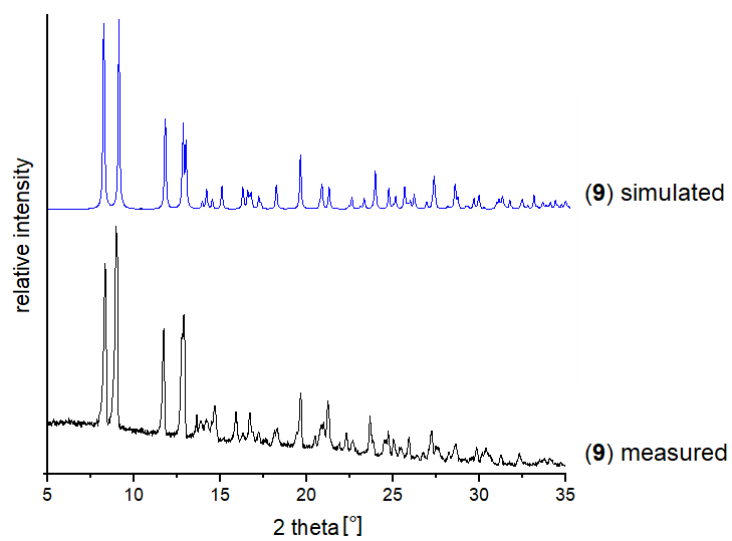


**Figure 79:** Measured powder pattern of (9) versus simulated pattern from single crystal data.

The measured powder pattern of (9) matches well with the simulated one.

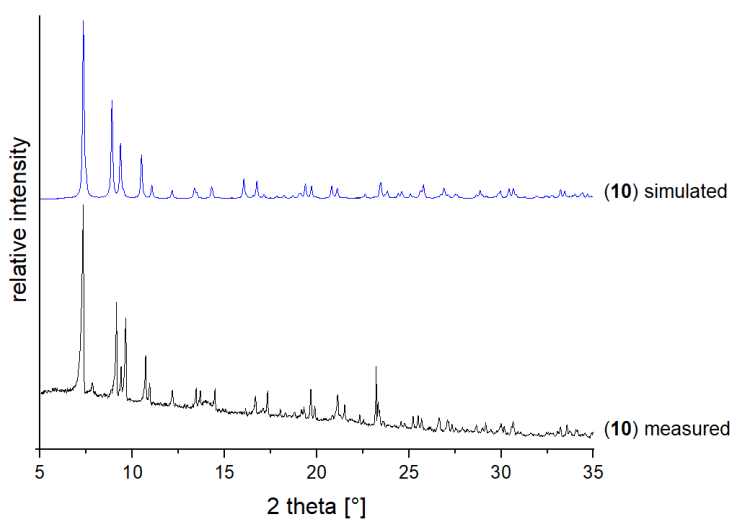


**Figure 80:** Measured powder pattern of (10) versus simulated pattern from single crystal data.

The measured powder pattern of (10) matches with the simulated one.

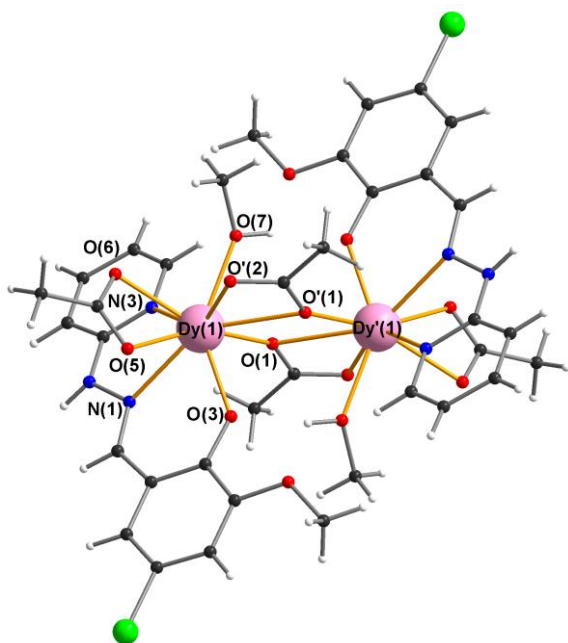


**Figure 81:** Structure of (9) with selected atoms labelled.

| Atom  | Atom   | Distance [Å] |
|-------|--------|--------------|
| Dy(1) | Dy'(1) | 4.1324(4)    |
| Dy(1) | O(1)   | 2.318(3)     |
| Dy(1) | O'(1)  | 2.623(3)     |
| Dy(1) | O'(2)  | 2.443(4)     |
| Dy(1) | O(3)   | 2.257(3)     |
| Dy(1) | O(5)   | 2.489(3)     |
| Dy(1) | O(6)   | 2.390(4)     |
| Dy(1) | O(7)   | 2.387(3)     |
| Dy(1) | N(1)   | 2.515(4)     |
| Dy(1) | N(3)   | 2.573(4)     |

| Atoms             | Angle [°]  |
|-------------------|------------|
| Dy(1)-O(1)-Dy'(1) | 113.36(12) |
| O(1)-Dy(1)-O'(1)  | 66.64(12)  |

**Table 11:** Selected bond lengths and angles of compound (9).

Compound (9) compares well with compound (6) because their only structural difference is the chlorine atom in the *para*-position on the phenoxy group on compound (9). The shown distances are quite close to those of compound (6). The only notable difference is the Dy-O' bond of the bridging oxygen atoms. In compound (6) this distance is 2.792 Å, here it is decreased to 2.623 Å which is a difference of over 6%. This makes it slightly shorter than the maximum distance suggested for a Dy-O bond length.<sup>[41]</sup>

| Atom  | Atom   | Distance [Å] |
|-------|--------|--------------|
| Dy(1) | Dy'(1) | 3.6755(4)    |
| Dy(1) | O(1)   | 2.547(3)     |
| Dy(1) | O(2)   | 2.342(2)     |
| Dy(1) | O'(2)  | 2.344(2)     |
| Dy(1) | O'(3)  | 2.678(3)     |
| Dy(1) | O(4)   | 2.219(2)     |
| Dy(1) | N(1)   | 2.529(3)     |
| Dy(1) | N(3)   | 2.611(3)     |
| Dy(1) | N(4)   | 2.483(3)     |
| Dy(1) | N(6)   | 2.507(3)     |

| Atoms             | Angle [°] |
|-------------------|-----------|
| Dy(1)-O(1)-Dy'(1) | 92.38(12) |
| Dy(1)-O(2)-Dy'(1) | 103.31(8) |

**Table 12:** Selected bond lengths and angles of compound (10).

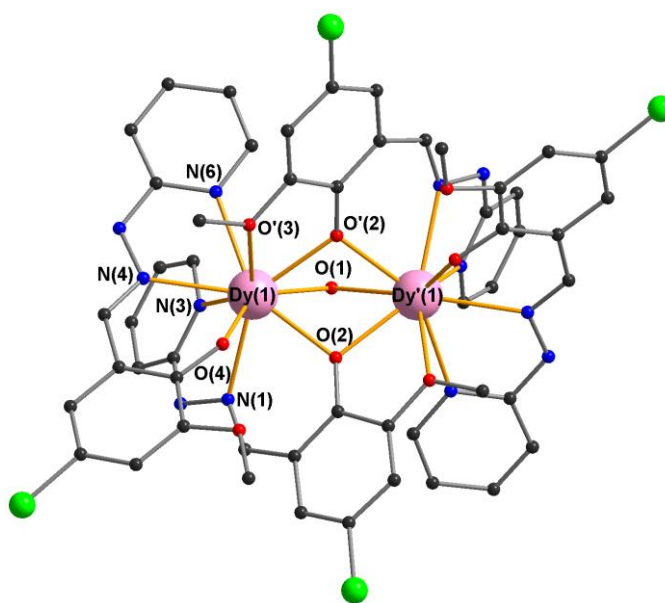


**Figure 82:** Structure of (10) with selected atoms labelled.

Since there is no further structure like (10), it makes little sense to compare (10) with previous compounds. The bond lengths of (10) are in line with what can be found in the literature.<sup>[41]</sup> In compound (10) we have two groups of the ligand (L5)<sup>-</sup>, the one- and two-pocket chelating ligands. Comparing the Dy-O and Dy-N bond lengths, it is noticeable that they are shorter for the one-pocket chelating ligands. The two-pocket chelating ligands have longer bond lengths. Differences in bond lengths can therefore be attributed solely to the molecular structure.

| Polyhedron                        | Deviation [%] |
|-----------------------------------|---------------|
| Muffin                            | 11.274        |
| Capped square antiprism           | 12.465        |
| Spherical capped square antiprism | 12.923        |

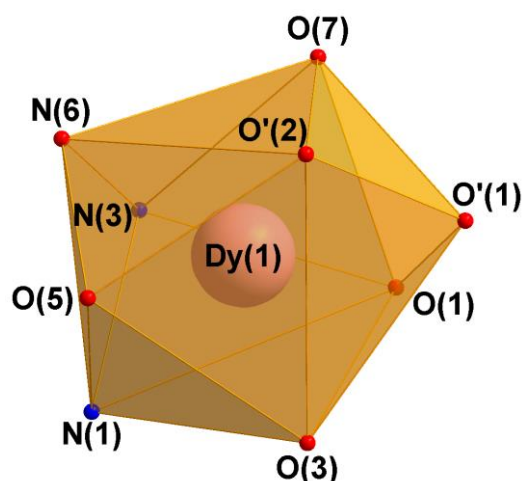
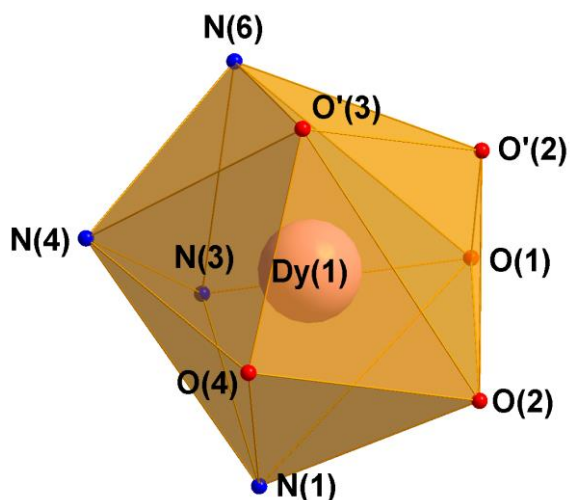


**Figure 83:** Nine-vertex polyhedron of **(9)** with SHAPE values.

None of the calculated shapes for the polyhedron of **(9)** fit satisfactory.



| Polyhedron                        | Deviation [%] |
|-----------------------------------|---------------|
| Capped square antiprism (J10)     | 4.103         |
| Muffin                            | 4.163         |
| Spherical capped square antiprism | 4.591         |

**Figure 84:** Nine-vertex polyhedron of **(10)** with SHAPE values.

All three calculated shapes for the possible polyhedron of **(10)** have similar values. The calculated shapes for polyhedron of **(10)** have lower deviations than the most previous compounds. The dysprosium centre is coordinated by three ligand molecule. One difference for **(10)** to compare to the previous compounds is the larger number of nitrogen atoms in its coordination sphere. It has a  $\text{DyO}_5\text{N}_4$  polyhedron instead of the usual  $\text{DyO}_7\text{N}_2$  or  $\text{DyO}_6\text{N}_2$ .

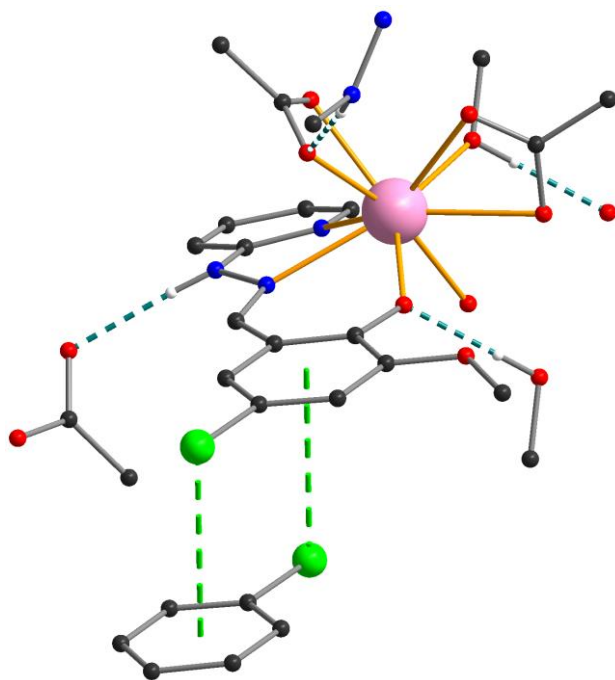


**Figure 85:** Intermolecular interactions of (9). Hydrogen bonds are shown as green dashed lines, chlorine- $\pi$ -system interactions shown as light green dashed lines. Only the asymmetric unit is shown for clarity. Hydrogen atoms on carbon are not displayed for better visualisation.

Compound (9) crystallises in the monoclinic space group  $C2/c$ . The crystal cell contains four molecules of the complex. Interestingly, this complex comes with no solvent molecules in its crystal cell packing. There is one intramolecular hydrogen bond. One intermolecular hydrogen bond arises from the interaction of the coordinated molecule with phenoxy group chelating to the neighbouring dimer. There are two types of intermolecular interactions. The hydrazone groups are forming hydrogen bonds to chelating acetate molecules of neighbouring molecules. The chlorine atoms are interaction with the  $\pi$ -system of the phenoxy ring making the molecules form chains in the crystal structure. The distance of the chlorine to the centre of the neighbouring phenoxy ring is 3.815 Å.

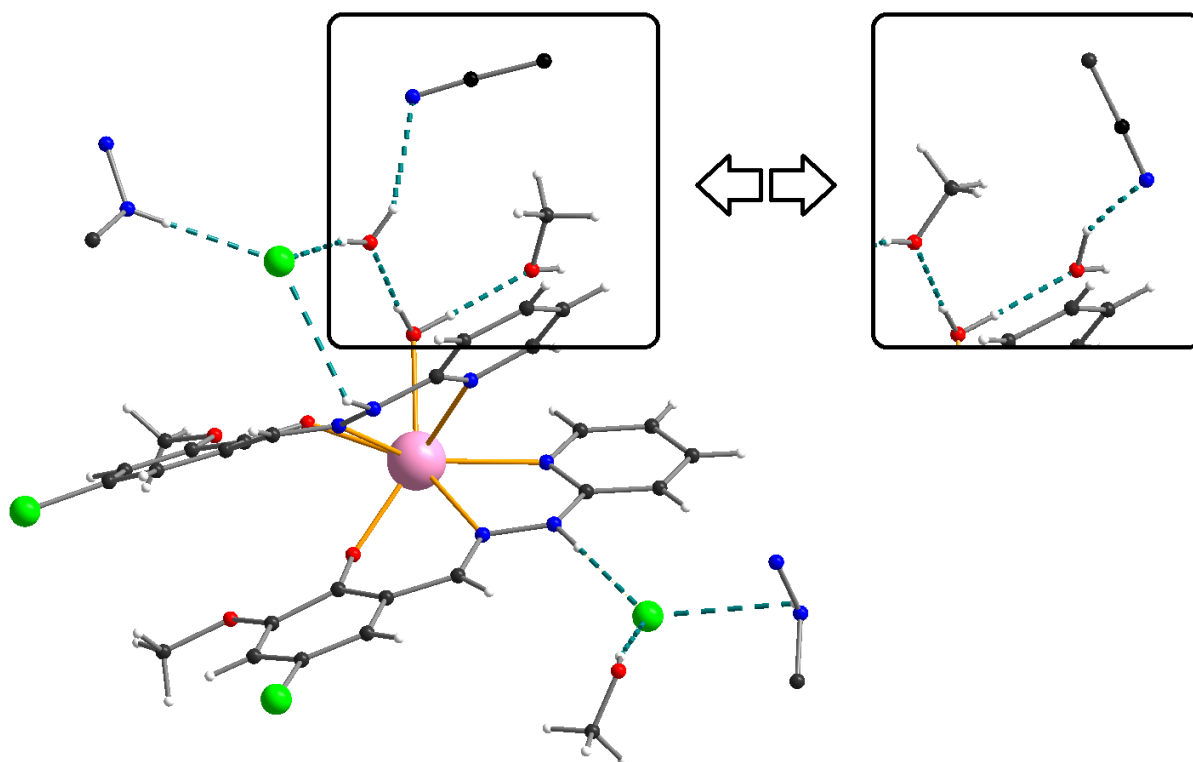


**Figure 86:** Intermolecular interactions of (**10**). The two different orientations for the lattice acetonitrile molecule are presented. Hydrogen bonds are shown as green dashed lines. The complex's asymmetric unit is shown for better visualisation.

Compound (**10**) crystallises in the orthorhombic space group  $P2_12_12$ . The unit cell contains two molecules of the complex, four chloride counter ions and two units of each solvent molecule. Hydrogen bonds form from the solvent molecules and the chloride counter ions. The acetonitrile is disordered about the crystal two-fold rotation axis around  $c$ . Depending on which way the acetonitrile is orientated, there is a hydrogen bond to a water molecule or no interaction to a methanol molecule (see figure 86). The ether molecule is heavily disordered and modelled using SQUEEZE.<sup>[50]</sup>

The chloride forms three interactions towards two hydrazone groups of neighbouring complexes and towards a water or methanol molecule. The water molecule bonds to the chloride and also to the acetonitrile and the water molecule ligand on dysprosium. The methanol bridges between this water and the chloride. The possibility of a weak hal-hal interaction between two complexes can be dismissed since their distance of  $3.551 \text{ \AA}$  would be slightly larger than their combined van der Waals radii of  $3.50 \text{ \AA}$ .<sup>[48]</sup>

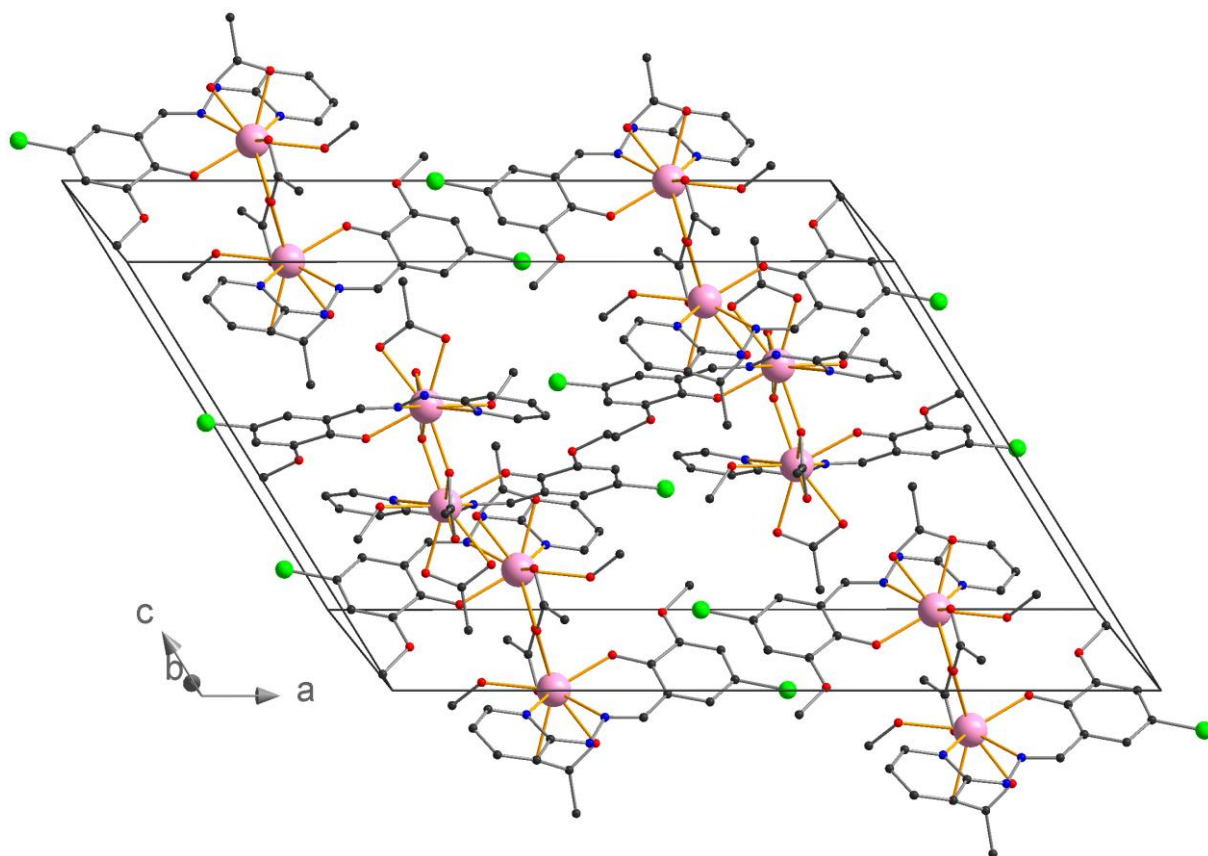


**Figure 87:** Unit cell packing of (9). Hydrogen atoms are not displayed for clarity.

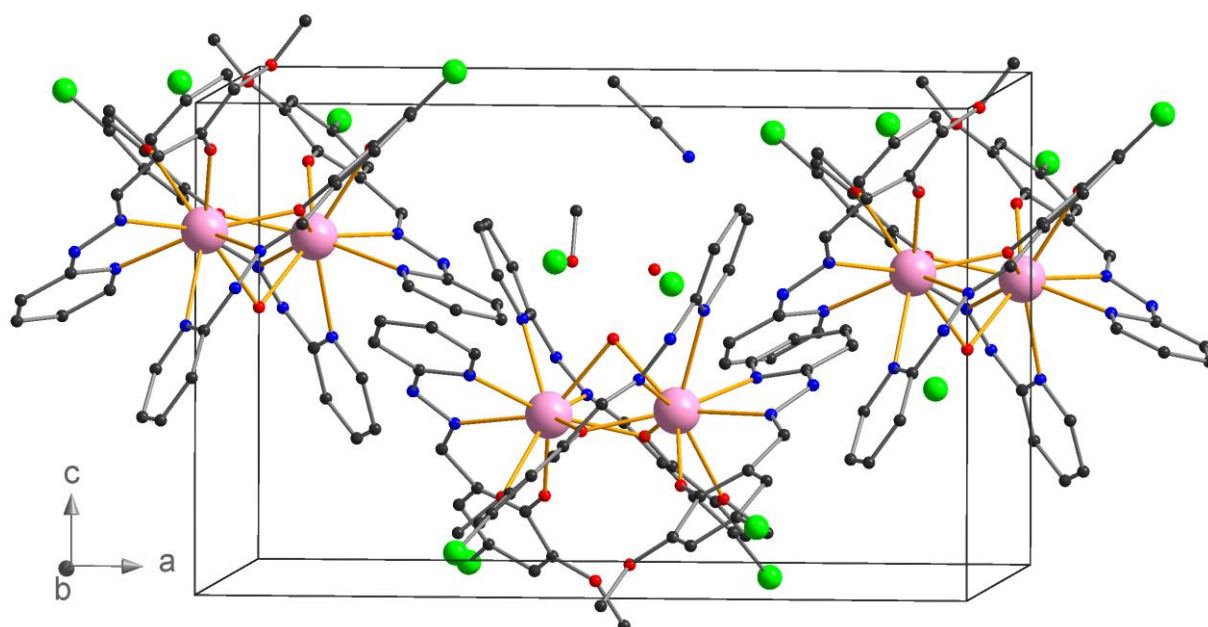
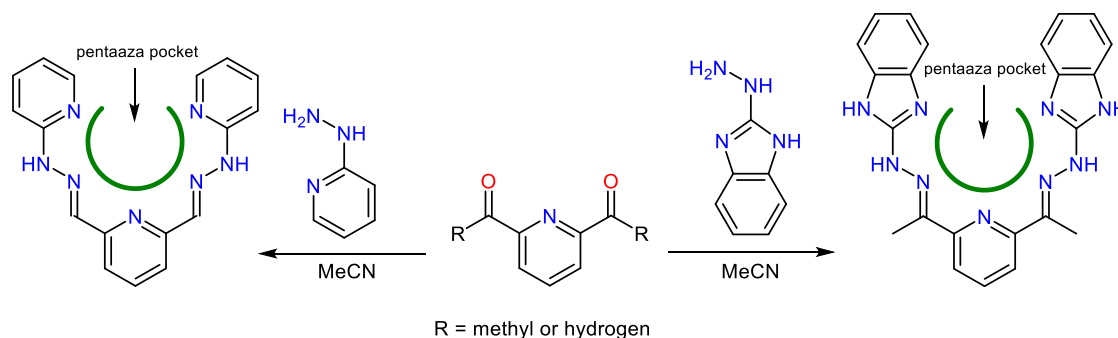


**Figure 88:** Unit cell packing of (10). For clarity hydrogen atoms are not displayed.

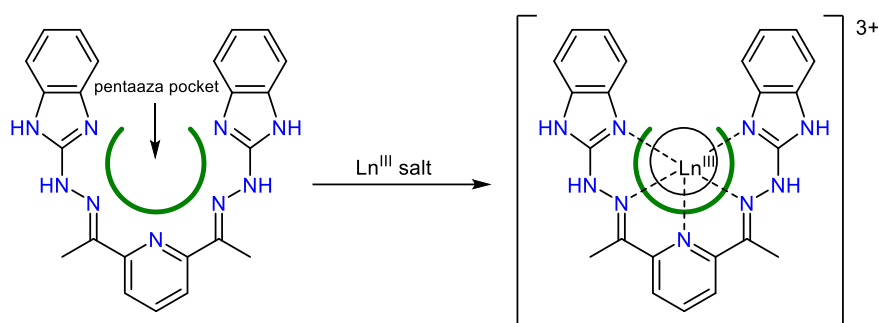
## 4.2 Mononuclear lanthanide systems with pentaaza ligands

A one-pocket ligand system was chosen for the syntheses of the mononuclear lanthanide<sup>III</sup> (Ln<sup>III</sup>) complexes. The large pocket can coordinate with a Ln<sup>III</sup> ion five times (see Scheme 10).



**Scheme 10:** Reaction scheme for the synthesis of the two one-pocket Schiff-base ligands.

Although a Ln<sup>III</sup> ion is five times coordinated equatorial in the pentaaza pocket, it is not yet completely enclosed. It takes other molecules in the axial position to enclose the Ln<sup>III</sup> ion. Solvent molecules or anions can coordinate from both sides to it. With this system a mononuclear structure consisting of one lanthanide and one ligand molecules is formed with a high probability (see Scheme 11).

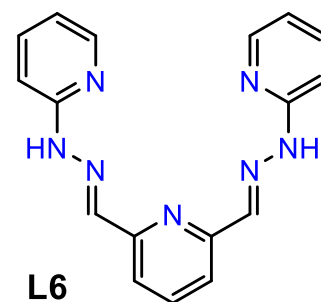


**Scheme 11:** Reaction scheme for the formation of the mononuclear lanthanide complexes.

It is a popular idea to have soft ligands in the equatorial plane and hard ligands in the axial position. In this way, a preferred orientation for the anisotropy axis can be created.<sup>[51]</sup>

#### 4.2.1 Mononuclear dysprosium complexes (**11**) and (**12**) obtained from L6

The two compounds presented here can be obtained in three steps. The ligand L6 is a slightly modified version of the pentaaza ligand system Rouven Pflieger used during his PhD research. The only difference are the missing methyl groups at the hydrazone carbon atoms. This change in the outer ligand's structure has little effect on its pocket and leads to two new



complexes that have similar structures to Rouven Pflieger's compounds<sup>[52, 53]</sup>. In the first step of the ligand's synthesis, an alcohol was oxidized to an aldehyde. 2,6-pyridinediyldimethanol reacts with selenium dioxide to 2,6-pyridinedicarbonylaldehyde using 1,4-dioxane as solvent. Although this reaction yields a mixture of substances, like the partially oxidised starting material, the synthesis route can proceed without purification.

In the second step, the reaction mixture is combined with 2-hydrazinepyridine in methanol. A Schiff-base reaction results in the ligand 1,1-(pyridine-2,6-diyl)bis(N-(pyridin-2-ylmethyl)methanimine) (L6). This molecule is not particularly polar and insoluble in methanol and forms a precipitate. The by-products remain in solution and the solid product can be separated by filtration. NMR-analysis confirms the purity of the product.

In the third step, the solid ligand was mixed with a solution of given lanthanide salts and taken up into solution by the complexation reaction. Slow evaporation of the solvents at room temperature was chosen as crystallisation technique. The lanthanide complexes (**11**) and (**12**) were synthesised this way (Figure 89).

[DyL6(H<sub>2</sub>O)<sub>4</sub>]Cl<sub>3</sub>·6H<sub>2</sub>O (**11**) was obtained using DyCl<sub>3</sub>·6H<sub>2</sub>O. The solvent mixture was methanol-acetonitrile 1:1. After ten days, yellow block-shaped crystals suitable for X-ray diffraction analysis had formed.

[DyL6(H<sub>2</sub>O)<sub>4</sub>]Br<sub>3</sub>·4.5H<sub>2</sub>O (**12**) was obtained using DyBr<sub>3</sub>·xH<sub>2</sub>O. The solvent mixture was methanol-acetonitrile 1:1. After ten days, light-brown block-shaped crystals suitable for X-ray diffraction analysis had formed.

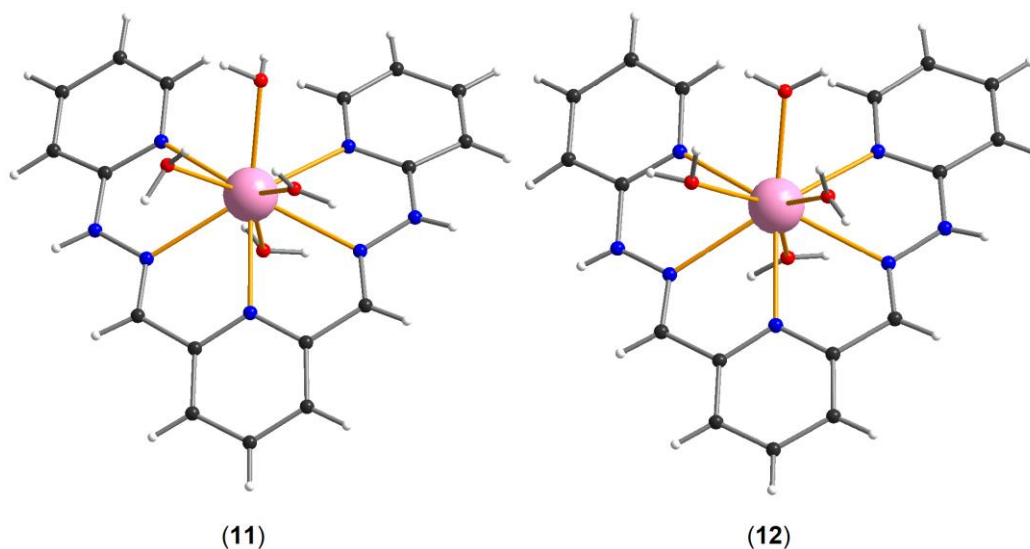


**Figure 89:** The mononuclear dysprosium complexes  $[\text{DyL6}(\text{H}_2\text{O})_4]\text{Cl}_3 \cdot 6\text{H}_2\text{O}$  (11) and  $[\text{DyL6}(\text{H}_2\text{O})_4]\text{Br}_3 \cdot 4.5 \text{H}_2\text{O}$  (12) using L6 as a ligand. Colour code: white = H; black = C; blue = N; red = O; rose = Dy.

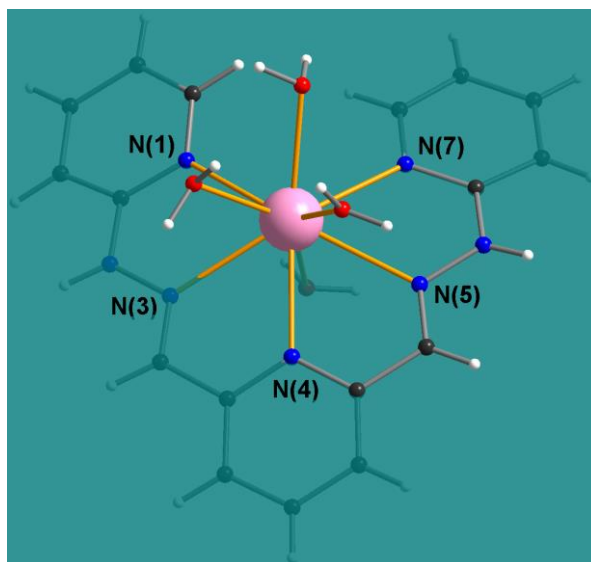


**Figure 90:** Compound (11) with a green plane crossing through the pyridine's nitrogen atoms.

The structures of compound (11) and (12) are very similar and can be described together. The  $\text{Dy}^{\text{III}}$  ion occupies the ligand's pocket consisting of five nitrogen atoms. This pocket is made up of three nitrogen atoms from the pyridine groups and two nitrogen atoms from the hydrazone groups. Looking at the plane on which the three nitrogen atoms of the pyridine groups (N1), (N4) and (N7) are located, (N5) is above and (N3) below this plane (see Figure 90). Additionally, four water molecules coordinate to the  $\text{Dy}^{\text{III}}$  ion, three above the plane and one below. This results in a coordination number of nine. The ligand as part of the complex is not flat but distorted. The external pyridine units are bend towards the side of the single coordinated water molecule (see Figure 91). Compound (11) is more distorted than compound (12).

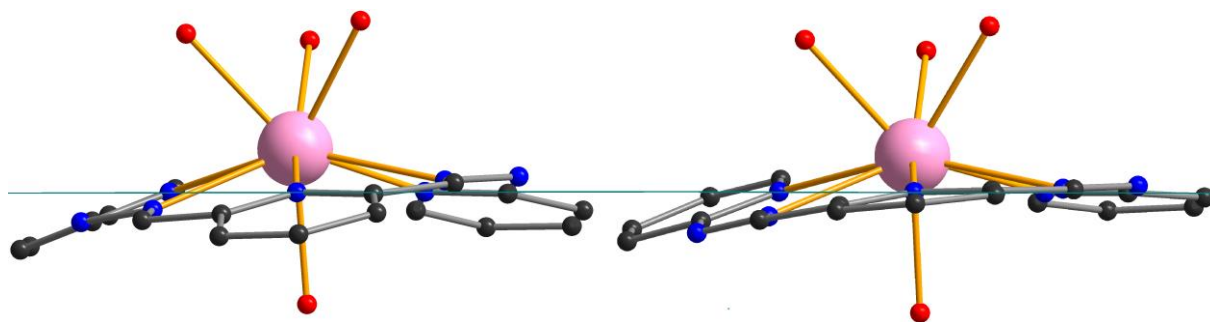


**Figure 91:** Compound (11) (left) and compound (12) (right) viewed from the side of the (N1)-(N4)-(N7)-plane. Hydrogen atoms have been removed for clarity.

In Figure 91 you can clearly see the structural difference between compound (11) and (12). In compound (11) the Dy<sup>III</sup> ion is located further away from the plane. The ligand is also significantly more bent. The pyridine groups show greater torsion. In compound (12) the Dy<sup>III</sup> ion is closer to centre of the pentaaza pocket. The ligand is less bent. This is shown in the difference in the N(7)-Dy(1)-N(1) angles. The change in the structure might be caused by the different counter ions and their attractive interaction on the coordination water molecules. The different unit cell packing of (11) and (12) can also have an effect.

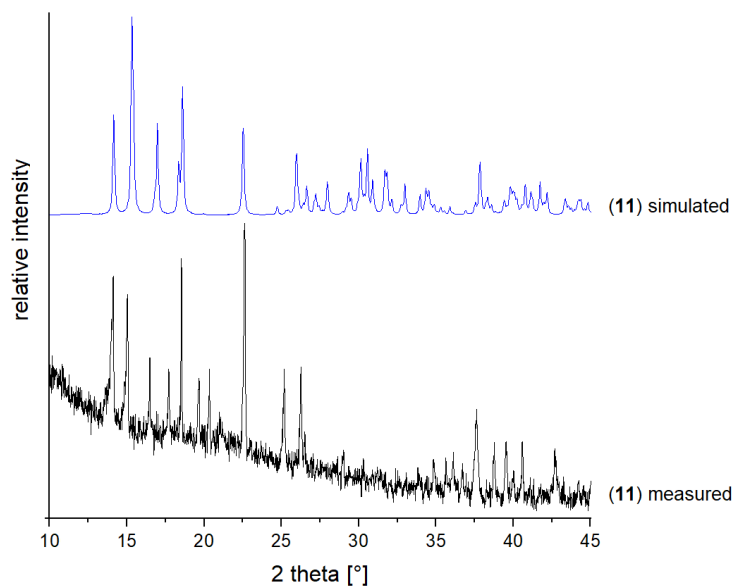


**Figure 92:** Measured powder pattern of (11) versus simulated pattern from single crystal data.

The measured powder pattern of (11) matches with the simulated one but seems to have some impurities.

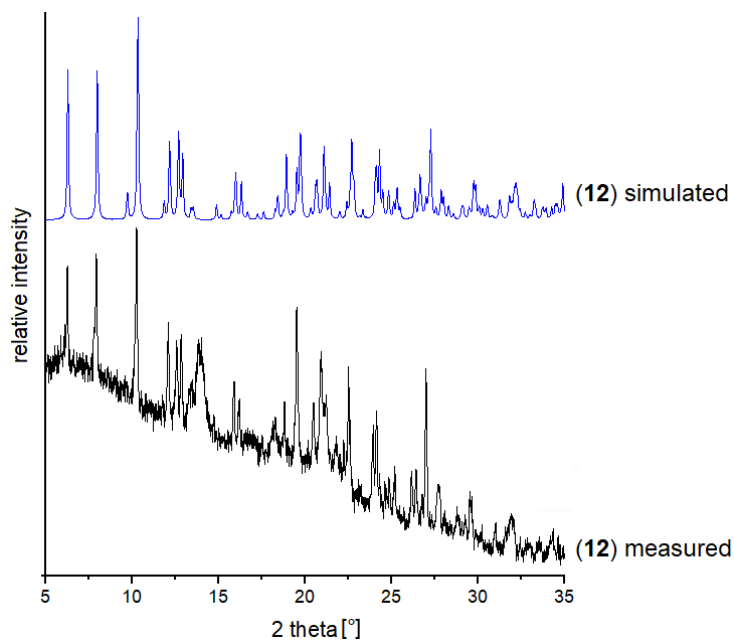


**Figure 93:** Measured powder pattern of (12) versus simulated pattern from single crystal data.

The measured powder pattern of (12) matches with the simulated one.

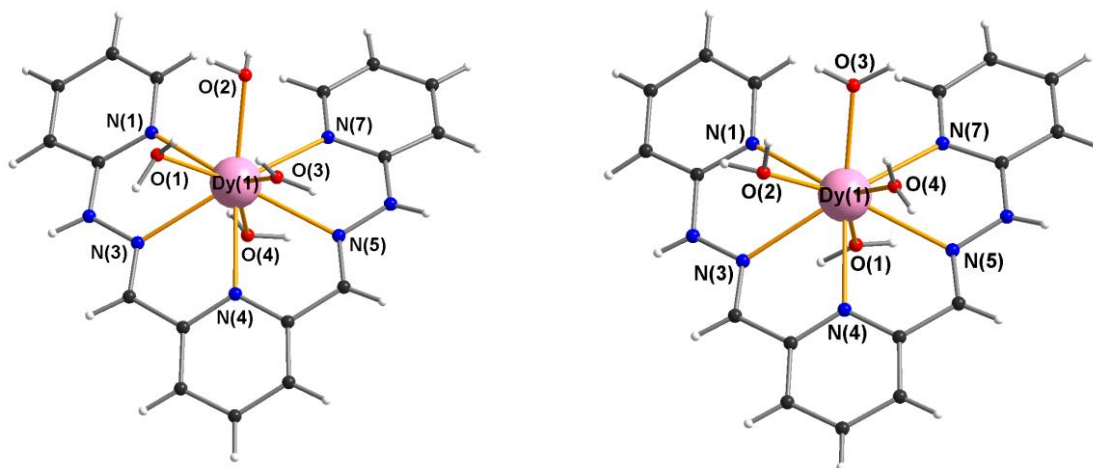


**Figure 94:** Structure of (11) (right) and (12) (left) with selected atoms labelled.

| Atom  | Atom | Distance [Å] |
|-------|------|--------------|
| Dy(1) | O(1) | 2.401(2)     |
| Dy(1) | O(2) | 2.390(2)     |
| Dy(1) | O(3) | 2.386(2)     |
| Dy(1) | O(4) | 2.336(2)     |
| Dy(1) | N(1) | 2.596(2)     |
| Dy(1) | N(3) | 2.530(2)     |
| Dy(1) | N(4) | 2.521(2)     |
| Dy(1) | N(5) | 2.532(2)     |
| Dy(1) | N(7) | 2.567(2)     |

| Atom  | Atom | Distance [Å] |
|-------|------|--------------|
| Dy(1) | O(1) | 2.343(4)     |
| Dy(1) | O(2) | 2.415(4)     |
| Dy(1) | O(3) | 2.350(4)     |
| Dy(1) | O(4) | 2.436(4)     |
| Dy(1) | N(1) | 2.581(5)     |
| Dy(1) | N(3) | 2.563(5)     |
| Dy(1) | N(4) | 2.519(5)     |
| Dy(1) | N(5) | 2.539(5)     |
| Dy(1) | N(7) | 2.572(5)     |

| Atoms           | Angle [°] |
|-----------------|-----------|
| N(1)-Dy(1)-N(3) | 62.72(7)  |
| N(3)-Dy(1)-N(4) | 62.47(7)  |
| N(4)-Dy(1)-N(5) | 62.54(7)  |
| N(5)-Dy(1)-N(7) | 61.88(7)  |
| N(7)-Dy(1)-N(1) | 96.19(7)  |

| Atoms           | Angle [°]  |
|-----------------|------------|
| N(1)-Dy(1)-N(3) | 62.07(15)  |
| N(3)-Dy(1)-N(4) | 61.72(15)  |
| N(4)-Dy(1)-N(5) | 62.70(15)  |
| N(5)-Dy(1)-N(7) | 61.87(15)  |
| N(7)-Dy(1)-N(1) | 101.04(15) |

**Table 13:** Selected bond lengths and angles of compound (11) (right) and (12) (left).

All Dy-O and Dy-N bond length have typical values. There are almost no differences in the bond length and angle values of compound (11) and (12). The only notable difference is the N(7)-Dy(1)-N(1) angle which is 5° larger in (12) than in (11). This can be explained by the fact that compound (12) is less acute than compound (11) (see Figure 91).

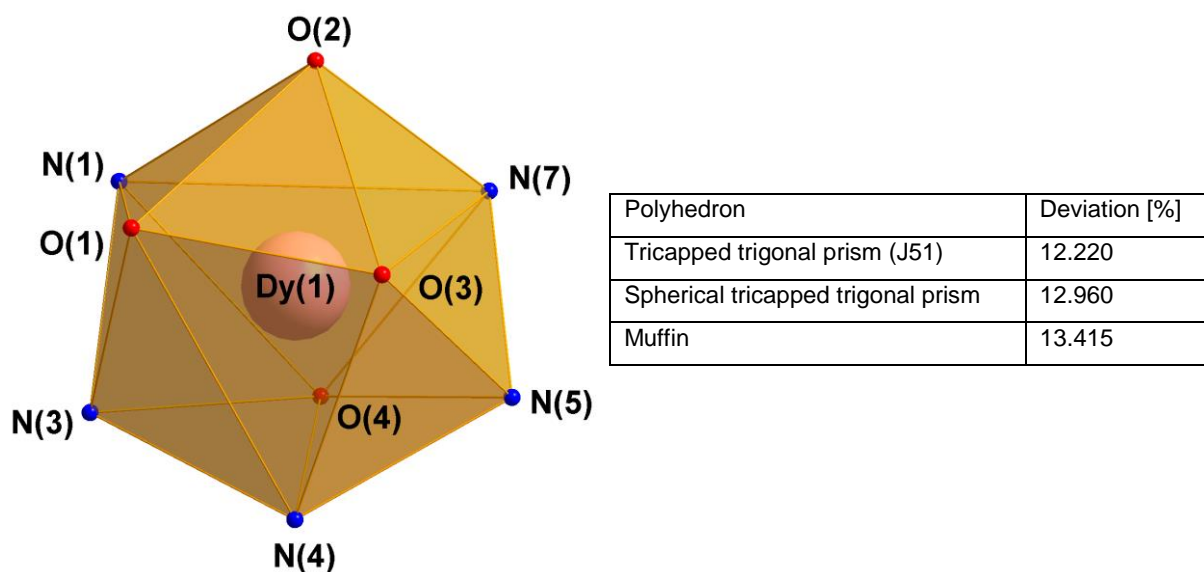


Figure 95: Nine-vertex polyhedron of (11) with SHAPE values.

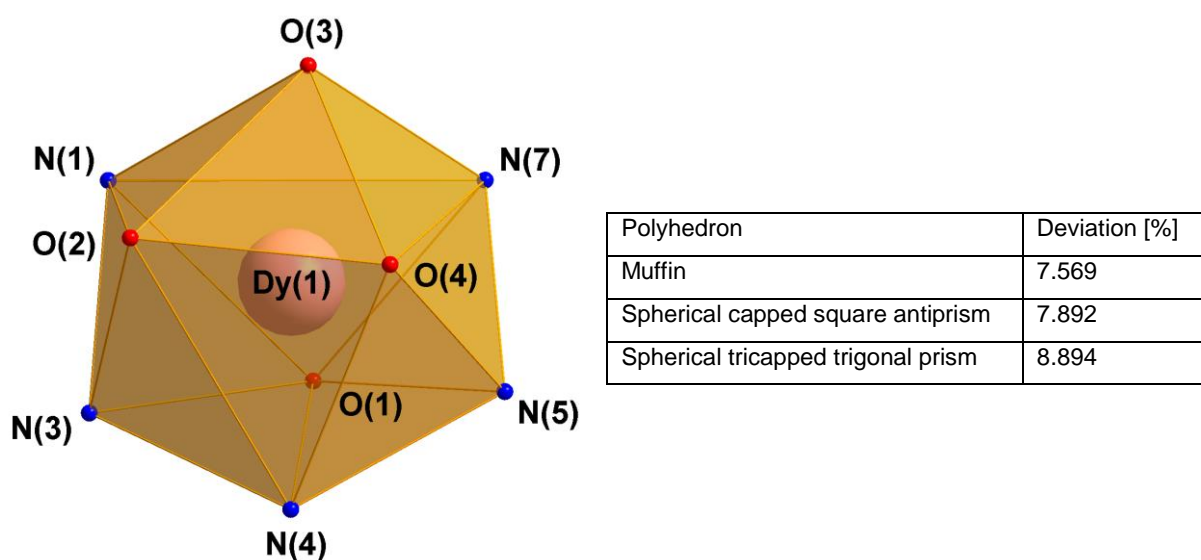
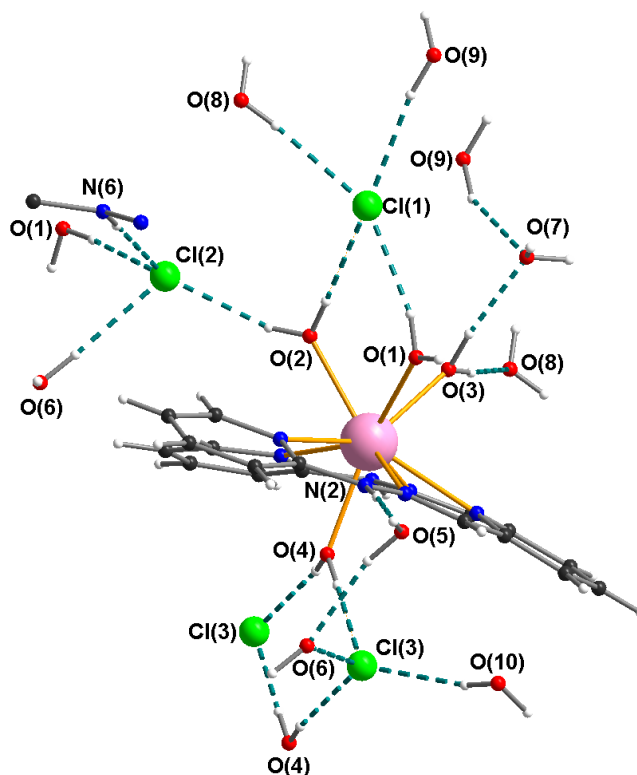


Figure 96: Nine-vertex polyhedron of (12) with SHAPE values.

While the structures of compound (11) and (12) are similar the deviations of the calculated shapes are significantly lower for (12) than for (11). This could be related to the fact that the Dy<sup>III</sup> in compound (11) is located further outside the ligand pocket. Compound (11) has no satisfactory fitting geometrical shape while (12) can be described best as a muffin.



**Figure 97:** Intermolecular interactions of (11). Selected atoms are labelled. Hydrogen bonds are shown as green dashed lines.

Compound (11) crystallises in the monoclinic space group  $P2_1/c$ . There is a total of twenty-four water molecules, four complex molecules and twelve chloride ions per unit cell forming hydrogen bonds (see Figure 97 and 99). The counter ion Cl(1) has four hydrogen bonds to different water molecules, two of them are lattice solvents and two coordinate to the  $Dy^{III}$  ion. Cl(2) forms bonds to three water molecules and one hydrazone group from a neighbouring complex. Cl(3) also makes four hydrogen bonds while bridging between the single sided coordinating water molecule containing O(4) to the neighbouring complex. There are three more lattice water molecules and the second hydrazone group forming hydrogen bonds.

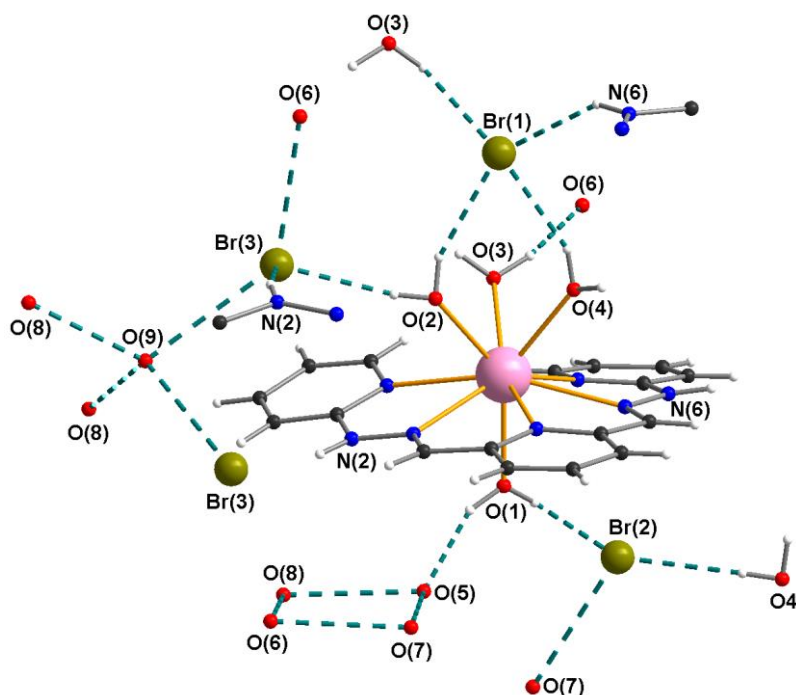


**Figure 98:** Intermolecular interactions of (12). Selected atoms are labelled. Hydrogen bonds are shown as green dashed lines. The hydrogen atoms of the lattice water are disordered and cannot be displayed.

Compound (12) crystallises in the monoclinic space group  $C2/c$ . There is a total of thirty-six water molecules, eight complex molecules and twenty-four bromide ions per unit cell forming hydrogen bonds (see Figure 98 and 100). The counter ion Br(1) has four bonds to three coordinating water molecules and one hydrazone group. Br(2) forms only three bonds to two coordinating water molecules and one lattice water. Br(3) forms only three bonds to two coordinating water molecules and one lattice water. Br(3) also makes four hydrogen bonds of which one is a coordinating water, two are lattice water and one is the second hydrazone group. There are two more lattice water molecules, containing O(5) and O(8) that only bond to other water molecules. The most interesting water molecule O(9) having four bond partners, instead of the usual three and sits on the cell's edge. It is shared equally by two unit cells resulting in the half-integral number of solvent molecules in  $[DyL6(H_2O)_4]Br_3 \cdot 4.5H_2O$ .

The different structure bending between compounds (11) and (12) can be explained by the different counter ions. In compound (11), the dysprosium is pulled more strongly from the plane of the nitrogen atoms because the chloride ion pulls more strongly on the coordinating water molecules than the bromide ion. The H-Cl hydrogen bond lengths in (11) range from 2.192 to 2.377 Å while the H-Br hydrogen bond lengths in (12) range from 2.342 to 2.602 Å.

If one compares the unit cells of (11) and (12), one sees that in both cases the complex molecules arrange themselves in layers. It is noticeable that in (11) the space between the layers is larger and is filled with more water molecules (see Figure 99 and 100).

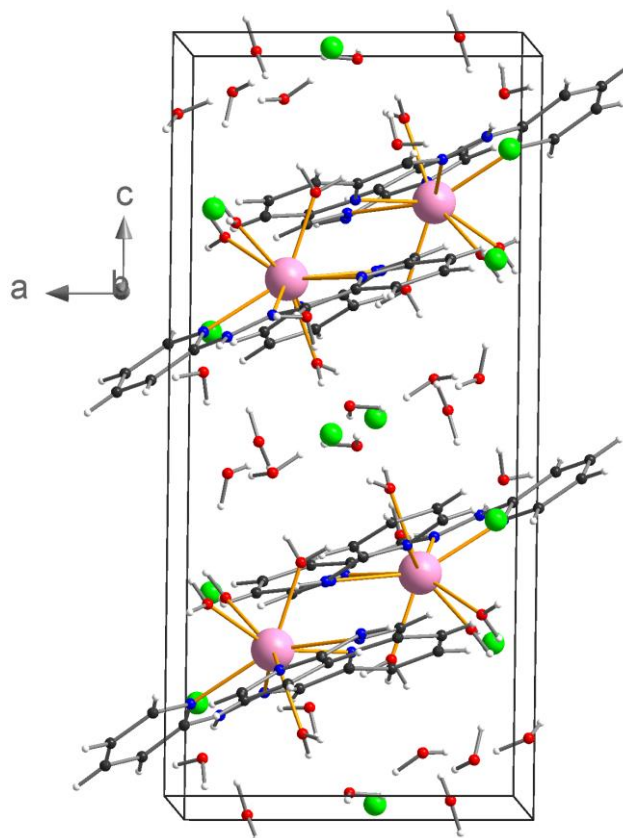


Figure 99: Unit cell packing of compound (11).

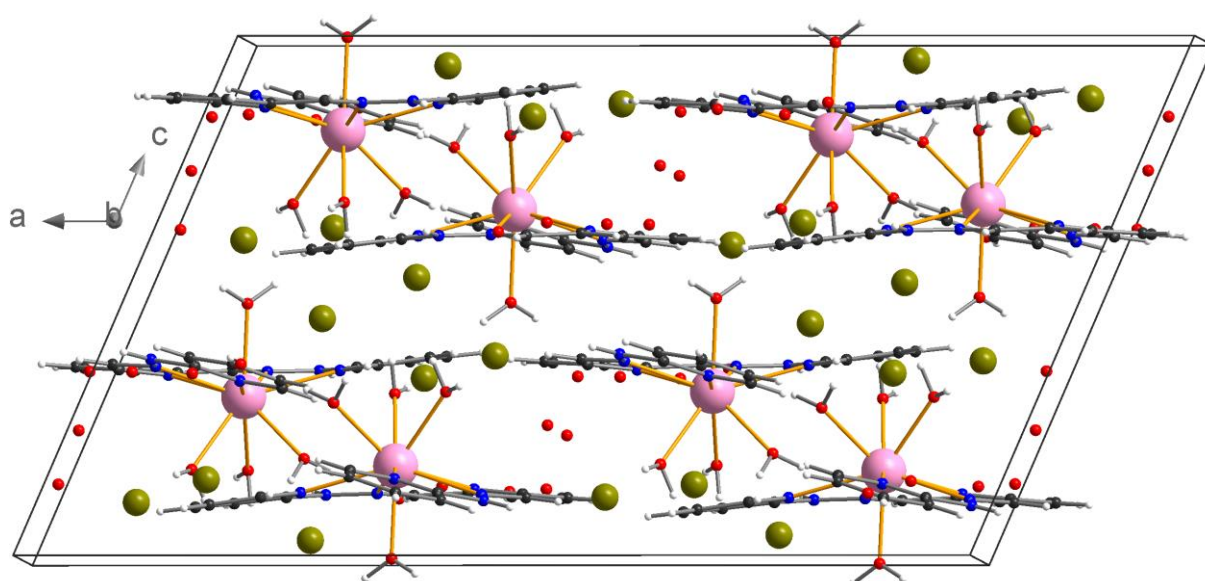
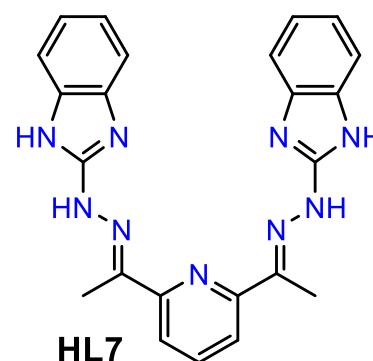


Figure 100: Unit cell packing of compound (12). Hydrogen atoms on lattice water are disordered and cannot be displayed.

#### 4.2.2 Mononuclear dysprosium complexes (13) to (16) obtained from HL7

The four compounds presented here can be obtained in two steps. The ligand HL7 is a modified version of L6. The external pyridine groups were replaced with benzimidazole. This change in the ligand's structure leads to four new complexes that utilise a similar pentaaza pocket as the previous compounds (11) and (12). In the first step, the ligand HL7 was synthesised using a Schiff-base reaction



with 2,6-diacetylpyridine and 2-hydrazino-1H-benzimidazole as reactants. In the second step, the ligand was mixed with a given lanthanide salt and other reagents in a mixture of solvents. Slow evaporation of the solvents at room temperature or temperature control were chosen as crystallisation techniques. The lanthanide complexes (13), (14), (15) and (16) were synthesised this way (Figure 101).

[Pr(HL7)(NO<sub>3</sub>)<sub>2</sub>CH<sub>3</sub>OH]NO<sub>3</sub>·2CH<sub>3</sub>OH·H<sub>2</sub>O (13) was obtained using Pr(NO<sub>3</sub>)<sub>3</sub>·6H<sub>2</sub>O. Methanol was chosen as solvent. After two days, red block-shaped crystals suitable for X-ray diffraction analysis had formed. Using Nd(NO<sub>3</sub>)<sub>3</sub>·6H<sub>2</sub>O leads to an isostructural compound.

[Sm(HL7)(NO<sub>3</sub>)<sub>2</sub>CH<sub>3</sub>OH]NO<sub>3</sub>·CH<sub>3</sub>OH (14) was obtained using Sm(NO<sub>3</sub>)<sub>3</sub>·6H<sub>2</sub>O. Methanol was chosen as solvent. After two days, red block-shaped crystals suitable for X-ray diffraction analysis had formed. Using Eu(NO<sub>3</sub>)<sub>3</sub>·6H<sub>2</sub>O yields an isostructural compound.

[Dy(L7)(NO<sub>3</sub>)<sub>2</sub>]·CH<sub>3</sub>OH (15) was obtained using Dy(NO<sub>3</sub>)<sub>3</sub>·5H<sub>2</sub>O and triethylamine as base. As solvents a 1:1 mixture of methanol and acetonitrile was chosen. After ten days, small red block-shaped crystals suitable for X-ray diffraction analysis had formed.

[Dy(HL7)(CH<sub>3</sub>COO)<sub>2</sub>]CF<sub>3</sub>SO<sub>3</sub>·CH<sub>3</sub>OH (16) was obtained using Dy(CF<sub>3</sub>SO<sub>3</sub>)<sub>3</sub> and anhydrous sodium acetate as co-ligand. As solvents a 1:1 mixture of methanol and acetonitrile was chosen. After two days, red rhomb-shaped crystals suitable for X-ray diffraction analysis had formed.

It was not possible to obtain the whole series of lanthanides complexes of HL7 in combination with lanthanide nitrates. The solubility of the formed complexes decreases with increasing atomic number of the given lanthanide. It seems as through the earlier and therefore larger  $\text{Ln}^{\text{III}}$  ions prefer going into the pentaaza pocket of HL7 and are axial coordinated with two nitrate anions. The complexes of Pr, Nd, Sm and Eu were synthesised this way (Pr/Nd = **(13)**, Sm/Eu = **(14)**). The dysprosium complex **(15)** could be obtained in a different approach by adding base, which resulted in the ligand being deprotonated on the hydrazone nitrogens. By replacing the nitrate co-ligand with an acetate co-ligand led to a similar structure for the dysprosium complex **(16)**.

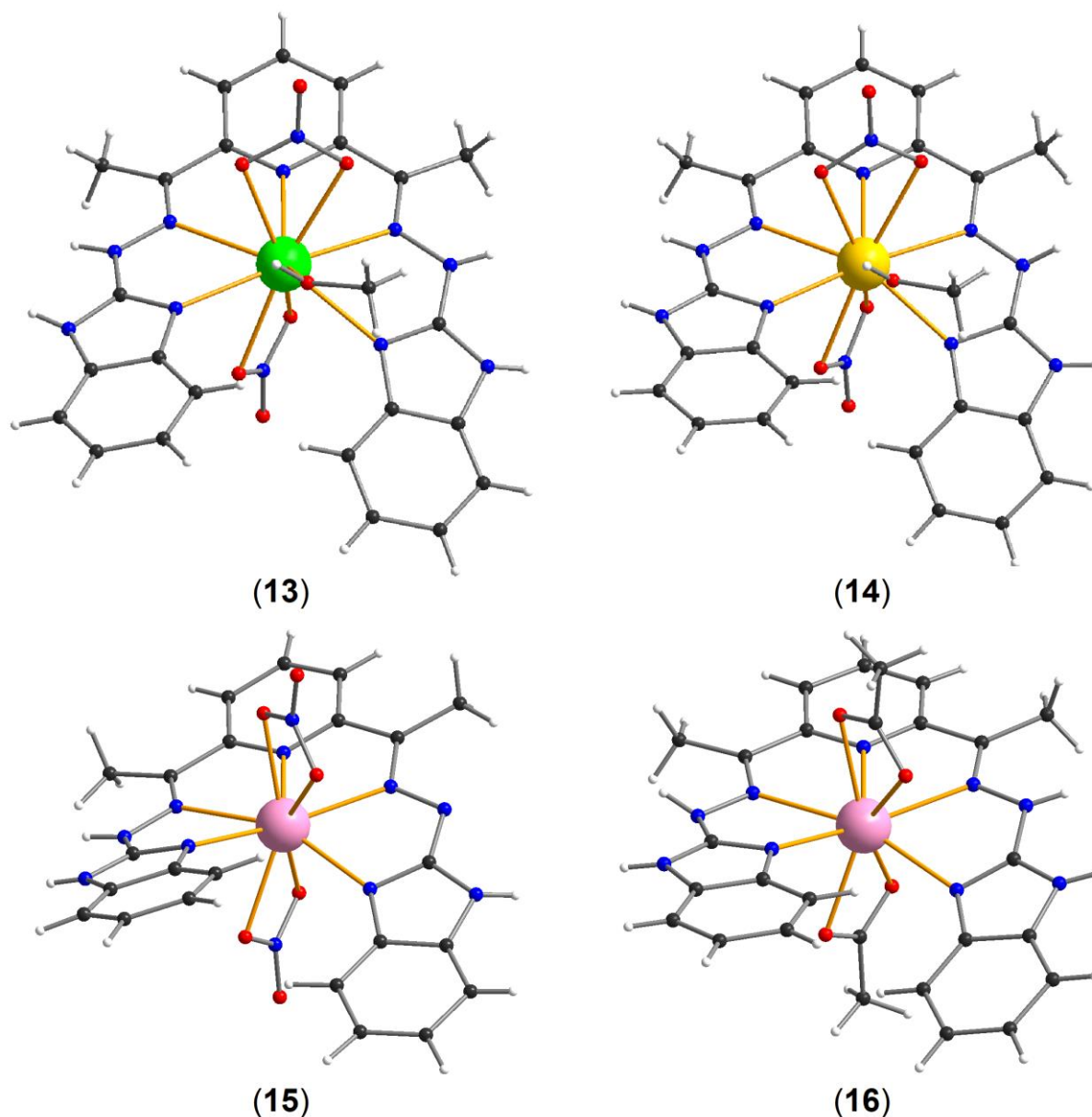


**Figure 101:** The four mononuclear lanthanide complexes using HL7 as ligand  $[\text{Pr}(\text{HL7})(\text{NO}_3)_2\text{CH}_3\text{OH}]$  (**13**),  $[\text{Sm}(\text{HL7})(\text{NO}_3)_2\text{CH}_3\text{OH}]$  (**14**),  $[\text{Dy}(\text{L7})(\text{NO}_3)_2]$  (**15**) and  $[\text{Dy}(\text{HL7})(\text{CH}_3\text{COO})_2]$  (**16**). Colour code: white = H; black = C; blue = N; red = O; light green = Pr; yellow = Sm; rose = Dy.

All four structures presented here are mononuclear lanthanide<sup>III</sup> compounds coordinated by HL7. The Ln<sup>III</sup> ion sits in the ligand's pocket consisting of five nitrogen atoms arranged around it. This pocket is made up of two nitrogen atoms from the benzimidazole groups, two nitrogen atoms from the hydrazone groups and nitrogen atom from the pyridine group. The complex is not flat. If one imagines a plane spanned by the coordinating pyridine and benzimidazole nitrogens, the lanthanide<sup>III</sup> ion does not lie central in this plane. One benzimidazole is above and one below this plane (see Figure 102).

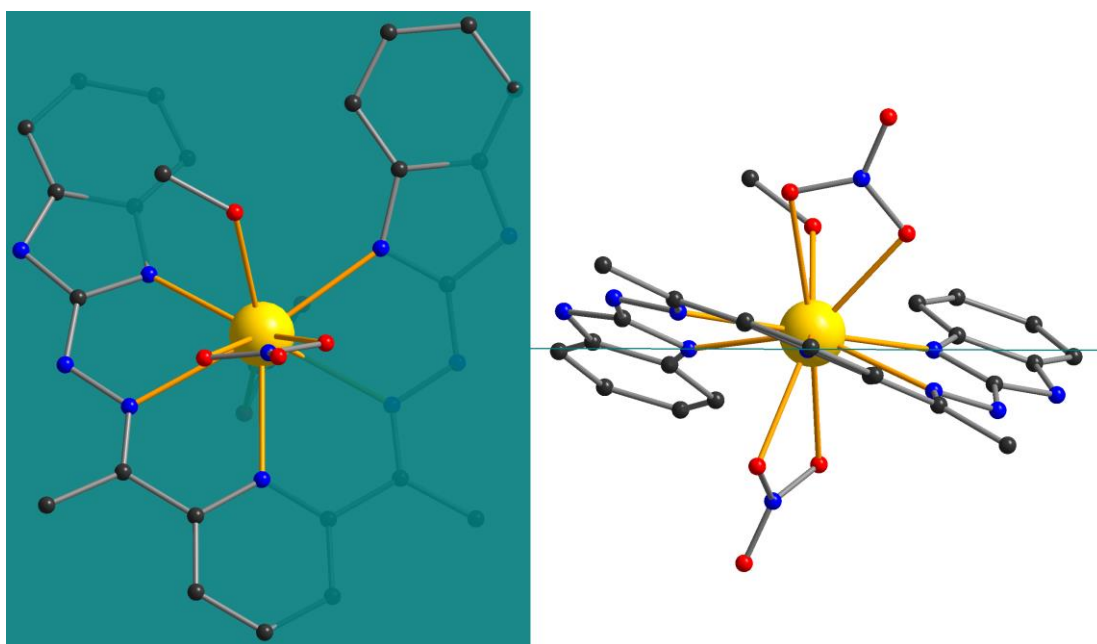


**Figure 102:** Compound (14) viewed from the top and side of the plane spanned through N(1), N(5) and N(9). Hydrogen atoms have been removed for clarity.

Compound (13) and (14) have their lanthanide<sup>III</sup> ion coordinated by two bidentate nitrate anions in the axial position. With one additional methanol molecule coordinating this adds up to a coordination number of the ten for both compounds.

In compound (15) the Dy<sup>III</sup> ion is also coordinated by two bidentate nitrate anions in the axial position. The key feature here is that the ligand is deprotonated at one of the hydrazone groups. This leads to a coordination number of nine.

In compound (16) the Dy<sup>III</sup> ion is coordinated by two bidentate acetate anions instead, at the axial positions resulting in a coordination number of nine.

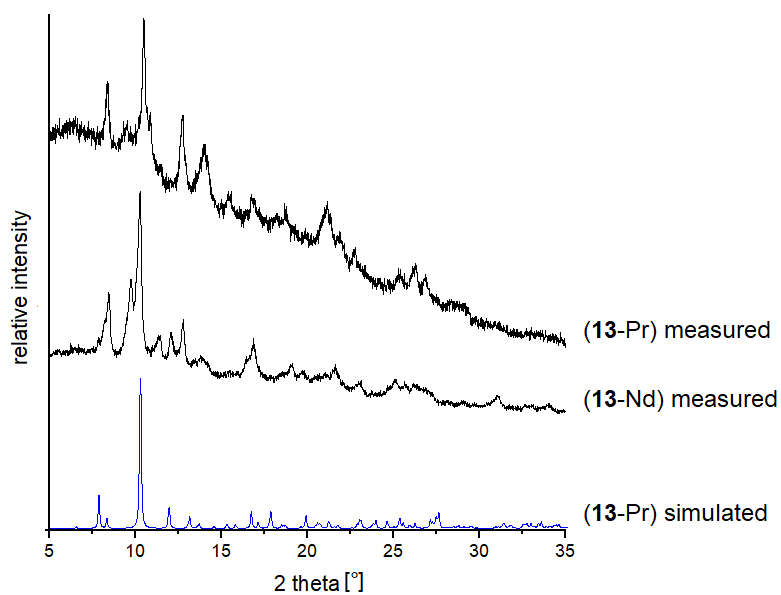


**Figure 103:** Powder patterns of  $[\text{Ln}(\text{HL7})(\text{NO}_3)_2\text{CH}_3\text{OH}]\text{NO}_3 \cdot 2\text{CH}_3\text{OH} \cdot \text{H}_2\text{O}$  ( $\text{Ln} = \text{Pr}$  and  $\text{Nd}$ ) versus the simulated pattern of **(13)**.

The measured powder pattern of **(13)** partially matches with its simulated pattern and the Nd-complex.

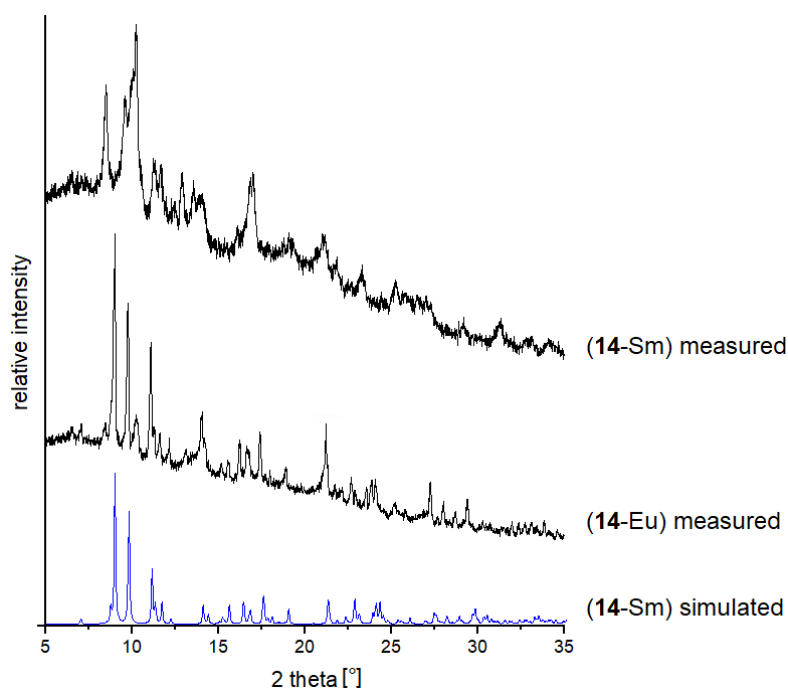


**Figure 104:** Powder patterns of  $[\text{Ln}(\text{HL7})(\text{NO}_3)_2\text{CH}_3\text{OH}]\text{NO}_3 \cdot \text{CH}_3\text{OH}$  ( $\text{Ln} = \text{Sm}$  and  $\text{Eu}$ ) versus the simulated pattern of **(14)**.

The measured powder pattern of **(14)** also partially matches with its simulated pattern and the Eu-complex. The crystal structure of Pr and Nd and of Sm and Eu agree. It seems like Nd and Sm form a mixture, where crystals of both structural types can be found.

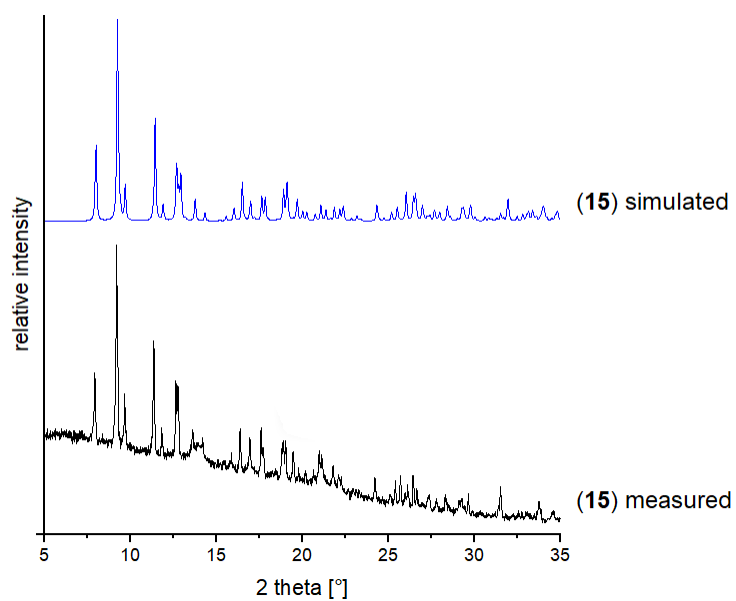


**Figure 105:** Measured powder pattern of (15) versus simulated pattern from single crystal data.

The measured powder pattern of (15) matches well with the simulated one.

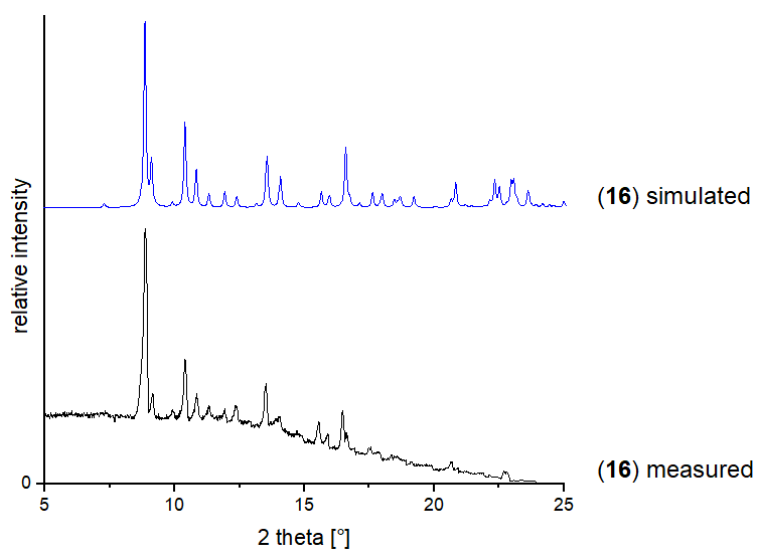


**Figure 106:** Measured powder pattern of (16) versus simulated pattern from single crystal data.

The measured powder pattern of (16) matches well with the simulated one.

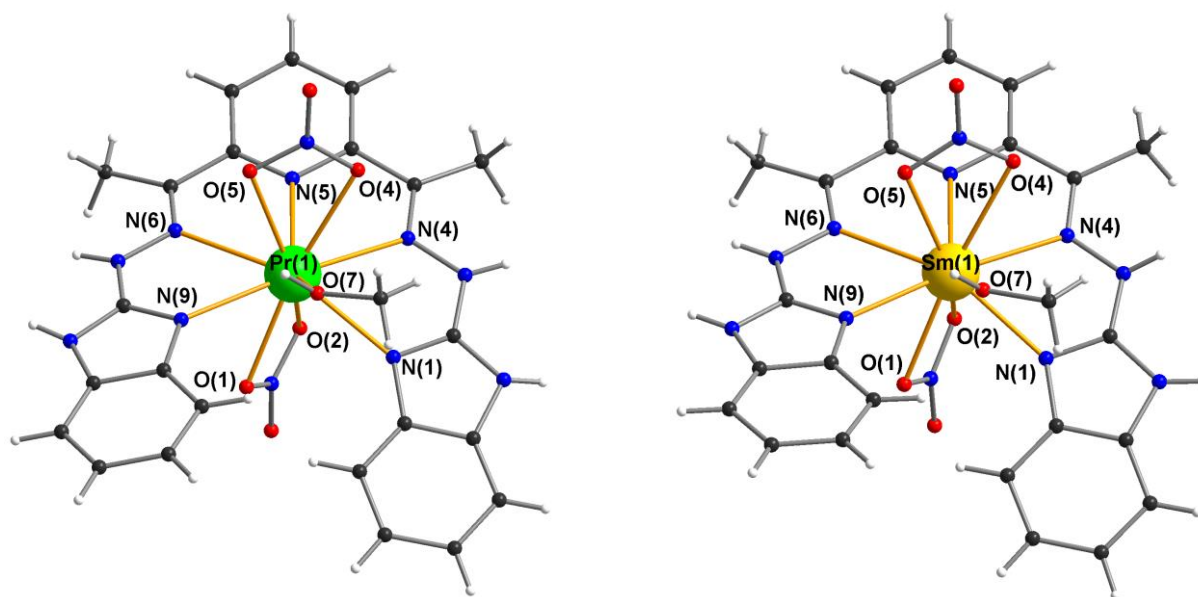


**Figure 107:** Structure of **(13)** (right) and **(14)** (left) with selected atoms labelled.

| Atom  | Atom | Distance [Å] |
|-------|------|--------------|
| Pr(1) | O(1) | 2.564(6)     |
| Pr(1) | O(2) | 2.572(6)     |
| Pr(1) | O(4) | 2.624(5)     |
| Pr(1) | O(5) | 2.544(5)     |
| Pr(1) | O(7) | 2.486(5)     |
| Pr(1) | N(1) | 2.574(6)     |
| Pr(1) | N(4) | 2.650(6)     |
| Pr(1) | N(5) | 2.638(6)     |
| Pr(1) | N(6) | 2.653(6)     |
| Pr(1) | N(9) | 2.637(6)     |

| Atom  | Atom | Distance [Å] |
|-------|------|--------------|
| Sm(1) | O(1) | 2.548(5)     |
| Sm(1) | O(2) | 2.524(5)     |
| Sm(1) | O(4) | 2.685(5)     |
| Sm(1) | O(5) | 2.478(5)     |
| Sm(1) | O(7) | 2.446(5)     |
| Sm(1) | N(1) | 2.506(6)     |
| Sm(1) | N(4) | 2.614(6)     |
| Sm(1) | N(5) | 2.569(6)     |
| Sm(1) | N(6) | 2.563(6)     |
| Sm(1) | N(9) | 2.549(5)     |

| Atoms           | Angle [°] |
|-----------------|-----------|
| N(1)-Pr(1)-N(4) | 61.3(2)   |
| N(4)-Pr(1)-N(5) | 60.26(18) |
| N(5)-Pr(1)-N(6) | 60.92(17) |
| N(6)-Pr(1)-N(9) | 62.15(18) |
| N(9)-Pr(1)-N(1) | 114.6(2)  |

| Atoms           | Angle [°]  |
|-----------------|------------|
| N(1)-Sm(1)-N(4) | 62.64(18)  |
| N(4)-Sm(1)-N(5) | 61.45(19)  |
| N(5)-Sm(1)-N(6) | 62.17(18)  |
| N(6)-Sm(1)-N(9) | 64.30(18)  |
| N(9)-Sm(1)-N(1) | 110.74(18) |

**Table 14:** Selected bond lengths and angles of compound **(13)** (right) and **(14)** (left).

All Ln-O and Ln-N bond lengths have typical values for ten coordinate Ln<sup>III</sup> ions. There are almost no differences in the bond length and angle values of compound **(13)** and **(14)**. The only noteworthy value is the 4° smaller N(9)-Ln(1)-N(1) angle for compound **(14)**. This is caused by the smaller ionic radius of Sm<sup>III</sup> compared to Pr<sup>III</sup>. The Sm<sup>III</sup> ion can slip further into the pentaaza pocket of the ligand.

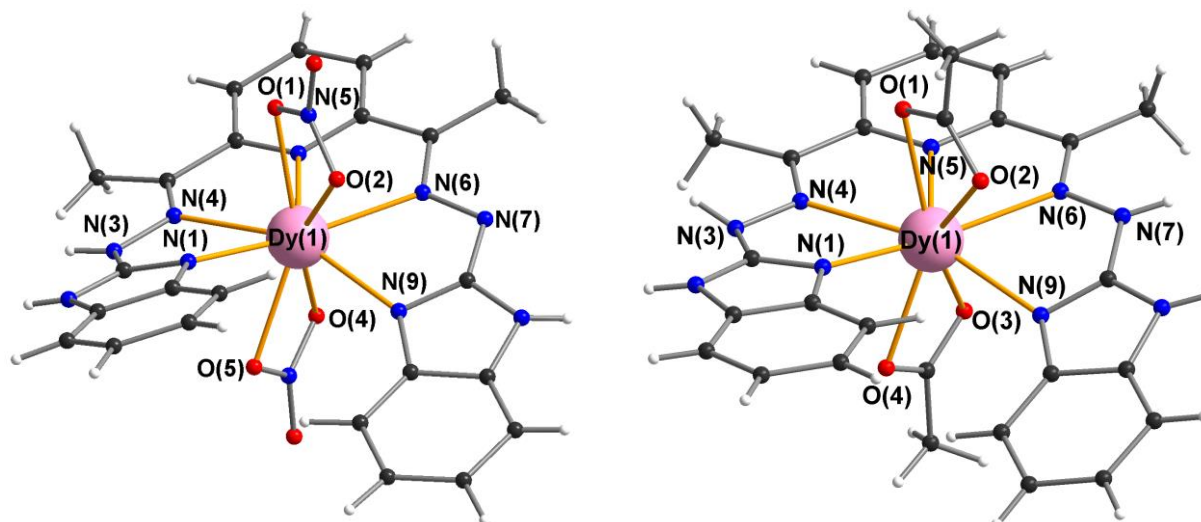


**Figure 108:** Structure of **(15)** (right) and **(16)** (left) with selected atoms labelled.

| Atom  | Atom | Distance [Å] |
|-------|------|--------------|
| Dy(1) | O(1) | 2.463(2)     |
| Dy(1) | O(2) | 2.445(2)     |
| Dy(1) | O(4) | 2.459(2)     |
| Dy(1) | O(5) | 2.469(3)     |
| Dy(1) | N(1) | 2.461(3)     |
| Dy(1) | N(4) | 2.492(3)     |
| Dy(1) | N(5) | 2.454(3)     |
| Dy(1) | N(6) | 2.465(3)     |
| Dy(1) | N(9) | 2.388(2)     |
| N(3)  | N(4) | 1.365(4)     |
| N(6)  | N(7) | 1.366(4)     |

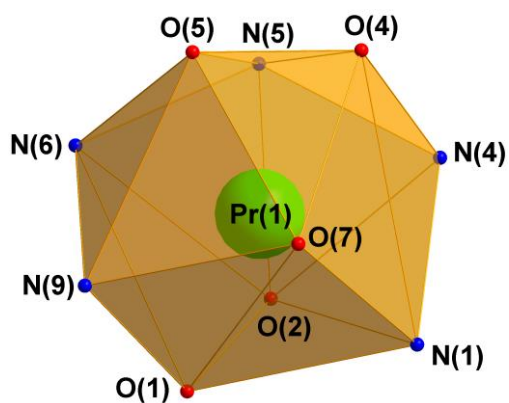
| Atom  | Atom | Distance [Å] |
|-------|------|--------------|
| Dy(1) | O(1) | 2.448(3)     |
| Dy(1) | O(2) | 2.446(3)     |
| Dy(1) | O(3) | 2.424(3)     |
| Dy(1) | O(4) | 2.415(3)     |
| Dy(1) | N(1) | 2.432(3)     |
| Dy(1) | N(4) | 2.504(3)     |
| Dy(1) | N(5) | 2.491(3)     |
| Dy(1) | N(6) | 2.487(3)     |
| Dy(1) | N(9) | 2.452(3)     |
| N(3)  | N(4) | 1.375(5)     |
| N(6)  | N(7) | 1.364(5)     |

| Atoms           | Angle [°] |
|-----------------|-----------|
| N(1)-Dy(1)-N(4) | 65.15(9)  |
| N(4)-Dy(1)-N(5) | 64.08(9)  |
| N(5)-Dy(1)-N(6) | 65.01(9)  |
| N(6)-Dy(1)-N(9) | 66.04(8)  |
| N(9)-Dy(1)-N(1) | 107.24(9) |

| Atoms           | Angle [°]  |
|-----------------|------------|
| N(1)-Dy(1)-N(4) | 64.91(11)  |
| N(4)-Dy(1)-N(5) | 64.00(11)  |
| N(5)-Dy(1)-N(6) | 64.09(11)  |
| N(6)-Dy(1)-N(9) | 65.71(11)  |
| N(9)-Dy(1)-N(1) | 105.95(12) |

**Table 15:** Selected bond lengths and angles of compound **(15)** (right) and **(16)** (left).

Again, all the Dy-O and Dy-N distances for **(15)** and **(16)** are as expected. What is perhaps surprising is that the deprotonated hydrazone group in compound **(15)** at N(7) seems to have no effect on the distances and angles. The N-N double bond lengths of both hydrazone groups are the same. The negative charge must be distributed evenly in the ligand's conjugated  $\pi$ -system with its five aromatic groups.



| Polyhedron             | Deviation [%] |
|------------------------|---------------|
| Sphenocorona           | 3.675         |
| Staggered Dodecahedron | 4.297         |
| Tetradecahedron        | 4.811         |

Figure 109: Ten-vertex polyhedron of (13) with SHAPE values.

| Polyhedron                | Deviation [%] |
|---------------------------|---------------|
| Sphenocorona              | 5.604         |
| Bicapped square antiprism | 7.536         |
| Staggered Dodecahedron    | 8.021         |

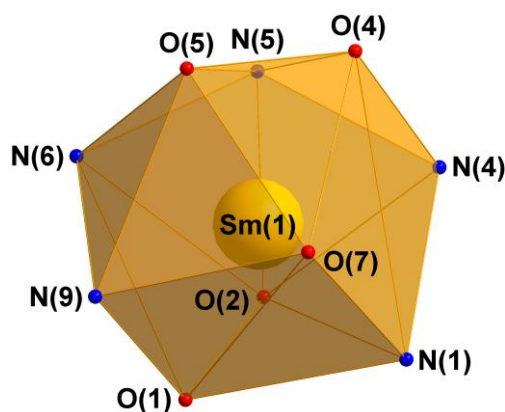
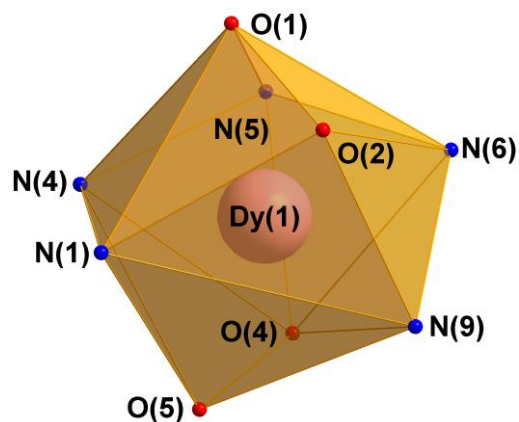


Figure 110: Ten-vertex polyhedron of (14) with SHAPE values.



| Polyhedron                         | Deviation [%] |
|------------------------------------|---------------|
| Muffin                             | 7.550         |
| Spherical tricapped trigonal prism | 7.805         |
| Spherical capped square antiprism  | 7.967         |

Figure 111: Nine-vertex polyhedron of (15) with SHAPE values.

| Polyhedron                         | Deviation [%] |
|------------------------------------|---------------|
| Spherical tricapped trigonal prism | 6.336         |
| Muffin                             | 6.788         |
| Spherical capped square antiprism  | 6.947         |

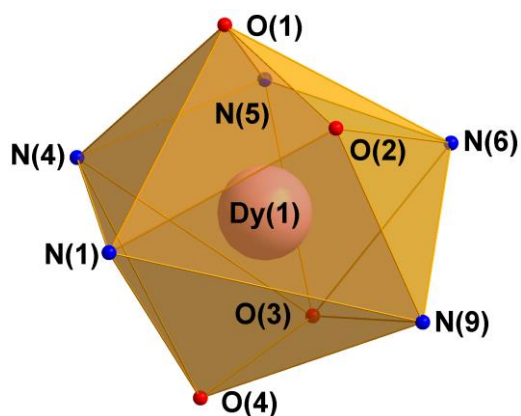
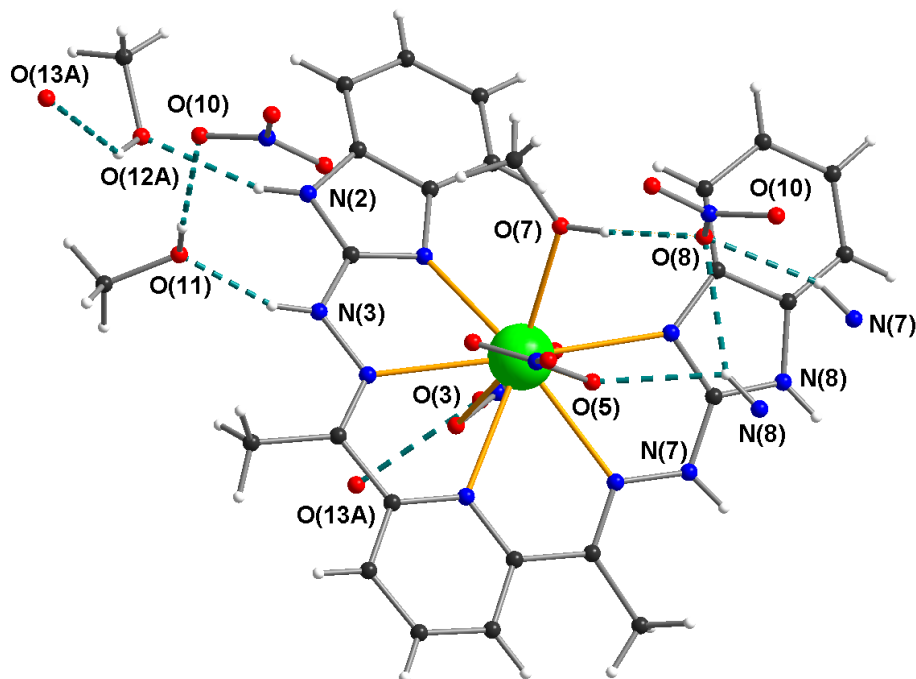


Figure 112: Nine-vertex polyhedron of (16) with SHAPE values.

The coordination environment of (**13**) can be described by a sphenocorona. The best fitting shape for (**14**) is also a sphenocorona but with a higher deviation than (**13**). This can possibly be explained by the smaller ionic radius of samarium compared to praseodymium, which results in shorter bond lengths. Neither compounds (**15**) nor (**16**) fit to one best-matching shape. Rather they fit several shapes with similar deviations.



**Figure 113:** Intermolecular interactions of (**13**). Hydrogen bonds are shown as green dashed lines. The hydrogen atoms of the lattice water O(13A) are disordered and cannot be displayed.

Compound (**13**) crystallises in the monoclinic space group  $P2_1/c$ . The unit cell has a total of four lattice water molecules, eight lattice methanol molecules and four nitrate counter ions. There are four complex molecules per unit cell connected by hydrogen bonds (see Figure 113). The nitrate counter ion bonds with O(8) to the hydrogens of the coordinating methanol, the hydrazone group N(7) and the imidazole group N(8). With O(10) it bonds to the lattice methanol containing O(11). This methanol molecule is also connected to the hydrazone group N(3). The other lattice methanol forms hydrogen bonds to the other imidazole group N(2) and the lattice water containing O(13A). That lattice water connects to O(3) on one coordinating nitrate. The imidazole group containing N(8) forms a second hydrogen bond to O(5) on the chelating nitrate, while the other imidazole group N(2) only forms one hydrogen bond to the lattice methanol O(12A).

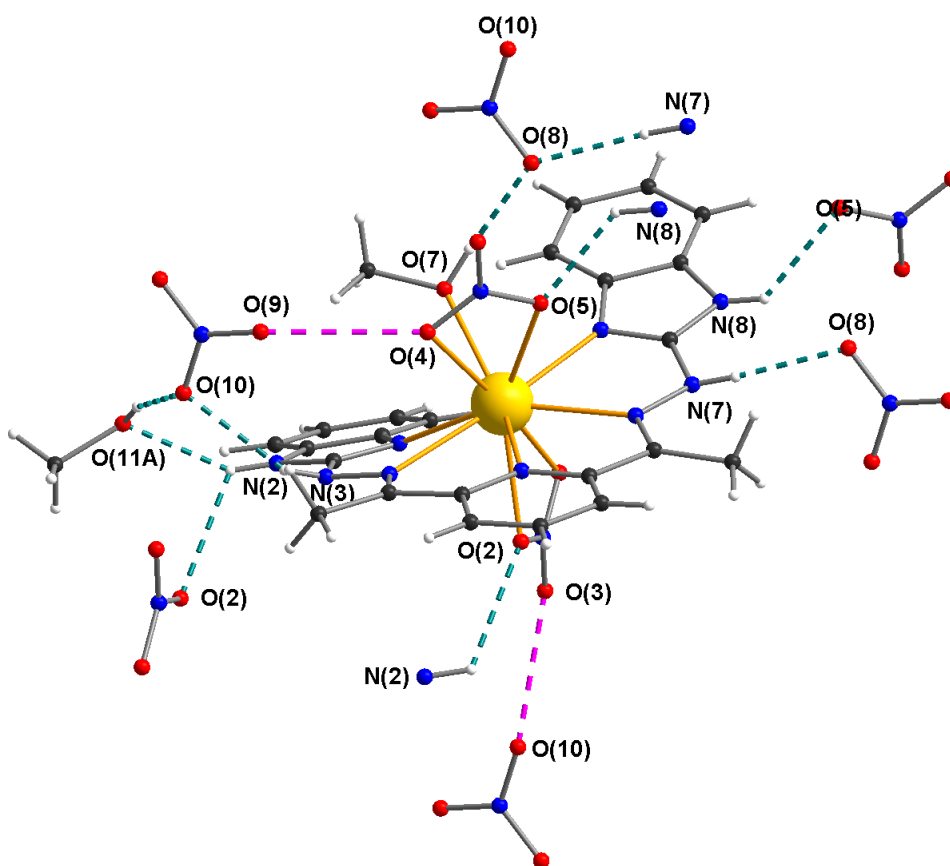


**Figure 114:** Intermolecular interactions of (14). Hydrogen bonds are shown as green dashed lines. The nitrate-nitrate interactions are displayed as a pink dashed lines.

Compound (14) crystallises in the triclinic space group  $\bar{P}1$ . There is a total of two lattice methanol molecules, two nitrate counter ions and two complex molecules per unit cell. Hydrogen bonds are formed between the complex and counter-ions/lattice solvents (see Figure 114). The nitrate counter ion bonds with O(8) to the hydrogens of the coordinating methanol and the hydrazone group N(7). This nitrate seems to form bonds to other nitrates via O-O interactions. With O(10) it bonds to O(3) of the first chelating nitrate and with O(9) to O(4) of the second chelating nitrate. O(10) also has a hydrogen bond to the lattice methanol containing O(11A) and to the hydrazone group containing N(2). The coordinating nitrates bonds with O(5) to the imidazole group of N(8). The other imidazole group bonds to the lattice methanol and the other chelating nitrate at O(2). The O(4)-O(9) distance is 2.994 Å and the O(3)-O(10) distance is 2.849 Å.

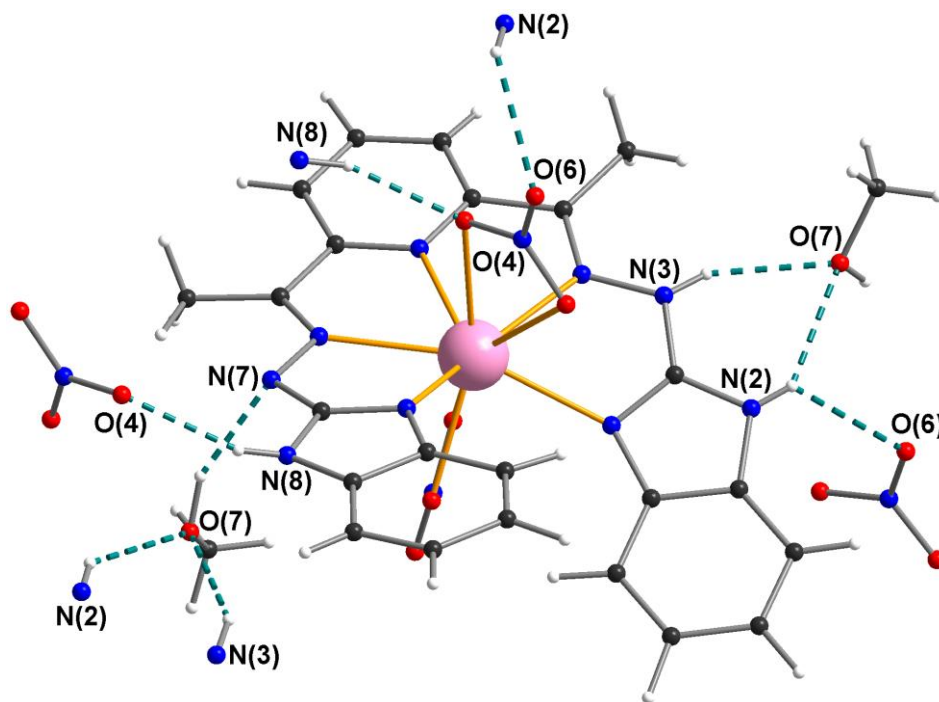


**Figure 115:** Intermolecular interactions of (15). Hydrogen bonds are shown as green dashed lines.

Compound (15) crystallises in the monoclinic space group  $P2_1/c$ . There is a total of four lattice methanol molecules and four complex molecules per unit cell forming hydrogen bonds (see Figure 115). The lattice methanol forms hydrogen bonds from its oxygen O(7) to the hydrazone group N(3) and the imidazole group N(2), while the hydrogen bonds to the deprotonated hydrazone nitrogen N(7). This fact shows that the ligand is always deprotonated on this side in crystalline form and there is no squeezing. One chelating nitrate bonds with O(6) to one imidazole group N(2) and with O(4) to the other imidazole group N(8) of a neighbouring molecule. Surprisingly, the other coordinating nitrate does not form hydrogen bonds.

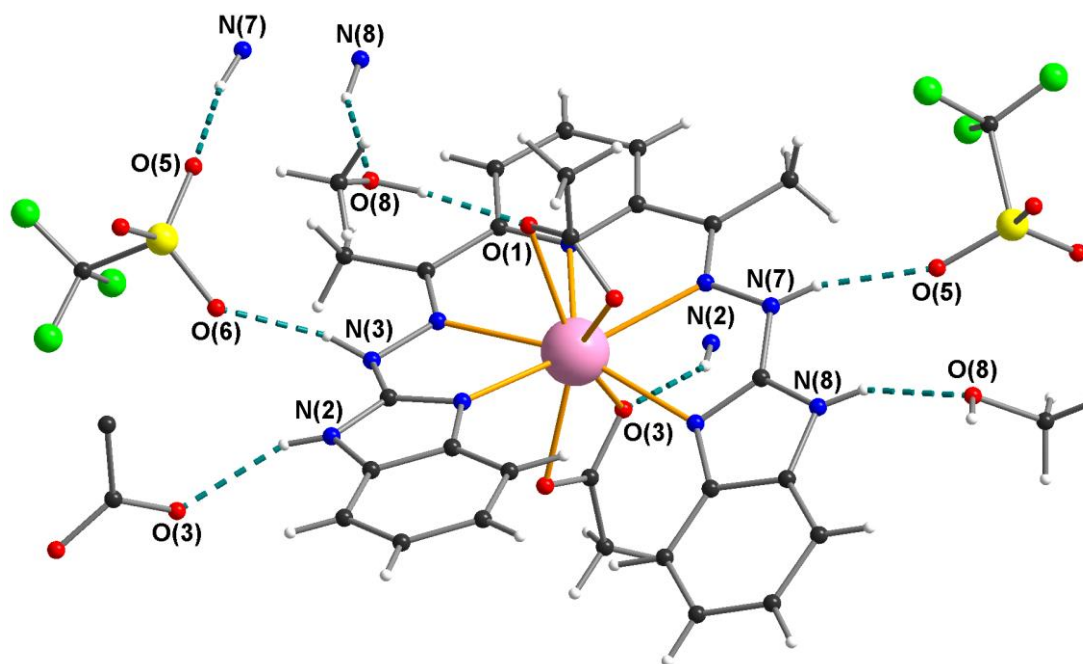


**Figure 116:** Intermolecular interactions of (16). Hydrogen bonds are shown as green dashed lines.

Compound (16) crystallises in the orthorhombic space group  $P2_12_12_1$ . There is a total of four lattice methanol molecules, four triflate counter ions and four complex molecules per unit cell forming hydrogen bonds (see Figure 116). The lattice methanol forms hydrogen bonds from its oxygen O(8) to the imidazole group N(8), while its hydrogen bonds to the oxygen O(1) of the chelating acetate. The other coordinating acetate bonds to the other imidazole group N(2). Both hydrazone groups N(3) and N(7), form hydrogen bonds to the oxygen atoms O(6) and O(5) of the triflate. Interestingly, the three chlorine atoms of the triflate counter ions do not seem to interact with any functional group.

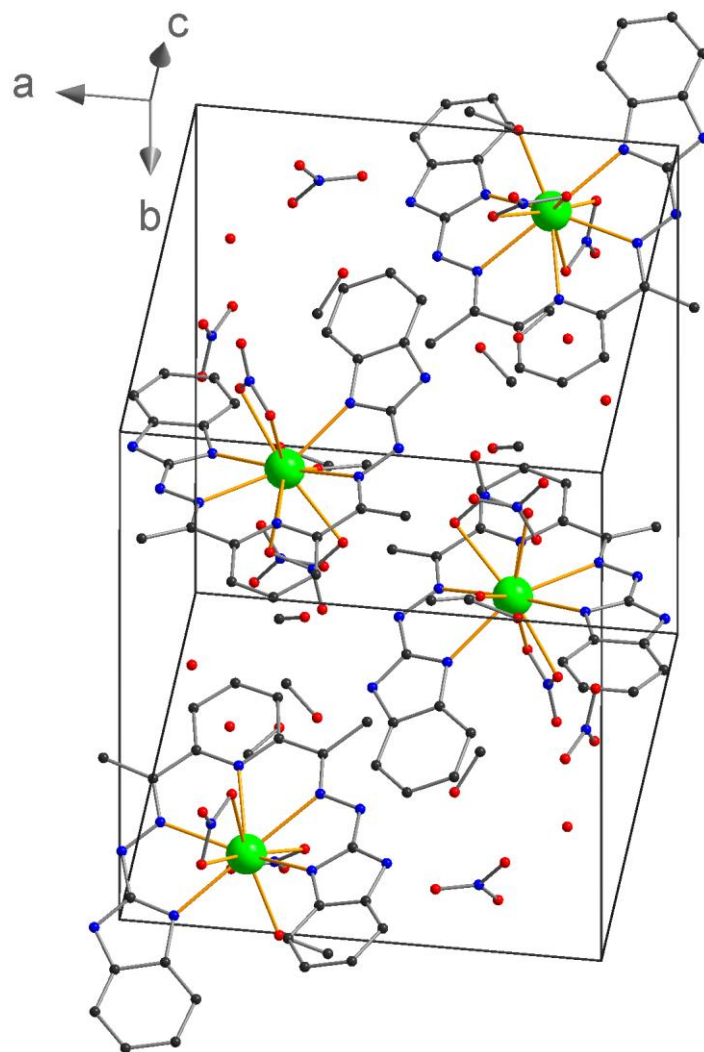


**Figure 117:** Unit cell packing of compound (13). For clarity hydrogen atoms are not displayed.

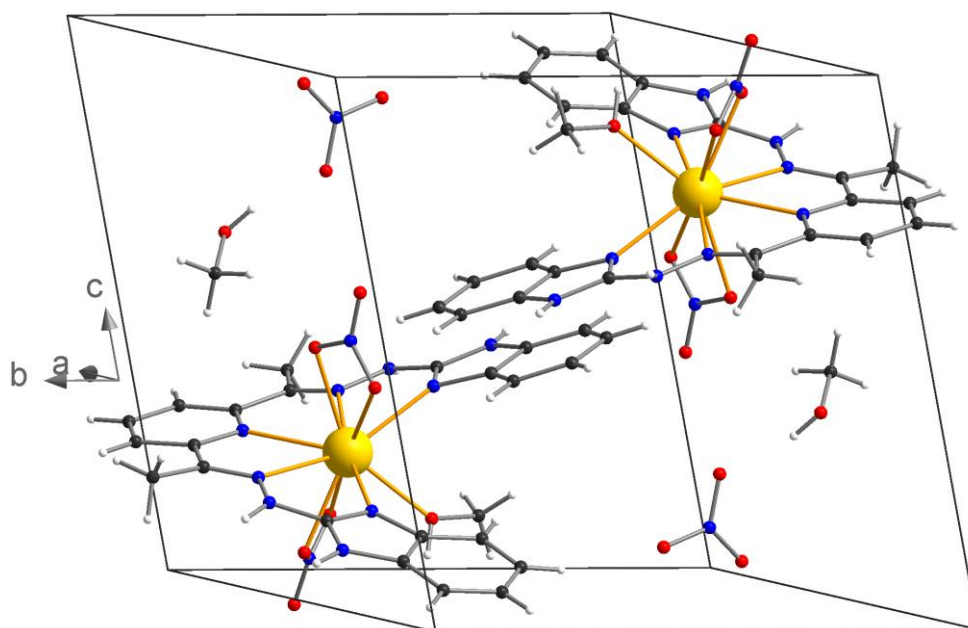


**Figure 118:** Unit cell packing of compound (14).

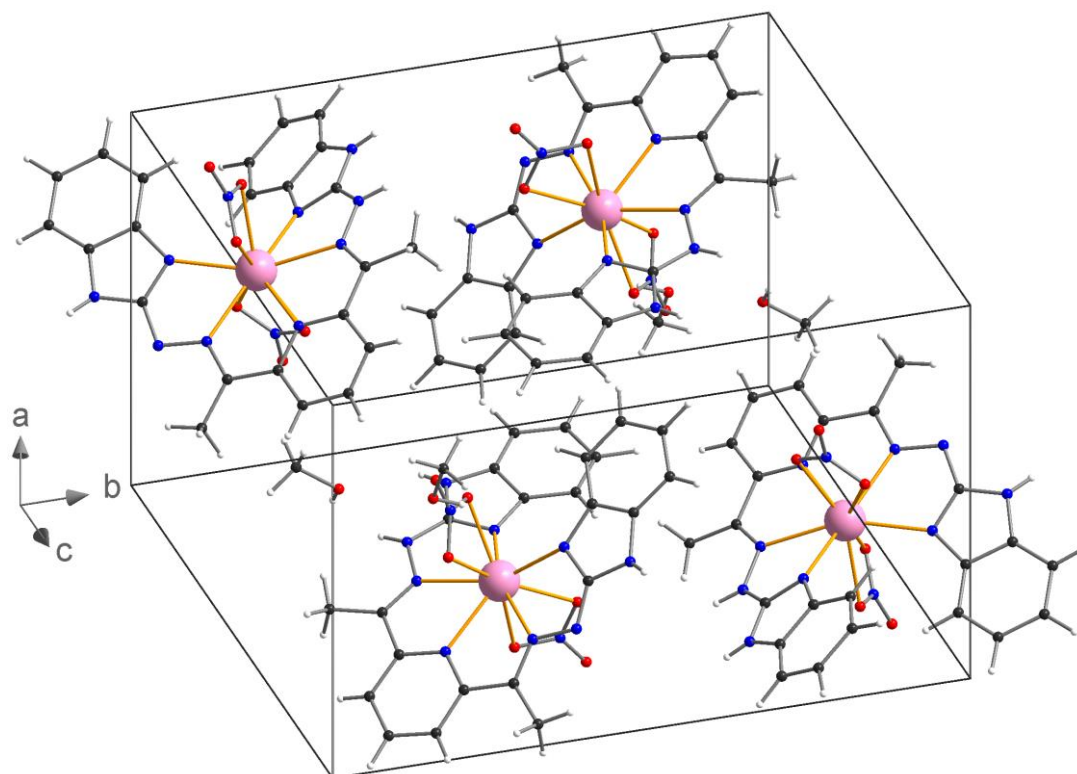


**Figure 119:** Unit cell packing of compound (15).

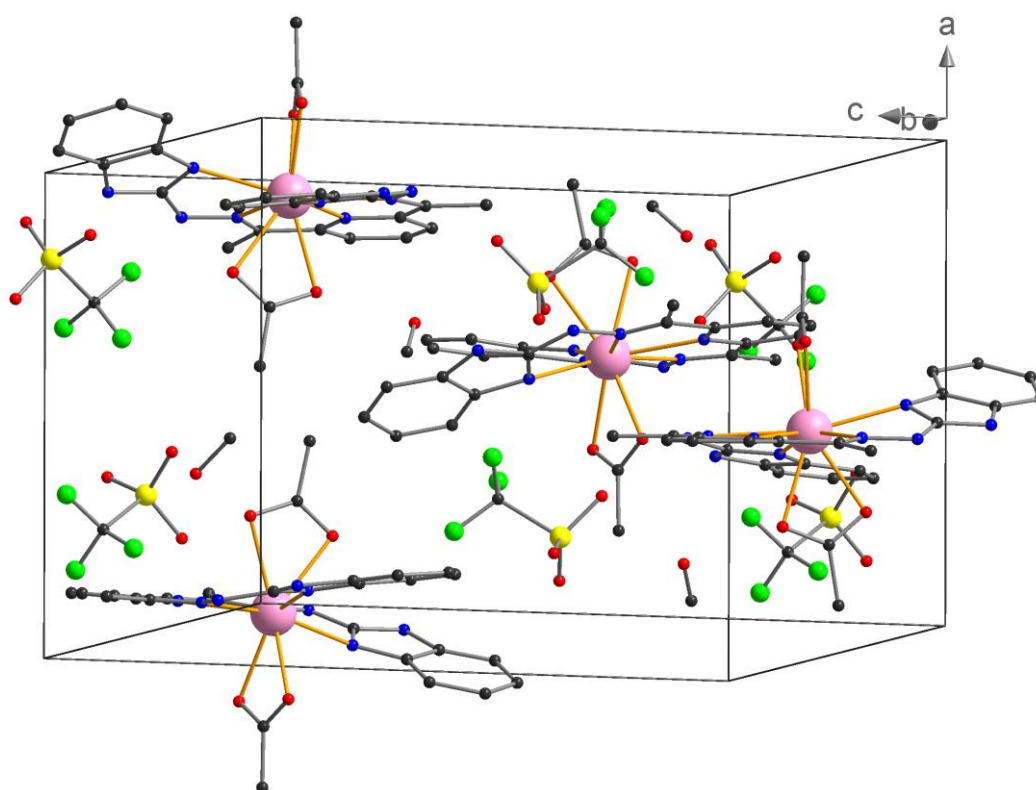


**Figure 120:** Unit cell packing of compound (16). For clarity hydrogen atoms are not displayed.

#### 4.2.2.1 Optical properties of complexes obtained from HL7

The lanthanide complexes obtained from HL7 all show an intense red colour in solution. The ligand itself has a beige colour, the lanthanide nitrates are pale green (Pr), violet (Nd) or pink (Ho and Er), while the others are white. The red colour must appear because a complex formed that absorbs light of a certain wavelength in the visible range. Adding base intensifies the colour to a dark red tone, adding acid causes the solution to turn yellow (see Figure 121).

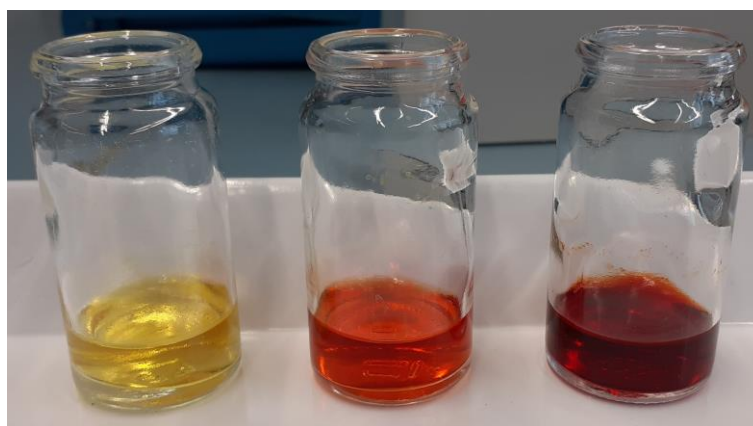


**Figure 121:** Combining  $\text{Eu}(\text{NO}_3)_3 \cdot 5\text{H}_2\text{O}$  and HL7 in methanol yields an isostructural complex to **(14)**. Additionally, in the left vial one drop of acetic acid was added, in the right vial one drop of triethylamine was added.

Absorption measurements on the ligand HL7 and on combinations of the ligand with lanthanide nitrates were performed. Methanol was the solvent of choice since it can dissolve the ligand and the lanthanide nitrate salts. The aim of these measurements was to gain a better understanding regarding the different colours under neutral conditions (see Figure 122).

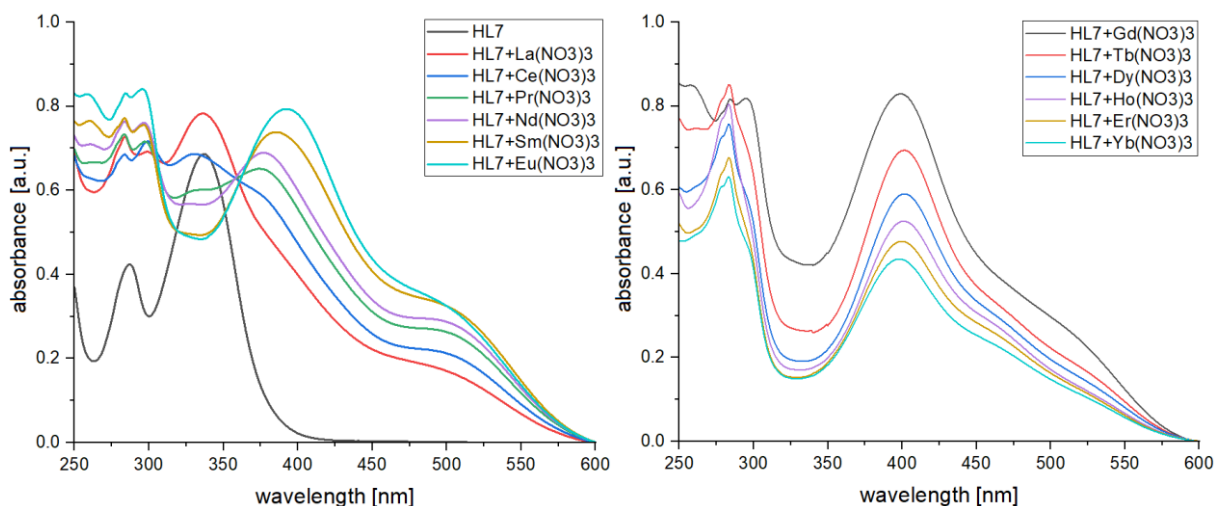
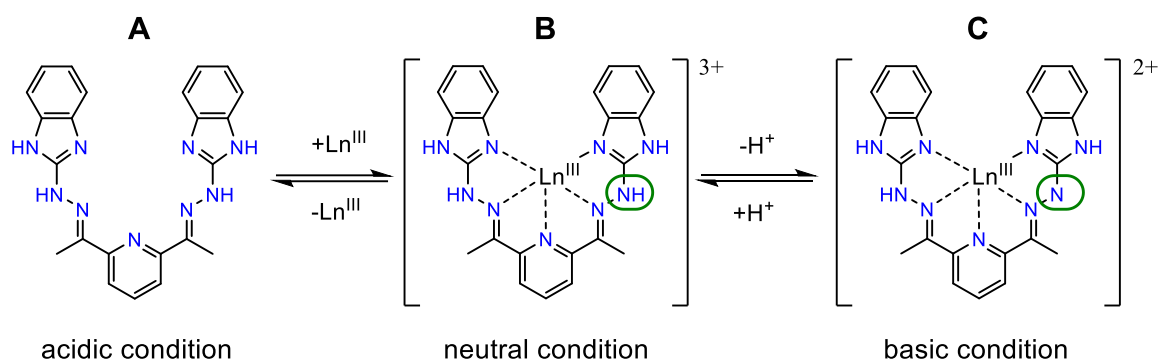


**Figure 122:** Absorption spectra of HL7 isolated and as complex with  $\text{Ln}(\text{NO}_3)_3 \cdot x\text{H}_2\text{O}$  (La-Er and Yb) in methanol with a concentration  $c = 66.7 \mu\text{mol/L}$ .

The isolated ligand has an absorption band at around 340 nm. This is in the range of blue light explaining the yellow colour of the ligand in solution. A similar band, but with lower absorption can be observed for the lanthanum and cerium complex but indicates that the concentration of this species is going down within the series. It seems the larger lanthanides do not form as much of the coordination compound as the smaller lanthanides. From praseodymium new absorption maxima appear at 375 nm. They shift to higher wavelengths along the series. The maximum for europium is at 395 nm. The Ln-HL7 complexes absorb in the blue and green range and tail into in the yellow range which make them appear reddish. It shows, that each lanthanide complex has a different absorption maximum for a given concentration. It can be seen that there are multiple overlapping absorption bands forming a characteristic pattern.

Given that the absorption band of the isolated ligand is around 340 nm and that complex can become deprotonated at its hydrazone group (see compound (15)) measurements with acetic acid and triethylamine were performed. The extensive conjugated  $\pi$ -system of the ligand means it is very easy to distribute one negative charge. Since the solvent is not water it is difficult to relate these observations to a pH-value. Nevertheless, the methanol has not been dried and lanthanide nitrates contain crystal water there must be some amount of water in solution for the formation of  $\text{H}_3\text{O}^+$  and  $\text{OH}^-$ .



**Scheme 12:** Behaviour of the HL7-complex system at different conditions in solution. Isolated species (A), protonated species (B) and deprotonated species (C).

The colour change in solution caused by adding base indicates that the complex system is gradually being deprotonated in solution. There is an equilibrium of at least three different species in solution. These are the free protonated ligand A, the protonated complex B and the deprotonated complex C (see Scheme 12).

A measurement series of  $\text{Eu}(\text{NO}_3)_3 \cdot 5\text{H}_2\text{O}$  combined with HL7 was performed. The formed complex is isostructural to (14). To begin with the concentration of acetic acid in solution was set to 20 mmol/L. Then after each measurement concentration of triethylamine was increased by 20 mmol/L. The concentration of the complex was kept constant.

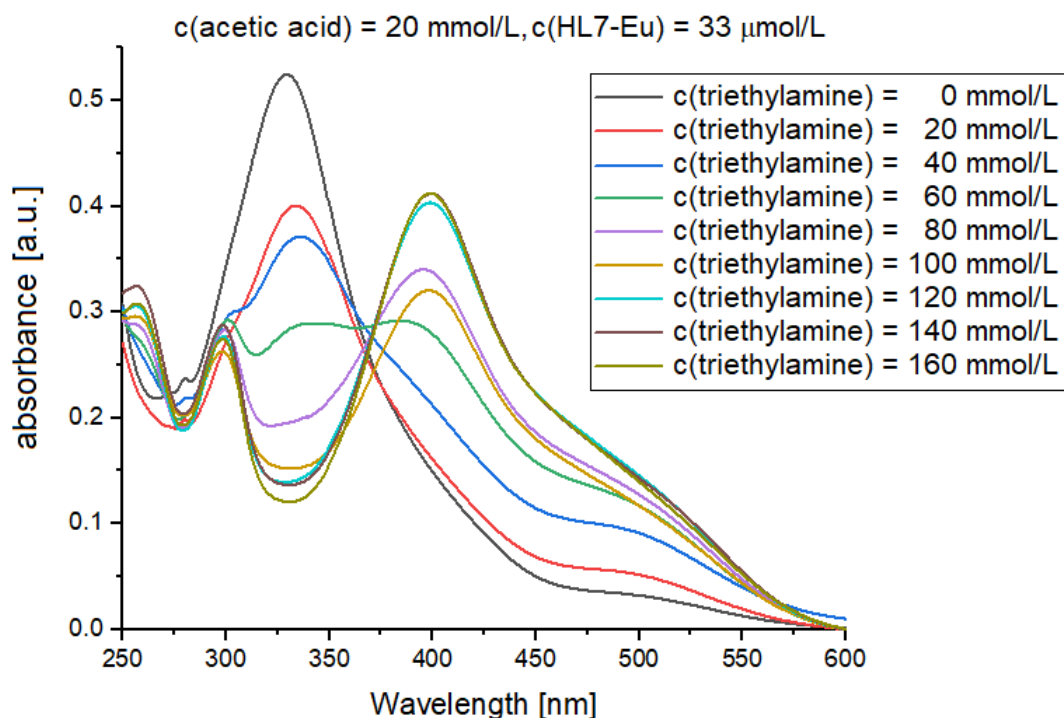
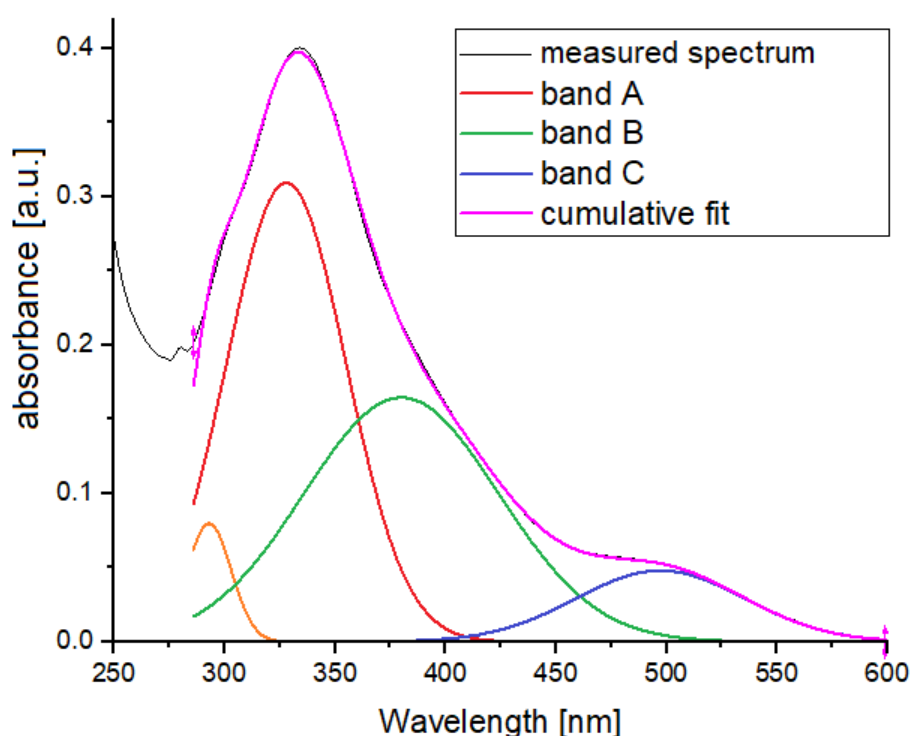


**Figure 123:** Absorption spectra of HL7 isolated and as complex with  $\text{Eu}(\text{NO}_3)_3 \cdot 5\text{H}_2\text{O}$  in methanol at a concentration of  $c = 33 \mu\text{mol/L}$ . Acetic acid was added in the beginning, then triethylamine subsequently.

The absorption band of the ligand at 337 nm decreases as more base is added. Two further bands appear at ca. 400 nm and at ca. 500 nm and these increase with increasing amount of base added. A fourth band at 298 nm does not seem to change. The bands at 337 nm (band A), ~400 nm (band B) and ~500 nm (band C) are of most interest. A single absorption band always has a Gaussian profile. Therefore, the absorption spectra should consist of multiple individual Gaussians. These should add up to the resulting observed spectrum. Fitting with Gaussian functions for all nine absorption spectra (0-8 times base concentration increased, see Figure 123) were performed to identify these bands (see Figure 124 for an example calculation).



| Modell           | Gauss  |                  |                  |                   |
|------------------|--|------------------|------------------|-------------------|
| Gleichung        | $y=y_0 + (A/(w*\sqrt{\pi/2}))*\exp(-2*((x-xc)/w)^2)$ |                  |                  |                   |
| Zeichnen         | Peak1(C)   | Peak2(C)         | Peak3(C)         | Peak4(C)          |
| y0               | 0 ± 0  | 0 ± 0            | 0 ± 0            | 0 ± 0             |
| xc               | 293 ± 0  | 327,9237 ± 0,117 | 380 ± 0,117      | 497,29527 ± 1,227 |
| w                | 20 ± 0   | 54,14706 ± 0,170 | 88,25063 ± 1,370 | 76,63609 ± 1,7969 |
| A                | 2 ± 0  | 21,00665 ± 0,127 | 18,20354 ± 0,267 | 4,60868 ± 0,14589 |
| Chi-Quadr Reduzi | 8,87513E-6   |                  |                  |                   |
| R-Quadrat (COD)  | 0,99946  |                  |                  |                   |
| Kor. R-Quadrat   | 0,99945  |                  |                  |                   |

**Figure 124:** Gaussian fit of the absorption pattern with four functions. As example the spectrum of  $\text{Eu}(\text{NO}_3)_3 \cdot 5\text{H}_2\text{O}$  in methanol at a concentration of  $c = 33 \mu\text{mol/L}$  and acetic acid and triethylamine at  $c = 20 \text{ mmol/L}$  is displayed.

From the results of the fitting for all nine lanthanides studied it can be seen that the position of the bands does not change, however the intensity does. The accuracy of the fits with  $R^2 > 0.999$  is given.

Next step is to investigate the equilibrium of the different species in solution. This can be quantified from the area underneath each Gaussian which in turn can be plotted the concentration of base added. The area of an absorption band should roughly be proportional to the concentration of its species. The areas of band A, B and C were plotted against the amount of base added (see Figure 125).

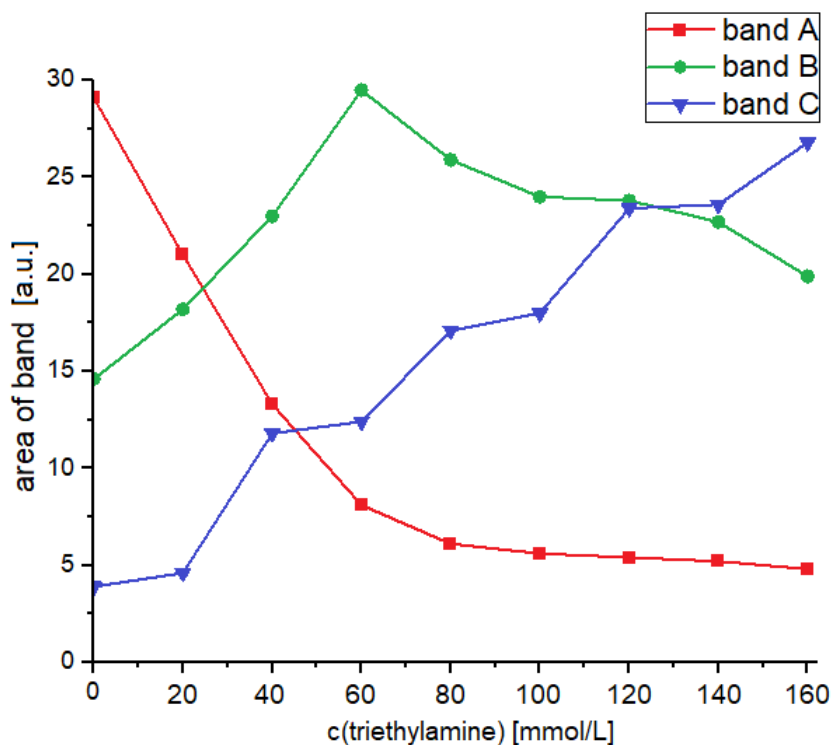


**Figure 125:** Plot of the areas of the bands versus the concentration of triethylamine in solution.

Band A decreases and band C increases with the amount of base added. Band B rises at first and later falls off again. Now every species in the equilibrium can be matched with a band. Band A is the isolated ligand, Band B is the protonated complex and C is the deprotonated ligand. Scheme 12 describes the equilibrium as expected.

In the next step concentration dependent measurements for each lanthanide were performed. No acid or base was added. It would to be expected that the absorption bands increase along the Y-direction, however this is not the case here. The Nd- and Eu-complexes were shown as examples (see Figure 126 and 127).

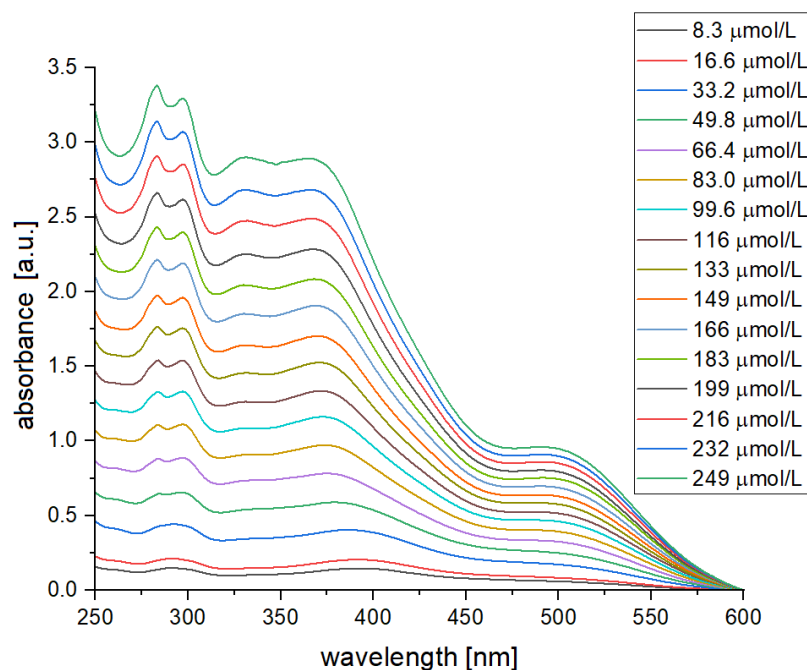


**Figure 126:** Absorption spectra of  $\text{Nd}(\text{NO}_3)_3\text{-HL7}$  complex in methanol at different concentrations.

For example, at low concentrations the Nd-complex has an absorption maximum at 393 nm and at the highest concentration the maximum is at 365 nm.

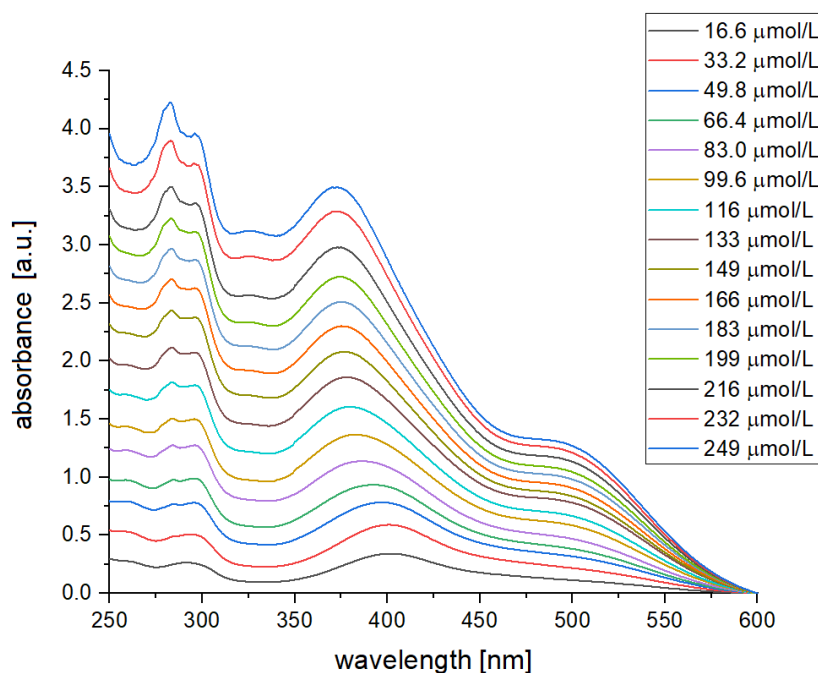


**Figure 127:** Absorption spectra of  $\text{Eu}(\text{NO}_3)_3\text{-HL7}$  complex in methanol at different concentrations.

Similarly, the Eu-complex has a maximum that shifts from 402 to 373 nm. All the other lanthanide complexes show a similar shift in their pattern, each with slightly different values. This pattern is caused by the overlapping absorption bands A, B and C.

It was to be expected that at increasing concentration the absorption of the bands should increase proportional. No acid or base was added this time. Instead the proportion of the bands seem to have changed.

Since the centres of the bands are known, fits were again performed to model the isolated bands. This was done for all lanthanides, for low concentrations the fits are imprecise due to the absorption spectra being flat.

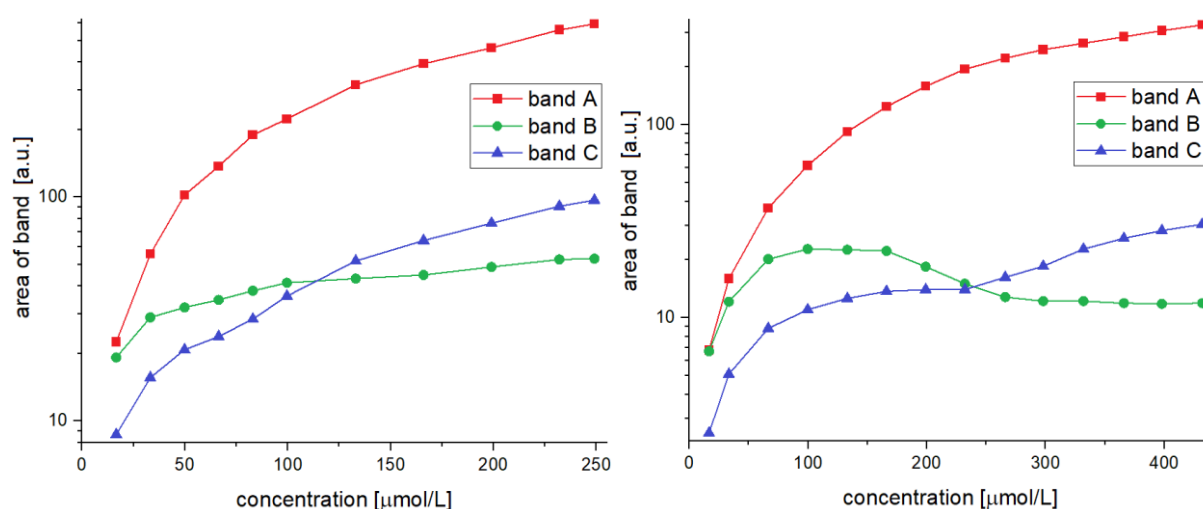


**Figure 128:** Areas of absorption bands of the  $\text{Eu}(\text{NO}_3)_3\text{-HL7}$  (left) and  $\text{Dy}(\text{NO}_3)_3\text{-HL7}$  complex (right) in methanol plotted logarithmic versus concentration.

For the larger lanthanides there is a trend that the amount of the protonated species (band B) increases slowly with increasing concentration, while the deprotonated species (band C) increases faster. For the smaller lanthanides the trend is that the protonated species first forms a maximum, than decreases slowly while the deprotonated species increases constantly. In a non-basic environment, the proportion of the free ligand (band A) is far higher than for the other two species (see Figure 128).

There seems to be an interaction between the complex molecules in solution which causes a shift in the equilibrium. With increasing concentration of the molecules in solution these intermolecular interactions also increase. As a result, the percentage of the deprotonated species (band A) increases more with higher concentration than the protonated species.

A closer inspection of the absorption spectra show that each lanthanide produces its characteristic pattern. One can connect the local maximum for different concentrations starting at around 400 nm and ending at around 360 nm. These curves were plotted for Nd to Lu (see Figure 129).

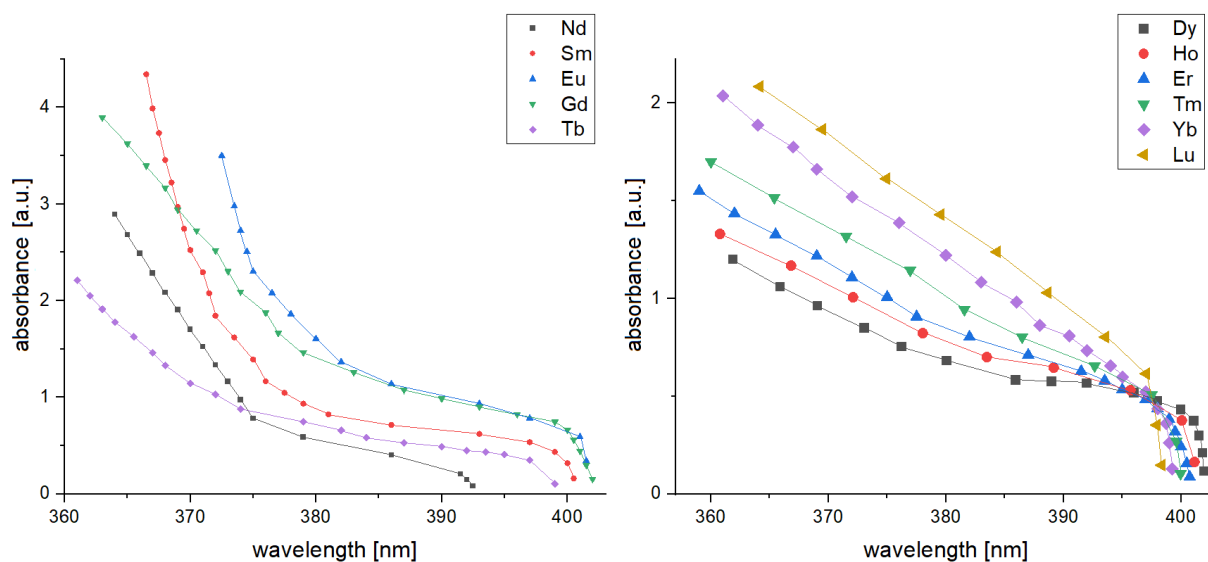


**Figure 129:** Absorption maxima at different concentrations for selected  $\text{Ln}(\text{NO}_3)_3\text{-HL7}$  complexes in methanol.

A characteristic curve results for each lanthanide. Nd to Tb show an S-shaped curve, Dy to Lu show an L-shaped curve. Like a fingerprint, one can identify most lanthanides using HL7 as ligand and measure the absorption in solution.

For comparison to the 4f elements the 3d metal  $\text{Fe}^{\text{III}}$  were also measured in combination with HL7. However, this sample resulted in a yellow solution (see Figure 130).

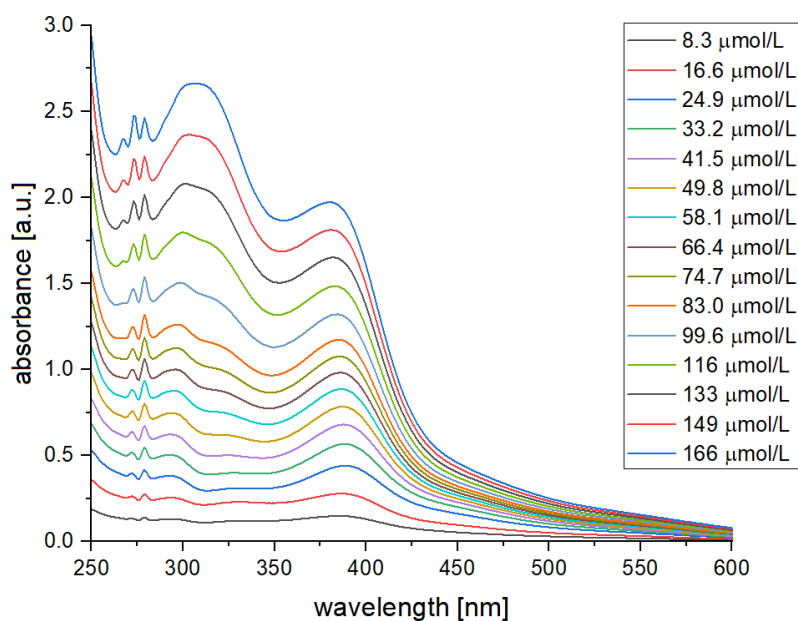


**Figure 130:** Absorption spectra of  $\text{Fe}(\text{NO}_3)_3$ -HL7 complex in methanol at different concentrations.

If one replaces the lanthanide ion with a 3d metal, like  $\text{Fe}^{\text{III}}$ , a completely different pattern can be observed. It is a combination of the absorption band of free  $\text{Fe}^{\text{III}}$  ions and the isolated ligand.<sup>[54]</sup> The ionic radius of 3d metals is simply too small to coordinate to all nitrogen atoms of the pentaaza pocket of the ligand.

Excitation emission spectroscopy measurements were performed on the Ln<sup>III</sup>-HL7 complexes and on the isolated HL7 ligand in methanol.

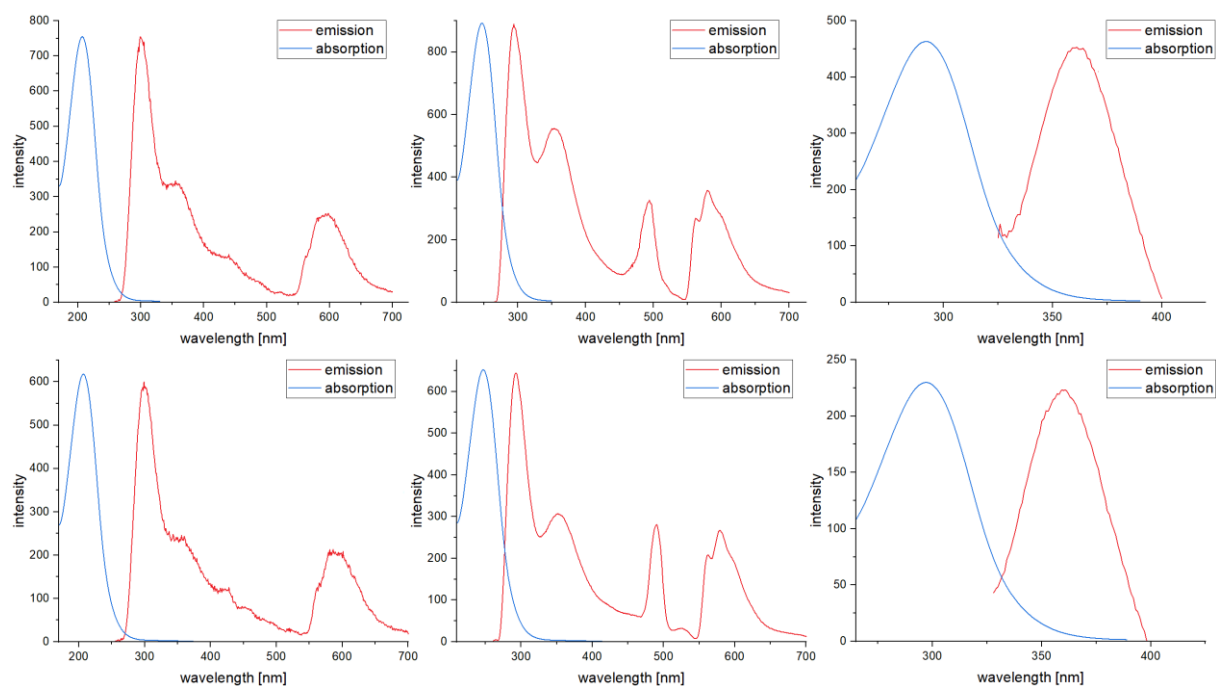


**Figure 131:** Absorption and emission spectra of the Nd-HL7-complex (top) and the ligand HL7 (bottom) in methanol. The samples were excited at 209 nm (left), 244 nm (middle) and 286 nm (right).

As can be seen in Figure 131, the spectra of the Nd-complex and the ligand alone are almost identical. From this it can be concluded that it is the ligand that absorbs and emits the photons, and not the metal ion.

In addition, it was found that the ligand only emits light when excited in the ultraviolet range. If the ligand is irradiated in the wavelength of the absorption maxima of band A, B and C, no emission is detected.

## 5 CONCLUSIONS

### 5.1 Dinuclear coordination compounds

In this thesis different two-pocket ligand systems were designed leading to a range of dinuclear lanthanide complexes. The ligands are Schiff-bases which have varied substituents allowing for changes in physical and structural properties. Their structures and magnetic properties were studied. The changes in the ligand system were intentionally kept small to make it easier to understand differences in structure and magnetism and if possible draw conclusions in terms of magneto-structural correlations. Due to their two pockets, the ligands used generally form dinuclear coordination compounds, which often consist of two molecules of the ligand and two lanthanide ions. In the absence of acetate in the system, both pockets can accommodate Ln<sup>III</sup> ions. In the presence of acetate *syn-anti* bridges form between the Ln<sup>III</sup> ions, without using the second pocket. These compounds often crystallize with an inversion centre relating the two metal ions.

In addition to the X-ray crystallographic analysis, investigations on the coordination spheres of the metal centres were carried out for all ten dinuclear compounds described in this thesis. For this purpose, continuous shape measures (CShM) using SHAPE were carried out. The SHAPE-analyses take into account the spatial orientation of all coordinating atoms. The results show that the coordination spheres not conform to regular polyhedral shapes. For example, it is not clear whether [Dy<sub>2</sub>(L2)<sub>2</sub>(CH<sub>3</sub>COO)<sub>4</sub>(CH<sub>3</sub>OH)<sub>2</sub>] (**6**), [Dy<sub>2</sub>(L3)<sub>2</sub>(CH<sub>3</sub>COO)<sub>4</sub>(H<sub>2</sub>O)<sub>2</sub>] (**7**) and [Dy<sub>2</sub>(L5)<sub>4</sub>(μ-H<sub>2</sub>O)]Cl<sub>2</sub> (**10**) are 8- or 9-coordinate, since it is difficult to define a maximum bond distance. Also, by comparing [Dy<sub>2</sub>(L1)<sub>2</sub>(NO<sub>3</sub>)<sub>4</sub>] (**1**) and [Nd<sub>2</sub>(L1)<sub>2</sub>(NO<sub>3</sub>)<sub>4</sub>CH<sub>3</sub>OH] (**2**), the effect of the ionic radius of the lanthanide on the structure was shown. A larger ionic radius leads to better fittings for SHAPE analyses and a higher coordination number.

Measurements of the magnetic properties were made on five selected dinuclear dysprosium complexes. The low temperature data shows that all five compounds have a weak antiferromagnetic coupling. [Dy<sub>2</sub>(L2)<sub>2</sub>(NO<sub>3</sub>)<sub>4</sub>] (**5**) shows no SMM behaviour, but the structurally similar compound (**1**) shows SMM properties. The isostructural cationic [Dy<sub>2</sub>(L1)<sub>2</sub>(H<sub>2</sub>O)<sub>6</sub>]Cl<sub>4</sub> (**3**) and [Dy<sub>2</sub>(L1)<sub>2</sub>(H<sub>2</sub>O)<sub>6</sub>]Br<sub>4</sub> (**4**) exhibit energy barriers that can be overcome by quantum tunnelling and Raman processes. The non-acetate bridged

[Dy<sub>2</sub>(Ligand)<sub>2</sub>] systems do not show any significant SMM behaviour. Compound **(6)** shows the best SMM properties, probably because the negative oxygen atoms of the phenoxy groups have aligned the anisotropy axes.

*Ab-initio* calculations were also carried out on the five mentioned compounds in order to get a better understanding of their electronic structure, zero-field splitting and anisotropy. The resulting zero-field splitting of the energies of the eight lowest Kramer doublets agrees with the results of the magnetic measurements. They correlate with the quality of the magnetic behaviour of the given SMMs. MAGELLAN calculations which only consider the electrostatic field were carried out for comparison with the anisotropy axes from the *ab-initio* calculations. This comparison helps to identify which molecular features lead to reliable results for MAGELLAN calculations. It was found that for compounds **(1)**, **(5)** and **(6)** both methods gave similarly orientated axes. For compound **(3)** and **(4)** there is a discrepancy between both methods because coordinating water molecules interfere with MAGELLAN calculations.

Future work on this ligand system will include investigations with new counter ions and co-ligands as well as other bridging ligands. Differently substituted ligands along with further magnetic measurements are planned for these systems.

## 5.2 Mononuclear coordination compounds

In this thesis different ligand systems with a large pocket were designed to study the structure and optical properties of mononuclear lanthanide complexes. The changes in the ligand system were intentionally kept small. This makes it easier to understand differences in structure and in optical properties and possibly draws conclusions regarding different species in solution.

In addition to powder and single-crystal X-ray crystallographic analyses, SHAPE analyses were performed to identify the best fitting shape for the polyhedra for all six mononuclear compounds presented in this thesis. As noted for the dinuclear compounds the geometries do not conform for regular polyhedral. The best fitting compound was  $[\text{Pr}(\text{HL7})(\text{NO}_3)_2\text{CH}_3\text{OH}]\text{NO}_3$  (**13**). Variation of the counter ions has a strong effect on where the lanthanide ion is placed within the pentaaza pocket. This was shown by structural differences in  $[\text{DyL6}(\text{H}_2\text{O})_4]\text{Cl}_3$  (**11**) and  $[\text{DyL6}(\text{H}_2\text{O})_4]\text{Br}_3$  (**12**). By comparing the isostructural compounds (**13**) and  $[\text{Sm}(\text{HL7})(\text{NO}_3)_2\text{CH}_3\text{OH}]\text{NO}_3$  (**14**), the effect of the ionic radius of the lanthanide on the structure and bond lengths was shown. The smaller ionic radii of the heavier lanthanides allow them to sit in the plane of the ligand's pocket. Depending on how central the lanthanide sits within the ligand's pocket, the terminal pyridine or benzimidazole groups of the ligand are twisted out of plane. It is also worth noting that the deprotonation of the ligand in  $[\text{DyL7}(\text{NO}_3)_2]$  (**15**) does not appear to have any significant effect on bond lengths and angles. The conjugated aromatic  $\pi$ -system of the 2,6-(1-(2-(1H-benzoimidazole-2-yl)hydrazineylidene)ethyl)pyridine system (HL7) can effectively delocalize the additional negative charge.  $[\text{Dy}(\text{HL7})(\text{CH}_3\text{COO})_2]\text{CF}_3\text{SO}_3$  (**16**) shows that a chelating nitrate can be replaced by an acetate without significantly changing the structure.

In this work gaining a better understanding of the optical properties of lanthanide complexes using absorption measurements on the HL7 system as a complex with lanthanides was explored. The resulting coordination compounds (**13**) and (**14**) absorb strongly in the visible range between 380 to 600 nm, making them deep red in colour. Concentration-dependent and acid-base-dependent absorption measurements were performed. Each species could be assigned to a single absorption band. In order to investigate the equilibria between the free ligand, protonated and deprotonated form of the ligand, the spectra were fitted using individual Gaussian shapes. Analyses of the Gaussian fittings reveal that the equilibria occur with pseudo pH-dependence. The

absorption of photons by the ligand is modulated by the nature of the lanthanide ion. Lanthanides are difficult to distinguish from one another due to their similar physical and chemical properties, however using the HL7 system, each lanthanide can be unequivocally identified via its characteristic fitted absorption pattern. Those patterns arise from speciation from the isolated, protonated and deprotonated species.

Further investigations on this system are planned for future work. There are a multitude of possible applications. On the one hand, one could use the HL7 ligand as an indicator for heavy metal ions. On the other hand, such metal ions can also be separated from an aqueous solution, since the resulting complexes are poorly soluble in water. However, the biggest challenge in dealing with lanthanides is their separation. For this purpose, solubility measurements in different solvents at different acid and base concentrations are planned. The idea here is to isolate different lanthanides due to their solubility properties.

In summary, the structures of sixteen different lanthanide complexes were determined by X-ray crystallography. Together with isostructural compounds, which were confirmed to be isomorphous by X-ray powder diffractometry, a total of thirty-five new structures could be characterised. The acetate-bridged dinuclear compounds were proven to be a promising system for the construction of single-molecule magnets. The HL7-lanthanide system has been shown to have useful optical properties resulting from an equilibrium of different species in solution and may find use as a quantification technique for determining lanthanide speciation.

## 6 EXPERIMENTAL

Images of molecules, elemental cell packing and coordination polyhedra were generated by the software Diamond Version 4.6.3.

Figures of graphs were created by the software Origins Version 2022b.

Schemes of organic molecules were made by the software Chemdraw Version 16.

Data from magnet measurements were plotted and fitted with the program CC-FIT2.

The software Mercury Version 3.10 was used to simulate powder patterns from the single-crystal X-ray data.

For the coordination polyhedron analyses the programme SHAPE Version 2.1 used the xyz-coordinates from the single-crystal X-ray data.<sup>[42]</sup>

UV/Vis absorption spectroscopy was performed on an Agilent Cary 5000 UV-Vis-NIR spectrometer from 250-600 nm using the Cary WinUV software.

IR spectra were measured on a Nicolet iS50 FTIR spectrometer operating from 400-4000  $\text{cm}^{-1}$  using the OMNIC software. The following abbreviations characterise the peak intensities: s = strong, m = medium, w = weak.

$^1\text{H}$ -NMR measurements were performed on an UltraShield PLUS spectrometer from BRUKER at 500 MHz and interpreted using the Topspin software. The abbreviations for multiplicities are s = singlet, d = doublet, dd = doublet of doublets, br = broad signal, m = multiplet.

CHNS elemental analyses were performed on a Perkin Elmer Vario EL.

X-ray powder diffraction analyses were performed on a STOE STADI P using Cu-K $\alpha$  radiation ( $\lambda = 1.544 \text{ \AA}$ ) and interpreted using WinXPOW.

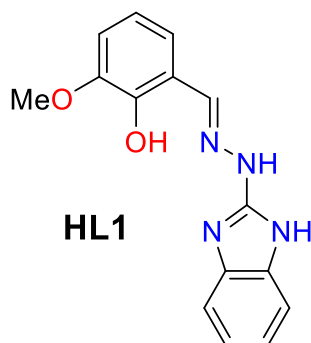
Single-crystal X-ray structural studies were performed on a STOE STADIVARI diffractometer using Ga-K $\alpha$  radiation ( $\lambda = 1.34143 \text{ \AA}$ ) from a MetalJet2 liquid rotating anode source. Structure solution by direct methods via intrinsic phasing (SHELXT)<sup>[50]</sup> was followed by full-matrix least-squares refinement against F<sup>2</sup> using all data (SHELXL-2018).<sup>[50]</sup> Anisotropic temperature factors were assigned to all non-H atoms except the atoms of the minor disorder component of the central nitrate in 3. All N-H H-atoms were refined, while C-H H-atoms were placed in idealised positions.

Direct current magnetic measurements were performed on a Quantum Design MPMS-XL7 SQUID magnetometer in the temperature range of 1.8-300K with an applied field up to 5 Tesla. Alternating current magnetic measurements were carried out at an oscillating fields up to 5250 Oersted and at a frequency of 1-1500 Hertz.

## 7 SYNTHESIS

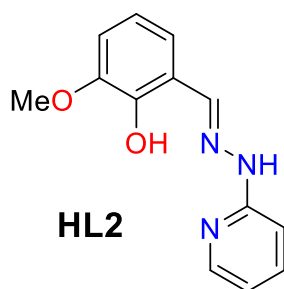
### 7.1 Synthesis of ligands

#### 7.1.1 2-(2-(1H-benzimidazol-2-yl)hydrazineylidene)methyl-6-methoxyphenol (HL1)



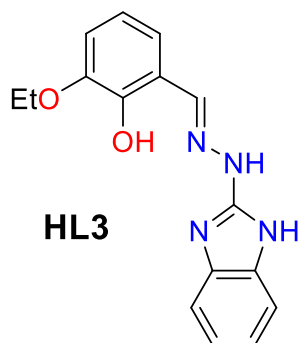
2.06 g (13.5 mmol; 1.00 Eq.) *o*-vanillin and 2.00 g (13.5 mmol; 1.00 Eq.) 2-hydrazino-1H-benzimidazole were dissolved in 300 ml acetonitrile. The yellow solution was stirred and heated under reflux for 4 hours. The resultant precipitate was isolated by filtration and washed with a small amount of cold acetonitrile. After drying under reduced pressure 2.90 g (10.3 mmol) of the product HL1 was collected as a light beige solid (76% yield). <sup>1</sup>H-NMR(500MHz, DMSO):  $\delta$ (ppm) = 3.83 (s, 3H, O-CH<sub>3</sub>), 6.84 (dd, *J* = 8 Hz, 1H, 4-CH *o*-methoxyphenol), 6.95 (d, *J* = 7.5 Hz, 1H, 3-CH *o*-methoxyphenol), 6.97 (m, 2H, 5-6-CH benzimidazole), 7.22 (m, 2H, 4-CH,7-CH benzimidazole), 7.42 (d, *J* = 8 Hz, 1H, 5-CH *o*-methoxyphenol), 8.35 (s 1H, N=CH), 10.67 (s, 1H, OH), 11.53 (s, 1H, NH).

#### 7.1.2 2-methoxy-6-(pyridin-2-yl-hydrazonomethyl)phenol (HL2)



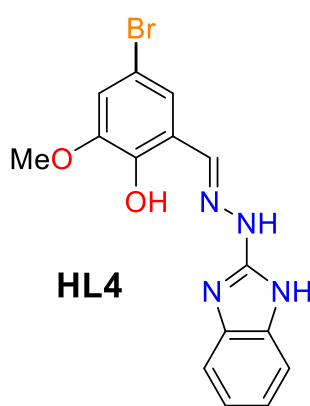
This compound was synthesised analogue to HL1 following literature procedure.<sup>[47]</sup>

### 7.1.3 2-((2-(1H-benzoimidazol-2-yl)hydrazineylidene)methyl)-6-ethoxyphenol (HL3)



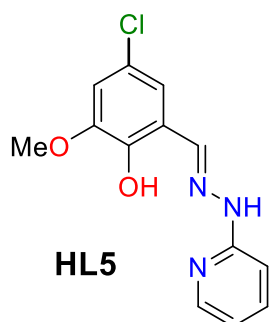
2.24 g (13.5 mmol; 1.00 Eq.) 3-ethoxy-2-hydroxybenzaldehyde and 2.00 g (13.5 mmol; 1.00 Eq.) 2-hydrazino-1H-benzimidazole were dissolved in 300 ml acetonitrile. The yellow solution was stirred and heated under reflux for 4 hours. The resultant precipitate was isolated by filtration and washed with a small amount of cold acetonitrile. After drying under reduced pressure 2.96 g (9.99 mmol) of the product HL3 was collected as a dark beige solid (74% yield).  $^1\text{H-NMR}$ (500MHz, DMSO):  $\delta$ (ppm) = 1.38 (t,  $J$  = 7 Hz, 3H,  $\text{CH}_2\text{-CH}_3$ ) 4.07 (q,  $J$  = 7 Hz, 2H,  $\text{O-CH}_2\text{-CH}_3$ ), 6.81 (dd,  $J$  = 8 Hz, 1H, 4-CH *o*-methoxyphenol), 6.93 (d,  $J$  = 7.5 Hz, 1H, 3-CH *o*-methoxyphenol), 6.96 (m, 2H, 5-6-CH benzimidazole), 7.19 (m, 2H, 4-CH,7-CH benzimidazole), 7.33 (d,  $J$  = 8 Hz, 1H, 5-CH *o*-methoxyphenol), 8.33 (s 1H,  $\text{N=CH}$ ), 11.06 (s, 1H, OH), 11.48 (s, 1H, NH).

### 7.1.4 2-((2-(1H-benzoimidazol-2-yl)hydrazineylidene)methyl)-4-bromo-6-methoxyphenol (HL4)



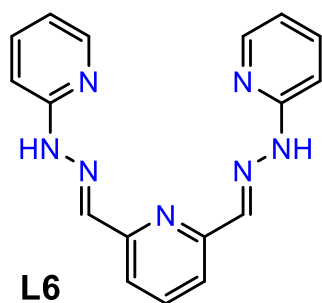
3.12 g (13.5 mmol; 1.00 Eq.) 5-brom-2-hydroxy-3-methoxybenzaldehyde and 2.00 g (13.5 mmol; 1.00 Eq.) 2-hydrazino-1H-benzimidazole were dissolved in 300 ml acetonitrile. The brown solution was stirred and heated under reflux for 4 hours. The resultant precipitate was isolated by filtration and washed with a small amount of cold acetonitrile. After drying under reduced pressure 2.90 g (10.3 mmol) of the product HL4 was collected as a light brown solid (78% yield).  $^1\text{H-NMR}$ (500MHz, DMSO):  $\delta$ (ppm) = 3.85 (s, 3H,  $\text{O-CH}_3$ ), 6.97 (m, 2H, 5-6-CH benzimidazole), 7.08 (s, 1H, 4-CH 5-Bromo-3-methoxysalicylaldehyde), 7.23 (m, 2H, 4-CH,7-CH benzimidazole), 7.72 (s, 1H, 6-CH 5-Bromo-3-methoxysalicylaldehyde), 8.29 (s, 1H,  $\text{N=CH}$ ), 10.60 (br, 1H, OH), 11.59 (s, 1H, NH benzimidazole).

### 7.1.5 4-chloro-2-methoxy-6-((2-(pyridin-2-yl)hydrazineylidene)methyl)phenol (HL5)



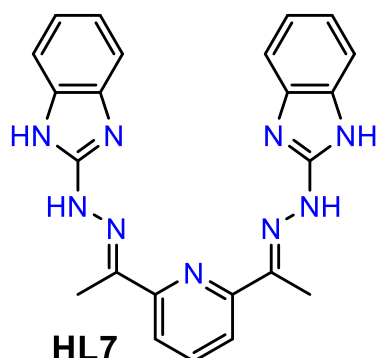
2.52 g (13.5 mmol; 1.00 Eq.) 5-chloro-2-hydroxy-3-methoxybenzaldehyde and 1.47 g (13.5 mmol; 1.00 Eq.) 2-hydrazineylpyridine were dissolved in 300 ml acetonitrile. The yellow solution was stirred and heated under reflux for 4 hours. The resultant precipitate was isolated by filtration and washed with a small amount of cold acetonitrile. After drying under reduced pressure 3.07 g (11.1 mmol) of the product HL5 was collected as a light yellow solid (82% yield). <sup>1</sup>H-NMR(500MHz, DMSO): δ(ppm) = 3.84 (s, 3H, O-CH<sub>3</sub>), 6.78 (dd, *J* = 6 Hz, 1H, 5-CH pyridine), 6.97 (s, 1H, 3-CH *o*-methoxyphenol), 7.14 (d, *J* = 8 Hz, 1H, 3-CH pyridine), 7.31 (s, 1H, 5-CH *o*-methoxyphenol), 7.65 (dd, *J* = 8 Hz, 1H, 4-CH pyridine), 8.12 (d, *J* = 4 Hz, 1H, 6-CH pyridine), 7.23 (m, 2H, 4-CH,7-CH benzimidazole), 8.27 (s, 1H, N=CH), 9.90 (s, 1H, OH), 11.01 (s, 1H, NH benzimidazole).

### 7.1.6 1,1-(pyridine-2,6-diyl)bis(N-(pyridin-2-ylmethyl)methanimine) (L6)



6.98 g (50.16 mmol; 1.00 Eq.) 2,6-pyridinediyl dimethanol and 5.56 g (50.16 mmol; 1.00 Eq.) selenium dioxide were dissolved in 150 ml 1,4-dioxan. The pale yellow solution was stirred and heated under reflux overnight. The reaction mixture was filtered. The solvent was removed under reduced pressure. Without further purification the resultant solid containing 2,6-pyridinedicarbaldehyde was used for the next reaction. It was dissolved together with 10.95 g (100.32 mmol; 2.00 Eq.) 2-hydrazinepyridine in 300 ml methanol. The yellow solution was stirred and heated under reflux for 2 hours. Afterwards the yellow precipitate was filtered off and washed with methanol. After drying under reduced pressure 3.82 g (12.0 mmol) of the product L6 was collected as a yellow solid (24% yield). <sup>1</sup>H-NMR(500MHz, DMSO): δ(ppm) = 6.79-6.86 (m, 2H, 5-CH pyridine<sub>external</sub>), 7.28-7.34 (m, 2H, 3-CH pyridine<sub>external</sub>), 7.64-7.73 (m, 2H, 4-CH pyridine<sub>external</sub>), 7.78-7.91 (m, 3H, 3-5-CH pyridine<sub>central</sub>), 8.06 (s, 2H, CH hydrazone), 8.13-8.19 (m, 2H, 6-CH pyridine<sub>external</sub>), 11.22 (brs, 2H, NH).

### 7.1.7 2,6-(1-(2-(1H-benzimidazole-2-yl)hydrazineylidene)ethyl)pyridine (HL7)



1.50 g (9.19 mmol; 1.00 Eq.) 2,6-diacetylpyridine and 2.72 g (18.4 mmol; 2.00 Eq.) 2-hydrazino-1H-benzimidazole were dissolved in 300 ml acetonitrile. The reddish solution was stirred and heated under reflux for 4 hours. The reaction mixture was left overnight in the fridge. The resultant precipitate was isolated by filtration and washed with a small amount of cold acetonitrile. After

drying under reduced pressure 2.06 g (10.3 mmol) of the product HL7 was collected as a beige solid (53% yield).  $^1\text{H-NMR}$ (500MHz, DMSO):  $\delta$ (ppm) = 2.48 (s, 6H,  $\text{CH}_3$ ), 7.01 (m, 4H, 5-CH, 6-CH benzimidazole), 7.27 (m, 4H, 4-CH, 7-CH benzimidazole), 7.87 (t, 1H,  $J = 8$  Hz, 4-CH pyridine), 8.43 (d, 2H,  $J = 7$  Hz, 3-CH, 5-CH pyridine), 10.92 (br, 2H, NH hydrazine), 11.57 (s, 2H, NH benzimidazole).

## 7.2 Synthesis of complexes

### 7.2.1 $[\text{Dy}_2(\text{L1})_2(\text{NO}_3)_4]\cdot 2\text{CH}_3\text{CN}$ (1) ( $\text{Ln} = \text{Gd}$ to $\text{Lu}$ ; Eu mixed type between (1) and (2))

141 mg HL1 (0.5 mmol) and 219 mg  $\text{Dy}(\text{NO}_3)_3\cdot 5\text{H}_2\text{O}$  (0.5 mmol) were added to a glass vial and dissolved in a 10 ml mixture of 1:1 methanol/acetonitrile. The solution was stirred for 20 min resulting in a clear yellow solution. The filtrate was left to evaporate at room temperature. After around five days, block-shaped crystals of  $[\text{Dy}_2(\text{L1})_2(\text{NO}_3)_4]\cdot 2\text{CH}_3\text{CN}$  suitable for X-ray diffraction analysis had formed. Yield: 0.080 g, 26%. IR  $\text{cm}^{-1}$ : 3533(br), 3348(br), 3180(w), 3112(w), 3059(w), 2922(m), 2853(m), 2250(w), 1614(s), 1593(m), 1535(w), 1483(s), 1458(s), 1437(s), 1387(m), 1368(w), 1293(s), 1266(s), 1242(s), 1292(s), 1172(w), 1083(m), 1052(m), 1032(s), 1012(w), 993(w), 965(m), 890(w), 848(w), 812(w), 785(w), 771(w), 753(w), 738(m), 723(w), 659(w), 500(w), 425(w). Calculated elemental analysis for  $\text{C}_{34}\text{H}_{32}\text{Dy}_2\text{N}_{14}\text{O}_{16}$  (1217.70 g/mol): C, 33.54; H, 2.65; N, 16.10. Found: C, 32.86; H, 2.71; N, 15.59.

### 7.2.2 $[\text{Nd}_2(\text{L1})_2(\text{NO}_3)_4\text{CH}_3\text{OH}]\cdot \text{CH}_3\text{CN}$ (2) ( $\text{Ln} = \text{Pr}$ to $\text{Sm}$ ; Eu mixed type between (1) and (2))

141 mg HL1 (0.5 mmol) and 219 mg  $\text{Nd}(\text{NO}_3)_3\cdot 6\text{H}_2\text{O}$  (0.5 mmol) were added to a glass vial and dissolved in a 10 ml mixture of 1:1 methanol/acetonitrile. The solution was stirred for 20 min resulting in a clear orange solution. The filtrate was left to evaporate at room temperature. After around five days, block-shaped crystals of  $[\text{Nd}_2(\text{L1})_2(\text{NO}_3)_4\text{CH}_3\text{OH}]\cdot \text{CH}_3\text{CN}$  suitable for X-ray diffraction analysis had formed. Yield: 0.053 g, 17%. IR  $\text{cm}^{-1}$ : 2953(m), 2921(s), 2853(m), 1616(w), 1462(w). Calculated elemental analysis for  $\text{C}_{33}\text{H}_{33}\text{Nd}_2\text{N}_{13}\text{O}_{17}$  (1172.2 g/mol): C, 33.81; H, 2.84; N, 15.53. Found: C, 32.15; H, 2.60; N, 14.82.

### 7.2.3 [Dy<sub>2</sub>(L1)<sub>2</sub>(H<sub>2</sub>O)<sub>6</sub>]Cl<sub>4</sub>·2.5CH<sub>3</sub>OH·2.5CH<sub>3</sub>CN (3)

141 mg HL1 (0.5 mmol) and 188 mg DyCl<sub>3</sub>·6H<sub>2</sub>O (0.5 mmol) were added to a glass vial and dissolved in a 10 ml mixture of 1:1 methanol/acetonitrile. The solution was stirred for 20 min resulting in a clear yellow solution. The filtrate was left to evaporate at room temperature. After around ten days, block-shaped crystals of [Dy<sub>2</sub>(L1)<sub>2</sub>(H<sub>2</sub>O)<sub>6</sub>]Cl<sub>4</sub>·2.5CH<sub>3</sub>OH·2.5CH<sub>3</sub>CN suitable for X-ray diffraction analysis had formed. Yield: 0.102 g, 31%. IR cm<sup>-1</sup>: 1737(s), 1367(m), 1216(s), 1123(w), 1032(s), 900(w). Calculated elemental analysis for C<sub>37.5</sub>H<sub>55.5</sub>Cl<sub>4</sub>Dy<sub>2</sub>N<sub>10.5</sub>O<sub>12.5</sub> (1320.22 g/mol): C, 34.12; H, 4.24; N, 11.14. Found: C, 32.28; H, 3.49; N, 10.23. Calculated elemental analysis for [Dy<sub>2</sub>(L1)<sub>2</sub>(H<sub>2</sub>O)<sub>6</sub>]Cl<sub>4</sub>·0.5CH<sub>3</sub>OH·0.5CH<sub>3</sub>CN: C, 32.13; H, 3.56; N, 10.14.

### 7.2.4 [Dy<sub>2</sub>(L1)<sub>2</sub>(H<sub>2</sub>O)<sub>6</sub>]Br<sub>4</sub>·2CH<sub>3</sub>OH·2CH<sub>3</sub>CN (4)

141 mg HL1 (0.5 mmol) and 246 mg DyBr<sub>3</sub>·xH<sub>2</sub>O (0.5 mmol, estimated x=5) were added to a glass vial and dissolved in a 10 ml mixture of 1:1 methanol/acetonitrile. The solution was stirred for 20 min resulting in a clear brown solution. The filtrate was left to evaporate at room temperature. After around ten days, block-shaped crystals of [Dy<sub>2</sub>(L1)<sub>2</sub>(H<sub>2</sub>O)<sub>6</sub>]Br<sub>4</sub>·2CH<sub>3</sub>OH·2CH<sub>3</sub>CN suitable for X-ray diffraction analysis had formed. Yield: 0.092 g, 24%. IR cm<sup>-1</sup>: 1738(s), 1367(m), 1215(s), 1124(w), 1031(s). Calculated elemental analysis for C<sub>39</sub>H<sub>56</sub>Br<sub>4</sub>Dy<sub>2</sub>N<sub>12</sub>O<sub>12</sub> (1529.59 g/mol): C, 30.62; H, 3.69; N, 10.99. Found: C, 29.31; H, 3.19; N, 10.41. Calculated elemental analysis for [Dy<sub>2</sub>(L1)<sub>2</sub>(H<sub>2</sub>O)<sub>6</sub>]Br<sub>4</sub>·0.5CH<sub>3</sub>OH·0.5CH<sub>3</sub>CN: C, 29.18; H, 3.23; N, 10.26.

### 7.2.5 [Dy<sub>2</sub>(L2)<sub>2</sub>(NO<sub>3</sub>)<sub>4</sub>]·2CH<sub>3</sub>CN (5) (Ln = Eu to Lu)

122 mg HL2 (0.5 mmol) and 219 mg Dy(NO<sub>3</sub>)<sub>3</sub>·5H<sub>2</sub>O (0.5 mmol) were added to a glass vial and dissolved in a 10 ml mixture of 1:1 methanol/acetonitrile. The solution was stirred for 20 min resulting in a clear yellow solution. The filtrate was left to evaporate at room temperature. After around five days, block-shaped crystals of [Dy<sub>2</sub>(L2)<sub>2</sub>(NO<sub>3</sub>)<sub>4</sub>]·2CH<sub>3</sub>CN suitable for X-ray diffraction analysis had formed. Yield: 0.111 g, 39%. IR cm<sup>-1</sup>: 3491(br), 2930(br), 1734(s), 1439(w), 1367(m), 1217(s), 1124(w), 1032(s), 901(w), 751(w), 600(w). Calculated elemental analysis for C<sub>30</sub>H<sub>30</sub>Dy<sub>2</sub>N<sub>12</sub>O<sub>16</sub> (1139.63 g/mol): C, 31.62; H, 2.65; N, 14.75. Found: C, 31.12; H, 2.59; N, 14.18.

### 7.2.6 [Dy<sub>2</sub>(L2)<sub>2</sub>(CH<sub>3</sub>COO)<sub>4</sub>(CH<sub>3</sub>OH)<sub>2</sub>]-4CH<sub>3</sub>OH (6)

122 mg HL2 (0.5 mmol), 305 mg Dy(CF<sub>3</sub>SO<sub>3</sub>)<sub>3</sub> (0.5 mmol), 82 mg anhydrous sodium acetate (1.0 mmol) and 51 mg triethylamine (0.5 mmol) were added to a glass vial and dissolved in a 10 ml mixture of 1:1 methanol/acetonitrile. The solution was stirred for 30 min resulting in a clear yellow solution. The filtrate was closed with a lid and left at room temperature. After one day, block-shaped crystals of [Dy<sub>2</sub>(L2)<sub>2</sub>(CH<sub>3</sub>COO)<sub>4</sub>(CH<sub>3</sub>OH)<sub>2</sub>]-4CH<sub>3</sub>OH suitable for X-ray diffraction analysis had formed. Yield: 0.195 g, 68 %. IR cm<sup>-1</sup>: 1738(s), 1367(w), 1215(s), 1124(w), 1032(s). Calculated elemental analysis for C<sub>40</sub>H<sub>60</sub>Dy<sub>2</sub>N<sub>6</sub>O<sub>18</sub> (1237.94 g/mol): C, 38.81; H, 4.89; N, 6.79. Found: C, 37.68; H, 4.47; N, 6.52.

### 7.2.7 [Dy<sub>2</sub>(L3)<sub>2</sub>(CH<sub>3</sub>COO)<sub>4</sub>(H<sub>2</sub>O)<sub>2</sub>]-2H<sub>2</sub>O-4CH<sub>3</sub>OH (7)

148 mg HL3 (0.5 mmol), 305 mg Dy(CF<sub>3</sub>SO<sub>3</sub>)<sub>3</sub> (0.5 mmol) and 82 mg anhydrous sodium acetate (1.0 mmol) were added to a glass vial and dissolved in a 10 ml mixture of 1:1 methanol/acetonitrile. The solution was stirred for 30 min resulting in a clear yellow solution. The filtrate was left to evaporate at room temperature. After five to ten days, needle-shaped crystals of [Dy<sub>2</sub>(L3)<sub>2</sub>(CH<sub>3</sub>COO)<sub>4</sub>(H<sub>2</sub>O)<sub>2</sub>]-2H<sub>2</sub>O-4CH<sub>3</sub>OH suitable for X-ray diffraction analysis had formed. Yield: 0.071 g, 22%. IR cm<sup>-1</sup>: 2951(s), 2918(s), 2867(m), 2839(m), 1376(w). Calculated elemental analysis for Dy<sub>2</sub>O<sub>20</sub>H<sub>66</sub>N<sub>8</sub>C<sub>44</sub> (1353.04 g/mol): C, 39.09; H, 4.92; N, 8.29. Found: C, 36.49; H, 3.46; N, 6.90.

### 7.2.8 [Dy<sub>2</sub>(L4)<sub>2</sub>(H<sub>2</sub>O)<sub>6</sub>]-Cl<sub>4</sub>-2CH<sub>3</sub>CN (8)

181 mg HL4 (0.5 mmol) and 188 mg DyCl<sub>3</sub>-6H<sub>2</sub>O (0.5 mmol) were added to a glass vial and dissolved in a 10 ml mixture of 1:1 methanol/acetonitrile. The solution was stirred for 20 min resulting in a clear yellow solution. The filtrate was left to evaporate at room temperature. After around ten days, block-shaped crystals of [Dy<sub>2</sub>(L4)<sub>2</sub>(H<sub>2</sub>O)<sub>6</sub>]-Cl<sub>4</sub>-2CH<sub>3</sub>CN suitable for X-ray diffraction analysis had formed. Yield: 0.161 g, 42%. IR cm<sup>-1</sup>: 1736(s), 1367(m), 1217(s), 1124(w), 1032(s), 901(w). Calculated elemental analysis for C<sub>34</sub>H<sub>42</sub>Br<sub>2</sub>Cl<sub>4</sub>Dy<sub>2</sub>N<sub>10</sub>O<sub>10</sub> (1377.38 g/mol): C, 29.52; H, 2.75; N, 9.10. Found: C, 24.73; H, 2.48; N, 7.72.

### 7.2.9 [Dy<sub>2</sub>(L5)<sub>2</sub>(CH<sub>3</sub>COO)<sub>4</sub>(CH<sub>3</sub>OH)<sub>2</sub>] (9)

139 mg HL5 (0.5 mmol), 305 mg Dy(CF<sub>3</sub>SO<sub>3</sub>)<sub>3</sub> (0.5 mmol) and 82 mg anhydrous sodium acetate (1.0 mmol) were added to a glass vial and dissolved in a 10 ml mixture of 1:1 methanol/acetonitrile. The solution was stirred for 30 min resulting in a clear yellow solution. The filtrate was left to evaporate at room temperature. After five to ten days, square-shaped crystals of [Dy<sub>2</sub>(L5)<sub>2</sub>(CH<sub>3</sub>COO)<sub>4</sub>(CH<sub>3</sub>OH)<sub>2</sub>] suitable for X-ray diffraction analysis had formed. Yield: 0.038 g, 13%. IR cm<sup>-1</sup>: 1735(s), 1367(w), 1216(s), 1124(w), 1032(s). Calculated elemental analysis for Dy<sub>2</sub>O<sub>14</sub>H<sub>42</sub>N<sub>6</sub>C<sub>36</sub>Cl<sub>2</sub> (1178.65 g/mol): C, 36.68; H, 3.59; N, 7.13. Found: C, 36.27; H, 3.23; N, 7.48.

### 7.2.10 [Dy<sub>2</sub>(L5)<sub>4</sub>(μ-H<sub>2</sub>O)]Cl<sub>2</sub>·H<sub>2</sub>O·CH<sub>3</sub>OH·CH<sub>3</sub>CN·(CH<sub>3</sub>CH<sub>2</sub>)<sub>2</sub>O (10)

139 mg HL5 (0.5 mmol) 188 mg DyCl<sub>3</sub>·6H<sub>2</sub>O (0.5 mmol) were added to a glass vial and dissolved in a 10 ml mixture of 1:1:1 methanol/acetonitrile/diethyl ether. The solution was stirred for 30 min resulting in a clear yellow solution. The filtrate was left to evaporate at room temperature. After ten to twenty day, square-shaped crystals of [Dy<sub>2</sub>(L5)<sub>4</sub>(μ-H<sub>2</sub>O)]Cl<sub>2</sub>·H<sub>2</sub>O·CH<sub>3</sub>OH·CH<sub>3</sub>CN·(CH<sub>3</sub>CH<sub>2</sub>)<sub>2</sub>O suitable for X-ray diffraction analysis had formed. Yield: 0.080 g, 38%. IR cm<sup>-1</sup>: 1735(s), 1368(w), 1216(s), 1124(w), 1031(s). Calculated elemental analysis for Dy<sub>2</sub>O<sub>12</sub>H<sub>65</sub>N<sub>13</sub>C<sub>59</sub>Cl<sub>6</sub> (1685.94 g/mol): C, 42.03; H, 3.89; N, 10.80. Found: C, 37.24; H, 3.21; N, 9.45.

### 7.2.11 [DyL6(H<sub>2</sub>O)<sub>4</sub>]Cl<sub>3</sub>·6H<sub>2</sub>O (11)

159 mg L6 (0.5 mmol) and 188 mg DyCl<sub>3</sub>·6H<sub>2</sub>O (0.5 mmol) were added to a glass vial and dissolved in a 10 ml mixture of 1:1 methanol/acetonitrile. The solution was stirred for 30 min resulting in a clear yellow solution. The filtrate was left to evaporate at room temperature. After two to four days, block-shaped crystals of [DyL6(H<sub>2</sub>O)<sub>4</sub>]Cl<sub>3</sub>·6H<sub>2</sub>O suitable for X-ray diffraction analysis had formed. Yield: 0.080 g, 21%. IR cm<sup>-1</sup>: 1605 (m), 1595 (m), 1561 (s), 1544 (m), 1645 (m), 1461 (m), 1437 (s), 1353 (w), 1333 (m), 1308 (m), 1263 (m), 1284 (m), 1273 (m), 1178 (s), 1141 (m), 1102 (w), 1080 (w), 1049 (w), 993 (m), 897 (m), 802 (w), 765 (m), 733 (m), 691 (m), 655 (m), 633 (w), 619 (w), 529 (w), 513 (w), 446 (w), 407 (w). Calculated elemental analysis for C<sub>17</sub>H<sub>35</sub>DyCl<sub>3</sub>N<sub>7</sub>O<sub>10</sub> (766.37 g/mol): C, 26.64; H, 4.60; N, 12.79. Found: C, 26.65; N, 12.69; H, 3.77.

### 7.2.12 [DyL6(H<sub>2</sub>O)<sub>4</sub>]Br<sub>3</sub>·4.5H<sub>2</sub>O (12)

159 mg L6 (0.5 mmol), 246 mg DyBr<sub>3</sub>·xH<sub>2</sub>O (0.5 mmol, estimated x=5) were added to a glass vial and dissolved in a 10 ml mixture of 1:1 methanol/acetonitrile. The solution was stirred for 30 min resulting in a clear brown solution. The filtrate was left to evaporate at room temperature. After two to four days, block-shaped crystals of [DyL6(H<sub>2</sub>O)<sub>4</sub>]Br<sub>3</sub>·4.5H<sub>2</sub>O suitable for X-ray diffraction analysis had formed. Yield: 0.079 g, 18%. IR cm<sup>-1</sup>: 1605 (m), 1595 (m), 1561 (s), 1544 (m), 1645 (m), 1461 (m), 1437 (s), 1353 (w), 1333 (m), 1308 (m), 1263 (m), 1284 (m), 1273 (m), 1178 (s), 1141 (m), 1102 (w), 1080 (w), 1049 (w), 993 (m), 897 (m), 802 (w), 765 (m), 733 (m), 691 (m), 655 (m), 633 (w), 619 (w), 529 (w), 513 (w), 446 (w), 407 (w). Calculated elemental analysis for C<sub>17</sub>H<sub>32</sub>DyBr<sub>3</sub>N<sub>7</sub>O<sub>8.5</sub> (872.72 g/mol): C, 23.40; H, 3.70; N, 11.24. Found: C, 22.57; H, 3.24; N, 10.87.

**7.2.13 [Pr(HL7)(NO<sub>3</sub>)<sub>2</sub>CH<sub>3</sub>OH]NO<sub>3</sub>·2CH<sub>3</sub>OH·H<sub>2</sub>O (13)** (Ln = Pr; Nd and Sm mixed type between (13) and (14))

212 mg HL7 (0.5 mmol) and 218 mg Pr(NO<sub>3</sub>)<sub>3</sub>·6H<sub>2</sub>O (0.5 mmol) were added to a glass vial and dissolved in 10 ml methanol. The solution was stirred for 20 min resulting in a red solution. The filtrate was closed with a lid and left in the fridge. After two days, block-shaped crystals of [Pr(HL7)(NO<sub>3</sub>)<sub>2</sub>CH<sub>3</sub>OH]NO<sub>3</sub>·3CH<sub>3</sub>OH suitable for X-ray diffraction analysis had formed. Yield: 0.066 g, 16%. IR cm<sup>-1</sup>: 2950(s), 2918(s), 2867(m), 2838(m), 1456(w), 1375(w). Calculated elemental analysis for C<sub>26</sub>H<sub>35</sub>PrN<sub>12</sub>O<sub>13</sub> (869.50 g/mol): C, 36.12; H, 4.08; N, 19.44. Found: C, 34.66; H, 3.56; N, 19.85.

**7.2.14 [Sm(HL7)(NO<sub>3</sub>)<sub>2</sub>CH<sub>3</sub>OH]NO<sub>3</sub>·CH<sub>3</sub>OH (14)** (Ln = Eu; Nd and Sm mixed type between (13) and (14))

212 mg HL7 (0.5 mmol) and 222 mg Sm(NO<sub>3</sub>)<sub>3</sub>·6H<sub>2</sub>O (0.5 mmol) were added to a glass vial and dissolved in 10 ml methanol. The solution was stirred for 20 min resulting in a red solution. The filtrate was closed with a lid and left in the fridge. After two days, block-shaped crystals of [Sm(HL7)(NO<sub>3</sub>)<sub>2</sub>CH<sub>3</sub>OH]NO<sub>3</sub>·CH<sub>3</sub>OH suitable for X-ray diffraction analysis had formed. Yield: 0.057 g, 13%. IR cm<sup>-1</sup>: 2950(s), 2918(s), 2867(m), 2839(m), 1456(w), 1375(w). Calculated elemental analysis for C<sub>25</sub>H<sub>29</sub>SmN<sub>12</sub>O<sub>11</sub> (823.93 g/mol): C, 36.44; H, 3.55; N, 20.40. Found: C, 33.88; H, 3.41; N, 20.25.

**7.2.15 [DyL7(NO<sub>3</sub>)<sub>2</sub>]-CH<sub>3</sub>OH (15)**

212 mg HL7 (0.5 mmol), 219 mg Dy(NO<sub>3</sub>)<sub>3</sub>·5H<sub>2</sub>O (0.5 mmol) and 51 mg triethylamine (0.5 mmol) were added to a glass vial and dissolved in a 10 ml mixture of 1:1 methanol/acetonitrile. The solution was stirred for 20 min resulting in a red solution. The filtrate was closed with a lid and left in the fridge. After 10 days, tiny block-shaped crystals of [DyL7(NO<sub>3</sub>)<sub>2</sub>]-CH<sub>3</sub>OH suitable for X-ray diffraction analysis had formed. Yield: 0.026 g, 8%. IR cm<sup>-1</sup>: 2950(s), 2918(s), 2867(m), 2839(m), 1455(w), 1375(w). Calculated elemental analysis for C<sub>24</sub>DyH<sub>24</sub>N<sub>11</sub>O<sub>7</sub> (741.04 g/mol): C, 38.90; H, 3.26; N, 20.79. Found: C, 36.34; H, 3.08; N, 19.72.

### 7.2.16 [Dy(HL7)(CH<sub>3</sub>COO)<sub>2</sub>]CF<sub>3</sub>SO<sub>3</sub>·CH<sub>3</sub>OH (16)

212 mg HL7 (0.5 mmol), 305 mg Dy(CF<sub>3</sub>SO<sub>3</sub>)<sub>3</sub> (0.5 mmol) and 82 mg anhydrous sodium acetate (1.0 mmol) were added to a glass vial and dissolved in a 10 ml mixture of 1:1 methanol/acetonitrile. The solution was stirred for 20 min resulting in a red solution. The filtrate was closed with a lid and left in the fridge. After two days, diamond-shaped crystals of [Dy(HL7)(CH<sub>3</sub>COO)<sub>2</sub>]CF<sub>3</sub>SO<sub>3</sub>·CH<sub>3</sub>OH suitable for X-ray diffraction analysis had formed. Yield: 0.066 g, 16%. IR cm<sup>-1</sup>: 2950(s), 2918(s), 2867(m), 2838(m), 1453(w), 1376(w). Calculated elemental analysis for C<sub>29</sub>H<sub>31</sub>DyF<sub>3</sub>N<sub>9</sub>O<sub>8</sub>S (885.19 g/mol): C, 39.35; H, 3.53; N, 14.24; S, 3.62. Found: C, 37.08; H, 2.87; N, 13.39; S, 2.85.

## 8 REFERENCES

**Note:** Figures and schemes for which no source is provided are self drawn.

- [1] E. Riedel, C. Janiak, *Anorganische Chemie*, 8. Auflage, Walter de Gruyter Verlag, Berlin, **2011**. e-ISBN: 978-3-11-022567-9 (Figure 3 was taken from page 669)
- [2] J. E. Geusic, H. M. Marcos, L. G. Van Uitert, *Laser oscillations in Nd-doped yttrium aluminum, yttrium gallium and gadolinium garnets*, *Appl. Phys. Lett.* **1964**, *4*, 182-184. DOI: 10.1063/1.1753928
- [3] J. D. Rinehart, J. R. Long, *Exploiting single-ion anisotropy in the design of f element single-molecule magnets*, *Chem. Sci.*, **2011**, *2*, 2078-2085. DOI: 10.1039/C1SC00513H (Figures 10, 11, 12 and 18 were taken from pages 2080-2082)
- [4] D. Julianne, *Mineral Resources Economy 1: Context and Issues, Geopolitics of Metals: Between Strategies of Power and Influence*, **2021**, 53-72. DOI: 10.1002/9781119850861.ch3
- [5] J. De Decker, *Functionalized Metal-Organic Frameworks as Selective Metal Adsorbents*, PhD thesis, Ghent University, **2017**.
- [6] M. N. Sudhindra, S. O. Sommerer, *Absorption Spectra of Lanthanide Complexes in Solution*, *Appl. Spec. Rev.* **1991**, *26*, 151-202. DOI: 10.1080/05704929108050880
- [7] C. E. Mortimer, U. Müller, *Chemie*, 9. Auflage, Georg Thieme Verlag, Stuttgart, **2007**. ISBN: 978-3134843095
- [8] C. E. Housecroft, E. C. Constable, *Chemistry, An integrated approach*, Addison Wesley Longman Limited, Edinburgh Gate, **1997**. ISBN: 0-582-25342-X
- [9] Y. Lu, B. Yan, *Lanthanide organic–inorganic hybrids based on functionalized metal–organic frameworks (MOFs) for a near-UV white LED*, *Chem. Commun.* **2014**, *50*, 15443-15446. DOI: 10.1039/C4CC07852G
- [10] J. Tang, P. Zhang, *Lanthanide Single Molecule Magnets*, Springer-Verlag Berlin Heidelberg, **2015**. e-ISBN 978-3-662-46999-6: (Figures 6, 9 and 38 were taken from pages 14 and 8)
- [11] L. K. Young, M. Z. Shona, J. G. Houston, *Absence of potential gadolinium toxicity symptoms following 22,897 gadoteric acid (Dotarem®) examinations, including 3,209 performed on renally insufficient individuals*, *Eur. Radio.* **2019**, *29*, 1922-1930. DOI: 10.1007/s00330-018-5737-z

- [12] G. Castro, M. Regueiro-figueroa, D. Esteban-gómez, R. Bastida, *Exceptionally Inert Lanthanide(III) PARACEST MRI Contrast Agents Based on an 18-Membered Macrocyclic Platform*, *Chem. Eur. J.* **2015**, *21*, 18662-18670. DOI: 10.1002/chem.201502937
- [13] R. Sessoli, D. Gatteschi, A. Caneschi, M. A. Novak, *Magnetic bistability in a metal-ion cluster*, *Nature* **1993**, *365*, 141-143. DOI: 10.1038/365141a0
- [14] J. M. D. Coey, *Magnetism and Magnetic Materials*, Cambridge University Press, Cambridge, **2010**. ISBN: 978-0-521-81614-4
- [15] J. E. Huheey, E. Keiter, R. Keiter, *Anorganische Chemie*, 3. Auflage, De Gruyter Verlag, Berlin **1995**. ISBN: 978-3110135572
- [16] J. Dreiser, *Molecular lanthanide single-ion magnets: from bulk to submonolayers*, *J. Phys. Condens. Matter* **2015**, *27*, 183203. DOI: 10.1088/0953-8984/27/18/183203
- [17] G. L. Rothermel, L. Miao, A. L. Hill, S. C. Jackels, *Macrocyclic ligands with 18-membered rings containing pyridine or furan groups: preparation, protonation, and complexation by metal ions*, *Inorg. Chem.* **1992**, *31*, 4854-4859. DOI: 10.1021/ic00049a025
- [18] R. A. Layfield, M. Murugesu, *Lanthanides and Actinides in Molecular Magnetism*, John Wiley & Sons Verlag, **2015**. ISBN: 978-3-527-33526-8
- [19] A. M. Ako, I. J. Hewitt, V. Mereacre, R. Clerac, W. Wernsdorfer, C. E. Anson, A. K. Powell, *A Ferromagnetically Coupled Mn<sub>19</sub> Aggregate with a Record S=83/2 Ground Spin State*, *Angew. Chem. Int. Ed.* **2006**, *45*, 4926-4929. DOI: 10.1002/anie.200601467
- [20] A. M. Ako, I. J. Hewitt, V. Mereacre, R. Clørac, W. Wernsdorfer, C. E. Anson, A. K. Powell, *Heterometallic [Mn<sub>5</sub>-Ln<sub>4</sub>] Single-Molecule Magnets with High Anisotropy Barriers*, *Angew. Chem.* **2006**, *14*, 5048-5051. DOI: 10.1002/chem.200800125
- [21] K. N. Shrivastava, *Theory of Spin-Lattice Relaxation*, *Phys. Stat. Sol.* **1983**, *117*, 437-458. DOI: 10.1002/pssb.2221170202
- [22] J. S. Miller, D. Gatteschi, *Lanthanides in molecular magnetism: old tools in a new field*, *Chem. Soc. Rev.* **2011**, *40*, 3092-3104. DOI: 10.1039/C0CS00185F
- [23] R. Skomski, *Simple Models of Magnetism*, Oxford University Press, Oxford, **2008**. ISBN: 978-0198570752
- [24] J. Sievers, *Asphericity of 4f-shells in their Hund's rule ground states*, *Z. Phys. B: Condens. Matter Quanta* **1982**, *45*, 289-296. DOI: 10.1007/BF01321865
- [25] C. Benelli, D. Gatteschi, *Magnetism of Lanthanides in Molecular Materials with Transition-Metal Ions and Organic Radicals*, *Chem. Rev.* **2002**, *102*, 2369-2387. DOI: 10.1021/cr010303r

- [26] H. B. Bebb, E. W. Williams, *Chapter 4: Photoluminescence I: Theory, Semiconductors and Semimetals* **1972**, 8, 181-320. DOI: 10.1016/S0080-8784(08)62345-5
- [27] T. Enoki, A. Miyazaki, *Magnetic TTF-Based Charge-Transfer Complexes*, *Chem. Rev.* **2004**, 104, 5449-5477. DOI: 10.1021/cr0306438
- [28] K. P. Goetz, D. Vermeulen, M. E. Payne, C. Kloc, L. E. McNeil, O. D. Jurchescu, *Charge-transfer complexes: new perspectives on an old class of compounds*, *J. Mater. Chem.* **2014**, 2, 3065-3076. DOI: 10.1039/C3TC32062F
- [29] C. J. Bender, *Theoretical Models of Charge-transfer Complexes*, *Chem. Soc. Rev.* **1986**, 15, 475-502. DOI: 10.1039/CS9861500475
- [30] P. L. Pauson, *Ferrocene and related compounds*, *Chemical Society* **1955**, 9, 391-414. DOI: 10.1039/QR9550900391
- [31] J. S. Miller, *Ferromagnetic Molecular Charge-Transfer Complexes*, *Chem. Rev.* **1988**, 88, 201-220. DOI: 10.1021/cr00083a010
- [32] K. Peter, C. Vollhardt, N. E. Schore, *Organische Chemie*, 4. Auflage, Wiley-VCH Verlag, Weinheim, **2005**. ISBN: 978-3527313808
- [33] L. D'Souza, J. R. Regalbuto, J. T. Miller, *Preparation of carbon supported cobalt by electrostatic adsorption of  $[\text{Co}(\text{NH}_3)_6]\text{Cl}_3$* , *Journal of Catalysis* **2008**, 254, 157-169. DOI: 10.1016/j.jcat.2007.12.007
- [34] K. Rajnak, B. G. Wybourne, *Configuration interaction in crystal field theory*, *J. Chem. Phys.* **1964**, 41, 565-569. DOI: 10.1063/1.1725909
- [35] J. S. Griffith, L. E. Orgel, *Ligand-field theory*, *Chem. Soc. Rev.* **1954**, 11, 381-393. DOI: 10.1039/QR9571100381
- [36] R. D. Shannon, *Revised Effective Ionic Radii and Systematic Studies of Interatomic Distances in Halides and Chalcogenides*, *Acta Cryst.* **1976**, A32, 751-767. DOI: 10.1107/S0567739476001551
- [37] P. Krisana, M. P. Merkel, O. Fuhr, A. K. Powell, *A designed and potentially decadentate ligand for use in lanthanide(III) catalysed biomass transformations: targeting diastereoselective trans-4,5-diaminocyclopentenone derivatives*, *Dalton Trans.* **2020**, 49, 2331-2336. DOI: 10.1039/D0DT00183J (Figure 21 was taken from page 2332)
- [38] A. Xavier, N. Srividhya, *Synthesis and study of Schiff base ligands*, *J. Appl. Chem.* **2014**, 7, 6-15. DOI: 10.9790/5736-071110615
- [39] J. Goura, J. P. S. Walsh, F. Tuna, V. Chandrasekhar, *Tetranuclear Lanthanide(III) Complexes in a Seesaw Geometry: Synthesis, Structure, and Magnetism*, *Inorg. Chem.* **2014**, 53, 3385-3391. DOI: 10.1021/ic4027915

- [40] J. Goura, J. P. S. Walsh, F. Tuna, V. Chandrasekhar, *Synthesis, structure, and magnetism of non-planar heptanuclear lanthanide(III) complexes*, *Dalton Trans.* **2015**, 44, 1142-1149. DOI: 10.1039/C4DT01603C
- [41] O. C. Gagné, *Bond-length distributions for ions bonded to oxygen: results for the lanthanides and actinides and discussion of the f-block contraction*, *Acta Cryst.* **2018**, 74, 49-62. DOI: 10.1107/S2052520617017425
- [42] D. Casanova, J. Cirera, M. Llunell, P. Alemany, D. Avnir, S. Alvarez, *Minimal Distortion Pathways in Polyhedral Rearrangements*, *J. Am. Chem. Soc.* **2004**, 126, 1755-1763. DOI: 10.1021/ja036479n
- [43] L. Gu, R. Wu, *Origins of slow magnetic relaxation in single-molecule magnets*, *Phys. Rev. Lett.* **2020**, 125, 117-203. DOI: 10.1103/PhysRevLett.125.117203
- [44] W. J. Hehre, *Ab initio molecular orbital theory*, *Acc. Chem. Res.* **1976**, 9, 399-406. DOI: 10.1021/ar50107a003
- [45] H. S. Wang, Y. Chen, Z. B. Hu, C. L. Yin, Z. Zhang, Z. Q. Pan, *Modulation of the directions of the anisotropic axes of Dy<sup>III</sup> ions through utilizing two kinds of organic ligands or replacing Dy<sup>III</sup> ions by Fe<sup>III</sup> ions*, *Cryst. Eng. Comm.* **2019**, 21, 5429-5439. DOI: 10.1039/C9CE00894B
- [46] N. F. Chilton, D. Collison, E. J. L. McInnes, R. E. P. Winpenny, A. Soncini, *An electrostatic model for the determination of magnetic anisotropy in dysprosium complexes*, *Nat. Commun.* **2013**, 4, 2551. DOI: 10.1038/ncomms3551
- [47] M. Mohan, et al., *On the nature of the high-spin (<sup>6</sup>A<sub>1</sub>) ⇌ low-spin (<sup>2</sup>T<sub>2</sub>) transition in [Fe(3-CH<sub>3</sub>OSPH)<sub>2</sub>]Y complexes*, *Inorg. Chim. Acta* **1988**, 141, 185-192. DOI: 10.1016/S0020-1693(00)83908-0
- [48] A. Bondi, *van der Waals Volumes and Radii*, *J. Phys. Chem.* **1964**, 68, 441-451. DOI: 10.1021/j100785a001
- [49] M. Li, H. Wu, S. Zhang, L. Sun, H. Ke, Q. Wei, G. Xie, S. Chen, S. Gao, *Fine-Tuning Ligand Fields with Schiff-Base Ligands in Dy<sub>2</sub> Compounds*, *Eur. J. Inorg. Chem.* **2017**, 4, 811-819. DOI: 10.1002/ejic.201601188
- [50] G. Sheldrick, *SHELXT - Integrated space-group and crystal-structure determination*, *Acta Crystallogr.* **2015**, 71, 3-8. DOI: 10.1107/S2053273314026370
- [51] M. Li, H. Wu, Z. Xia, V. Montigaud, O. Cador, B. Le Guennic, H. Ke, W. Wang, G. Xie, S. Chen, *Bromine-bridged Dy<sub>2</sub> single-molecule magnet: magnetic anisotropy driven by cis/trans stereoisomers*, *Chem. Commun.* **2019**, 55, 14661-14664. DOI: 10.1039/C9CC07552F

- [52] R. F. Pflieger, S. Schlittenhardt, M. P. Merkel, M. Ruben, K. Fink, C. E. Anson, J. Bendix, A. K. Powell, *Terminal Ligand and Packing Effects on Slow Relaxation in an Isostructural Set of  $[Dy(H_2dapp)X_2]^+$  Single Molecule Magnets*, *Chem. Eur. J.* **2021**, 27, 15086-15095. DOI: 10.1002/chem.202102918
- [53] R. Pflieger, *Design of Lanthanide Coordination Compounds with Unusual Ligands and High Symmetry for Molecular Magnetism*, PhD thesis, Karlsruher Institut für Technologie, **2021**.
- [54] J. J. N. Segoviano-Garfias, G. A. Zanol, F. Ávila-Ramos, E. Y. Bivián-Castro, C. A. Rubio-Jiménez, *Spectrophotometric Determination of Formation Constants of Iron(III) Complexes with Several Ligands*, *Chem.* **2022**, 4, 701-716. DOI: 10.3390/chemistry4030050

## 9 APPENDIX

### 9.1 Crystallographic data

| Compound                             | (1)   | (2)   |
|--------------------------------------|---|---|
| Formula                              | C <sub>34</sub> H <sub>32</sub> Dy <sub>2</sub> N <sub>14</sub> O <sub>16</sub> | C <sub>33</sub> H <sub>33</sub> N <sub>13</sub> Nd <sub>2</sub> O <sub>17</sub> |
| FW / g·mol <sup>-1</sup>             | 1217.73   | 1172.20   |
| Crystal System                       | Triclinic   | Triclinic   |
| Space Group                          | P $\bar{1}$   | P $\bar{1}$   |
| a / Å                                | 9.7221(4)   | 12.5853(3)  |
| b / Å                                | 10.5871(5)  | 12.7266(3)  |
| c / Å                                | 11.0108(5)  | 14.3730(4)  |
| $\alpha$ / °                         | 114.070(3)  | 106.861(2)  |
| $\beta$ / °                          | 104.817(3)  | 104.195(2)  |
| $\gamma$ / °                         | 90.020(3)   | 105.058(2)  |
| U / Å <sup>3</sup>                   | 993.32(8)   | 1995.38(9)  |
| Z                                    | 1   | 2   |
| T / K                                | 150   | 150   |
| F(000)                               | 594   | 1156  |
| D <sub>c</sub> / Mg m <sup>-3</sup>  | 2.036   | 1.951   |
| m(Ga-K $\alpha$ ) / mm <sup>-1</sup> | 19.839  | 2.667   |
| Data Measured                        | 11078   | 30575   |
| Unique Data                          | 4139  | 8714  |
| R <sub>int</sub>                     | 0.0485  | 0.0319  |
| Data with I $\geq$ 2s(I)             | 3645  | 6806  |
| wR <sub>2</sub> , (all data)         | 0.1506  | 0.0772  |
| S (all data)                         | 1.037   | 0.970   |
| R <sub>1</sub> [I $\geq$ 2s(I)]      | 0.0558  | 0.0301  |
| Parameters/<br>Restraints            | 306/11  | 617/14  |
| Data Completeness<br>/ %             | 98.6  | 99.1  |
| Biggest diff.<br>peak/hole           | 2.072/-1.888  | 1.261/-1.255  |

**Table 16:** Crystallographic data and structure refinement for (1) and (2).

| Compound                             | (3)  | (4)   |
|--------------------------------------|--|---|
| Formula                              | C <sub>37.5</sub> H <sub>55.5</sub> Cl <sub>4</sub><br>Dy <sub>2</sub> N <sub>10.5</sub> O <sub>12.5</sub> | C <sub>39</sub> H <sub>56</sub> Br <sub>4</sub> Dy <sub>2</sub> N <sub>12</sub> O <sub>12</sub> |
| FW / g·mol <sup>-1</sup>             | 1320.22  | 1529.59   |
| Crystal System                       | Triclinic  | Triclinic   |
| Space Group                          | P $\bar{1}$  | P $\bar{1}$   |
| a / Å                                | 7.7898(4)  | 8.0308(2)   |
| b / Å                                | 12.6637(5)   | 11.2971(3)  |
| c / Å                                | 14.1023(5)   | 15.6710(4)  |
| $\alpha$ / °                         | 70.942(3)  | 92.034(2)   |
| $\beta$ / °                          | 84.010(4)  | 96.608(2)   |
| $\gamma$ / °                         | 74.082(3)  | 105.126(2)  |
| U / Å <sup>3</sup>                   | 1264.32(10)  | 1360.19(6)  |
| Z                                    | 1  | 1   |
| T / K                                | 150  | 150   |
| F(000)                               | 654  | 742   |
| D <sub>c</sub> / Mg m <sup>-3</sup>  | 1.734  | 1.867   |
| m(Ga-K $\alpha$ ) / mm <sup>-1</sup> | 17.035   | 16.743  |
| Data Measured                        | 14550  | 14685   |
| Unique Data                          | 14550  | 6348  |
| R <sub>int</sub>                     | 0.0182   | 0.0180  |
| Data with I $\geq$ 2s(I)             | 12784  | 6261  |
| wR <sub>2</sub> , (all data)         | 0.0698   | 0.0681  |
| S (all data)                         | 1.070  | 1.029   |
| R <sub>1</sub> [I $\geq$ 2s(I)]      | 0.0260   | 0.0248  |
| Parameters/<br>Restraints            | 323/11   | 6348/14   |
| Data Completeness<br>/ %             | 98.8   | 97.7  |
| Biggest diff.<br>peak/hole           | 0.983/-0.808   | 1.029/-0.666  |

**Table 17:** Crystallographic data and structure refinement for (3) and (4).

| Compound                             | (5)   | (6)  |
|--------------------------------------|---|--|
| Formula                              | C <sub>30</sub> H <sub>30</sub> Dy <sub>2</sub> N <sub>12</sub> O <sub>16</sub> | C <sub>40</sub> H <sub>60</sub> Dy <sub>2</sub> N <sub>6</sub> O <sub>18</sub> |
| FW / g·mol <sup>-1</sup>             | 1139.66   | 1237.94  |
| Crystal System                       | Triclinic   | Triclinic  |
| Space Group                          | P $\bar{1}$   | P $\bar{1}$  |
| a / Å                                | 9.8637(6)   | 10.7669(5)   |
| b / Å                                | 10.2288(6)  | 11.2241(5)   |
| c / Å                                | 11.0147(6)  | 11.7184(5)   |
| $\alpha$ / °                         | 63.258(4)   | 75.342(3)  |
| $\beta$ / °                          | 75.286(4)   | 85.131(3)  |
| $\gamma$ / °                         | 89.490(5)   | 62.498(3)  |
| U / Å <sup>3</sup>                   | 952.73(10)  | 1214.40(10)  |
| Z                                    | 1   | 1  |
| T / K                                | 150   | 180  |
| F(000)                               | 554   | 618  |
| D <sub>c</sub> / Mg m <sup>-3</sup>  | 1.986   | 1.693  |
| m(Ga-K $\alpha$ ) / mm <sup>-1</sup> | 20.933  | 3.129  |
| Data Measured                        | 10445   | 14444  |
| Unique Data                          | 10445   | 8097   |
| R <sub>int</sub>                     | 0.0252  | 0.0727   |
| Data with I $\geq$ 2s(I)             | 8196  | 6188   |
| wR <sub>2</sub> , (all data)         | 0.0633  | 0.1539   |
| S (all data)                         | 1.038   | 0.972  |
| R <sub>1</sub> [I $\geq$ 2s(I)]      | 0.0249  | 0.0607   |
| Parameters/<br>Restraints            | 276/1   | 307/0  |
| Data Completeness<br>/ %             | 98.3  | 99.1   |
| Biggest diff.<br>peak/hole           | 0.900/-1.017  | 3.029/-2.838   |

**Table 18:** Crystallographic data and structure refinement for (5) and (6).

| Compound                             | (7)  | (8)   |
|--------------------------------------|--|---|
| Formula                              | C <sub>44</sub> H <sub>66</sub> Dy <sub>2</sub> N <sub>8</sub> O <sub>20</sub> | C <sub>34</sub> H <sub>42</sub> Br <sub>2</sub> Cl <sub>4</sub> Dy <sub>2</sub> N <sub>10</sub> O <sub>10</sub> |
| FW / g·mol <sup>-1</sup>             | 1352.04  | 1377.39   |
| Crystal System                       | Triclinic  | Triclinic   |
| Space Group                          | P $\bar{1}$  | P $\bar{1}$   |
| a / Å                                | 9.6829(3)  | 7.7956(2)   |
| b / Å                                | 10.9671(3)   | 13.0105(3)  |
| c / Å                                | 14.4192(4)   | 14.9481(4)  |
| $\alpha$ / °                         | 92.595(2)  | 65.179(2)   |
| $\beta$ / °                          | 102.512(2)   | 82.936(2)   |
| $\gamma$ / °                         | 111.426(2)   | 75.080(2)   |
| U / Å <sup>3</sup>                   | 1378.44(7)   | 1329.47(6)  |
| Z                                    | 1  | 1   |
| T / K                                | 293  | 180   |
| F(000)                               | 678  | 666   |
| D <sub>c</sub> / Mg m <sup>-3</sup>  | 1.629  | 1.720   |
| m(Ga-K $\alpha$ ) / mm <sup>-1</sup> | 14.348   | 17.135  |
| Data Measured                        | 20046  | 15378   |
| Unique Data                          | 6537   | 6341  |
| R <sub>int</sub>                     | 0.0280   | 0.0262  |
| Data with I $\geq$ 2s(I)             | 6006   | 5863  |
| wR <sub>2</sub> , (all data)         | 0.0843   | 0.1191  |
| S (all data)                         | 1.092  | 1.099   |
| R <sub>1</sub> [I $\geq$ 2s(I)]      | 0.0309   | 0.0434  |
| Parameters/<br>Restraints            | 340/5  | 270/0   |
| Data Completeness<br>/ %             | 98.7   | 97.8  |
| Biggest diff.<br>peak/hole           | 1.523/-1.596   | 2.241/-1.570  |

**Table 19:** Crystallographic data and structure refinement for (7) and (8).

| Compound                            | (9)  | (10)  |
|-------------------------------------|--|---|
| Formula                             | C <sub>36</sub> H <sub>42</sub> Cl <sub>2</sub> Dy <sub>2</sub> N <sub>6</sub> O <sub>14</sub> | C <sub>59</sub> H <sub>65</sub> Cl <sub>6</sub> Dy <sub>2</sub> N <sub>13</sub> O <sub>12</sub> |
| FW / g·mol <sup>-1</sup>            | 1178.65  | 1685.94   |
| Crystal System                      | Monoclinic   | Orthorhombic  |
| Space Group                         | C2/c   | P2 <sub>1</sub> 2 <sub>1</sub> 2  |
| a / Å                               | 25.7038(4)   | 18.5074(2)  |
| b / Å                               | 11.7943(2)   | 15.7734(2)  |
| c / Å                               | 17.3004(3)   | 11.7563(2)  |
| α / °                               | 90   | 90  |
| β / °                               | 123.303(1)   | 90  |
| γ / °                               | 90   | 90  |
| U / Å <sup>3</sup>                  | 4383.46(13)  | 3431.95(8)  |
| Z                                   | 4  | 2   |
| T / K                               | 180  | 180   |
| F(000)                              | 2312   | 1680  |
| D <sub>c</sub> / Mg m <sup>-3</sup> | 1.786  | 1.631   |
| m(Ga-Kα) / mm <sup>-1</sup>         | 18.638   | 12.973  |
| Data Measured                       | 28841  | 50363   |
| Unique Data                         | 5459   | 8230  |
| R <sub>int</sub>                    | 0.0492   | 0.0189  |
| Data with I ≥ 2σ(I)                 | 4979   | 8086  |
| wR <sub>2</sub> , (all data)        | 0.1286   | 0.0526  |
| S (all data)                        | 1.052  | 1.035   |
| R <sub>1</sub> [I ≥ 2σ(I)]          | 0.0450   | 0.0205  |
| Parameters/<br>Restraints           | 282/2  | 412/4   |
| Data Completeness<br>/ %            | 99.7   | 99.8  |
| Biggest diff.<br>peak/hole          | 1.423/-2.172   | 1.025/-0.557  |

**Table 20:** Crystallographic data and structure refinement for (9) and (10).

| Compound                            | (11)   | (12)  |
|-------------------------------------|--|---|
| Formula                             | C <sub>17</sub> H <sub>35</sub> Cl <sub>3</sub> DyN <sub>7</sub> O <sub>10</sub> | C <sub>17</sub> H <sub>32</sub> Br <sub>3</sub> DyN <sub>7</sub> O <sub>8.5</sub> |
| FW / g·mol <sup>-1</sup>            | 766.37   | 872.72  |
| Crystal System                      | Monoclinic   | Monoclinic  |
| Space Group                         | P2 <sub>1</sub> /c   | C2/c  |
| a / Å                               | 9.0786(3)  | 24.1793(13)   |
| b / Å                               | 15.8413(5)   | 18.1694(8)  |
| c / Å                               | 19.8975(6)   | 14.2531(7)  |
| α / °                               | 90   | 90  |
| β / °                               | 90.585(3)  | 113.458(4)  |
| γ / °                               | 90   | 90  |
| U / Å <sup>3</sup>                  | 2861.45(16)  | 5744.2(5)   |
| Z                                   | 4  | 8   |
| T / K                               | 180  | 293   |
| F(000)                              | 1532   | 3376  |
| D <sub>c</sub> / Mg m <sup>-3</sup> | 1.779  | 2.018   |
| m(Ga-Kα) / mm <sup>-1</sup>         | 2.951  | 17.210  |
| Data Measured                       | 22602  | 17421   |
| Unique Data                         | 9262   | 6778  |
| R <sub>int</sub>                    | 0.0237   | 0.0449  |
| Data with I ≥ 2σ(I)                 | 7462   | 5505  |
| wR <sub>2</sub> , (all data)        | 0.0730   | 0.1410  |
| S (all data)                        | 1.035  | 1.012   |
| R <sub>1</sub> [I ≥ 2σ(I)]          | 0.0293   | 0.0511  |
| Parameters/<br>Restraints           | 420/29   | 361/11  |
| Data Completeness<br>/ %            | 99.3   | 98.4  |
| Biggest diff.<br>peak/hole          | 1.961/-2.149   | 1.673/-1.501  |

**Table 21:** Crystallographic data and structure refinement for (11) and (12).

| Compound                            | (13)   | (14)   |
|-------------------------------------|--|--|
| Formula                             | C <sub>26</sub> H <sub>35</sub> N <sub>12</sub> O <sub>13</sub> Pr | C <sub>25</sub> H <sub>29</sub> N <sub>12</sub> O <sub>11</sub> Sm |
| FW / g·mol <sup>-1</sup>            | 864.57   | 823.95   |
| Crystal System                      | Monoclinic   | Triclinic  |
| Space Group                         | P2 <sub>1</sub> /c   | P1̄  |
| a / Å                               | 13.4841(6)   | 11.2564(11)  |
| b / Å                               | 17.1978(7)   | 12.2229(11)  |
| c / Å                               | 14.8180(8)   | 12.7992(11)  |
| α / °                               | 90   | 79.099(7)  |
| β / °                               | 90.409(4)  | 86.086(7)  |
| γ / °                               | 90   | 63.855(7)  |
| U / Å <sup>3</sup>                  | 3436.2(3)  | 1552.1(3)  |
| Z                                   | 4  | 2  |
| T / K                               | 180  | 180  |
| F(000)                              | 1752   | 826  |
| D <sub>c</sub> / Mg m <sup>-3</sup> | 1.671  | 1.763  |
| m(Ga-Kα) / mm <sup>-1</sup>         | 11.593   | 14.908   |
| Data Measured                       | 17032  | 13159  |
| Unique Data                         | 6002   | 5506   |
| R <sub>int</sub>                    | 0.0806   | 0.0432   |
| Data with I ≥ 2s(I)                 | 3978   | 4903   |
| wR <sub>2</sub> , (all data)        | 0.1395   | 0.1415   |
| S (all data)                        | 0.928  | 1.045  |
| R <sub>1</sub> [I ≥ 2s(I)]          | 0.0548   | 0.0520   |
| Parameters/<br>Restraints           | 510/24   | 473/10   |
| Data Completeness<br>/ %            | 96.1   | 97.6   |
| Biggest diff.<br>peak/hole          | 2.239/-0.758   | 1.276/-1.537   |

**Table 22:** Crystallographic data and structure refinement for (13) and (14).

| Compound                            | (15)   | (16)   |
|-------------------------------------|--|--|
| Formula                             | C <sub>24</sub> H <sub>24</sub> DyN <sub>11</sub> O <sub>7</sub> | C <sub>29</sub> H <sub>31</sub> DyF <sub>3</sub> N <sub>9</sub> O <sub>8</sub> S |
| FW / g·mol <sup>-1</sup>            | 741.04   | 885.19   |
| Crystal System                      | Monoclinic   | Orthorhombic   |
| Space Group                         | P2 <sub>1</sub> /c   | P2 <sub>1</sub> 2 <sub>1</sub> 2 <sub>1</sub>                                    |
| a / Å                               | 10.7732(2)   | 11.9291(2)   |
| b / Å                               | 18.7426(5)   | 16.2341(3)   |
| c / Å                               | 14.1343(3)   | 17.7045(3)   |
| α / °                               | 90   | 90   |
| β / °                               | 104.805(2)   | 90   |
| γ / °                               | 90   | 90   |
| U / Å <sup>3</sup>                  | 2759.22(11)  | 3428.62(10)  |
| Z                                   | 4  | 4  |
| T / K                               | 150  | 180  |
| F(000)                              | 1468   | 1764   |
| D <sub>c</sub> / Mg m <sup>-3</sup> | 1.784  | 1.715  |
| m(Ga-Kα) / mm <sup>-1</sup>         | 14.379   | 12.098   |
| Data Measured                       | 26955  | 24233  |
| Unique Data                         | 6592   | 8383   |
| R <sub>int</sub>                    | 0.0392   | 0.0231   |
| Data with I ≥ 2s(I)                 | 5996   | 8128   |
| wR <sub>2</sub> , (all data)        | 0.0884   | 0.0675   |
| S (all data)                        | 1.052  | 1.052  |
| R <sub>1</sub> [I ≥ 2s(I)]          | 0.0327   | 0.0258   |
| Parameters/<br>Restraints           | 452/4  | 480/5  |
| Data Completeness<br>/ %            | 99.3   | 99.7   |
| Biggest diff.<br>peak/hole          | 0.846/-0.897   | 0.391/-0.925   |

**Table 23:** Crystallographic data and structure refinement for (15) and (16).